VNIVERSITAT DE VALÈNCIA

Tesis Doctoral

Programa de Doctorat en Física

Phenomenology of Quasi-Dirac neutrinos and a study of high-dimensional neutrino masses

Author: Gaetana Anamiati

IFIC - Universitat de València - CSIC - Department de Física Teórica

Director: Martin Hirsch

Valencia, December 2018

A nonna Enza che mi insegnó le tabelline.

Alla mia famiglia che mi ha dato ali per volare e radici per cui tornare.

Non so come il mondo potrà giudicarmi ma a me sembra soltanto di essere un bambino che gioca sulla spiaggia, e di essermi divertito a trovare ogni tanto un sasso o una conchiglia più bella del solito, mentre l'oceano della verità giaceva inesplorato davanti a me.
(Isaac Newton)

Come l'uomo più evoluto che si innalza con la propria intelligenza e che sfida la natura con la forza incontrastata della scienza.
Con addosso l'entusiasmo di spaziare senza limiti nel cosmo è convinto che la forza del pensiero sia la sola libertà.
(Giorgio Gaber)

Martin Hirsch,
Investigador Cientifico de IFIC/CSIC de València,

CERTIFICA:

Que la presente memoria "Phenomenology of Quasi-Dirac neutrinos and a study of high-dimensional neutrino masses" ha sido realizada bajo su dirección en el Instituto de Física Corpuscular, centro mixto de la Universidad de Valencia y del CSIC, por Gaetana Anamiati y constituye su Tesis para optar al grado de Doctor en Física.

Y para que así conste, en cumplimiento de la legislación vigente, presenta en el Departamento de Física Teórica de la Universidad de Valencia la referida Tesis Doctoral, y firma el presente certificado.

Valencia, a 26 de Julio de 2018.

Martin Hirsch

Contents

Resumen de la Tesis

Con la observación de las oscilaciones de neutrinos [1], [2] sabemos que los neutrinos son partículas con masa y esto implica física más allá del Modelo Estándar. Las oscilaciones de neutrino [3], [4] surgen de una mezcla entre el sabor y los autoestados de masa, las dos bases están relacionadas por una transformación unitaria, llamada *matriz de mezcla*. Cuando un neutrino se propaga en el espacio, oscila y la probabilidad de oscilación del neutrino depende de la energía del neutrino, la distancia recorrida, el cuadrado de la diferencia de los dos estados de masa y los elementos de la matriz de mezcla. Con el descubrimiento de las oscilaciones de los neutrinos no solo sabemos que tienen masa sino que la masa de los tres tipos (m_1, m_2, m_3) son diferentes. Sabemos por el ajuste global actual $\Delta m^2_{12} = 7.56 \cdot 10^{-5} eV^2$ y $\Delta m^2_{13} = 2.55 \cdot 10^{-3} eV^2$ [5]. Sin embargo, dado que los experimentos de oscilación solo pueden sondear el cuadrado de la diferencia de masa, los valores absolutos de m_1, m_2, m_3 permanecen desconocidos, y también se desconoce si m_2 pesa más que m_3. La última pregunta está conocida como *problema de jerarquia de masa de neutrinos*. Si $m_2 < m_3$ la jerarquía se llama *normal*, en caso contrario se llama *inverted*.
Las masas de neutrinos pueden generarse introduciendo campos de neutrinos dextrógiros en el contenido de partículas, de modo que se emparejen con el levógiro para producir términos de masa de Dirac. Por otro lado, existe otra posibilidad que requiere un solo estado de quiralidad, aunque el número leptónico (una simetría accidental en el Modelo Estándar) se rompe. Si el número leptónico ya no se conserva, un neutrino es su antiparticula y es una partícula de *Majorana*. Si los neutrinos son partículas de Majorana, se vuelve natural explicar la pequeñez de las masas de neutrinos en comparación con las masas de los fermiones cargados. En este contexto, el operador de orden más bajo que genera masas de neutrinos de Majorana después de

la ruptura de la simetría electrodébil es unicamente el operador de Weinberg de dimensión 5 [6]. Solo hay tres formas de generar el operador $d = 5$ a nivel árbol [7]. Estos se conocen como mecanismo see-saw de tipo I, tipo II, tipo III con un singlete fermiónico $SU(2)$, triplete escalar y triplete fermiónico respectivamente. Sin embargo, este mecanismo no es fenomenológicamente comprobable debido a la escala de energía muy alta. La masa del neutrino liviano viene dada por $m_{\nu_{\alpha\beta}} = c_{\alpha\beta}v^2/\Lambda$, donde v es el valor esperado del campo de Higgs en el vacío. Entonces, para un acoplamiento orden ~ 1, Λ toma el valor del orden de $\sim 10^{14}$ GeV que está fuera del rango de los experimentos actuales y previsibles. Otra alternativa interesante viene dada por el mecanismo see-saw inverso [8] que es una realización diferente del see-saw en el sentido de que la pequeñez de las masas de neutrinos se debe a la violación del número leptonico en una escala de energía más baja. Eso predice neutrinos dextrógiros en la escala TeV que pueden ser probados en los experimentos de *Large Hadron Collider*.
Como vemos, aunque los experimentos de neutrinos han demostrado que los neutrinos oscilan y, por lo tanto, tienen masa, todavía hay muchas preguntas fundamentales a las que no tenemos respuestas: ¿Cuál es el valor de la escala de masa de neutrinos? ¿Los neutrinos son partículas de Majorana o de Dirac? ¿Cuál es la jerarquía de masas? ¿Por qué las masas de neutrinos son tan pequeñas respecto de los otros fermiones?
Motivados por estas preguntas, estudiamos algunas extensiones teóricas del Modelo Estándar que expliquen las masas de neutrinos y su mezcla. La tesis está organizada de la siguiente manera, el segundo capítulo es una breve reseña de la física de neutrinos. Luego, habrá dos capítulos dedicados a los neutrinos cuasi-Dirac. Finalmente, en el quinto capítulo, el tema cambia, nos enfocamos en la generación de masas de neutrinos con operadores de dimension alta.

El see-saw inverso discutido anteriormente predice que los neutrinos pesados N_R serán cuasi-Dirac. Esto motivó el estudio llevado en el tercer Capítulo. Aquí, discutimos las señales de violación de número leptónico (LNV) que podría originarse en escenarios con neutrinos cuasi-Dirac. En particular, nosotros nos centramos en el ratio dentro de eventos con dos leptones de signo igual a aquellos con signo opuesto R_{ll}, que es el LNV

observable más prometedor para la investigación experimental en el LHC. Es bien sabido que si los eventos con dos leptones se originan en la producción/decaimiento de neutrinos pesados de Majorana, se espera que el valor de R_{ll} sea 1. Nosotros mostramos que en el caso cuasi-Dirac, en el régimen en el que la diferencia de masas ΔM entre la pareja de neutrinos dextrógiros pesados es del orden de sus anchuras, cualquier valor dentro del intervalo $R_{ll} \in [0, 1]$ es posible y $R_{ll} = 0$ se aborda en el límite $\Delta M/\Gamma \to 0$ que define el límite de puro Dirac de la pareja de neutrinos cuasi-Dirac. Mostramos que $R_{ll} = \Delta M^2/(2\Gamma^2 + \Delta M^2)$ donde ΔM es el término que viola el número leptónico. En particular, en el apéndice damos la descripción matemática correcta de las oscilaciones de neutrino-neutrino y neutrino-antineutrino y mostramos en detalle el cálculo realizado para obtener el resultado obtenido para R_{ll}.

Entonces está claro que un resultado experimental $R_{ll} < 1(\neq 0)$ podría proporcionar información valiosa sobre el mecanismo de generación de las masas de neutrinos ligeros. Realizamos nuestra discusión en la estructura del *modelo simetrico left-right* equipado con el mecanismo del see-saw inverso, ya que esta configuración parece ser de interés experimental prominente en la busqueda actual de señales de LNV y de neutrinos destrógiros en el LHC. Queremos enfatizar que nuestro resultado principal para R_{ll} no depende de la realización particular del modelo del escenario de neutrinos cuasi-Dirac (otras características, como por ejemplo la tasa total de eventos para la producción de neutrinos, obviamente depende del modelo específico).

Al desarrollar nuestro análisis, introducimos una nueva parametrización del see-saw inverso que permite escanear el espacio de parámetros de la teoría fundamental, respetando de forma automática, en el mismo, todas las restricciones fenomenológicas de la teoría efectiva a baja energía. El uso de esta parametrización ha demostrado ser muy conveniente para realizar nuestro estudio numérico. Al discutir la fenomenología del LHC, señalamos que los valores específicos de $R_{ll} \neq 0.1$ se pueden correlacionar con características especiales de observables en los modos de decaimiento de los neutrinos pesados, y esta correlación puede ayudar a probar el escenario. En nuestro marco teórico pueden ocurrir todos los modos de decaimiento siguientes, y todos con cocientes de desintegración considerables:

$$\begin{aligned} N \to W_L^{\pm} + l^{\pm}\,, \qquad & N \to Z_L + \nu\,, \quad N \to h + \nu\,, \\ N \to (W_R)^* + l^{\pm} \to jjl^{\pm} \quad , \quad & N \to (Z_R)^* + \nu \to (jj \text{ or } l^+l^-)\nu\,, \end{aligned} \tag{1}$$

donde W_L y Z_L son los bosones de norma del Modelo Estándar, h es el boson de Higgs con masa $m_h \simeq 125$ GeV, y ν representa un neutrino ligero de cualquier sabor. En nuestro análisis también asumimos $m_N < m_{W_R}$, donde m_N denota colectivamente la pareja de valores propios de masa $(M_R^{\pm})_{11}$ para los neutrinos pesados más ligeros, para que los bosones de norma levógiros $(W_R)^*$ y $(Z_R)^*$ estén fuera de la capa de masas desde los decaimientos de los neutrinos pesados N. También asumimos por simplicidad $(M_R^{\pm})_{ii} > m_{W_R}$ para $i > 1$ para que una sola pareja de neutrinos dextrógiros contribuya a la señal (esta segunda hipotesis no es necesaria cada vez que las diferentes parejas de neutrinos pesados sean suficientemente separadas en masa para que las diferentes masas invariantes de los productos de decaimiento se puedan reconstruir con buena confianza). En el análisis numérico también incluimos el modo de decaimiento $N \to (Z_R)^* + \nu$ aunque su cociente de desintegración esté suprimido por el see-saw, y por lo tanto, en gran medida irrelevante con respecto a los otros decaimientos. Además de los modos de decaimiento que se muestran en eq. (1), decaimientos en escalares adicionales además del Higgs también podrían ser posibles, si ellos son más livianos que N. Esto sin embargo, depende de detalles desconocidos del sector escalar. Por lo tanto, para ser definitivos, asumiremos que cualquier nuevo escalar es más pesado que N para que los modos de decaimientos dominantes estén todos listados en eq. (1). Aquí presentamos algunos ejemplos de resultados numéricos que corresponden a un valor fijo de m_{W_R} y de m_N. Esto se justifica por el hecho de que la detección de señales de $lljj$ en el LHC implicaría que m_{W_R} y al menos un m_{N_i} serán medidos. Los datos de neutrinos de baja energía se mantienen fijos en su mejor ajuste para un espectro jerárquico normalmente ordenado (no surgen diferencias cualitativas para las jerarquías invertidas).

La Fig. 1 muestra algunos valores típicos de los cocientes de desintegración para diferentes estados finales versus el parámetro LNV μ que varia dentro del intervalo $[10^{-5}, 10^{-1}]$ GeV. Eligimos los dos valores representativos $m_N = 0.2$ TeV (líneas continuas) y $m_N = 0.5$ TeV (líneas discontinuas) y dos valores diferentes para la masa de W_R, $m_{W_R} = 2$ TeV (panel izquierdo)

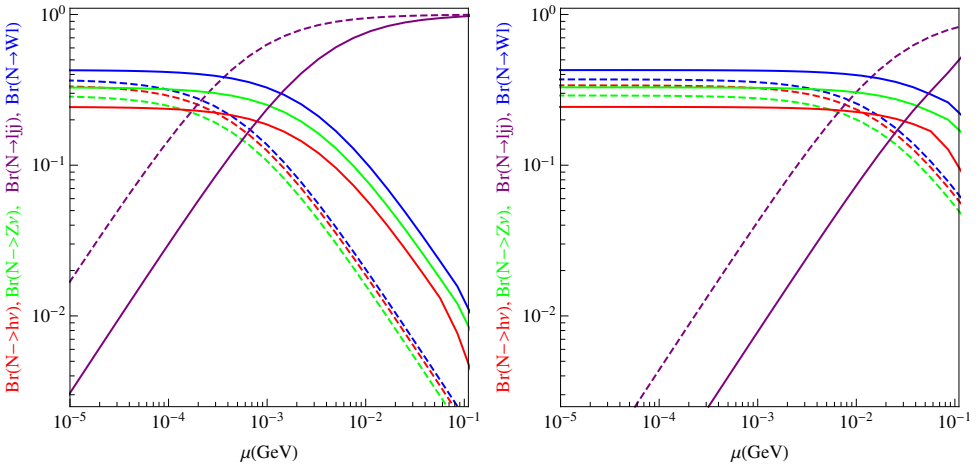

Figure 1: Los cocientes de desintegración para los decaimientos de los neutrinos pesados en función de μ. Las líneas azules son para $\Gamma(N \to W+l)$, verde para $\Gamma(N \to Z+\nu)$, rojo para $\Gamma(N \to h^0+\nu)$ y morado para el decaimiento a tres cuerpos $\Gamma(N \to ljj)$. Las líneas continuas corresponden a $m_N = 0.2$ TeV y líneas discontinuas a $m_N = 0.5$ TeV. El panel izquierdo es para $m_{W_R} = 2$ TeV y el panel derecho para $m_{W_R} = 5$ TeV. Los estados finales leptónicos (y quark) se suman sobre los índices de sabor para que no haya dependencia de las mezclas de fermiones.

y $m_{W_R} = 5$ TeV (panel derecho). El valor más bajo de m_{W_R} corresponde aproximadamente al exceso de masa encontrado en CMS en [49], sin embargo, este exceso no está confirmado en su último análisis [56]. El valor más grande corresponde aproximadamente al máximo m_{W_R} que el LHC puede sondear en los próximos años de ejecución. En los estados finales sumamos sobre las diferentes generaciones de quarks y leptones, para que los resultados sean independientes de la mezcla de los neutrinos. Para valores pequeños de μ, los decaimientos a los bosones de norma del Modelo Estándar dominan las tasas de decaimiento. Los cocientes de desintegración para $N \to W_R^* + l^\mp \to l^\mp jj$ y para los decaimientos a los bosones de norma del Modelo Estándar se vuelven similares para los valores intermedios de μ, el intervalo detallado donde pasa eso depende, sin embargo, fuertemente de los valores de m_N y de m_{W_R}. Para valores grandes de μ los decaimientos a tres cuerpos se vuelven dominantes. En el see-saw inverso, las masas de los neutrinos ligeros están dadas por

$$m_\nu \simeq m_D^T \frac{1}{M_R^T} \mu \frac{1}{M_R} m_D.$$

La ecuación contiene las tres matrices m_D, M_R y μ como parámetros libres. Manteniendo fijas las masas de los neutrinos ligeros a valores de acuerdo con los datos experimentales y para valores fijos de M_R, se obtiene una escala $m_D \propto 1/\sqrt{\mu}$. Dado que todos los acoplamientos de los neutrinos pesados a los bosones de norma del Modelo Estándar son proporcionales a m_D, decaimientos a bosones del Modelo Estándar dominan cuando μ es pequeño. En el intento de escudriñar otros efectos de violación del sabor (LFV) en el escenario del see-saw inverso, también calculamos cocientes de desintegraciones para procesos que violen el sabor leptónico a baja energía, el más relevante de los cuales es $\mathrm{Br}(\mu \to e\gamma)$. Nosotros encontramos que $\mathrm{Br}(\mu \to e\gamma)$ puede proporcionar restricciones aditionales relevantes solo para valores muy pequeños de μ ($\mu \ll 10^{-6}$ GeV), que corresponda al régimen en el cual el límite de Dirac puro se acerca y se espera que R_{ll} sea ≈ 0.

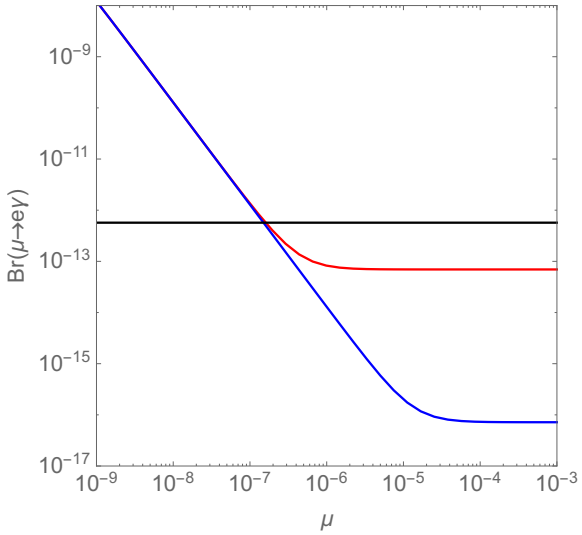

Figure 2: El cociente de desintegración $\mu \to e\gamma$ en función de μ. $m_{R_1} = 200$ GeV, $m_{R_2} = 1$ TeV, $m_{R_3} = 1.5$ TeV. La línea roja es para $m_{W_R} = 2$ TeV, la línea azul para $m_{W_R} = 5$ TeV. La línea negra muestra el limite superior encontrado por el experimento MEG.

El comportamiento mostrado en la Fig.2 se entiende fácilmente. La contribución debida al acoplamiento de los neutrinos pesados a los bosones de norma del Modelo Estándar que son proporcionales a m_D domina cuando μ es pequeño, mientras que para los valores grandes de μ, $\mu > 10^{-6}$ si $m_{W_R} = 2$ TeV y $\mu > 10^{-5}$ si $m_{W_R} = 5$ TeV, domina la contribución debida al acoplamiento de los neutrinos pesados a los bosones W_R.

En el cuarto capítulo discutimos la fenomenología de las oscilaciones de neutrinos cuasi-Dirac. Fenomenológicamente, esto corresponde a la existencia de tres parejas de neutrinos con masas ligeramente diferentes, por lo tanto, los experimentos de oscilación son sensibles no solo a las escalas de masa atmosférica y solar habituales, sino también a tres pequeñas divisiones masivas ε_i. Además, para neutrinos cuasi-Dirac hay más de 3+1 ángulos y fases que se tienen que considerar. En este capítulo, analizamos las restricciones de estos parámetros de neutrinos cuasi-Dirac impuestos por los actuales datos de oscilación de neutrinos. Discutimos una parametrización

completamente general del sector leptónico para tres generaciones de neutrinos cuasi-Dirac. Además de las masas leptonicas cargadas, hay un total de 6 masas, 12 ángulos y 12 fases. Los experimentos de oscilación no son sensibles a la escala global de masa de neutrinos ni a a las 5 fases (que son del tipo Majorana). Por lo tanto, nos queda un modelo de espacio de 24 dimensiones, en comparación con el espacio de seis dimensiones para un caso ordinario de tres generaciones ($\Delta m^2_{\odot}$, $\Delta m^2_{\rm Atm}$, θ_{12}, θ_{13}, θ_{23} y δ). Numéricamente es dificultoso manejar una cantidad tan grande de parámetros al mismo tiempo, por lo tanto, hemos analizado varios casos especiales diferentes. Primero, tomamos una única diferencia de masa $\varepsilon_i^2 \neq 0$. Si dividimos dos neutrinos con masa m_i en una pareja de particulas cuasi-degeneradas con masas $\sqrt{m_i^2 - \varepsilon_i^2/2}$ y $\sqrt{m_i^2 + \varepsilon_i^2/2}$ entonces aparece una nueva longitud de oscilación $L \propto 1/\varepsilon_i^2$ que está asociada a la conversión de neutrinos activos a estériles. Se pueden derivar límites muy estrictos para ε_i^2 en esta extensión a un parámetro, del orden de 10^{-11}eV^2 para $\varepsilon^2_{1,2}$ (de datos de neutrinos solares) y 10^{-5}eV^2 para ε^2_3 (dominado por los datos de neutrinos atmosféricos de Super-K). A continuación, consideramos el caso de cuando una diferencia en masa y uno de los ángulos no estándar puedan tomar valores distintos de cero al mismo tiempo. En esta situación, pueden aparecer degeneraciones de la función χ^2, lo que implica que a partir de un solo experimento en muchos casos ya no será posible derivar límites significativos sobre los parámetros individuales. Estas degeneraciones se pueden resolver considerando datos de más de un experimento, accediendo a diferentes $P\left(\nu_\alpha \to \nu_\beta\right)$. Luego consideramos la posibilidad de anular completamente los efectos de ε_i cambiando algunas combinaciones particulares de los ángulos θ_{ij} de nuestra parametrización. En lugar de buscar la forma exacta de estas combinaciones de parámetros bastante complejas, discutimos una definición más simple, describiendo 3 ángulos φ_i asociados a rotaciones entre las columnas i y $i+3$ de la matriz de mezcla cuasi-Dirac, de modo que en el límite donde estos ángulos son iguales a $\pi/4$ ($3\pi/4$) la columna $i+3$ (i) de la matriz de mezcla se desvanece y, por lo tanto, la masa de neutrinos asociada desaparece de la fórmula de probabilidad de oscilación. Queremos enfatizar que para estas combinaciones particulares de parámetros no se pueden derivar límites sobre ε_i de experimentos de oscilación. En este contexto, es interesante notar la tensión entre el valor de la escala de masa solar preferida por ajustes globales ($\sim 7.6 \times 10^{-5}\text{eV}^2$) y el valor mas

bajo preferido por datos solares ($\sim 4 \times 10^{-5}\text{eV}^2$). Eso podría resolverse con un valor distinto de cero tanto para ε_1 y para ε_2. Por último, consideramos la posibilidad de que las diferencias de masa ε_i sean demasiado pequeñas para medirlas en experimentos de oscilación. Incluso en este escenario, uno puede tener salidas del escenario de Dirac que conserva el número leptónico debido a los nuevos ángulos θ_{ij} (y fases ϕ_{ij}). Como se mencionó anteriormente, hay una gran cantidad de dichos parámetros. Sin embargo, se puede demostrar que con 3 parejas de neutrinos con la misma masa, las oscilaciones solo dependerán en un total de 13 combinaciones de ángulos y fases. Además, si nos enfocamos solo en neutrinos electronicos y muonicos (debido a la escasez de datos en τ neutrinos, lo ignoramos por completo), este número está reducido a 7, que corresponde a 6 ángulos y 1 fase. Llamamos estas combinaciones de parámetros $X_{1\ldots7}$ y enfatizamos que no se pueden identificar con θ_{12}, θ_{13}, θ_{23} ni δ, ya que estas cantidades por sí mismas no son físicas. En cambio, los 7 X_i corresponden a combinaciones de éstos y fases adicionales θ_{ij} angles y ϕ_{ij}. A través de un escaneo en 7 dimensiones de estos X_i parámetros en ausencia de divisiones masivas encontramos los límites impuestos por la información actual. Fundamentalmente, para los neutrinos Dirac solo hay 4 parámetros. Por lo tanto, el límite de Dirac corresponde a 3 relaciones entre los 7 X_i. Al probar estas relaciones, encontramos que $\min\left(\chi^2_{\text{Dirac}}\right) - \min\left(\chi^2\right) = 1.9$, es decir, los datos actuales son compatibles con el escenario de Dirac.

En nuestro análisis no tomamos en cuenta los datos de cada experimento de oscilación existente. Nos enfocamos en los experimentos que deberían proporcionar las restricciones más importantes para cuasi-Dirac neutrinos. En primer lugar, consideramos KamLAND [65] ya que determina de manera más exacta, la diferencia de masa solar $\Delta m^2_{\odot}$. KamLAND [117] demostró la naturaleza oscilatoria de la transformación del sabor del neutrino mediante la observación de antineutrinos electrónicos ($\bar{\nu}_e$) de reactores nucleares con energías de unos pocos MeV ubicados a diferentes distancias. La idea de este experimento fue explotar el antiguo sitio subterráneo de Kamiokande y la presencia de grandes reactores de energía nuclear ubicados a diferentes distancias en el intervalo $[160, 824]$ km. Estos reactores producen $\bar{\nu}_e$ isotrópicamente en el decaimiento β de los fragmentos de la fisión de neutrones. Los anti-neutrinos electronicos se capturan en protones en el detector de centelleo líquido de acuerdo con la reacción: $\bar{\nu}_e + p \to e^+ + n$. Estos eventos se

detectan utilizando la coincidencia retardada entre la emisión de positrones y los rayos gamma de la captura de neutrones.
A partir de los experimentos con neutrinos solares, ajustamos los datos de dispersión elástica de Super-K [110] y las mediciones de flujos de *pp* [111] y ^7Be [112] en Borexino. Esta elección está motivada por el hecho de que Super-K [110] tiene los datos más precisos en altas energías, mientras Borexino fija la parte de baja energía del espectro de neutrinos solares. Tomamos los datos de neutrinos atmosféricos de [113]. Nosotros nos concentramos en nuestro ajuste en la muestra sub-GeV, ya que los neutrinos con energía más bajas serán más sensibles a los pequeños valores de ε_i^2. El detector de Borexino se encuentra a gran profundidad (3.800 m de agua equivalente) en el laboratorio del Gran Sasso, localizado en el centro de Italia. Borexino detecta los neutrinos solares midiendo la energía depositada en el objetivo del centelleo líquido retrocediendo electrones después de la dispersión elástica de neutrinos y electrones. El centelleador convierte rápidamente la energía cinética de electrones en fotones, detectada y convertida en señales electrónicas (fotoelectrones). La interacción en el centelleador de partículas ionizantes, como las que resultan de las desintegraciones radiactivas dentro del detector (el fondo), puede imitar y cubrir la señal esperada. Se hicieron todos los esfuerzos posibles para minimizar la contaminación radiactiva del centelleador y de todos los materiales del detector circundante. El objetivo principal del experimento es la detección de los neutrinos monocromáticos que se emiten en el decaimiento de captura de electrones de ^7Be en el sol [112] y el estudio espectral de otros componentes del espectro solar, como los neutrinos pp.
Super-K [124] es un gran detector de agua Cherenkov, se encuentra a 1000 m bajo tierra (2700 m de agua equivalente) en el Observatorio Kamioka, en lo profundo de la mina Kamioka en Gifu Prefecture, Japón. El detector consta de dos partes: el detector interno, que estudia los detalles de las interacciones de neutrinos, y el detector externo, que identifica las partículas cargadas entrantes y salientes. En particular, sobre los neutrinos solares, Super-K es sensible a ^8B y hep neutrinos solares en el intervalo de energía alrededor de 4 a 18.7 MeV y mide con precisión el tiempo de interacción del neutrino.
Además, utilizamos los datos de la colaboración MINOS (supervivencia de neutrinos muónicos y antimuónicos) [114] y T2K (supervivencia de neutrinos

muonicos y la transición del neutrino muonico al neutrino electrónico) [115], ya que estos dos experimentos determinan Δm^2_{Atm} mejor que los datos atmosféricos. El experimento MINOS realiza mediciones de precisión de la oscilación de neutrinos a través de la desaparición de ν_μ. La característica principal de este experimento es que por primera vez se usan dos conjuntos de datos diferentes [114]: neutrinos producidos en el acelerador NuMI [125] y los producidos por las interacciones de los rayos cósmicos en la atmósfera. El acelerador proporciona una fuente de neutrinos con una línea de base fija y un espectro de energía que alcanza un máximo de $L/E \sim 250$ km/GeV, cerca de la región donde la probabilidad de supervivencia de ν_μ alcanza su primer mínimo. Los neutrinos atmosféricos se producen con un intervalo de $E \sim (0.5 - 10^4)$ GeV y $L \sim (10 - 10^4)$ km. La combinación de estas dos muestras aumenta la precisión de las mediciones de oscilación. Además, MINOS tiene la capacidad de separar neutrinos y antineutrinos caso por caso.

T2K (Tokai a Kamioka) [127], [128] es un experimento *long baseline* de oscilación de neutrinos que utiliza un intenso haz de neutrinos muónicos para medir el ángulo de mezcla θ_{13} a través de la aparición ν_e [129] y el ángulo de mezcla θ_{23} y la diferencia de masa Δm^2_{23} a través de la desaparición de ν_μ [130]. Este experimento fue posible gracias a la construcción del acelerador de protones de alta intensidad J-PARC a 295 km de distancia del detector Super-Kamiokande (SK) [131]. A partir de la interacción del haz de protones de 30 GeV extraído de J-PARC y el objetivo de grafito se generan piones que decaen rápidamente a muones y neutrinos muonicos.

Y, finalmente, tenemos en cuenta los datos de DayaBay [116], ya que de los tres actuales experimentos de neutrino de reactor, Daya Bay determina θ_{13} con el error más pequeño. El complejo de energía nuclear de Daya Bay se encuentra en la ciudad de Shenzhen, China. Consiste en seis reactores de agua presurizada de 2.9 GWth que producen aproximadamente $3.5 \times 10^{21} \bar{\nu_e}/s$. El experimento de Daya Bay consta de tres salas experimentales subterráneas (EH) conectadas con túneles horizontales, las dos salas cercanas (EH1 y EH2) y la sala alejada (EH3). Ocho detectores de antineutrino (AD) se instalan en las tres salas, con dos en EH1, dos en EH2 y cuatro en EH3. Las ubicaciones de las salas experimentales se determinaron para optimizar la sensibilidad a θ_{13}.

El experimento de Daya Bay midió la tasa y el espectro de energía de los

antineutrinos de electrones emitidos y se observó un total de interacciones de decaimiento beta inverso de $2.5 \times 10^6 \nu_e$. Las estadísticas sin precedentes de esta muestra permitieron la medición más precisa de la desaparición de ν_e.

También discutimos brevemente el potencial del experimento futuro JUNO para mejorar las restricciones existentes. El observatorio subterráneo de neutrinos de Jiangmen (JUNO) [134], un detector de centelleo líquido subterráneo polivalente de 20 kton, se propuso con la determinación de la jerarquía de masa de neutrinos como objetivo primario. La detección de antineutrinos generados por un clúster de centrales nucleares permitirá la determinación de la jerarquía de masa de neutrinos con un significancia de $3 - 4\sigma$ a seis años de funcionamiento de JUNO. La medición del espectro del antineutrino con una excelente resolución energética también conducirá a la determinación precisa de los parámetros de oscilación de neutrinos $\sin^2\theta_{12}, \Delta m^2_{12}$ y Δm^2_{ee} con una precisión superior a 1%, que jugará un papel crucial en la prueba futura de unitariedad de la matriz de mezcla. Mientras tanto, JUNO también puede suministrar excelentes oportunidades para probar la hipótesis de neutrinos estériles a escala eV, utilizando o fuentes de neutrinos radiactivos o un haz de neutrinos producido en un ciclotrón.

En nuestros ajustes, para determinar los intervalos permitidos de los parámetros del modelo, usamos el método χ^2. Tomamos errores estadísticos y sistemáticos de las publicaciones experimentales, a lo que agregamos un mayor error sistemático (pequeño) para las incertidumbres en nuestros cálculos teóricos. Este último error sistemático fue elegido de tal manera que nuestra simulaciones reproducen los rangos de parámetros permitidos para los parametros de oscilación estandar, determinados por el experimento respectivo, típicamente dentro del intervalo (1-1.5) σ c.l. Tenga en cuenta que no intentamos hacer un ajuste global de precisión para la oscilación estándar de neutrinos parámetros. Más bien, consideramos reproducir los resultados experimentales para el caso estándar como una prueba de la fiabilidad de nuestro límites derivados.

Para concluir, progresos en la prueba para cuasi-Diracidad se pueden hacer en el futuro con una medición más precisa de $P(\nu_e \to \nu_\mu)$ y $P(\nu_\mu \to \nu_\mu)$. Por lo tanto, más estadísticas tomada en T2K, MINOS+ o NOVA y, en particular, las futuras mediciones más precisas posibles en DUNE deberían

proporcionar una prueba mas sensible para esta configuración particular de neutrinos cuasi-Dirac sin nuevas escalas masivas.

En el quinto capítulo discutimos las masas de neutrinos procedentes de operadores de dimensión alta. Como ya mencionamos, para las masas de neutrinos de Majorana, el operador de menor dimensión es el operador de Weinberg a $d = 5$. Como mencionamos, la pequeñez de las masas de neutrinos depende de la escala de la violación del número leptónico $\Lambda(10^{14})$ GeV, demasiado grande para ser probada. Sin embargo, para los neutrinos Majorana, se puede escribir [9]

$$m_\nu \propto \epsilon \cdot \left(\frac{1}{16\pi^2}\right)^n \cdot \left(\frac{v}{\Lambda}\right)^{d-5} \cdot \frac{v^2}{\Lambda}. \tag{2}$$

Aquí, la masa del neutrino está relacionada con el número de bucles (n) en que se genere y la dimensión (d) del operador. Significa que, fijados los parámetros n y d uno puede estimar la escala tipica Λ para la cual se generan masas de neutrinos. Aquí discutimos la posibilidad de que las masas de neutrinos se originen a partir de operadores de dimensión superior. Visto que ejemplos de realizaciones de 1-bucle, 2-bucle y 3-bucle del operador de Weinberg se estudiaron ampliamente en la literatura [9], [10], [11] así como análisis de masas de neutrinos en $d = 7$ a nivel árbol [12] y 1-bucle [13], [14], nosotros estudiamos la deconstrucción de los $d = 9$, $d = 11$ y $d = 13$ operadores de masa de neutrinos a nivel de árbol. Veremos que para estos operadores de dimensión alta Λ está en el intervalo $[10^2 - 10^4]$ GeV, que se puede probar en un futuro cercano. Nuestro objetivo es construir, para cada operador, todas las topologías posibles y luego identificar las topologías que permiten construir modelos genuinos. Aquí, un modelo es considerado genuino en el nivel d si automáticamente prohíbe masas de neutrino al orden inferior *sin* el uso de simetrías adicionales. Esta suposición implica que el nivel de árbol a d=5 y d=7, así como las contribuciones de d=5 1-bucle y d=7 1-bucle deberían estar ausentes. Muy pocos modelos genuinos pueden construirse, a pesar del hecho de que el número de las topologías aumenten rápidamente con la dimensión del operador. Con vértices renormalizables, uno puede construir 18 topologías y 66 diagramas al nivel $d = 9$; estos números aumentan a 92 topologías y 504 diagramas en el nivel $d = 11$, y

finalmente en $d = 13$ uno encuentra 576 topologías y 4199 diagramas. De todos estos, sólo encontramos 10 modelos genuinos: 2 modelos a $d = 9$ y $d = 11$ cada uno, y 6 modelos en $d = 13$. Discutimos como nuestra definición de un modelo genuino de masa requiere que todos estos modelos de alta dimensión usen grandes representaciones $SU(L)$. Por ejemplo, los dos modelos de $d = 9$ requieren cuatrupletes y quintupletes. Por otro lado, para algunos $d = 13$ modelos se necesitan septupletes escalares. Estos modelos de alta dimensión no requieren solo representaciones más grandes pero también mas de ellas: tres partículas nuevas son suficientes para uno de los dos modelos $d = 9$, mientras que para $d = 11$ ($d = 13$) se necesitan cuatro (cinco) campos exóticos. Por lo tanto, los modelos serán necesariamente más barrocos con dimensiones más grandes. Este hecho, junto con la escala de la nueva física requerida para los operadores de dimensión alta, hace que estos modelos sean comprobables en experimentos de aceleradores y también en búsquedas de violación de sabor leptónico.

Resumiendo, esta tesis se centra en dos temas de investigación. El primero es la "cuasi-Diracidad" de neutrinos. En general, los neutrinos pueden tener términos de masa que violen el número leptónico (Majorana) y que consirven el número leptónico (Dirac). Si los términos masivos que violan el número leptónico son más pequeños que los que conservan, los neutrinos son partículas *cuasi-Dirac*. El segundo es la generación de masas de neutrinos con operadores de alta dimensión y la catalogación de los diagramas genuinos de neutrinos. La palabra "genuino" aquí se refiere a los diagramas que proporcionan la contribución dominante a la matriz de masa de neutrinos, suponiendo que ninguna simetrías más allá del Modelo Estándar sea añadida. Más allá del estudio de la literatura sobre los temas presentados, el trabajo ha sido llevado a cabo tanto con herramientas analíticas como numéricas: MATHEMATICA y FORTRAN.

List of publications

- G. Anamiati, M. Hirsch and E. Nardi, "Quasi-Dirac neutrinos at the LHC", JHEP **1610** (2016) 010 doi:10.1007/JHEP10(2016)010, arXiv:1607.05641.
- G. Anamiati, R. M. Fonseca and M. Hirsch, "Quasi Dirac neutrino oscillations", Phys. Rev. **D 97** (2018) no.9, 095008 doi:10.1103/PhysRevD.97.095008, arXiv:1710.06249.
- G. Anamiati, Oscar Castillo-Felisola, Renato M. Fonseca, J. C. Helo, M. Hirsch, "High dimensional neutrino masses, in phase of publication", arxiv: 1806.07264.

Chapter 1

Introduction

With the observation of neutrino oscillations [1], [2] we know that neutrinos are massive particles and this implies physics beyond the Standard Model. Neutrino oscillations [3], [4] arise from a mixing between the flavour and the mass eigenstates, the two eigenbasis are related by a unitary transformation, the so-called *mixing matrix*. When a neutrino propagates in space it oscillates and the neutrino oscillation probability depends on the neutrino energy, the distance traveled, the square of the difference of the two mass states and the elements of the mixing matrix. With the discovery of neutrino oscillations it is now known that not only they have mass but the mass of the three types (m_1, m_2, m_3) are different. We know from the current global fit $\Delta m^2_{12} = 7.56 \cdot 10^{-5} eV^2$ and $\Delta m^2_{13} = 2.55 \cdot 10^{-3} eV^2$ [5]. However, since oscillation experiments can only probe the square of the mass difference, the absolute values of m_1, m_2, m_3 remain unknown, as well as the question of whether or not m_2 is heavier than m_3 is still unknown. The latter question is known as *neutrino mass hierarchy problem*. If $m_2 < m_3$ the hierarchy is called *normal*, viceversa it is called *inverted*.
Neutrino masses can be generated by introducing right-handed neutrino fields in the particle content, such that they pair with the left-handed one to produce Dirac mass terms. On the other hand there is another possibility that requires just one chirality state although lepton number (an accidental symmetry in the Standard Model) gets broken. If the lepton number is no longer conserved, a neutrino is its antineutrino and it is a *Majorana* particle. If neutrinos are Majorana particles it becomes naturally

to explain the smallness of neutrino masses compared to the masses of the charged fermion. In this context the lowest order operator which generates Majorana neutrino masses after the electroweak symmetry breaking is the unique $d = 5$ Weinberg operator [6]. There are only three ways to generate the $d = 5$ operator at tree level [7]. These are known as type I, type II, type III see-saw mechanism with an $SU(2)$ singlet fermion, triplet scalar and triplet fermion respectively. However this mechanism is not phenomenologically testable because of the very high energy scale. The light neutrino mass is roughly given by $m_{\nu_{\alpha\beta}} = c_{\alpha\beta}v^2/\Lambda$, where v is the vacuum expectation value of the Higgs. So, for coupling to the order of ~ 1, Λ takes the value of the order of $\sim 10^{14}$ GeV which is out of the range of current and foreseeable expriments. Another interesting alternative is given by the inverse see-saw mechanism [8] that is a different realization of the see-saw in the sense that the smallness of the neutrino masses is due to the violation of lepton number at a lower energy scale. It predicts right-handed neutrinos at the TeV scale which may be probed at the *Large Hadron Collider* experiments.
As we see, although neutrino experiments have proven that neutrinos oscillate and thus have mass, there are still many fundamental questions to which we have no answers:

- What is the value of the neutrino mass scale?
- Are neutrinos Majorana or Dirac particle?
- What is the mass hierarchy?
- Why are neutrino masses so small with respect to the other fermions?

Motivated by this list we study some theoretical extension of the Standard Model which explain neutrino masses and mixing. The thesis is organized as follows, the second Chapter is a short review on neutrino physics. Then, there will be two Chapters dedicated to Quasi-Dirac neutrinos.
The inverse see-saw discussed above predicts heavy neutrinos N_R to be quasi-Dirac. This motivated the study carried out in the third Chapter. We have already mentioned that the Majorana nature of the neutrino is related to lepton number violation. One of the best known search at the LHC is using same-sign lepton plus two jets from the production and the

subsequent decay of heavy neutrinos. A heavy Majorana neutrino decays in equal amount to either a lepton (l^-) or an antilepton (l^+) plus two jets. One can therefore measure at the LHC the ratio (R_{ll}) of SS to opposite sign (OS) dilepton events produced via $W \to lN \to lljj$. R_{ll} is expected 1 for a Majorana neutrino and 0 for a Dirac neutrino. We show that for quasi-Dirac neutrinos R_{ll} can assume any value in the interval $[0, 1]$. We show that $R_{ll} = \Delta M^2/(2\Gamma^2 + \Delta M^2)$ where ΔM is the mass term that violates lepton number. Our result on R_{ll} does not depend on the particular model realization of the quasi-Dirac neutrino scenario. We have carried out our discussion in the framework of a left-right symmetric model equipped with an inverse seesaw mechanism. The choice to work in the LR symmetric model has been dictated by the interesting phenomenology that appears in this setup in view of the ongoing searches for signals of LNV and of RH neutrinos at the LHC. In discussing the LHC phenomenology, we point out that specific values of $R_{ll} \neq 0, 1$ can be correlated with special features of observables in the decay modes of the heavy neutrinos, and this correlation can help to test the scenario. In the appendix we give the correct mathematical description of neutrino-neutrino and neutrino-antineutrino oscillations and we show in detail the calculation done to get the result obtained in this Chapter for the ratio of sime sign to opposite sign.
In the fourth Chapter we discuss the case of light active quasi-Dirac neutrinos. We discuss the phenomenology of quasi-Dirac neutrino oscillations and derive limits on the relevant parameter space from various experiments. We consider a model with three active and three sterile neutrinos. If the mass terms that violate lepton number are zero the neutrinos are Dirac particles. If the lepton number is no longer conserved it is possible to construct quasi-Dirac neutrino pairs. In particular, departures from the Dirac case can be either new mass splittings (ϵ_i^2) or new mixing angles (or, in general, both). For a system of 3 pairs of quasi-Dirac neutrinos there are 30 free parameters: two independent Δm_{ij}^2 plus one overall mass scale, three ϵ_i^2, twelve angles and twelve phases. The number of parameters is too large to be fitted simultaneously, so we consider two simplified scenarios. First, we show the limits on the three ϵ_i^2 adding them one at a time to the formula for the oscillation probability. From a single experiment degenerate minima can occur. They disappear when we consider the combination of more experiments. In the last case, the bounds found for $\epsilon_{1,2}^2$ are of the order of

$10^{-11}eV^2$ and for ϵ_3^2 of the order of $10^{-5}eV^2$. Then we consider the case with two new parameters in the formula of the oscillation probability: a mass splitting and a new angle. Again, degeneracies can occur and for a single experiment it is impossible to derive limits on the parameters. These degeneracies can be resolved considering combined experiments. Secondly, we discuss the limit where mass splittings are too small to be measured in oscillation experiments, hence there are just angles and phases to deal with. In this situation, it can be shown that from the 24 parameters only 13 combinations enter the oscillation probabilities of active neutrinos. Moreover, since in our analysis we focused on the charged current data for e and μ neutrinos and anti-neutrinos ignoring data on τ neutrinos, due to the scarcity of information, from the 13 combinations only 7 can be constrained. We discuss the construction of these 7 quantities, the current constraints and possible tests for quasi-Dirac neutrinos in this limit. We will see that current data is compatible with pure Dirac and does not provide stringent test on this scenario.
In the fifth Chapter the topic changes, we focus on the generation of neutrino masses. As we already mentioned, for Majorana neutrino masses the lowest dimensional operator possible is the Weinberg operator at $d = 5$. As we mentioned, for the tree level d=5 operator the smallness of the neutrino masses depends on the scale of lepton number violation $\Lambda(10^{14})$ GeV, too large to be tested. However, for Majorana neutrinos, one can write [9]

$$m_\nu \propto \epsilon \cdot \left(\frac{1}{16\pi^2}\right)^n \cdot \left(\frac{v}{\Lambda}\right)^{d-5} \cdot \frac{v^2}{\Lambda}. \tag{1.1}$$

Here, the neutrino mass is related also to the number of loops (n) at which it is generated and the dimension (d) of the operator. It means that, fixed the parameters n and d one can estimate the typical scale Λ for which neutrino masses are generated. Here we discuss the possibility that neutrino masses originate from higher dimensional operators. Examples of 1-loop, 2-loop and 3-loop realizations of the Weinberg operator have been studied extensively in the literature [9] [10] [11] as well as analysis of $d = 7$ neutrino masses at tree level [12] and 1-loop [13] [14]. Therefore we consider all tree-level decompositions of the $d = 9$, $d = 11$ and $d = 13$ neutrino mass operators. We will see that for these higer operators the scale Λ is in the range $[10^2 - 10^4]$ GeV, that is testable in the near future. Our aim

is constructing, for each operator, all possible topologies and then identify those topologies which allow to construct genuine models. Here, a model is considered genuine at level d if it automatically forbids lower order neutrino masses *without* the use of additional symmetries. This assumption implies that the d=5 and the d = 7 tree-level, as well as the d = 5 1-loop, d = 7 1-loop contributions should be absent. To conclude, with renormalizable interactions only, we found 18 topologies and 66 diagrams for $d = 9$, and 92 topologies plus 504 diagrams at the $d = 11$ level. At $d = 13$ we found already 576 topologies and 4199 diagrams. However, among all these there are only very few genuine neutrino mass models: At $d = (9, 11, 13)$ we found only (2,2,2) genuine diagrams and a total of (2,2,6) models. We also briefly discuss how neutrino masses and angles can be easily fitted in these high-dimensional models.
In summary, this thesis concentrates on two subjects: the "quasi-Diracness" of neutrinos both for heavy and light neutrinos and the generation of neutrino masses for high-dimensional operators.

Chapter 2

Neutrino physics

We briefly review in this chapter the key facts about neutrinos. The goal is to give the basis on neutrino physics in order to understand the next chapters. We refer the interested reader to [3] [4] for books on neutrino physics. In section 2.1 we describe neutrinos oscillation both in vacuum and in matter, in section 2.2 we describe the neutrino nature and finally in section 2.3 we focus on the mechanisms generating neutrino masses.

2.1 Neutrino oscillations

2.1.1 Neutrino oscillations in vacuum

Let us consider a neutrino with flavor α created in a leptonic W decay together with the charged lepton of the same flavor. It is a superposition of the mass eigenstates ν_i

$$|\nu_\alpha > \;\; = \;\; \sum_i U_{\alpha i} |\nu_i >, \tag{2.1}$$

where U is a unitary matrix, the so-called *lepton mixing matrix*. After a time t the evolution of the initial state gives

$$|\nu_\alpha(t) > \;\; = \;\; \sum_i e^{-iE_i t} U_{\alpha i} |\nu_i >, \tag{2.2}$$

where E_i and p_i are respectively the energy and momentum of ν_i in the laboratory frame. The energy is given by the relativistic energy-momentum relation

$$E_i = \sqrt{|\vec{p}|^2 + m_i^2}, \tag{2.3}$$

in which we are supposing that our ν_α has been produced with a definite momentum $\vec{p}$, so that all of its mass-eigenstate components have this common momentum. In the ultrarelativistic limit, $|\vec{p}_i| = p_i >> m_i$, we can approximate the energy as

$$E_i = \sqrt{|\vec{p}|^2 + m_i^2} \sim p + \frac{m_i^2}{2p} \sim E + \frac{m_i^2}{2E}, \tag{2.4}$$

and since in this limit $t \sim L$

$$|\nu_\alpha(L) > = \sum_i e^{-i(\frac{m_i^2}{2E})L} U_{\alpha i} |\nu_i > . \tag{2.5}$$

So, the probability of finding a ν_β in an originally ν_α beam is

$$\begin{aligned} P_{\nu_\alpha \to \nu_\beta} &= | < \nu_\beta | \nu_\alpha(L) > |^2 \\ &= | \sum_i e^{-i(\frac{m_i^2}{2E})L} U_{\alpha i} U^*_{\beta i} |^2. \end{aligned} \tag{2.6}$$

Let's suppose now that only two neutrinos mix, the 2×2 unitary matrix takes the simple form [15]

$$U = \begin{pmatrix} \cos(\theta) & \sin(\theta) \\ -\sin(\theta) & \cos(\theta) \end{pmatrix}, \tag{2.7}$$

with θ the so-called *mixing angle*. Inserting U in eq. (2.6) we immediately find that:

$$P_{\nu_\alpha \to \nu_\beta} = \sin^2(2\theta) \sin^2 \left(\frac{\Delta m^2 L}{4E} \right), \tag{2.8}$$

and for the survival probability we get:

$$P_{\nu_\alpha \to \nu_\alpha} = 1 - \sin^2(2\theta)\sin^2\left(\frac{\Delta m^2 L}{4E}\right), \tag{2.9}$$

where Δm^2 is the squared mass difference of the two mass eigenstates: $\Delta m^2 = m_2^2 - m_1^2$.
Now, we should include the omitted factors $\hbar$ and c in the oscillatory quantity $\sin^2(\Delta m^2 L/(4E))$ to get a quantitative estimate. This can be done by dimensional analysis. With Δm^2 in eV^2, L in km, E in GeV, $\Delta m^2 L/(4E)$ has dimension $[eV^2 Km/c^2 GeV]$. Since it is the argument of a trigonometric function, it must be dimensionless. It is easy to verify that one can rewrite it as $\sin^2(\Delta m^2 L c^3/(4E\hbar))$.

$$\begin{aligned} P_{\nu_\alpha \to \nu_\alpha} &= 1 - P_{\nu_\alpha \to \nu_\beta} \\ &\sim 1 - \sin^2(2\theta)\sin^2\left(1.27\frac{\Delta m^2(eV^2)L(km)}{E(GeV)}\right). \end{aligned} \tag{2.10}$$

From this equation we can note some features of neutrino oscillation:

- **the angle** θ: it defines how different the flavor states are from the mass states. If $\theta = 0$, the flavor states are identical to the mass states. Clearly, in this case, oscillations cannot happen.

- **the mass squared difference** Δm^2: the oscillation probability depends only on neutrino squared mass splitting. So for neutrino oscillation to occur at least one of the mass states must be non-zero This means that the neutrino **must have mass**. Moreover, the experiments can give us detailed information on the difference between the mass values but not on the absolute mass of the states.

- L/E: this is the parameter that experimentalists control. L is the distance between the source and the detector and E is the neutrino energy. If the parameter L/E is fixed one can deduce what will be the sensitivity of an experiment that measures neutrino masses. One has the first peak of oscillation at

$$\frac{1.27\Delta m^2 L}{4E} = \frac{\pi}{2},$$

if for example $L \sim 10^4 km$ and $E \sim 1GeV$, the experiment will be sensitive to Δm^2 down to $\sim 10^{-4} eV^2$

2.1.2 Neutrino oscillations in matter

In the previous section we showed how to arrive at the oscillation probability formula of neutrinos travelling in vacuum. Here we want to describe neutrino oscillations in matter and we will follow the description given in [15].
In matter, neutrino propagation is affected by interactions. If we assume that the neutrino interactions with matter are the flavor-conserving ones described by the Standard Model [16], there are two types of interactions that we have to take into account. First, for electron neutrinos - and only in this case - they can exchange a W boson with the electron. This fact gives rise to an extra-potential

$$V_W = \pm\sqrt{2} G_F N_e, \tag{2.11}$$

where G_F is the Fermi coupling constant and N_e the number density of electrons, the positive (negative) sign applies to ν_e ($\bar{\nu}_e$).
Secondly, a neutrino in matter can exchange a Z boson with an electron, proton or neutron. The Standard Model tells us that, at zero momentum transfer, any flavor of neutrinos can do this and moreover that the Z couplings to electron and proton are equal and opposite. So, since the matter through which the neutrino is travelling is electrically neutral, the electron and proton contributions cancel out and the new potential will be proportional to the number density of neutrons:

$$V_Z = \mp\frac{\sqrt{2}}{2} G_F N_n. \tag{2.12}$$

Let's consider the Schroedinger equation in the laboratory frame:

$$i\frac{\partial}{\partial t}|\nu(t)> = \mathcal{H}|\nu(t)>, \tag{2.13}$$

where $|\nu(t)>$ is the multi-component neutrino state vector, each component corresponds to each neutrino flavor. Let's continue by considering only two

neutrino flavors for simplicity. $\mathcal{H}$ will be a 2×2 matrix in $\nu_e - \nu_\mu$ space. It is instructive to show what would be the Hamiltonian in the vacuum case. Assuming that the neutrino has definite momentum, common to all its mass eigenstate components and using the relativistic approximation (2.4), it is easy to verify that

$$\mathcal{H}_v = \frac{\Delta m^2}{4E} \begin{bmatrix} -\cos(2\theta) & \sin(2\theta) \\ \sin(2\theta) & \cos(2\theta) \end{bmatrix} + \left(E + \frac{m_1^2 + m_2^2}{4E} \right) \begin{bmatrix} 1 & 0 \\ 0 & 1 \end{bmatrix}. \quad (2.14)$$

Here, the last contribution is a multiple of the identity matrix and we can freely subtract it without affecting the difference of the eigenvalues of $\mathcal{H}_v$. Let's construct the corresponding Hamiltonian for propagation in matter. As we have seen we have to consider the two interaction potentials V_W and V_Z:

$$\mathcal{H}_m = \mathcal{H}_m + V_W \begin{bmatrix} 1 & 0 \\ 0 & 0 \end{bmatrix} + V_Z \begin{bmatrix} 1 & 0 \\ 0 & 1 \end{bmatrix}. \quad (2.15)$$

Recall that V_W affect only ν_e's, for this reason only the upper left term is non-vanishing. The V_Z term affects all the flavors, so a diagonal identity matrix is required. One can write

$$\mathcal{H}_m = \mathcal{H}_m + \frac{V_W}{2} \begin{bmatrix} 1 & 0 \\ 0 & -1 \end{bmatrix} + \frac{V_W}{2} \begin{bmatrix} 1 & 0 \\ 0 & 1 \end{bmatrix} + V_Z \begin{bmatrix} 1 & 0 \\ 0 & 1 \end{bmatrix}. \quad (2.16)$$

The two last contributions on the right-hand side are again multiple of the identity matrix and again can be dropped. Finally we have

$$\mathcal{H}_m = \frac{\Delta m^2}{4E} \begin{bmatrix} -(\cos(2\theta) - x) & \sin(2\theta) \\ \sin(2\theta) & (\cos(2\theta) - x) \end{bmatrix}, \quad (2.17)$$

in which

$$x = \frac{V_W/2}{\Delta m^2/4E} = \frac{2\sqrt{2} G_F N_e E}{\Delta m^2}. \quad (2.18)$$

Now, if we define

$$\begin{aligned} \cos(2\theta_M) &= (\cos(2\theta) - x)Y, \\ \sin(2\theta_M) &= \sin(2\theta)Y, \\ \Delta m^2_M &= \frac{\Delta m^2}{Y}, \end{aligned} \tag{2.19}$$

solving the equations we find

$$Y = \sqrt{\sin^2(2\theta) + (\cos(2\theta) - x)^2} \tag{2.20}$$

and we can rewrite eq.(2.17) in the form of (2.14):

$$\mathcal{H}_{\mathcal{M}} = \frac{\Delta m^2_M}{4E} \begin{bmatrix} -\cos(2\theta_M) & \sin(2\theta_M) \\ \sin(2\theta_M) & \cos(2\theta_M) \end{bmatrix}. \tag{2.21}$$

Thus, Δm^2_M and θ_M are the splitting between the effective squared-masses of the eigenstates in matter and the effective mixing angle in matter respectively. Just as $\mathcal{H}_v$ leads to the vacuum oscillation probability in eq.(2.8), $\mathcal{H}_{\mathcal{M}}$ must lead to the matter oscillation probability

$$P_{M(\nu_\alpha \to \nu_\beta)} = \sin^2(2\theta_M) \sin^2\left(\frac{\Delta m^2_M L}{4E}\right). \tag{2.22}$$

There is a special case in which matter effects can be dramatically large. From eqs.(2.19) and (2.21) we see that if the vacuum mixing angle θ is very small and $x \sim \cos(2\theta)$, $\sin^2(2\theta_M) \sim 1$, its maximum value. This phenomenon, known as the Mikheyev-Smirnov-Wolfenstein resonance effect [16], was believed to occur inside the sun. However, we now know that the solar neutrino mixing angle is quite large in vacuum (34°). So, the effect of solar matter on neutrinos is still very significant but it is not quite as dramatic as once thought. Finally, a discussion on the sign of the parameter x is necessary. Recall that the mass splitting Δm^2 is defined as $m_2^2 - m_1^2$, so Δm^2 is positive or negative depending on if ν_2 is heavier or lighter than ν_1. Moreover, if the neutrinos are replaced by antineutrinos, the potential energy V_W would be negative. As a consequence, Δm^2_M and θ_M will have different values for antineutrinos than they do for neutrinos. It

means that there exists an asymmetry between antineutrino oscillation and neutrino oscillation that is induced by matter effects. This fact can be used to investigate whether the neutrino we have called ν_2 is heavier or lighter than the one we have called ν_1.

2.1.3 Neutrino parameters

In the last section we gave the oscillation probability formula 2.6 valid for any number of generations, then we treated the specific case of two generations. However, in the real world, there are three neutrinos so, neutrino oscillations require mixing among the three flavor states $\alpha = e, \mu, \tau$. For three generations, the standard parametrization of the lepton mixing matrix is

$$U = \begin{pmatrix} c_{12}c_{13} & s_{12}c_{13} & s_{13}e^{-i\delta} \\ -s_{12}c_{23} - c_{12}s_{23}s_{13}e^{i\delta} & c_{12}c_{23} - s_{12}s_{23}s_{13}e^{i\delta} & s_{23}c_{13} \\ s_{12}s_{23} - c_{12}c_{23}s_{13}e^{i\delta} & -c_{12}s_{23} - s_{12}c_{23}s_{13}e^{i\delta} & c_{23}c_{13} \end{pmatrix} \cdot \begin{pmatrix} e^{i\alpha_1/2} & 0 & 0 \\ 0 & e^{i\alpha_2/2} & 0 \\ 0 & 0 & 1 \end{pmatrix} \quad (2.23)$$

where c_{ij} and s_{ij} are $\cos(\theta_{ij})$ and $\sin(\theta_{ij})$ respectively. It is parametrized by three angles and three phases. If the massive neutrinos are Dirac particles only one phase is physical. It is because the Dirac Lagrangian is invariant under the global $U(1)$ transformation $\nu_{L,R} \to e^{i\alpha}\nu_{L,R}$ so through a redefinition of the fields one can eliminate two of the three phases. If the massive neutrinos are Majorana particles the Lagrangian is not invariant under the same transformation so these phases cannot be absorbed. In any case, they do not enter in the oscillation phenomena. A discussion on the neutrino nature will be given in the next section.
Experiments observing the oscillations of neutrinos produced in the sun have determined the squared difference of the masses m_1 and m_2, $\Delta m^2_{12} = \Delta m^2_{sol}$. The squared difference between the masses m_1 and m_3, $\Delta m^2_{13} = \Delta m^2_{atm}$, has been measured using the oscillation of neutrinos produced in the Earth's atmosphere. However, since oscillation experiments are only sensitive to mass-squared splittings the absolute values of m_1, m_2, m_3, as well as the question of whether or not m_2 is heavier than m_3 remains unknown. The latter question is known as the *hierarchy problem*:

- $m_1 < m_2 < m_3$ - Normal Hierarchy

parameter	best fit $\pm$ 1σ	2σ range	3σ range
Δm^2_{21} $[10^{-5}]$	$7.55^{+0.20}_{-0.16}$	7.20–7.94	7.05–8.14
$\lvert\Delta m^2_{31}\rvert$ $[10^{-3}]$ (NO)	2.50$\pm$0.03	2.44–2.57	2.41–2.60
$\lvert\Delta m^2_{31}\rvert$ $[10^{-3}]$ (IO)	$2.42^{+0.03}_{-0.04}$	2.34–2.47	2.31-2.51
$\sin^2\theta_{12}/10^{-1}$	$3.20^{+0.20}_{-0.16}$	2.89–3.59	2.73–3.79
$\theta_{12}/$	$34.5^{+1.2}_{-1.0}$	32.5–36.8	31.5–38.0
$\sin^2\theta_{23}/10^{-1}$ (NO)	$5.47^{+0.20}_{-0.30}$	4.67–5.83	4.45–5.99
$\theta_{23}/$	$47.7^{+1.2}_{-1.7}$	43.1–49.8	41.8–50.7
$\sin^2\theta_{23}/10^{-1}$ (IO)	$5.51^{+0.18}_{-0.30}$	4.91–5.84	4.53–5.98
$\theta_{23}/$	$47.9^{+1.0}_{-1.7}$	44.5–48.9	42.3–50.7
$\sin^2\theta_{13}/10^{-2}$ (NO)	$2.160^{+0.083}_{-0.069}$	2.03–2.34	1.96–2.41
$\theta_{13}/$	$8.45^{+0.16}_{-0.14}$	8.2–8.8	8.0–8.9
$\sin^2\theta_{13}/10^{-2}$ (IO)	$2.220^{+0.074}_{-0.076}$	2.07–2.36	1.99–2.44
$\theta_{13}/$	$8.53^{+0.14}_{-0.15}$	8.3–8.8	8.1–9.0
δ/π (NO)	$1.21^{+0.21}_{-0.15}$	1.01–1.75	0.87–1.94
$\delta/$	218^{+38}_{-27}	182–315	157–349
δ/π (IO)	$1.56^{+0.13}_{-0.15}$	1.27–1.82	1.12–1.94
$\delta/$	281^{+23}_{-27}	229–328	202–349

Table 2.1: Neutrino parameters from the global fit [5]

- $m_1 > m_2 > m_3$ - Inverted Hierarchy

So, to describe neutrino oscillations we need six different parameters: two masses, three mixing angles and one phase. We present in table 2.1 the current values for the oscillation parameters, which are extracted from a global fit from [5].

2.2 Dirac or Majorana?

With the observation of neutrino oscillations we know that neutrinos are massive particles and this implies physics beyond the Standard Model. Neutrino masses can be generated by introducing a right-handed neutrino

field in the particle content such that it pairs with the left-handed one to produce a Dirac mass term. On the other hand there is another possibility that requires just one chirality state although lepton number (an accidental symmetry in the Standard Model) gets broken. If the lepton number is no longer conserved, a neutrino is its antineutrino and it is a *Majorana* particle.

2.2.1 Dirac and Majorana particles

A Dirac particle is described by a four-component spinor ψ, which can be written as

$$\psi = \begin{pmatrix} \chi \\ \sigma_2 \phi^\star \end{pmatrix} \tag{2.24}$$

where χ and ϕ are two-component Weyl spinors and σ_2 is a Pauli matrix. The left-handed and right-handed components are defined as

$$\psi_L = P_L \psi \qquad \psi_R = P_R \psi \tag{2.25}$$

where $P_{L,R} = 1/2(1 \mp \gamma_5)$ are the chirality projectors. Therefore, in terms of Dirac spinors we have

$$\psi_L = \begin{pmatrix} \chi \\ 0 \end{pmatrix} \qquad \psi_R = \begin{pmatrix} 0 \\ \sigma_2 \phi^\star \end{pmatrix}. \tag{2.26}$$

We can further apply the charge conjugation to ψ

$$\psi^c = C\bar{\nu}^T = -\gamma^2\gamma^0\bar{\nu}^T = \begin{pmatrix} \phi \\ \sigma_2 \chi^\star \end{pmatrix}, \tag{2.27}$$

and see that the Weyl spinors χ and ϕ get exchanged. However, neutral massive fermions can be described by simpler spinors carrying only two independent components instead of four, as it was proposed by Ettore Majorana in 1937. A Majorana spinor has the following form

$$\psi = \begin{pmatrix} \lambda \\ \sigma_2 \lambda^\star \end{pmatrix}. \tag{2.28}$$

It is easy to see that the charge conjugation leaves Majorana spinors invariant. So, for a Majorana spinor

$$\psi^c = \psi. \tag{2.29}$$

2.2.2 Dirac and Majorana masses

The Dirac mass term for a particle ψ has the form

$$\mathcal{L}_D^{mass} = m_D \bar{\psi}_L \psi_R + h.c. \tag{2.30}$$

As we see, the mass term connects opposite chirality fields (the left-handed particle ψ_L to the right-handed ψ_R). Since the right-handed fields $\nu_{eR}, \nu_{\mu R}, \nu_{\tau R}$ do not exist in the SM a Dirac mass term is in principle precluded for neutrinos. However, it is a straightforward extension to add the three right-handed fields as singlets under the total SM gauge group, so that neutrinos become similar to the other massive fermion fields. In this way the mass term 2.30 can be generated by the same Higgs mechanism which is responsible for the mass terms for the other fermions.
A left-handed Majorana mass term has the form

$$\mathcal{L}_M^{mass} = M^M \bar{\psi}_L^c \psi_L + h.c. \tag{2.31}$$

So, in a theory that has only left-handed neutrinos, the neutrino could be massless or can have a Majorana mass as in eq. 2.31, which violates the lepton number by two units.

2.3 The Weinberg operator

The lowest order operator which generates Majorana neutrino masses after electroweak symmetry breaking is the unique $d = 5$ Weinberg operator [6]:

$$\mathcal{L} \;=\; \frac{1}{2} c_{\alpha\beta}^{d=5} \left(\bar{L_\alpha^c} \tilde{H}^\star \right) \left(\tilde{H}^\dagger L_\beta \right) + h.c., \tag{2.32}$$

where $L = (\nu_L, l_L)^T$ is the lepton doublet of the Standard Model, $H = (H^+, H^0)^T$ is the Higgs doublet, $\tilde{H} = i\sigma_2 H^\star$ and $c_{\alpha\beta}^{d=5} \propto 1/\Lambda$ is a model dependent coefficient suppressed by the scale of new physics Λ. The Greek indices represent flavor indices. The Majorana mass for the light neutrinos is of the form

$$m_\nu = c\frac{v^2}{\Lambda}, \tag{2.33}$$

where v is the vacuum expectation value (vev) of the Higgs. There are only three ways to generate the $d = 5$ operator at tree level, these are known as type-I [17]- [20], type-II [21]- [26], type-III [27] seesaw mechanisms depending on the heavy fields exchanged: the singlet fermion, the triplet scalar and the triplet fermion respectively. In this section we present all of them and finally we introduce the inverse see-saw [8] since, as we will see, in the next Chapter we concentrate on it.

2.3.1 See-saw type I

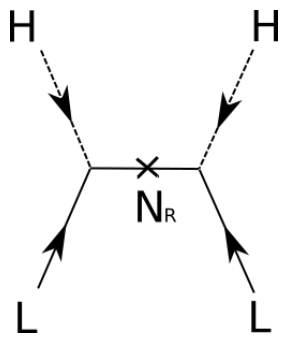

Figure 2.1: See-saw type-I diagram

In see-saw type I, three new fermion singlets without gauge interaction are added to the SM and play the role of the intermediate particle. They are right-handed neutrinos that here we call N_{Ri}. We can write the Lagrangian mass term as:

$$\mathcal{L}_\nu^{mass} = \frac{1}{2}(\bar{\nu}_L^c, \bar{N}_R) M \begin{pmatrix} \nu_L \\ N_R^c \end{pmatrix} + h.c. \tag{2.34}$$

with

$$M = \begin{pmatrix} 0 & m_D \\ m_D^T & M_R \end{pmatrix},$$

the mass matrix for the neutrino. Here both Dirac mass terms m_D and Majorana mass terms M_R are present. m_D is a generic 3×3 matrix and M_R is a symmetric matrix. If $M_R >> m_D$, after the diagonalization of the mass matrix, the singlet N_R becomes "heavy" acquiring a mass $\sim M_R$ and the light neutrino Majorana mass matrix takes the form

$$m_\nu \sim -m_D M_R^{-1} m_D^T \tag{2.35}$$

that explains the smallness of the light neutrino mass. On the other hand, if $M_R = 0$ the conservation of the lepton number is restored and the left-handed neutrino will have a Dirac mass $m_\nu = m_D$.

2.3.2 See-saw type II

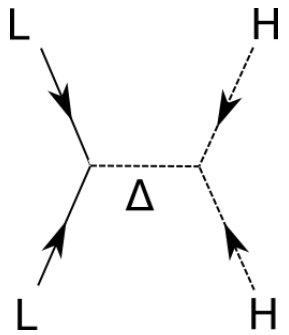

Figure 2.2: See-saw type-II diagram

In see-saw type II, a $SU(2)_L$ scalar triplet with hypercharge 1 is added to the SM. Here we call it Δ. In the doublet representation of $SU(2)_L$, using $\vec{\sigma} = (\sigma^1, \sigma^2, \sigma^3)$ and $\vec{\Delta} = (\Delta_1, \Delta_2, \Delta_3)$, the triplet can be written as a 2×2 matrix:

$$\Delta \;=\; \frac{1}{\sqrt{2}} \vec{\sigma} \vec{\Delta} = \begin{pmatrix} \Delta^+ & \Delta^{++} \\ \Delta_0 & -\Delta^+ \end{pmatrix}, \tag{2.36}$$

where we defined $\Delta^{++} = (\Delta_1 - i\Delta_2)/\sqrt{2}$, $\Delta^{+} = \Delta_3/\sqrt{2}$, $\Delta^{0} = (\Delta_1 + i\Delta_2)/\sqrt{2}$, with third component of isospin $I_3 = 1, 0, -1$. The Lagrangian terms will be

$$\mathcal{L} = -M_\Delta^2|\Delta|^2 - \lambda_\Delta L\Delta L - \mu_h H\Delta H + h.c., \tag{2.37}$$

where we have omitted gauge and flavor indices for simplicity. When the Higgs field gets a vev v the neutrino Majorana mass is generated:

$$m_\nu = \lambda_\Delta v_\Delta = \frac{\lambda_\Delta \mu_h v^2}{2M_\Delta^2}, \tag{2.38}$$

where v_Δ is the vev of the triplet. As long as M_Δ^2 is positive and large, v_Δ will be small in agreement with the constraints from the ρ parameter [28].

2.3.3 See-saw type III

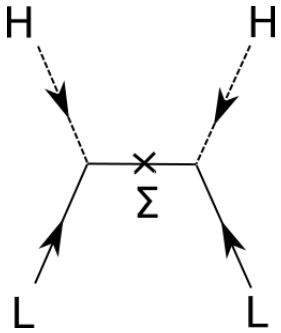

Figure 2.3: See-saw type-III diagram

In see-saw type III, three $SU(2)_L$ fermion triplets with zero hypercharge are added to the SM. Here we call them Σ_i. The Lagrangian mass term is

$$\mathcal{L}_\nu^{mass} = \frac{1}{2}(\bar{\nu}_L^c, \bar{\Sigma}^0)\begin{pmatrix} 0 & m_D \\ m_D^T & M_R \end{pmatrix}\begin{pmatrix} \nu_L \\ \Sigma^{0c} \end{pmatrix} + h.c. \tag{2.39}$$

which is the same as in type I seesaw just replacing N_R by Σ^0 and therefore leads to a light neutrino Majorana mass matrix

$$m_\nu \sim -m_D M_R^{-1} m_D^T. \tag{2.40}$$

2.3.4 Inverse see-saw

An alternative to the simplest type I see-saw model is the inverse see-saw [8]. It is obtained by extending the seesaw lepton content by adding three extra $SU(2)$ singlets S_i. After the electroweak symmetry breaking the mass matrix is:

$$M = \begin{pmatrix} 0 & m_D^T & M_L^T \\ m_D & 0 & M_R \\ M_L & M_R^T & \mu \end{pmatrix} \tag{2.41}$$

in the basis ν, N_R, S. If $M_L = 0$ and $\mu \neq 0$, it is called *inverse see-saw*, while if $M_L \neq 0$ and $\mu = 0$ it is called *linear see-saw* [29]. Let us focus on the inverse see-saw limit, the Lagrangian mass term is

$$\mathcal{L}^{mass} = -m_D \bar{\nu}_L N_R - M_R \bar{N}_R S - \mu \bar{S}^c S + h.c., \tag{2.42}$$

where μ is the parameter that violates the lepton number. If we assume $m_D, \mu << M_R$, the Majorana mass matrix for the light neutrinos is approximately given by

$$m_\nu = m_D^T (M_R^T)^{-1} \mu M_R^{-1} m_D. \tag{2.43}$$

Although M_R is a large Dirac ($\Delta L = 0$) mass scale suppressing the light neutrino masses, it can be much smaller than in type-I see-saw, in fact, the core of the inverse see-saw is that the smallness of the neutrino masses is guaranteed by assuming that μ is small. In the limit $\mu = 0$ the lepton number is conserved and the three light neutrinos are massless.

Chapter 3

Heavy Quasi-Dirac neutrinos

Lepton number violation is searched for at the LHC using the ratio of same-sign vs opposite-sign leptons (plus two jets). This ratio is 1 for Majorana neutrinos and 0 for Dirac ones. In this Chapter, based on [30] we show that for "quasi-Dirac" neutrinos, it can take any value in the interval [0,1]. We focus on the case of an inverse see-saw in the Left-Right Symmetric Model and we also discuss how a measurement of this ratio is correlated with heavy neutrinos decays. The Chapter is organized as follows. In the next section, we explain the motivation that led us to focus on this topic. In section 3.2, for completeness, we present the Left-Right symmetric model since it is the scenario in which we worked. Then, in section 3.3 we recall the main features of the inverse seesaw model [8], we describe in some details the steps to achieve approximate diagonalization of the full 9×9 neutrino mass matrix, and we write down the heavy neutrino couplings to the LR gauge bosons and to the Higgs. In the same section we also introduce a convenient parametrization which, in the inverse seesaw, plays an analogous role as the Casas-Ibarra parametrization [31] in the type-I seesaw. In section 3.4 we derive the expression for the ratio R_{ll}. Our result shows that the condition required for obtaining values of $R_{ll} \neq 0, 1$ is that the mass degeneracy of the quasi-Dirac neutrino pairs must be of the order of their decay width. In section 3.5 we discuss all relevant phenomenology (two and three body decays and branching ratios) that could be measured at the LHC.

3.1 Preliminaries

We have seen that the smallness of the neutrino masses can be more elegantly explained under the assumption that neutrinos are Majorana particles. Majorana neutrinos necessarily imply lepton number violation (LNV), a well known LNV process is for example neutrinoless double beta decay (for reviews on $0\nu\beta\beta$ see for example [32, 33]). LNV is also searched for at the LHC, using as a signature final states containing two same-sign (SS) leptons (plus jets and no missing energy in the event). This signature, specific for hadron collider searches, was originally proposed in [34] in the context of left-right (LR) symmetric extensions of the standard model (SM) [25, 35, 36].[1] A heavy Majorana neutrino, once produced on mass-shell, decays with equal probabilities to either a lepton (l^-) or an anti-lepton (l^+) (plus, for example, jets). Therefore, for dilepton events produced via $W \to lN \to lljj$ a ratio of SS to opposite sign (OS) dileptons $R_{ll} = 1$ is expected.[2] For a Dirac neutrino $R_{ll} = 0$ since lepton number is conserved. Here, we point out that in models with so-called "quasi-Dirac" neutrinos, R_{ll} can instead assume any value in the interval [0,1]. Hence a measurement of R_{ll}, different from zero or one, would provide valuable information on the mechanism underlying the generation of neutrino masses. "Quasi-Dirac" refers to a pair of Majorana neutrinos with a small mass splitting and a relative CP-sign between the two states, and that would correspond to a Dirac neutrino in the limit of exact mass degeneracy. Pairs of quasi-Dirac neutrinos often appear in seesaw-type models at scales not far from the electroweak scale, such as the inverse [8] and the linear [42, 43] seesaw, so that the possibility of observing $R_{ll} \neq 1, 0$ is naturally interweaved with the possibility of producing new heavy neutrinos in high energy collisions.[3]

[1] Although it is not widely known, SS dilepton events are not a distinctive feature of LR scenarios. They can also arise, in principle, in a variety of LNV models [37] some of which do not introduce right-handed neutrinos.

[2] Via loop corrections small departures from exact $R_{ll} \equiv 1$ are possible. This signals CP violation and is a necessary ingredient for models of leptogenesis [38] (see [39–41] for reviews).

[3] Scenarios with quasi degenerate right-handed neutrinos with masses and couplings allowing for their production at the LHC, but of the Dirac type [44], or effectively yielding lepton number conservation [45], have been also proposed.

When we started this work, both the ATLAS [46, 47] and the CMS collaboration [48, 49] had published results for dilepton plus jets ($\ell\ell jj$) events. In general, the sensitivities of ATLAS and CMS are quite similar. Nevertheless, there were some important differences in the analysis of the two collaborations. ATLAS, in its first publication [46], gave results for both, SS and OS lepton events separately. Since no excess was observed and the background in the OS sample is considerably larger than in the SS sample, the limits derived from the combined data are dominated by the SS sample. Note that this combination assumes implicitly $R_{ll} = 1$. Probably for this reason, in the latest analysis [47] ATLAS gave only the limits derived from the SS sample. CMS, on the other hand, gave only combined results for OS and SS samples [48, 49], despite the fact that CMS routinely measures the lepton charge. In the CMS analysis, which uses the full $\sqrt{s} = 8$ TeV statistics, an excess in the electron sample around $m_{eejj} \simeq 2$ TeV was reported. The excess contained 14 events with an estimated background of 4 events, corresponding to a local significance of about 2.8 σ c.l. No excess was observed in the muon sample. CMS points out that (i) only one of the 14 events is SS and (ii) no localized excess in $m_{\ell_2 jj}$, as would be expected from the decay of an on-shell intermediate N, was observed, and thus it was concluded that the excess was not consistent with the expectations from LR symmetric models. ATLAS, on the other hand, had zero events in the same invariant mass bin, but since in [47] ATLAS did not provide results for OS dileptons, their result was not inconsistent with CMS. The CMS excess had caused a flurry of theoretical activity [50], several of the proposed explanations were based on LR symmetric models, see for example the works in [51–55], where however $R_{ll} = 1$ is generally expected. Note that $R_{ll} = 0$ is expected in LR models with a linear seesaw [29], while $R_{ll} < 1$ can be obtained in the R-parity violating supersymmetric model of [56]. However, in the latest CMS analysis, which uses the full $\sqrt{s} = 13$ TeV statistics [57], the most significant excess, of $\sim 1.5\sigma$, is observed at $m_{eejj} \sim 3.4$ TeV in the electron channel. The $\sim 2.8\sigma$ excess seen at $m_{eejj} \sim 2.1$ TeV with the 8 TeV analysis is thus not confirmed by the present data.

Particularly relevant for our study was [58] which also focuses on a LR symmetric model equipped with the inverse see-saw mechanism, and where it is stressed that heavy pseudo-Dirac neutrinos allow to arrange for a suppression of SS versus OS dilepton events, and hence for a value of $R_{ll} < 1$.

Although we agreed on the general statement, we found disagreement as concerns the dependence of R_{ll} on the relevant model parameters. In particular, differently from [58], we found that the value of R_{ll} does not display a parametric dependence on the overall right-handed (RH) neutrino mass scale.[4] However, one year later, the same authors published another paper [60] in which the analytical result for R_{ll} now agrees with ours.

Neutrino oscillation experiments have established that neutrino flavor numbers are not conserved. By now we have very precise information on the active neutrino mixing angles, see for example [61]. Basically the "solar", $\sin^2\theta_\odot \simeq 1/3$, and "atmospheric", $\sin^2\theta_{\rm Atm} \simeq 1/2$, angles are large, while the "reactor" angle, $\sin^2\theta_{\rm R} \simeq 0.0234$, is smaller. It is therefore quite unnatural to assume that heavy neutrinos, if they exist, would only decay to the same lepton flavor associated with their production (as for example in $W_R^+ \to \ell_j^+ N_R \to \ell_j^+ \ell_j^- W_R^*$). From the theoretical point of view, different flavor dilepton events $\ell_i^+\ell_j^-$ and $\ell_i^+\ell_j^+$ with $i \neq j$ are expected to contribute sizeably to the whole dilepton samples, and for some choices of the model parameters they could even dominate the total signal. The relative amount of different flavor dilepton events could also provide valuable information about the structure of the seesaw matrices. Unfortunately, both ATLAS and CMS use $e\mu$ dilepton samples to estimate the backgrounds, giving results only for ee and $\mu\mu$ samples separately. We would like to stress that different flavor dilepton events should also be considered as a possible signal, and that presenting experimental results separately for each specific flavor channel would provide additional valuable information.

3.2 The Left-Right symmetric model

An extension of the SM is the LR symmetric model where all the left-handed fermions have a right-handed partner. It therefore follows that a new particle is introduced, the right-handed neutrino, that leads automatically to massive neutrinos. Moreover, in the symmetric phase of this model,

[4] The authors of [59] study the inverse seesaw within the standard model group. We agree with their expression for the LNV amplitude. However, different from the LR case, which we study in this paper, [59] concludes that LNV events are not observable for heavy neutrino masses above 100 GeV in their setup.

weak interactions conserve parity as in electromagnetic, strong and gravitational interactions. The minimal LR model [3] is based on the gauge group $SU(2)_L \times SU(2)_R \times U(1)_\alpha$. The gauge generators are $2^2 - 1$ for each $SU(2)$, they satisfy the Lie algebra:

$$[I_{iL,R}, I_{jL,R}] = i\epsilon_{ijk} I_{kL,R} \tag{3.1}$$

and one for the group $U(1)$. In total there are seven generators to which correspond seven bosons, three of them are the three new W_{iR} that balance the symmetry with the three W_{iL}. These fields are not mass eigenstates and we will discuss this later. In order to define the quantum number α we can consider the formula for the electric charge. For this model it acquires the form:

$$Q = I_{3L} + I_{3R} + \alpha, \tag{3.2}$$

and from this formula one can easily check that $\alpha = n_B - n_L$, where n_B and n_L are the baryonic and leptonic number respectively. In the SM n_B and n_L are global symmetries and are separately conserved, in this model they are taken together to form the parameter of a gauge symmetry.

3.2.1 General structure of the Left-Right symmetric model

In this model the fermions are represented in left and right doublets

$$\begin{aligned} Q_L &= \begin{bmatrix} u_L \\ d_L \end{bmatrix} : (2, 1, 1/3), \qquad Q_R = \begin{bmatrix} u_R \\ d_R \end{bmatrix} : (1, 2, 1/3), \\ l_L &= \begin{bmatrix} \nu_L \\ e_L \end{bmatrix} : (2, 1, -1), \qquad l_R = \begin{bmatrix} N_R \\ e_R \end{bmatrix} : (1, 2, -1). \end{aligned} \tag{3.3}$$

For each fermion, the numbers in the parenthesis are the quantum numbers associated to the $SU(2)_L$, $SU(2)_R$ and $U(1)_\alpha$ gauge groups respectively.

The covariant derivative, as prescribed from Yang-Mills theory is

$$D = \partial - ig_L W_{LJ} I_{Lj} - ig_R W_{Rj} I_{Rj} - ig'(n_B - n_L)B, \tag{3.4}$$

where W_L, W_R and B are the gauge bosons corresponding to the groups $SU(2)_L$, $SU(2)_R$ and $U(1)_{(n_B-n_L)}$ respectively and g_L, g_R and g' are the corresponding gauge coupling constants. One now requires that the theory be invariant under parity operation $\mathcal{P}$ under which the fields transform as follows:

$$l_L \leftrightarrow l_R, \qquad Q_L \leftrightarrow Q_R, \qquad W_L \leftrightarrow W_R. \tag{3.5}$$

This requires $g_L = g_R = g$. The gauge bosons transform as

$$W'^i_{\mu L,R} = W^i_{\mu L,R} + \epsilon^{ijk} W^k_{\mu L,R} - \frac{1}{g}\partial_\mu \theta^i_{L,R}(x), \tag{3.6}$$

$$B'_\mu = B_\mu - \frac{1}{g'} f(x) \tag{3.7}$$

where $f(x)$ and $\theta^i_{L,R}(x)$ are the gauge parameters of $U(1)_Y$ and $SU(2)_{L,R}$ respectively. While the fermions transform as

$$\Psi'_{L,R}(x) = e^{-iI_{jL,R}\theta_j(x)}\Psi(x), \tag{3.8}$$

for the group $SU(2)_{L,R}$ and

$$\Psi'(x) = e^{-i(n_B-n_L)f(x)}\Psi(x), \tag{3.9}$$

for the group $U(1)_{(n_B-n_L)}$. In this case the symbol Ψ refers either to quarks or to leptons. The gauge invariant Lagrangian for the quarks and leptons is

$$\begin{aligned} \mathcal{L}_{gauge} &= i(\bar{\Psi}_L \not{D}\Psi_L + \bar{\Psi}_R \not{D}\Psi_R) - \frac{1}{4}F_{\mu\nu}F^{\mu\nu} \\ &- \frac{1}{4}G^i_{L\mu\nu}G^{i\mu\nu}_L - \frac{1}{4}G^i_{R\mu\nu}G^{i\mu\nu}_R, \end{aligned} \tag{3.10}$$

with $\not{D} = \gamma_\mu D^\mu$.

$$F_{\mu\nu} = \partial_\mu B_\nu - \partial_\nu B_\mu, \tag{3.11}$$
$$G_{\mu\nu} = \partial_\mu W^i_{\nu L,R} - \partial_\nu W^i_{\mu L,R} + g\epsilon^{ijk} W^j_{\mu L,R} W^k_{\nu L,R}. \tag{3.12}$$

3.2.2 Spontaneous Symmetry breaking and gauge boson masses

Consider now the breaking of this gauge symmetry. There are various ways to achieve this goal. One of the most used is by introducing the following scalar content [25]:

$$\Delta_L = \begin{bmatrix} \Delta_L^{++} \\ \Delta_L^{+} \\ \Delta_L^{0} \end{bmatrix} : (3,1,2), \qquad \Delta_R = \begin{bmatrix} \Delta_R^{++} \\ \Delta_R^{+} \\ \Delta_R^{0} \end{bmatrix} : (1,3,2), \tag{3.13}$$

$$\phi = \begin{pmatrix} \phi_1^0 & \phi_2^+ \\ \phi_1^- & \phi_2^0 \end{pmatrix} : (2,2,0)\,. \tag{3.14}$$

As we will see, this choice will lead to the see-saw mechanism for neutrino masses. The spontaneous symmetry breaking occurs in two steps. First, the electrically neutral component of Δ_R acquires a vev v_R and breaks the gauge symmetry down to $SU(2)_L \times U(1)_Y$. The parity symmetry breaks down at this stage too. Successively the electrically neutral components of ϕ acquire the vevs k and k' and break the symmetry down to $U(1)_{em}$. Experimental contraints force the relation that $k, k' << v_R$. Applying the covariant derivative to the Higgs fields it is easy to see that the charged right handed gauge bosons, $W_R^\pm$ and Z' acquire masses proportional to v_R and become much heavier than the SM $W_L^\pm$ and Z bosons that acquire masses proportional to k and k'. The charged gauge bosons mix leading to the following mass matrix:

$$\begin{pmatrix} \frac{1}{2}g^2(k^2 + k'^2 + 2v_L^2) & g^2 k k' \\ g^2 k k' & \frac{1}{2}g^2(k^2 + k'^2 + 2v_R^2) \end{pmatrix}. \tag{3.15}$$

Here v_L is the vev of the electrically neutral component of Δ_L which is assumed to be much smaller than k, k'. The eigenstates of this matrix are

$$\begin{aligned} W_1 &= W_L \cos(\zeta) + W_R \sin(\zeta), \\ W_2 &= -W_L \sin(\zeta) + W_R \cos(\zeta). \end{aligned} \tag{3.16}$$

Replacing 3.16 into 3.15, one finds

$$\tan(2\zeta) = \frac{2kk'}{v_R^2 - v_L^2}. \tag{3.17}$$

Being ζ a small number the mass eigenstates W_1 and W_2 are nearly the same as W_L and W_R. The masses of these gauge bosons are the diagonal elements of the matrix 3.15:

$$M_{W_1}^2 \sim M_{WL}^2 \sim g^2 \frac{k^2 + k'^2}{2}, \tag{3.18}$$

$$M_{W_2}^2 \sim M_{WR}^2 \sim g^2 (\frac{k^2 + k'^2}{2} + v_R^2) \sim g^2 v_R^2. \tag{3.19}$$

The situation is completely analogous for the neutral gauge bosons W_{3L}, W_{3R} and B. First, they mix leading to the following mass matrix:

$$\begin{pmatrix} \frac{g^2}{4}(k^2 + k'^2 + 4v_L^2) & -\frac{g^2}{4}(k^2 + k'^2) & -gg'v_L^2 \\ -\frac{g^2}{4}(k^2 + k'^2) & \frac{g^2}{4}(k^2 + k'^2 + 4v_R^2) & -gg'v_R^2 \\ -gg'v_L^2 & -gg'v_R^2 & g'^2(v_L^2 + v_R^2) \end{pmatrix}. \tag{3.20}$$

The matrix is diagonalized using the following transformation:

$$\begin{aligned} A &= \sin(\theta_W)(W_{3L} + W_{3R}) + \sqrt{\cos(2\theta_W)}B, \\ Z &= \cos(\theta_W)W_{3L} - \sin(\theta_W)\tan(\theta_W)W_{3R} - \tan(\theta_W)\sqrt{\cos(2\theta_W)}B, \\ Z' &= \frac{\sqrt{\cos(2\theta_W)}}{\cos(\theta_W)}W_{3R} - \tan(\theta_W)B. \end{aligned} \tag{3.21}$$

One can verify that A is massless and it is identified with the photon. At this step, the two massive neutral gauge bosons Z and Z' mix to produce

the mass eigenstates Z_1 and Z_2

$$\begin{aligned} Z_1 &= Z\cos(\eta) + Z'\sin(\eta), \\ Z_2 &= -Z\sin(\eta) + Z'\cos(\eta), \end{aligned} \tag{3.22}$$

so that the neutral boson masses can be calculated from the relations

$$M_Z^2 = M_{Z1}^2\cos^2(\eta) + M_{Z2}^2\sin^2(\eta) \tag{3.23}$$

$$M_Z^{2\prime} = M_{Z1}^2\sin^2(\eta) + M_{Z2}^2\cos^2(\eta). \tag{3.24}$$

One finds

$$M_Z^2 = \frac{g^2}{2\cos^2(\theta_W)}(k^2 + k'^2 + 4v_L^2) \tag{3.25}$$

$$\begin{aligned} M_{Z'}^2 &= \frac{g^2}{2\cos^2(\theta_W)\cos(2\theta_W)} \times \\ &\quad (4v_R^2\cos^4(\theta_W) + (k^2 + k'^2)\cos^2(2\theta_W) + 4v_L^2\sin^4(\theta_W)), \end{aligned} \tag{3.26}$$

and the mixing angle η, neglecting v_L and using $k^2 + k'^2 << v_R^2$ is given by

$$\tan(2\eta) = 2\sqrt{\cos(2\theta_W)}\frac{M_Z^2}{M_{Z'}^2}. \tag{3.27}$$

As $v_R \to \infty, \eta \to 0$, so that $M_{Z_1}^2 \to M_Z^2$. In this limit, the masses of W_1 and Z_1 satisfy the Standard Model relation $M_{W_1} = M_{Z_1}\cos(\theta_W)$.

3.2.3 Yukawa sector

In this section we concentrate only on the leptonic sector. The most general Yukawa couplings involving the leptons are given by

$$\begin{aligned} \mathcal{L}_{yukawa}^{lep} &= \bar{l}_{L_i}(h_{ij}\phi + \widetilde{h}_{ij}\widetilde{\phi})l_{R_j} \\ &+ \bar{l}_{L_i}^c f_{ij} i\sigma_2 \Delta_L l_{L_j} + \bar{l}_{R_i}^c f_{ij} i\sigma_2 \Delta_R l_{R_j} + h.c., \end{aligned} \tag{3.28}$$

where $\widetilde{\phi} = \sigma_2\phi^\star\sigma_2$ and i,j refer to different generations. At the first stage of symmetry breaking, assuming $< \Delta_L^0 >= v_L = 0$, we have $< \Delta_R^0 >= v_R \neq 0$ leading to a heavy Majorana mass for the right-handed neutrinos, given by

the matrix $f_{ij}v_R$. At the second stage, once the neutral components in ϕ develop non-zero vevs we obtain the following form for the mass matrix of the neutrinos:

$$\begin{pmatrix} 0 & m_D \\ m_D & fv_R \end{pmatrix}, \tag{3.29}$$

where $m_D = h_{ij}k + \widetilde{h}_{ij}k'$.

3.2.4 Left-Right Symmetric Model with inverse see-saw

Since the framework in which we worked was the Left-Right symmetric Model equipped with an inverse see-saw, we want to give in this subsection the basic idea to understand how to realize this scenario. The particle content is [62]:
Fermions:

$$\begin{aligned} Q_L &= \begin{bmatrix} u_L \\ d_L \end{bmatrix} : (2,1,1/3), \qquad Q_R = \begin{bmatrix} u_R \\ d_R \end{bmatrix} : (1,2,1/3), \\ l_L &= \begin{bmatrix} \nu_L \\ e_L \end{bmatrix} : (2,1,-1), \qquad l_R = \begin{bmatrix} N_R \\ e_R \end{bmatrix} : (1,2,-1), \\ S &: (1,1,1) \end{aligned} \tag{3.30}$$

Scalars:

$$\chi_L = \begin{bmatrix} \chi_L^+ \\ \chi_L^0 \end{bmatrix} : (2,1,1), \qquad \chi_R = \begin{bmatrix} \chi_R^+ \\ \chi_R^0 \end{bmatrix} : (1,2,1), \tag{3.31}$$

$$\phi = \begin{pmatrix} \phi_1^0 & \phi_2^+ \\ \phi_1^- & \phi_2^0 \end{pmatrix} : (2,2,0)\,. \tag{3.32}$$

Here the $< \chi_R^0 >= v_R$ has the same role of $< \Delta_R >$ in the previous section. The fermion sector comprises of the usual quarks and leptons plus one extra fermion singlet per generation. The Yukawa Langrangian for inverse seesaw

mechanism is given by

$$\begin{aligned}\mathcal{L}^{lep}_{yukawa} &= \bar{l}_{L_i}(h_{ij}\phi + \widetilde{h}_{ij}\widetilde{\phi})l_{R_j} + \bar{l}_{R_i}f_{ij}\chi_R S^c + \mu\bar{S}^c S + h.c.,\\ &= m_D\bar{\nu}_L N_R + M_R\bar{N}_R S + \mu\bar{S}^c S + h.c.\end{aligned}$$

In the basis $\mathcal{N} = (\nu_L, N^c_R, S^c)^T$ the inverse see-saw mass matrix is:

$$\mathcal{M} = \begin{pmatrix} 0 & m_D^T & 0 \\ m_D & 0 & M_R \\ 0 & M_R^T & \hat{\mu} \end{pmatrix}, \tag{3.34}$$

and with the assumption that $\mu, m_D << M_R$ the light neutrino mass matrix is given by

$$m_\nu \simeq m_D^T \frac{1}{M_R^T}\hat{\mu}\frac{1}{M_R}m_D\,. \tag{3.35}$$

In the next section we will discuss in detail the inverse see-saw mechanism.

3.3 The inverse see-saw

In this section we discuss the inverse seesaw mechanism. In subsection 3.3.1 we present the inverse seesaw mass matrix and parameter counting, in 3.3.1.1 we describe an approximate diagonalization procedure for the 9×9 mass matrix, in 3.3.2 we give the neutrino couplings to gauge (and Higgs) bosons, and in 3.3.3 we provide a re-parametrization of the inverse seesaw that allows to fulfill automatically the experimental constraints from low-energy neutrino data. While we are mostly interested in a LR symmetric setup with a gauge group $SU(3)_C \times SU(2)_L \times SU(2)_R \times U(1)_{nB-nL}$, most of the discussion in this section applies also to inverse seesaw within the SM. We will formulate this section in the LR context and we will comment on differences between inverse seesaw within the LR symmetric and the SM scenarios at the end of the section.

3.3.1 Setup

We work in the basis in which the mass matrix of the charged leptons is diagonal, with the e, μ, τ flavors identified by the mass eigenvalues. We write the inverse see-saw mass matrix in the interaction basis for the neutral states $\mathcal{N} = (\nu_L, N_R^c, S^c)^T$

$$\mathcal{M} = \begin{pmatrix} 0 & m_D^T & 0 \\ m_D & 0 & M_R \\ 0 & M_R^T & \hat{\mu} \end{pmatrix} , \tag{3.36}$$

where the sub-matrix $\hat{\mu}$ (as well as the full $\mathcal{M}$) is complex symmetric. Any complex symmetric matrix m of any dimension can be factorized in a unique way as $m = W^* \hat{m} W^\dagger$ where $\hat{m}$ is diagonal with real and positive eigenvalues, and W is unitary. Then, by redefining the gauge singlets S via a unitary rotation $W(\mu)$ we can always bring μ into diagonal form $\hat{\mu}$ as is implicit in 3.36. As regards M_R, if the fields N_R were unrelated to the SM leptons further field redefinitions would be possible. However, in the LR model the N_R's sit in the same $SU(2)_R$ multiplets with the RH SM leptons, and once a redefinition of ℓ_R (together with a redefinition of ℓ_L) is used to bring into diagonal form the charged lepton mass matrix, the only residual freedom is in three vectorlike phase redefinitions of $\ell_{L,R}$ proportional to the three diagonal $U(3)$ generators I, λ_3, λ_8 which commute with the diagonal mass matrix. This can be used to remove three phases from M_R which remains otherwise generic with 9+6 (real + imaginary) parameters. Finally, because of LR symmetry in exchanging the L and R labels, the complex matrix m_D is symmetric.

Exact diagonalization of the mass matrix 3.36 can be performed via a transformation of the field basis with a unitary matrix $\mathcal{V}$ such that

$$\hat{\mathcal{M}} = \mathcal{V}^T \mathcal{M} \mathcal{V} , \tag{3.37}$$

is diagonal. Of course, in the general case this can only be done numerically (our numerical study indeed relies on a precise numerical diagonalization of the full 9×9 matrix). However, assuming that the three sub-matrices in 3.36 have mass scales arranged hierarchically μ, $m_D \ll M_R$, an approximate

diagonalization can be performed in analytic form yielding:

$$\hat{\mathcal{M}}' = \mathcal{V}'^T \mathcal{M} \mathcal{V}' \approx \hat{\mathcal{M}} \tag{3.38}$$

where $\mathcal{V}' \approx \mathcal{V}$ is non-unitary by terms of $\mathcal{O}(m_D/M_R)$ (we denote with a prime non-unitary transformation matrices, as well as mass matrices obtained via non-unitary transformations). Clearly $\hat{\mathcal{M}}'$ deviates from exact diagonal form: terms of $\mathcal{O}(\mu\, m_D/M_R)$ will appear in the non-diagonal entries coupling the light and heavy sectors, and terms of $\mathcal{O}(\mu)$ will appear in the non diagonal entries of the heavy sector. Below we give a brief description of this approximate diagonalization procedure, which will also be useful to establish notations.

3.3.1.1 Stepwise approximate diagonalization

Approximate diagonalization can be carried out in four steps. The first step is to bring M_R into diagonal form. Let us decompose M_R in terms of two unitary matrices U_R, V_R and a diagonal matrix of mass eigenvalues $\hat{M}_R$:

$$M_R = U_R \hat{M}_R V_R^\dagger \,. \tag{3.39}$$

As we have remarked above, M_R contains nine real and six imaginary parameters. Then, by matching the number of parameters between the LH and RH sides of 3.39 we see that U_R and V_R can be taken as special unitary, with three real angles and three phases each. The matrix U_R is an important quantity since, for example, it will appear in the RH charged currents coupling N_R to the charged leptons. By defining a block-diagonal matrix $V_1 = \mathrm{diag}\,(\mathbb{1}_3, U_R^*, V_R)$, where $\mathbb{1}_3$ is the 3×3 identity matrix, it is easy too see that in the matrix $\mathcal{M}_1 = V_1^T \mathcal{M} V_1$ an exact diagonalization $M_R \to \hat{M}_R$ is obtained, while at the same time $\hat{\mu} \to \mu^V \equiv V_R^T \hat{\mu} V_R$ and the entries m_D (m_D^T) get replaced by D (D^T) defined as:

$$D \equiv U_R^\dagger m_D \,. \tag{3.40}$$

The next step $\mathcal{M}_2 = V_2^T \mathcal{M}_1 V_2$ with $V_2 = \frac{1}{\sqrt{2}}\mathrm{diag}(\sqrt{2}, \sigma_1 - \sigma_3) \otimes \mathbb{1}_3$ brings $\hat{M}_R$ to the block-diagonal (2,2) and (3,3) entries and also adds to these

entries small corrections of $\mathcal{O}(\mu^V)$. The D terms 3.40 remain in the first row $(\mathcal{M}_2)_{1j} = v_D^T = \frac{1}{\sqrt{2}}(0, -D^T, D^T)$ and first column $(\mathcal{M}_2)_{j1} = v_D$. Let us note that since V_1 and V_2 are both unitary, no approximation has been made so far in $\mathcal{M}_2$. The next step requires suppressing the off-diagonal entries of order m_D. This is obtained with a matrix V_3' such that $(V_3')_{1j} = w_D^\dagger = (\mathbb{1}_3, D^\dagger, D^\dagger)\frac{1}{\sqrt{2}\hat{M}_R}$, $(V_3')_{j1} = -w_D$ and $(V_3')_{jj} = \mathbb{1}_3$. It can be easily checked that $V_3' V_3'^\dagger$ deviates from the identity by $\mathcal{O}(m_D^2/M_R^2)$. With this rotation, the off-diagonal light-heavy entries in $\mathcal{M}_3' = V_3'^T \mathcal{M}_2 V_3'$ get suppressed to $\mathcal{O}(\hat{\mu}D/M_R^2)$ which, in the seesaw approximation, can be neglected. We have thus singled out in the (1,1) block the light neutrino mass matrix m_ν, which can now be expressed, as is customary, in terms of the initial matrices in 3.36 as:

$$m_\nu \simeq m_D^T \frac{1}{M_R^T} \hat{\mu} \frac{1}{M_R} m_D \,. \tag{3.41}$$

We see from this equation that suppression of the light neutrino masses can be obtained thanks to small values of $\hat{\mu}$, without the need of exceedingly small values of m_D/M_R. This can allow for N_R to live at relatively low energy scales, possibly within experimental reach. Being symmetric by construction, m_ν can be diagonalized as

$$\hat{m}_\nu = {V_L}^T \, m_\nu \, V_L \,, \tag{3.42}$$

with V_L unitary. Note that V_L differs from the exact (non-unitary) light neutrinos mixing matrix V_L' by $\mathcal{O}(\frac{m_D}{M_R})$. In our study we will neglect these small terms and we will identify $V_L = V_L'$. A last rotation, by means of the unitary matrix $V_4 = \mathrm{diag}\,(V_L,\, i\,\mathbb{1}_3,\, \mathbb{1}_3)$, can now be performed on $\mathcal{M}_3'$ to bring m_ν into diagonal form (this also renders positive the heavy mass entries in the (2,2) block that have acquired a negative sign). Neglecting the small off-diagonal entries, the final matrix $\mathcal{M}' = V_4^T \mathcal{M}_3' V_4$ reads:

$$\mathcal{M}' \simeq \begin{pmatrix} \hat{m}_\nu & 0 & 0 \\ 0 & \hat{M}_R^- & 0 \\ 0 & 0 & \hat{M}_R^+ \end{pmatrix}. \tag{3.43}$$

The eigenvalues of the two 3×3 heavy-heavy blocks $\hat{M}_R^\pm$ receive corrections of $\mathcal{O}(m_D^2/\hat{M}_R)$ after the V_4 rotation. However, these corrections are the

same for both blocks, so that they can be conventionally absorbed into a common term $\hat{M}_R$. Instead, contributions of order $\hat{\mu}$ appear with opposite sign, and this is important because it generates small splittings between pairs of heavy states. For our analysis it is then sufficient to define the heavy mass eigenvalues in 3.43 as $\hat{M}_R^{\pm} = \hat{M}_R \pm \frac{1}{2}\mu^V$, keeping in mind that they represent three pairs of almost degenerate (quasi-Dirac) neutrinos with large masses $(\hat{M}_R)_{ii}$, split by three small quantities $(\Delta M)_{ii} = (\hat{M}_R^+)_{ii} - (\hat{M}_R^-)_{ii} = (\mu^V)_{ii}$ where $\mu^V \equiv V_R^T \hat{\mu} V_R^T$ (this last definition is given here for the sake of precision, but being V_R and $\hat{\mu}$ in any case arbitrary, in the following we will simply denote the mass splittings generically as $\Delta M = \mu$).

3.3.2 Couplings to the gauge bosons and to the Higgs

The approximate mixing matrix $\mathcal{V}' = V_1\, V_2\, V_3'\, V_4$ derived in the previous section controls the structure of the couplings between the LR gauge bosons and the mass eigenstates. Its explicit form is:

$$\mathcal{V}' = \begin{pmatrix} V_L & \frac{i}{\sqrt{2}}\xi^\dagger & \frac{1}{\sqrt{2}}\xi^\dagger \\ 0 & -\frac{i}{\sqrt{2}}U_R^* & \frac{1}{\sqrt{2}}U_R^* \\ -V_R\xi V_L & \frac{i}{\sqrt{2}}V_R & \frac{1}{\sqrt{2}}V_R \end{pmatrix} \tag{3.44}$$

where for convenience we have introduced the 3×3 matrix of small mixings:

$$\xi = \frac{1}{\hat{M}_R}\, D = \frac{1}{\hat{M}_R}\, U_R^\dagger\, m_D\,. \tag{3.45}$$

The derivation of the charged current (CC) couplings to $W_{L,R}^{\pm}$ and of the neutral current (NC) couplings to $Z_{L,R}$ is outlined below. It is left understood that the known SM couplings fix the normalization modulo a factor of the ratio of the gauge couplings g_R/g_L. Let us introduce a vector $E = (e_L, e_R^c, 0)^T$ for the left-handed (mass eigenstate) charged fermions, and recall that the neutral states are arranged in another vector $\mathcal{N} = (\nu_L, N_R^c, S_R^c)^T$. The LH and RH charged currents can be written (in two

component notations) as:

$$J_L^{-\mu} = \frac{1}{\sqrt{2}} E^\dagger \bar{\sigma}^\mu P_L \mathcal{N}\,, \tag{3.46}$$

$$J_R^{-\mu} = \frac{1}{\sqrt{2}} E^\dagger \bar{\sigma}^\mu P_R \mathcal{N}\,, \tag{3.47}$$

where $\bar{\sigma}^\mu = (1, -\vec{\sigma})$ are the spinor matrices, and $P_{L,R}$ are the projectors onto the neutral members of the L and R multiplets corresponding to 9×9 matrices which, in 3×3 block notation, are given by $(P_L)_{11} = \mathbb{1}_3$, $(P_R)_{22} = \mathbb{1}_3$ with zero in all other entries. In the seesaw approximation, the neutral mass eigenstates are related to the interaction eigenstates as $\mathcal{N} = \mathcal{V}' N$ with $N = (\nu, N_-, N_+)^T$, where ν represents the three light neutrinos and $N_\pm$ correspond to the heavy neutrinos respectively with mass eigenvalues $M_R^\pm$. Projecting onto the mass eigenstates and converting to the usual four-component spinor notation for gauge currents we have:

$$J_L^{-\mu} = \frac{1}{\sqrt{2}} \bar{e}_L \gamma^\mu V_L \nu + \frac{1}{2} \bar{e}_L \gamma^\mu \xi^\dagger (N_+ + i N_-)\,, \tag{3.48}$$

$$J_R^{-\mu} \sim \frac{1}{2} \overline{e_R^c}\, \gamma^\mu U_R^* (N_+ - i N_-)\,. \tag{3.49}$$

NC couplings are also important since they can give rise to $N_\pm \to Z\nu$ decays. In the interaction basis the NC for the neutral states are:

$$J_L^{0\mu} = \frac{1}{2} \mathcal{N}^\dagger i \bar{\sigma}^\mu P_L \mathcal{N}\,, \tag{3.50}$$

$$J_R^{0\mu} = \frac{1}{2} \mathcal{N}^\dagger i \bar{\sigma}^\mu P_R \mathcal{N}\,, \tag{3.51}$$

which in the mass eigenstate basis yields:

$$J_L^{0\mu} = \frac{1}{2} \bar{\nu} \gamma^\mu P_L \nu + \frac{1}{2\sqrt{2}} \left[\bar{\nu} \gamma^\mu V_L^\dagger \xi^\dagger (N_+ + i N_-) + H.c. \right]\,, \tag{3.52}$$

$$J_R^{0\mu} = \frac{1}{4} (\bar{N}_+ + i \bar{N}_-) \gamma^\mu (N_+ - i N_-)\,. \tag{3.53}$$

In the first equation we have neglected additional terms involving N-N couplings which are suppressed as $\xi\xi^\dagger$. As can be seen from the second equation,

in the approximation in which terms of order $\mu/\hat{M}_R\xi$ are neglected there are no R-handed neutral currents between heavy and light neutrinos. Finally, the fermion-scalar coupling $\frac{1}{v}N_R^\dagger m_D \nu_L\, H$ gives the following interactions between the heavy $N_\pm$'s, the Higgs and the light neutrinos:

$$\begin{aligned}\mathcal{L}_H &= \frac{1}{\sqrt{2}}(\bar{N}_+ + i\bar{N}_-)\left[U_R^T \frac{m_D}{v}\, V_L\right]\nu\, H \\ &+ \frac{1}{2}(\bar{N}_+ + i\bar{N}_-)\left[U_R^T \frac{m_D}{v}\xi^\dagger\right](N_+ + iN_-)H + H.c.\,.\end{aligned} \tag{3.54}$$

3.3.3 A useful parametrization of the inverse seesaw in LR models

In [31] a clever parametrization of the Dirac mass matrix of the type I seesaw was put forth, and it is referred to as the Casas-Ibarra (CI) parametrization. In this parametrization m_D is expressed in terms of low energy observables (light neutrino mass eigenvalues and mixing angles), of the seesaw heavy mass eigenvalues, and of an arbitrary complex orthogonal matrix $\mathcal{R}$. One of the most useful features of the CI parametrization is that it allows to generate random samples of m_D which by construction reproduce all the low energy data, which is a quite valuable property when one wants to scan over the model parameter space. As we detail below, also for the inverse seesaw in LR models it is possible to introduce a parametrization that has analogous properties, namely that allows to scan over the unknown physical masses and couplings (U_R, V_R, m_D, M_R, $\hat{\mu}$) while automatically reproducing all the low energy data.

Let us start by writing the light neutrino mass matrix in diagonal form (see 3.41 and 3.42):

$$\hat{m}_\nu = V_L^T m_D^T \frac{1}{M_R^T}\hat{\mu}\frac{1}{M_R} m_D V_L\,. \tag{3.55}$$

Let us now write m_D as:

$$m_D = M_R \frac{1}{\sqrt{\hat{\mu}}}\,\mathcal{R}\,\sqrt{\hat{m}}\,V_L^\dagger\,. \tag{3.56}$$

By inserting 3.56 into the RH side of 3.55 (or by extracting directly $\mathcal{R}$ from 3.56) it can be verified that $\mathcal{R}$ must satisfy the condition $\mathcal{R}\mathcal{R}^T = \mathcal{R}^T\mathcal{R} = I$, but is otherwise arbitrary, and thus it can be written as a generic 3×3 orthogonal matrix in terms of three complex angles. Rewriting M_R in the previous equation according to 3.39 we obtain

$$D = U_R^\dagger \, m_D = \hat{M}_R \, V_R^\dagger \, \frac{1}{\sqrt{\hat{\mu}}} \, \mathcal{R} \, \sqrt{\hat{m}} \, V_L^\dagger \, . \tag{3.57}$$

The RH side of this equation is written in terms of the low energy observables $(\sqrt{\hat{m}}, V_L^\dagger)$ while the other quantities are arbitrary. The crucial point now is to factor the generic 3×3 complex matrix D as defined in 3.57 into a unitary matrix $(U_R^\dagger)$ and a symmetric matrix (m_D). This can be achieved by factorizing D in its singular value decomposition (SVD) in terms of two unitary matrices W and Q and a real diagonal matrix with non-negative entries $\hat{D}$:

$$D = W \cdot \hat{D} \cdot Q^\dagger = (W Q^T) \cdot (Q^* \hat{D} Q^\dagger) \equiv \tilde{U}_R^\dagger \tilde{m}_D \, , \tag{3.58}$$

where, in the second step, we have inserted $Q^T Q^* = \mathbb{I}_3$ in order to build up a unitary matrix $\tilde{U}_R$ and the symmetric matrix $\tilde{m}_D$. However, $\tilde{U}_R$ and $\tilde{m}_D$ found in this way are just one among a threefold infinite class of possibilities, spanned by the freedom in switching phases between $\tilde{U}_R$ and $\tilde{m}_D$ (all the moduli are instead uniquely fixed). This is due to the fact that the SVD decomposition is not unique, since there are 9 phases in D and 12 in its decomposition in terms of $W, \hat{D}$ and Q. However, as discussed below 3.39, without loss of generality U_R can be taken special unitary with just 3 phases, and doing so the counting of parameters between the LH and RH sides of 3.58 matches. Let us then introduce a diagonal matrix of phases $\Phi = \mathrm{diag}(e^{i\varphi_1}, e^{i\varphi_2}, e^{i\varphi_3})$ and make the identification

$$U_R = Q^* \Phi^* W^\dagger \, , \qquad m_D = Q^* \Phi^* \hat{D} Q^\dagger \, , \tag{3.59}$$

which clearly preserves $U_R^\dagger m_D = D$ and the symmetric nature of m_D. The values of φ_i can then be fixed to achieve the desired form for U_R. Therefore, in the LR inverse-seesaw, given for example a set of RH neutrino masses $\hat{M}_R$ and of LNV parameters $\hat{\mu}$ of specific interest, the parametrization 3.58

together with 3.59 yields both m_D and U_R in terms of two arbitrary matrices: a complex orthogonal matrix $\mathcal{R}$ and a special unitary matrix V_R with just three phases, while, by construction, all the low energy neutrino data are automatically reproduced.

The discussion in this section assumed an inverse seesaw within the left-right symmetric group. However, it is straightforward to adapt most of our discussion to inverse seesaw models with the same block structure of $\mathcal{M}$ as in 3.36, but for which N_R is not related to ℓ_R, i.e. the standard model gauge group. In this case m_D is not constrained to be symmetric and we gain the freedom of redefining N_R via a $U(3)$ transformation. This allows to reabsorb U_R defined in 3.39 via a field rotation, while V_R remains defined in terms of three real and three imaginary parameters. Then $U_R^\dagger$ can be simply dropped from 3.57 whereas $D = m_D$ remains generic. [5]

3.4 Opposite sign to same sign dilepton ratio

In this section we estimate the ratio of production of pairs of leptons with the same sign and we compare it with the rate of production of pairs of leptons of opposite sign. The ratio between these two observables is denoted as R_{ll}. In both cases the production rates are dominated by processes with on-shell (or nearly on-shell) N_R's and therefore, under the natural assumption that the mass splitting between the different pairs is large (we typically expect $M_{Rj}^{\pm} - M_{Rk}^{\pm} \sim \mathcal{O}(M_R)$), it is sufficient to study just a single pair of quasi-Dirac $N_{\pm}$. SS dilepton production occurs for example through the LNV process $\bar{q}q \to W_R^+ \to \ell_\alpha^+ N_\pm \to \ell_\alpha^+ \ell_\beta^+ W_R^*$, where $(\bar{q})q$ denote (anti-)quark partons inside the colliding protons, N_+ and N_- are the two heavy neutrinos mass eigenstates, W_R^* is an off-shell RH gauge boson that will eventually decay dominantly to two jets, and ℓ_α, ℓ_β are two leptons not necessarily of the same flavor. Opposite sign pairs of leptons can be produced via the LN conserving process $\bar{q}q \to W_R^+ \to \ell_\alpha^+ N_\pm \to \ell_\alpha^+ \ell_\beta^- W_R^*$. Clearly, in order to produce the $N_\pm$ intermediate states on-shell via the decay of an on-shell W_R, $M_{W_R} > M_R^\pm$ is required. In order to symplify the

[5] Of course, within the SM group there are no right-handed gauge interactions, see section 3.3.2.

formula we further assume $M_{W_R} \not\gg M_R^{\pm}$ so that the $N_{\pm}$ mass eigenstates can be treated in the non-relativistic approximation.

Before entering into details let us try to figure out qualitatively what type of result we can expect. When the on-shell W_R^+ decays, an ℓ^+ anti-lepton is produced together with a heavy neutrino of ℓ-flavor N_ℓ, which corresponds to a coherent superposition of the two mass eigenstates $N^{\pm}$. Given that the same decay channels are open for both $N^{\pm}$, the time-evolution of the initial N_ℓ will be characterized by a typical oscillating behavior with frequency $\Delta M = M^+ - M^- = \mu$. There is another important scale in the problem, that is the $N^{\pm}$ lifetime $\tau = 1/\Gamma$.[6] If $\Delta M \gg \Gamma$ the lifetime is long enough that complete separation of the $N^{\pm}$ wave packets can occur. Coherence between the two mass eigenstates is completely lost before the decays, and decays will then proceed as in the usual Majorana case, yielding equal probabilities for SS and OS dileptons events, i.e. $R_{ll} = 1$. (Ideally, in this situation we can imagine that the mass of the intermediate state can be reconstructed from the invariant mass of the N decay products $m_{\ell_2 jj}$ to be M^+ or M^-, in which case the above result is obvious.) In the opposite limit $\Delta M \ll \Gamma$ decays occur at a time $t_D \sim \tau \ll 1/\Delta M$, that is before the onset of oscillation effects, so that $N_\ell(t_D) \approx N_\ell(0)$. In this case only the LN conserving transition $N_\ell(t_D) \to \ell^-$ can occur and $R_{ll} = 0$. Namely, when the $N^{\pm}$ mass degeneracy (in units of Γ) is sufficiently strong, the pure Dirac case is approached. It is then clear that the interesting regime occurs when the oscillation frequency is of the order of the lifetime, viz when $\mu = \Delta M \approx \Gamma$. Only in this case we can expect $R_{ll} \neq 0, 1$. In the appendix A we give a full mathematical description of neutrino-neutrino and neutrino-antineutrino oscillations. Here, we only provide the main steps of the calculation.

From 3.44 we can write the N_ℓ heavy state produced in the decay $W_R^+ \to \bar{\ell} N_\ell$ and its conjugate state $N_{\bar{\ell}}$ produced in the decay $W_R^- \to \ell N_{\bar{\ell}}$ in terms

[6] Since $N^{\pm}$ have the same decay channels, and only a tiny mass difference, we expect for the width difference $\Delta\Gamma = \Gamma^+ - \Gamma^- \ll \Delta M$ so that $\Delta\Gamma$ is always negligible. This is analogous to what happens in the $B^0 - \bar{B}^0$ meson system (see e.g. ref. [63]).

of the mass eigenstates as:[7]

$$N_\ell = \frac{1}{\sqrt{2}}(N_+ - iN_-)\,, \tag{3.60}$$

$$N_{\bar{\ell}} = \frac{1}{\sqrt{2}}(N_+ + iN_-)\,. \tag{3.61}$$

In writing these linear combinations we have neglected for convenience the flavor mixing matrices U_R (see 3.44) since the products of their matrix elements appearing in the LN conserving and LNV amplitudes cancels in the ratio R_{ll}. However, it should be kept in mind that these matrix elements control the flavor composition of both the SS and OS dilepton final states $\ell_i\ell_j$, and we reiterate that for generic mixing structures, $i \neq j$ events have no reason to be suppressed with respect to $i = j$ events.

After a time t, the states in 3.60, 3.61 have evolved into [63]

$$N_\ell(t) = g_+(t)N_\ell + g_-(t)N_{\bar{\ell}}\,, \tag{3.62}$$

$$N_{\bar{\ell}}(t) = g_-(t)N_\ell + g_+(t)N_{\bar{\ell}}\,, \tag{3.63}$$

where the oscillating amplitudes read

$$g_+(t) = e^{-iMt}e^{-\frac{\Gamma}{2}t}\cos\left(\frac{\Delta M}{2}t\right)\,, \tag{3.64}$$

$$g_-(t) = i\,e^{-iMt}e^{-\frac{\Gamma}{2}t}\sin\left(\frac{\Delta M}{2}t\right)\,, \tag{3.65}$$

with $M = \frac{1}{2}(M_+ + M_-)$ and, according to the discussion above, we have neglected the effects of $\Delta\Gamma$. Since the typical heavy neutrino widths are too large to allow observing displaced vertices (see next section), individual oscillation patterns cannot be resolved. The SS to OS ratio R_{ll} is then given by the ratio of the time-integrated amplitudes squared (note that they

[7] One remark is in order: in the presence of CP violating effects, the modulus of the ratio of the two coefficients in the linear combinations (3.60) and (3.61) can deviate from unity (CP violation in mixing [63]). In the regime $\mu \sim \Gamma$ this type of CP violation can get resonantly enhanced, and in principle observable effects on the ratio R_{ll} could be possible. We neglect this possibility in our treatment.

include the time dependent weight factor of the heavy neutrinos lifetime):

$$R_{ll} = \frac{\int_0^\infty |g_-|^2 \, dt}{\int_0^\infty |g_+|^2 \, dt} = \frac{\Delta M^2}{2\Gamma^2 + \Delta M^2} \, . \tag{3.66}$$

This result correctly reproduces the limiting cases discussed at the beginning of this section, that is $R_{ll} \to 1$ as $\Gamma/\Delta M \to 0$ (limiting Majorana case) and $R_{ll} \to 0$ as $(\Gamma/\Delta M)^{-1} \to 0$ (limiting Dirac case).[8]

3.5 LHC Phenomenology

In searching for heavy RH neutrinos within the framework of LR symmetric models, both the ATLAS [46,47] and the CMS collaboration [48,49] assume that the heavy neutrino decays proceed via an off-shell W_R bosons, with a branching ratio of 100% for the decay mode $N \to l^\pm jj$ where l represents a charged lepton of any flavor and N represents a generic heavy neutrino. While this is a reasonable expectation for LR models with an ordinary seesaw mechanism, the situation is very different in models based on the inverse seesaw. In our framework in fact all the following decay modes can occur, and all with sizeable branching ratios:

$$\begin{aligned} N \to W_L^\pm + l^\pm \, , \quad & N \to Z_L + \nu \, , \quad N \to h + \nu \, , \\ N \to (W_R)^* + l^\pm \to jjl^\pm \quad , \quad & N \to (Z_R)^* + \nu \to (jj \text{ or } l^+l^-)\nu \, , \end{aligned} \tag{3.67}$$

where W_L and Z_L are the (mostly) SM gauge bosons, h is the SM Higgs with mass $m_h \simeq 125$ GeV, and ν represents a light neutrino of any flavor. In our analysis we also assume $m_N < m_{W_R}$, where m_N denotes collectively the pair of mass eigenvalues $(M_R^\pm)_{11}$ for the lightest heavy neutrinos, so that the RH gauge bosons $(W_R)^*$ and $(Z_R)^*$ from $N = N_{1\pm}$ decays are off-shell. We also assume for simplicity $(M_R^\pm)_{ii} > m_{W_R}$ for $i > 1$ so that a single pair of RH neutrinos contributes to the signal (this second assumption is not necessary whenever the different pairs of heavy neutrinos are sufficiently separated in mass so that the different invariant masses of the decay products can be reconstructed with good confidence). In the numerical analysis we have also

[8] This result agrees with eq.(32) of ref. [60].

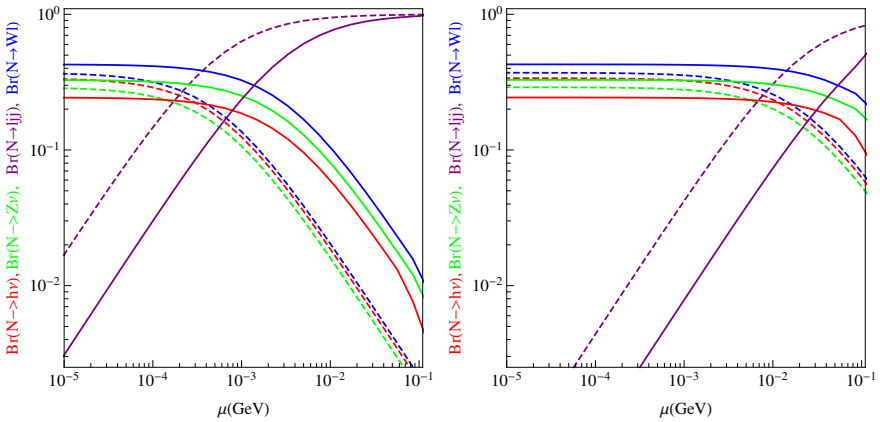

Figure 3.1: Branching ratios for heavy neutrino decays as a function of μ. The blue lines are for $\Gamma(N \to W + l)$, green for $\Gamma(N \to Z + \nu)$, red for $\Gamma(N \to h^0 + \nu)$ and purple for the three-body decay $\Gamma(N \to ljj)$. Solid lines correspond to $m_N = 0.2$ TeV and dashed lines to $m_N = 0.5$ TeV. The left panel is for $m_{W_R} = 2$ TeV and the right panel for $m_{W_R} = 5$ TeV. Lepton (and quark) final states are summed over flavor indices so that there is no dependence on fermion mixings.

included the decay mode $N \to (Z_R)^* + \nu$ although its branching is seesaw suppressed, and therefore largely irrelevant with respect to the other decays (see the comment below 3.53). In addition to the decay modes shown in eq. (3.67), decays into additional scalars besides the Higgs could also be possible, if they are lighter than N. This however, depends on unknown details of the scalar sector. Therefore, for definiteness we will assume that any new scalar is heavier than N so that the dominant decay modes are all listed in 3.67.

We first present some examples of numerical results corresponding to some fixed value of m_{W_R} and of m_N. This is justified by the fact that detection of $lljj$ signals at the LHC would imply that m_{W_R} and at least one m_{N_i} will be measured. In all the plots low energy neutrino data are kept fixed at their best fit point values for a normally ordered hierarchical spectrum (no qualitative differences arise for inverted hierarchies). We start by showing results for some fixed arbitrary choice of the matrices V_R and $\mathcal{R}$ (see section 3.3.3).

Fig. 3.1 shows some typical values of the branching ratios for different final states as a function of the LNV parameter μ ranging within the interval $[10^{-5}, 10^{-1}]$ GeV. We have chosen the two representative values $m_N = 0.2\,\text{TeV}$ (solid lines) and $m_N = 0.5\,\text{TeV}$ (dashed lines), and two different values for the W_R mass $m_{W_R} = 2\,\text{TeV}$ (left panel) and $m_{W_R} = 5\,\text{TeV}$ (right panel). The lowest m_{W_R} value corresponds roughly to the mass of the CMS excess found in [49], however, as we have seen, this excess is not confirmed in their last analysis [56]. The largest m_{W_R} corresponds roughly to the maximum m_{W_R} that the LHC can probe in the next few years of running. In the final states we sum over the different quark and lepton generations, so that the results are independent of neutrino mixing. For small values of μ, decays to SM gauge bosons dominate the decay rates. The branching ratios for $N \to W_R^* + l^\mp \to l^\mp jj$ and for decays to SM gauge bosons become similar for intermediate values of μ, the detailed ranges in which this occurs depend, however, rather strongly on the values of m_N and of m_{W_R}. For large values of μ three body decays become dominant. The qualitative behavior shown in fig. 3.1 can be understood from the equations presented in the previous section. In the inverse seesaw, the light neutrino masses are given by eq. (3.41). The equation contains the three matrices m_D, M_R and μ as free parameters. Keeping fixed the light neutrino masses at values in agreement with the experimental data and for fixed values of M_R, a scaling $m_D \propto 1/\sqrt{\mu}$ is obtained. Since all the couplings of the heavy neutrinos to SM gauge bosons are proportional to m_D (see the equations in section 3.3.2) decays to SM gauge bosons dominate when μ is small.

Fig. 3.2 shows the partial widths and branching ratios for N decays as a function of m_N for the two values $\mu = 10^{-5}\,\text{GeV}$ (solid lines) and $\mu = 10^{-4}\,\text{GeV}$ (dashed lines). Typical widths are in the range of $\Gamma \simeq [10^{-7}, 10^{-2}]$ GeV, much too small to be directly measured at the LHC, and too large to produce a displaced vertex. For small values of m_N, $N \to W_L l^\pm$ decays dominate the other two-body decays. However, it is important to notice that for $m_N \gg m_h$ the branching ratios of N decays to W_L, Z_L and h summed over light flavors become all equal. This can allow to infer the branching ratio for N decays to $W_L + Z_L + h$ from the measurement of $\text{Br}(N \to W^\pm + \sum_\alpha l_\alpha^\mp)$ alone.

Note also that the W_L gauge bosons decay to jets with a branching ratio of about $2/3 < 1$, and that Z_L and h do not lead to ljj final states.

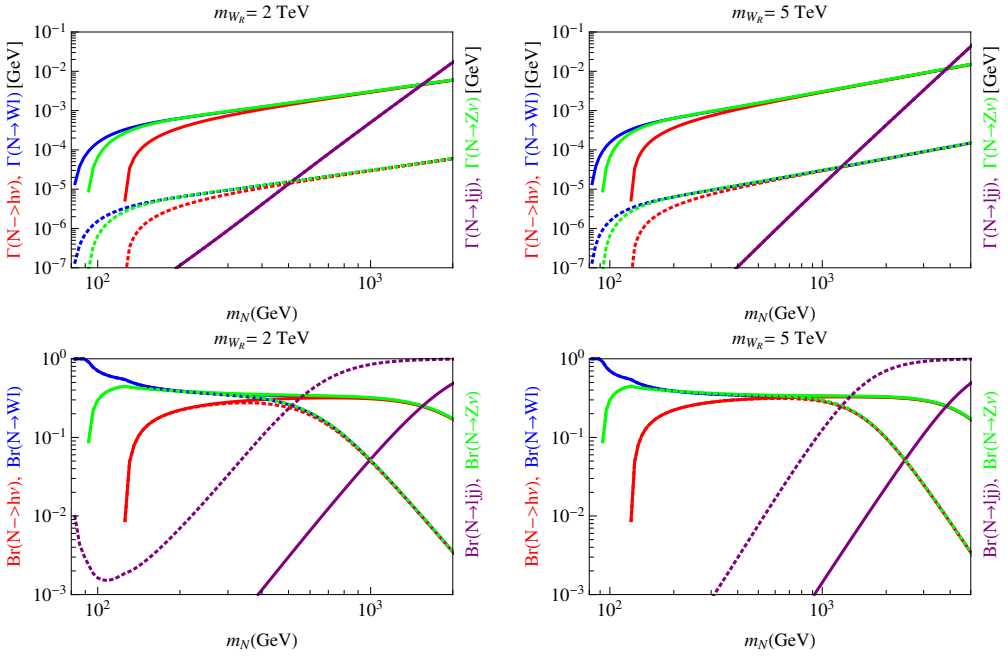

Figure 3.2: Partial decay widths in GeV (top panel) and branching ratios (bottom panel) for N decays. The blue, green and red lines are respectively for $\Gamma(N \to W + l)$, $\Gamma(N \to Z + \nu)$ and $\Gamma(N \to h^0 + \nu)$ while the purple lines are for the three-body decay $\Gamma(N \to ljj)$. Solid lines correspond to $\mu = 10^{-5}\,\text{GeV}$ and dashed lines to $\mu = 10^{-4}\,\text{GeV}$. Left panels correspond to $m_{W_R} = 2\,\text{TeV}$ and right panels to $m_{W_R} = 5\,\text{TeV}$.

This implies a reduction in the number of expected $lljj$ events. In the extreme case of very small μ and for $m_N \gg m_h$, when the decays into SM bosons dominates, only 1/9 of the total number of decays are into $lljj$ final states occurring mainly via the $N \to W_L + l \to ljj$ decay chain. Let us recall that experimental estimates are instead based on the assumption that the only decay channel is $N \to W_R^* l^\pm$, implying that 100% of the decays correspond to ljj final states. Therefore, we can expect that, within the present framework, the lower limit on m_{W_R} should be somewhat looser than the one quoted by the LHC collaborations. Let us also note that since W_L's are produced on-shell, for $N \to W_L + l \to ljj$ decays, the invariant mass of the jets should be peaked in correspondence to m_{W_L}. Thus it should be possible to separate kinematically these events from the off-shell W_R events. Such a measurement could be important to establish large "heavy-light" mixing in the neutrino sector, that is a general prediction of the inverse seesaw model. Finally, the fact that in the inverse seesaw models decays to SM bosons can dominate in a wide region of parameter space is again apparent also from fig. 3.2.

Up to now we have kept the values of the entries of the V_R and $\mathcal{R}$ matrices in the parametrization given in 3.57 fixed at some arbitrary constant values. We recall that V_R is a unitary matrix with three angles and three phases, while $\mathcal{R}$ is complex orthogonal and can be defined in the usual way in terms of sin and cos of three complex angles ζ_i. For our numerical scan, we parametrize these angles as:

$$\zeta_i = \kappa \cdot e^{2i\pi x_i}, \tag{3.68}$$

with x_i a randomly generated real number $\in [0, 1]$, and $\kappa \in [0, \kappa_{\max}]$. The upper limit $\kappa_{\max}$ represents a measure of how much fine tuning is allowed in the parametrization 3.58 in order to allow for particularly large values of m_D (or alternatively of the Yukawa couplings generating m_D) while still respecting all the constraints from low energy neutrino data. For $\kappa_{\max} \lesssim 1$ there is no fine tuning: all the tree-level formulas presented above remain valid and in particular loop corrections to neutrino masses and mixing angles remain at the level of few percent. However, for $\kappa_{\max} \gtrsim 2-3$, similarly large values of κ become possible and the corresponding results would be highly questionable, since the tree-level approximation starts to break down and in

particular, when loop corrections are taken into account, some low energy neutrino parameters might well drop out the experimentally allowed range. We have then plotted the results in fig. (3.3) adopting the educated choice $\kappa_{\max} = 1$.

In the left panel of fig. 3.3 we depict R_{ll} versus $\Delta M/\Gamma$ for some arbitrary value of the heavy neutrino mass, scanning randomly over the entries in V_R and $\mathcal{R}$. We see that for ΔM larger than a few times Γ, R_{ll} approaches rapidly the Majorana limit $R_{ll} = 1$. This result is independent of the absolute mass scale of the heavy neutrinos.

As we have already noticed, the expected widths for the heavy neutrino decays are too small to be directly measured at the LHC (see fig. 3.2). However, the ratio of two-body versus three-body N decays can be measurable. At fixed values of m_N and m_{W_R} this ratio is controlled by the value of μ, which also fixes the mass splitting of the quasi-Dirac neutrino pair, therefore we can expect a correlation between the ratio of two body versus three body N decays, and R_{ll}. This is shown in the right panel in fig. (3.3) where this ratio is plotted versus R_{ll} (summed over lepton flavors). The sum of the two body decays in the numerator of the ratio (y-axis in the right panel), has been rescaled by $(m_N/m_{W_R})^4$ to compensate for the W_R-propagator suppression for the three body decay. This renders the correlation between the two observables nearly independent of the values of the W_R and N masses. As the figure shows, if a large value $R_{ll} \sim 1$ is measured, the present scenario predicts that the rate for decays into SM bosons should be smaller than a few percent of the rate for three body decays times $(m_N/m_{W_R})^4$. On the other hand, if a small value $R_{ll} \sim 10^{-2}$ is measured (or an upper bound of the same order is set), the prediction is that a sizeable fraction of RH neutrino decays should proceed via on-shell SM bosons. Note that this correlation does not depend on the type of light neutrino spectrum (normal versus inverted hierarchy). Thus, the inverse seesaw not only allows for generic values $R_{ll} < 1$, but it also implies a testable correlation between R_{ll} and the RH neutrino decay modes.

As we have already said, the results depicted in the plots have been obtained by summing over the final state lepton flavors. However, given that the mixing matrices controlling the flavor composition of the dilepton final states are in principle generic, different flavor final states such as μejj can naturally occur with large branching ratios, while respecting the full set of

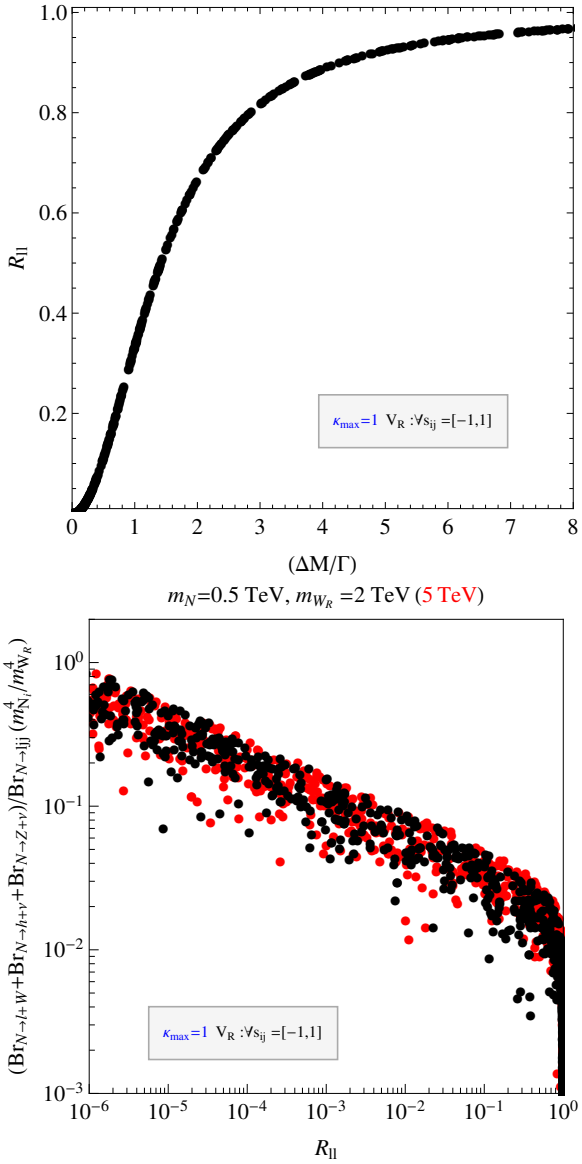

Figure 3.3: Top panel: the SS to OS ratio R_{ll} versus $\Delta M/\Gamma$. Bottom panel: the sum of the branching ratios of N decays to SM bosons divided by the branching ratio to ljj, versus R_{ll}. The numerator has been rescaled by $(m_N/m_{W_R})^4$ to compensate for the W_R-propagator suppression in the denominator. Black points are for $m_{W_R} = 2$ TeV, red points for $m_{W_R} = 5$ TeV, and $m_N = 0.5$ TeV.

low energy constraints (we have checked that numerically generated dilepton samples do not show suppressions of different flavor dilepton events). Thus, we stress again that SS and OS dilepton events of different flavors should be included as a potential contribution to the signal and, most importantly, they should not be used as an estimate of the backgrounds in experimental analyses.

3.5.1 Lepton flavor violation phenomenology

In the attempt of scrutinizing further lepton flavor violating (LFV) effects in the inverse seesaw scenario, we have also calculated branching ratios for low energy LFV processes, the most relevant of which is $\mathrm{Br}(\mu \to e\gamma)$. Fig. 3.4 shows the branching ratio for $\mu \to e\gamma$ as a function of the parameter μ. We see that it can provide additional relevant constraints only for very small values of μ ($\mu \ll 10^{-6}$ GeV), which corresponds to the regime in which the pure Dirac limit is approached and $R_{ll} \approx 0$ is expected.

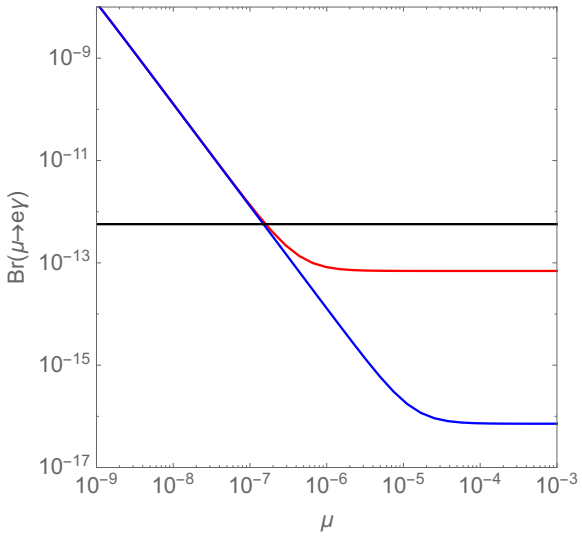

Figure 3.4: Branching ratio for $\mu \to e\gamma$ as a function of μ. $m_{R_1} = 200$ GeV, $m_{R_2} = 1$ TeV, $m_{R_3} = 1.5$ TeV. Red line is for $m_{W_R} = 2$ TeV, blue line for $m_{W_R} = 5$ TeV. The black line shows the upper limit from MEG experiment.

The behaviour shown in Fig.3.4 is easily understood. The contribution due to the coupling of the heavy neutrinos to SM gauge bosons that are proportional to m_D dominate when μ is small, while for big values of μ, $\mu > 10^{-6}$ GeV if $m_{W_R} = 2$ TeV and $\mu > 10^{-5}$ GeV if $m_{W_R} = 5$ TeV, the contribution due to the coupling of the heavy neutrinos to the W_R bosons dominate.

The main conclusion of this Chapter is that LR models equipped with an inverse seesaw mechanism for the light neutrino masses naturally yield pairs of quasi-Dirac RH neutrinos. In the specific region of parameter space corresponding to $\Delta M \approx \Gamma$, the ratio R_{ll} can have any value within the range [0,1]. Moreover, this value correlates in a specific way with the value of the ratio between two-body and three-body RH neutrino decays, and gross violations of this prediction would disfavor the scenario, and possibly rule it out.

Chapter 4

Light Quasi-Dirac neutrinos

This Chapter is based on the paper [64]. Here, the quasi-Dirac neutrinos are not the heavy N_R of the previous Chapter. The idea is to study the nature of neutrino through its oscillations. The experiments cannot establish if neutrinos are Dirac or Majorana particles, however, we will see that, starting from a model with Dirac neutrinos and adding small sources of lepton number violation thus creating a quasi-Dirac scenario, oscillation probabilities will change. So, we discuss the phenomenology of quasi-Dirac neutrino oscillations and derive limits on the standard and new parameters (mass splittings and mixing angles) from various experiments. The Chapter is organized as follows: in section (4.2) we discuss the general parametrization of masses and mixing angles for scenarios with three generations of quasi-Dirac neutrinos. In section 4.4 we describe all the experiments from which we derived the limits on the parameters. Finally, in section (4.5.2) we present the results. We will see that in one parameter perturbation of the Dirac limit, very stringent bounds can be derived on the mass splittings between the almost degenerate pairs of neutrinos. However, we also demonstrated that with suitable changes to the lepton mixing matrix, limits on such mass splittings are much weaker, or even completely absent. Finally, we consider the possibility that the mass splittings are too small to be measured and discuss bounds on the new, non-standard lepton mixing angles from current experiments for this case.

4.1 Introduction to Quasi-Dirac neutrinos and motivation

Neutrino oscillation experiments cannot distinguish Dirac from Majorana neutrinos, hence it is still unknown whether or not lepton number is conserved. Other processes, such as neutrinoless double beta decay [32, 33], need to be probed in order to answer this question. However, while the nature of neutrinos is often seen as a dichotomy, presenting two sharply distinct scenarios, the Dirac neutrino case can be seen as a limit of the more general Majorana case in which lepton number violating mass terms are zero, and this limit can be approached smoothly.

In practice, one can start with a model of $2n$ Majorana neutrinos and get a phenomenology arbitrarily close to the one of a model of n Dirac neutrinos. This can already be seen with only one generation of active (ν) and sterile neutrinos (N^c). In the basis $(\nu, N^c)^T$ the most general mass matrix reads:

$$m_\nu = \begin{pmatrix} m_L & m_D \\ m_D & m_R \end{pmatrix} . \tag{4.1}$$

If $m_L = m_R = 0$, lepton number is preserved and neutrinos are Dirac particles. This limit can alternatively be characterized by two *exactly* degenerate mass eigenstates composed in equal parts of ν and N^c: $\nu_1 = 1/\sqrt{2}\,(\nu + N^c)$ and $\nu_2 = i/\sqrt{2}\,(-\nu + N^c)$.[1] Small deviations from the limit $m_L = m_R = 0$ lead to a *quasi-Dirac* scenario where lepton number is no longer exactly preserved.

Let us rewrite eq. (4.1) using:

$$\varepsilon = \frac{(m_L + m_R)}{2m_D}, \tag{4.2}$$

$$\theta = \frac{(m_L - m_R)}{4m_D}. \tag{4.3}$$

[1] Note the factor i in ν_2. One could equally well choose the two mass eigenstates to be $\pm m_D$ instead.

As long as ε and θ are much smaller than one, we obtain:

$$m_{1,2} \simeq m_D \left(1 \pm \varepsilon\right) , \tag{4.4}$$

$$\nu_1 \simeq 1/\sqrt{2}\left[\left(1+\theta\right)\nu + \left(1-\theta\right)N^c\right] , \tag{4.5}$$

$$\nu_2 \simeq i/\sqrt{2}\left[\left(-1+\theta\right)\nu + \left(1+\theta\right)N^c\right] . \tag{4.6}$$

Departures from the Dirac case therefore can manifest themselves as either new mass splittings or new mixing angles (or, in general, both). Moreover, as this simple example shows, mass splittings and mixing angles are completely independent of each other. Note that for small values of ε and θ, lepton number violation is naturally suppressed, as expected. This can be most easily seen in our one generation scenario for the double beta decay observable $\langle m_\nu \rangle$: for $\theta = 0$ ($\varepsilon = 0$) it is straightforwardly calculated to be $\langle m_\nu \rangle \simeq \varepsilon m_D$ ($\langle m_\nu \rangle \simeq 2\theta m_D$).

We have therefore the following situation. Oscillation experiments cannot distinguish a model with n Majorana neutrinos (containing n Weyl spinors) from one with n Dirac neutrinos (containing $2n$ Weyl spinors) with matching masses and mixing angles. Nevertheless, once we add to a model with Dirac neutrinos small sources of lepton number violation, oscillation probabilities will change. Some illustrative examples are shown in fig. (4.1). We plot there the electron neutrino survival probability for low-energy (reactor) neutrinos at distances up to (and slightly larger than) the typical distances of the KamLAND experiment [65]. In all plots the black lines show the expectation for the current global best fit point [5] for the ordinary neutrino parameters in the standard three generation case, to which we have added either a non-zero mass splitting to a Dirac state (top row) or one particular new quasi-Dirac angle (bottom row). From the examples shown in fig. (4.1) one can read off already some basic facts about oscillations of quasi-Dirac neutrinos. First, small non-zero values of ε's are equivalent to introducing new, large oscillation lengths. Thus, the best constraints on ε will come from oscillation experiments with the largest possible baselines. And secondly, even if mass splittings are negligibly small, the new, non-standard angles which appear in this setup (called θ above) may affect oscillation probabilities in a way similar to standard angles, hence creating parameter degeneracies. For example, as fig. (4.1) shows, from P_{ee} alone one cannot provide limits on a single angle. (In this example variations of

θ_{14} can be compensated by varying θ_{12}.) Even by combining more than one oscillation probability, constraints can only be derived for certain combinations of angles and phases of the mixing matrix.

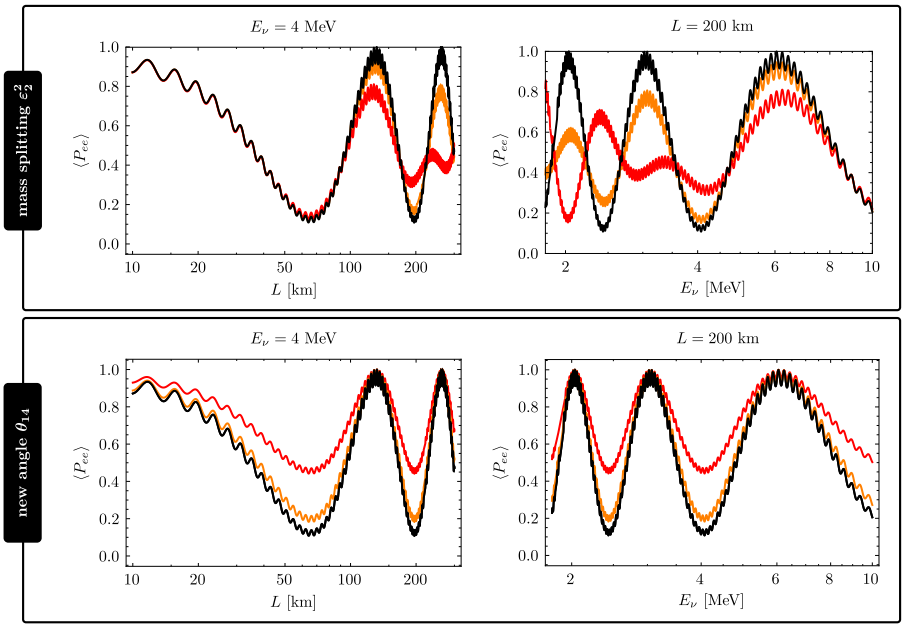

Figure 4.1: Electron neutrino survival probability for quasi-Dirac neutrinos with a fixed energy $E_\nu = 4$ MeV as a function of distance (left), and for fixed distance $L = 200$ km as function of E_ν (right). The standard 3-generation neutrino oscillation parameters have been fixed at their best fit point values [5], to which a small perturbation has been added. In the top row, we show the effect of mass splittings: $\varepsilon_2^2 = 0$ (black), $\varepsilon_2^2 = 10^{-5}$ eV^2 (orange) and $\varepsilon_2^2 = 2\times10^{-5}$ eV^2 (red). In the bottom row, it is possible to see the effect of introducing a non-standard angle: $\theta_{14} = 0$ (black), $\theta_{14} = \pi/8$ (orange) and $\theta_{14} = \pi/4$ (red). The exact definition of ε_2 and θ_{14} will be given latter in section (4.2).

A word on nomenclature. The terminologies *quasi-Dirac* and *pseudo-Dirac* neutrinos appear nearly interchangeably in the literature. We prefer

to define quasi-Dirac (QD) neutrinos as being a mixture of active and sterile states, in contrast with pseudo-Dirac (PD) neutrinos [2] which are composed of active states only. In both cases, the structure of mass and mixing matrices must be such that the lepton sector is close to preserving one or more $U(1)$ symmetries.

With this definition, quasi-Dirac and pseudo-Dirac neutrinos are then very different objects, both theoretically and phenomenologically. Let us briefly mention that various aspects of pseudo-Dirac neutrinos have been considered in the literature: Magnetic moments and double beta decay [68], possible mass textures [69–71], and oscillatory behavior [72–75]. We note in passing that models of pseudo-Dirac neutrinos require neutrino mass matrices which no longer fit the solar and atmospheric neutrino oscillation data [76–78]. [3]

Many more papers discussed the phenomenology of quasi-Dirac neutrinos. For example, double beta decay was first discussed in this context in [67], while [80] and [81, 82] consider quasi-Dirac neutrinos as a possible explanation of the atmospheric and solar neutrino problems, respectively. More ambitiously, explaining atmospheric, solar and LSND neutrino oscillations simultaneously was discussed in [83–85]. However, all these proposals are by now ruled out experimentally, since they predict too much oscillations into sterile neutrinos. Limits on quasi-Dirac neutrino parameters, on the other hand, have been derived from solar neutrino data [86] as well as from solar, atmospheric neutrino data and cosmology [87]. Furthermore, in [88–91] QD neutrinos have been discussed in the context of neutrino telescopes, such as IceCube.

Quasi-Dirac neutrino oscillations were also discussed in [92], where it was claimed that to leading order in $m_{R,L}/m_D$ the flavor composition of

[2] This distinction is based on two early papers on the subject [66, 67]. Wolfenstein [66] discussed pairs of active neutrinos, which almost preserve lepton number (due to a relative CP-sign) if the mixing angle between them is close to maximal and the mass splitting is small. He called such particles "pseudo-Dirac" neutrinos. Near the end of the paper, Wolfenstein then extended the terminology to mass matrices which contain both, active and sterile states. In [67], on the other hand, Valle proposed to use the terminology "quasi-Dirac" neutrinos for active-sterile pairs, to differentiate them from "pseudo-Dirac" (active-active pairs).

[3] PD neutrinos have mass matrices with entries close to zero on the diagonal. This is similar to the case discussed in [76–78] for the Zee model [150].

the mass eigenstates does not change (only mass splittings appear), hence oscillations for $n = 3$ pairs of quasi-Dirac neutrinos are described by the standard mixing matrix. This assertion was taken to be true by others [88–90, 93], yet we want to stress that this claim is not correct, as can be seen from eqs. (4.4)–(4.6). Already for one generation, these expressions show that the mass splitting and the departure from maximal mixing are both linearly dependent on $m_{R,L}$ and, more importantly, they are controlled by orthogonal combinations of these two parameters. As such, it is even possible to have no mass splittings at all and at the same time have arbitrary mixing angles.

There are also a number of more theoretical papers discussing how quasi-Dirac neutrinos could arise. One possibility is the so-called "singular" seesaw where the mass matrix for the singlet neutrinos (N^c) has a determinant equal or close to zero [94]. Quasi-Dirac neutrinos from such a singular seesaw with additional type-II seesaw contributions have been discussed in [95]. Another possibility [93] involves introducing additional singlets (S), as it is done for the inverse seesaw mechanism [8]. A double seesaw is then responsible for producing very light S states which, together with the active states, form quasi-Dirac neutrinos [93]. The authors of [96] use a Dirac seesaw to explain the necessary smallness of the Dirac neutrino mass terms first, and then generate quasi-Dirac states by the addition of a very small seesaw type-II term. The "mirror world" model of [97] is another way to obtain these particles.

In models with extended gauge groups quasi-Dirac neutrinos can also appear. An example is the E_6 inspired 331 model of [98]. Here, several electroweak triplets of the gauge group $SU(3)_L$ are needed to accomodate the Standard Model leptons, and the observed active light neutrinos are automatically quasi-Dirac states [99]. A very different idea, based on supergravity has been discussed in [100]. There it was pointed out that if neutrino Dirac terms are generated from the Kähler potential (instead of the superpotential), neutrinos would be quasi-Dirac, since Majorana terms come from higher order Kähler potential terms and thus are expected to be suppressed. This idea [100] is particularly attractive, since it could, at least in principle, explain the observed smallness of the Dirac neutrino mass terms.

In addition to n active neutrinos, models of Dirac neutrinos require the introduction of n Weyl spinors transforming trivially under the electroweak gauge group. For this reason, the study of quasi-Dirac neutrinos necessarily has some overlap with the physics of sterile neutrinos. Many experiments have searched for sterile neutrinos. Most famously, the SNO neutral current measurement rules out dominant contributions of sterile neutrinos to the solar neutrino oscillations [101]. Super-Kamiokande searched for steriles in atmospheric neutrinos [102]. OPERA [103], MINOS and DayaBay [104], IceCube [105] and NOνA [106] published searches for sterile neutrinos. For a more complete list of references see the recent reviews [107, 108]. Note, however, that constraints on sterile are usually derived assuming best fit point values for the standard oscillation parameters, to which two new parameters (one angle and one mass splitting) are added in the fit. This approach does not cover the general quasi-Dirac neutrino parameter space. In particular, keeping the standard neutrino parameters fixed can lead to misleading conclusions about limits for the new/extra parameters.

There are also some hints for the existence of sterile neutrinos. However, all these hints point to a new and *much larger* mass scale in oscillations, i.e. $\Delta m^2 \simeq \mathcal{O}(1)$ eV^2. Since these indications imply masses and mixings very different from those of the standard oscillations, they can not be explained by quasi-Dirac neutrinos. We thus do not discuss these hints any further and refer only to the recent review [108].

4.2 Definitions for quasi-Dirac neutrino oscillations

Dirac neutrinos can be described either in the weak or in the mass basis. The two pictures are equivalent. We will choose the latter one. Consider then a lepton-number preserving model with three active and three sterile neutrinos (ν and N^c).[4] In the basis where the charged lepton mass matrix is diagonal, the relevant part of the Lagrangian reads

$$\mathscr{L} = \frac{g}{\sqrt{2}} \overline{\ell_L} 1 \gamma^\mu \nu W^-_\mu + \bar{\nu} m_\nu N^c + \text{h.c. [flavor basis]}\,. \tag{4.7}$$

[4]Fields with no flavor indices should be seen as vectors.

In order to diagonalize the matrix m_ν, both active and sterile neutrinos must be rotated, $\nu \to V\nu$ and $N^c \to V_N N^c$, such that $m_\nu^{(\mathrm{diag})} = V^T m_\nu V_N$:

$$\mathscr{L} = \frac{g}{\sqrt{2}} \overline{\ell_L} V \gamma^\mu \nu W_\mu^- + \bar{\nu} m_\nu^{(\mathrm{diag})} N^c + \text{h.c.} \;\; [\text{mass basis 1}] \,. \tag{4.8}$$

Strictly speaking, the neutrino mass matrix is not yet diagonal since it is still mixing different states (active and sterile neutrinos). This can be solved by rewriting ν_i and N_i^c $(i = 1, 2, 3)$ as $\psi_i \equiv 1/\sqrt{2}\,(\nu_i + N_i^c)$, and $\psi_{i+3} \equiv i/\sqrt{2}\,(-\nu_i + N_i^c)$:

$$\mathscr{L} = \frac{g}{\sqrt{2}} \overline{\ell_L} \Omega \gamma^\mu \psi W_\mu^- + \sum_{j=1}^{6} m_j^\psi \bar{\psi}_j \psi_j^c + \text{h.c.} \;\; [\text{mass basis 2}] \,. \tag{4.9}$$

where the masses and the 3×6 mixing matrix Ω have a special form (V is a 3×3 square matrix):

$$m_j^\psi = (m_1, m_2, m_3, m_1, m_2, m_3) \qquad [\text{Dirac limit}] \,, \tag{4.10}$$

$$\Omega = \frac{1}{\sqrt{2}} \begin{bmatrix} \ddots & & & \ddots & & \\ & V & & & iV & \\ & & \ddots & & & \ddots \end{bmatrix} \qquad [\text{Dirac limit}] \,. \tag{4.11}$$

If the pattern of masses and mixing in eqs. (4.10) and (4.11) is perturbed, neutrinos are no longer Dirac particles and lepton number is violated. Note that this is equivalent to switching on the lepton number violating masses m_L and m_R in eq. (4.1). We shall now look into the possible departures from the Dirac limit as seen from the mass basis.

In the case of masses, it is possible to split the three pairs of $\left(m_i^\psi, m_{i+3}^\psi\right)$, hence we may introduce three ε_i such that

$$\left(m_i^\psi\right)^2, \left(m_{i+3}^\psi\right)^2 \to m_i^2 - \frac{\varepsilon_i^2}{2}, m_i^2 + \frac{\varepsilon_i^2}{2} \,, \tag{4.12}$$

with the understanding that, for quasi-Dirac neutrinos, the ε_i are small in comparison to the atmospheric and solar mass scales. In total there are now five mass parameters relevant for oscillation experiments: the usual $\Delta m^2_{\mathrm{Atm}}$

and $\Delta m^2_{\odot}$, plus three new ε_i mass splittings. (As usual, the overall mass scale of neutrinos does not enter the oscillation probabilities.)

Let us now turn our attention to a generic mixing matrix Ω with dimensions $n \times m$. Such a matrix can be described by $2nm$ real numbers, yet orthonormality of rows ($\Omega\Omega^\dagger = 1$) imposes n^2 conditions on them, and furthermore it is possible to absorb n phases into the charged lepton fields, hence there is a total of $n\,(2m - n - 1)$ real physical degrees of freedom in Ω. For a 3×6 matrix, this corresponds to 12 angles and 12 phases, but note that 5 of these phases cannot be observed in neutrino oscillation experiments (they correspond to column phases). The matrix Ω can be explicitly parametrized as follows [22] (called below the SV parametrization). First, consider an elementary rotation in the (i, j) entries given by the complex number $\widetilde{\theta}_{ij} \equiv \theta_{ij} \exp i\phi_{ij}$ such that, in the (1,2) case, it has the form

$$R\left(\widetilde{\theta}_{12}\right) = \begin{pmatrix} \cos\theta_{12} & -e^{i\phi_{12}}\sin\theta_{12} & 0 & \cdots \\ e^{-i\phi_{12}}\sin\theta_{12} & \cos\theta_{12} & 0 & \cdots \\ 0 & 0 & 1 & \cdots \\ \vdots & \vdots & \vdots & \ddots \end{pmatrix}. \tag{4.13}$$

In the SV parametrization, the i-th row of Ω ($\equiv \Omega_i$) is then given by the expression

$$\Omega^T_{SV,i} = \prod_{a=1}^{i} \prod_{b=a+1}^{6} R\left(\widetilde{\theta}_{ab}\right) e^{(i)}\,, \tag{4.14}$$

where $e^{(i)}$ is a column vector with entries $e^{(i)}_j = \delta_{ij}$. We do not give here Ω_{SV} in full because the expression is very lengthy.

For a particular arrangement of the 24 angles and phases in eq. (4.14), Ω takes the special form (4.11) which is associated with the Dirac limit. Note that, as usual, one can write the 3×3 square matrix V with three angles and one phase:

$$V = \begin{pmatrix} 1 & 0 & 0 \\ 0 & \cos\theta_{23} & \sin\theta_{23} \\ 0 & -\sin\theta_{23} & \cos\theta_{23} \end{pmatrix} \begin{pmatrix} \cos\theta_{13} & 0 & \sin\theta_{13}e^{-i\delta} \\ 0 & 1 & 0 \\ -\sin\theta_{13}e^{i\delta} & 0 & \cos\theta_{13} \end{pmatrix} \begin{pmatrix} \cos\theta_{12} & \sin\theta_{12} & 0 \\ -\sin\theta_{12} & \cos\theta_{12} & 0 \\ 0 & 0 & 1 \end{pmatrix}. \tag{4.15}$$

Unfortunately, it is very complicated to describe the Dirac limit in the SV parametrization. Hence we make a small modification by introducing the following 6×6 rotation matrix:

$$\Omega\left(\theta_{ij}, \phi_{ij}\right) \equiv \Omega_{SV}\left(\theta_{ij}, \phi_{ij}\right) U \ , \ U = \frac{1}{\sqrt{2}} \begin{pmatrix} \mathbb{1} & i\mathbb{1} \\ \mathbb{1} & -i\mathbb{1} \end{pmatrix} . \tag{4.16}$$

With this definition, the mixing matrix in eq. (4.11), with V parametrized as in eq. (4.15), corresponds to $\Omega\left(\theta_{ij}, \phi_{ij}\right)$, as in (4.16), with $\theta_{i4} = \theta_{i5} = \theta_{i6} = 0$ $(i = 1, 2, 3)$, $\phi_{12} = \phi_{23} = 0$ and $\phi_{13} = \delta$. In other words, with this definition the Dirac limit for Ω simply corresponds to keeping only the standard three generation neutrino mixing angles non-zero.

We can then write the probability of neutrino oscillation from a flavor α to a flavor β for an energy E and after a length L as:[5]

$$P\left(\nu_\alpha \to \nu_\beta\right) = \left| \sum_{j=1}^{6} \Omega_{\beta j} \Omega_{\alpha j}^{*} \exp\left(-\frac{i m_j^2 L}{2E}\right) \right|^2 \tag{4.17}$$

Note that this expression is insensitive to column rephasings:
$\Omega \to \Omega\, \mathrm{diag}\left(e^{i\kappa_1}, e^{i\kappa_2}, e^{i\kappa_3}, e^{i\kappa_4}, e^{i\kappa_5}, e^{i\kappa_6}\right)$. It is easy to show that eq. (4.17) reduces to the standard oscillation formula in the Dirac limit.

4.3 χ^2 statistic

In statistics, we are interested to use a given sample of data to assess the validity of a model or determine the values of its parameters. One of the most used method for this purpose is the χ^2 method [109]. Consider a set of N indipendent measurements y_i. The measurement y_i is assumed to be Gaussian distribuited. Suppose that we want to describe these measured quantities by a function f_i and we want to test the *goodness of the fit*, i.e. the agreement between the data and the hypothesized theory used in the

[5] This is true as long as the rows of Ω are orthonormal, i.e. $\Omega\Omega^\dagger = 1$.

fit. The quantity to be calculated is

$$\chi^2 = \sum_i \frac{(y_i - f_i)^2}{\sigma_i^2}, \tag{4.18}$$

where σ_i^2 is the variance that in general is a sum of two kinds of error, statistical and systematic

$$\sigma^2 = \sigma^2_{stat.} + \sigma^2_{syst.}, \tag{4.19}$$

with the statistical error

$$\sigma^2_{i\,stat.} = e_i. \tag{4.20}$$

If the hypothesis f_i is "reasonable", the ratio $\chi^2/n.d.f \sim 1$, with n.d.f the number of degree of freedom given from the number of measurements N minus the number of fitted parameters.
It can also happen that the hypothesis f_i depends on a set of parameters $\Theta = (\theta_1, \theta_2, ..., \theta_n)$ whose values are unknown. In this case one can find the values of the parameters Θ that minimize the χ^2.

4.4 Solar and Atmospheric experiments

In our analysis we do not take into account the data from every existing oscillation experiment. Given the scarcity of data on τ neutrinos, we ignored it altogether, concentrating instead on the available charged current data for e and μ neutrinos and anti-neutrinos. Also, we focus on those experiments, which should provide the most important constraints for quasi-Dirac neutrinos. First, we consider KamLAND [65] since it fixes most accurately the so-called solar mass splitting $\Delta m^2_{\odot}$. From the solar neutrino experiments we fit Super-K elastic scattering data [110] and from Borexino the measured pp [111] and ^7Be fluxes [112]. This choice is motivated by the fact that Super-K [110] has the most accurate data in the high energy range, while [111, 112] fix the low energy part of the solar neutrino spectrum.

We take the atmospheric neutrino data from [113]. We concentrate in our fit on the sub-GeV sample, since the lowest energetic neutrinos will

be most sensitive to small values of ε_i^2, as demonstrated in fig. (4.2). In addition, we use data from the MINOS collaboration (muon and anti-muon neutrino survival) [114] and T2K (muon neutrino survival and muon to electron neutrino transition) [115], since these two experiments determine Δm^2_{Atm} better than atmospheric data. And, finally, we take into account data from DayaBay [116], since from the three current reactor neutrino experiments DayaBay determines θ_{13} with the smallest error.
In subsection 4.4.1 we give a description of all the experiments mentioned above and in subsection 4.4.2 we discuss the correlation between the data taken from three different experiments and the theoretical prediction. As an example we chose KamLAND, MINOS and T2K. We show the results obtained from our analysis for every single experiment, differently from section 5 in which we present the results for combined experiments.

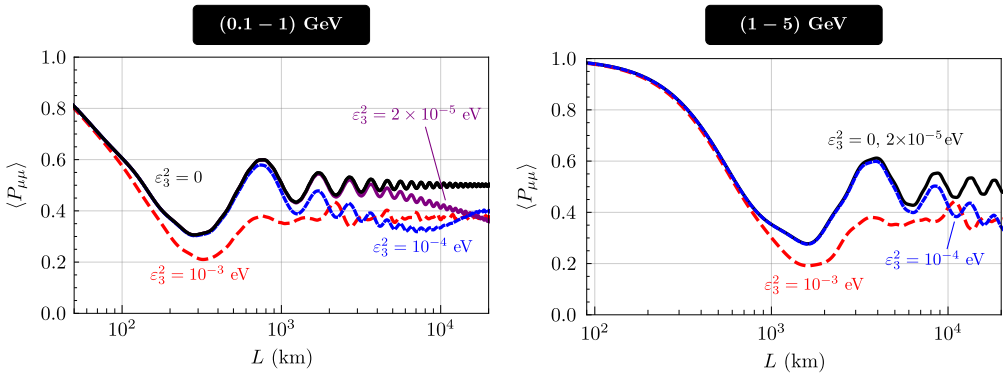

Figure 4.2: Averaged atmospheric muon neutrino survival probability for neutrinos with energies $E_\nu = (0.1 - 1)$ GeV (left) and $E_\nu = (1 - 5)$ GeV (right), as a function of distance (L), for different choices of ε_3^2. Lower neutrino energies are more sensitive to small ε_3 values. This plot is calculated with the simplifying assumptions of $\sin^2\theta_{23} = 1/2$, $\theta_{13} = 0$ and $\Delta m^2_\odot = 0$.

4.4.1 Description of experiments and their results

4.4.1.1 KamLAND experiment

The Kamioka Liquid-scintillator Antineutrino Detector [117] demonstrated the oscillatory nature of neutrino flavor transformation by observing electron anti-neutrinos ($\bar{\nu}_e$) with energies of a few MeV from nuclear reactors located at different distances. The idea of this experiment was to exploit the old Kamiokande underground site and the presence of large nuclear power reactors located at different distances in the range $[160, 824]$ km. There are several commercial nuclear power plants in Japan supplying one-third of the total electric power in the country. At the Kamioka site there is an anti-neutrino flux of $1.3 \times 10^6 cm^{-2} s^{-1}$ for $E_{\bar{\nu}} > 1.8$ MeV at maximum power from these reactors. Of this flux 80% comes from reactors between 140 km and 210 km away. The very large ratio of this distance to the neutrino energy makes the experiment sensitive as small as $\Delta m^2_{12} \sim 7 \cdot 10^{-6} eV^2$ for large mixing. This covers one of the possible solutions to the solar neutrino problem (specifically the large mixing angle solution (LMA)) [118]. In the KamLAND experiment nuclear reactors produce $\bar{\nu}_e$ isotropically in the β decay of the neutron-rich fission fragments. Electron anti-neutrinos are captured on protons in the detector liquid scintillator according to the reaction: $\bar{\nu}_e + p \rightarrow e^+ + n$. These events are detected using the delayed coincidence between positron emission and the gamma ray from neutron capture. The analysis [65] gave a best fit at $\Delta m^2_{12} = 7.59^{+0.21}_{-0.21} 10^{-5} eV^2$ and $\tan^2(\theta_{12}) = 0.47^{+0.06}_{-0.05}$.

4.4.1.2 Borexino experiment

Solar neutrino experiments [119] [120] [121] [122] have revealed important information about the Sun [123] and have shown that solar neutrinos undergo flavour transitions that are well described by Mikheyev-Smirnov-Wolfenstein Large Mixing Angle ("MSW-LMA") type flavour oscillations [16]. The MSW theory predicts a transition in the solar ν_e survival probability at neutrino energies of about 1-4 MeV. Therefore, in order to test MSW-LMA more thoroughly and to further improve our understanding of the Sun, it is important that experimental measurements of the low energy solar neutrino fluxes be improved.

The Borexino detector [111] is located deep underground (3,800 m of water equivalent) at the Gran Sasso laboratory, in central Italy. Borexino detects solar neutrinos by measuring the energy deposited in the liquid scintillator target by recoiling electrons following neutrino-electron elastic scattering. The scintillator promptly converts the kinetic energy of electrons into photons, detected and converted into electronic signals (photoelectrons). The interaction in the scintillator of ionizing particles, such as those resulting from radioactive decays inside the detector (the background), can mimic and cover the expected signal. Every effort was made to minimize radioactive contamination of the scintillator and all surrounding detector materials. The main goal of the experiment is the detection of the monochromatic neutrinos that are emitted in the electron capture decay of ^7Be in the Sun [112] and the spectral study of other solar neutrino components, such as the pp neutrinos.

Searching for *pp* neutrinos

In the Sun, hydrogen is transformed into helium predominantly via the pp cycle, a chain of reactions releasing 26.73 MeV and electron neutrinos ν_e, and summarized as $4p \rightarrow {}^4He + 2e^+ + 2\nu_e$. The cycle begins with the fusion of two protons into a deuteron, which occurs 99.76% of the time by means of the primary reaction $p + p \rightarrow {}^2H + e^+ + \nu_e$. Neutrinos produced in this step are referred to as pp neutrinos. The pp neutrino analysis is performed through a fit of the energy distribution of events selected to maximize the signal-to-background ratio. The selection criteria remove residual cosmic muons, decays of muon-produced isotopes, and electronic noise events. Furthermore, to suppress background radiation from external detector components, only events whose position is reconstructed inside the central detector volume are used in the analysis. The fit is done within a chosen energy interval and includes all relevant solar neutrino components and those from various backgrounds, mostly from residual radioactivity traces dissolved in the scintillator. The data used for the analysis were acquired from January 2012 to May 2013 (408 days of data; Borexino Phase 2). The pp neutrino rate has been extracted by fitting the measured energy spectrum of the selected events in the 165-590 keV energy window with the expected spectra of the signal and background components. The solar pp neutrino interaction rate measured by Borexino is $144 \pm 13(stat.) \pm 10(syst.) counts/(day \cdot 100 ton)$ [111].

Measurement of the ^7Be solar neutrinos
At 862 keV, the abundant, mono-energetic, ^7Be solar neutrinos can provide a precise probe of the survival probability in the low energy region.Borexino's result is based on the analysis of 740.7 live days (after cuts) of data which were recorded in the period from May 16, 2007 to May 8, 2010, and which correspond to a 153.6 $ton \cdot yr$ fiducial exposure. Fits to the spectrum of observed event energies are used to distinguish between this neutrino scattering feature and backgrounds from radioactive decays. Two independent fit methods were used, one of which is Monte Carlo based and one which uses an analytic description of the detector response. The best value for the interaction rate of 862 keV 7^Be solar neutrinos in Borexino is $46.0 \pm 1.5(stat) + 1.5 - 1.6(syst) counts/(day \cdot 100 ton)$ [112].

4.4.1.3 Super-K experiment

Super-K [124] is a large water Cherenkov detector, it is located 1000 m underground (2700 m of water equivalent) in Kamioka Observatory, deep within the Kamioka mine in Gifu Prefecture, Japan. The detector consists of two parts: the inner detector, which studies the details of neutrino interactions, and the outer detector, which identifies the incoming and outgoing charged particles.

Solar neutrinos
Currently there are two types of testable signatures unique to neutrino oscillations, the first being the observation and precision test of the Mikheyev-Smirnov-Wolfenstein (MSW) resonance curve [16], the characteristic energy dependence of the flavor conversion: higher energy solar neutrinos (higher energy ^8B and hep neutrinos) undergo adiabatic resonant conversion within the Sun, while the flavor changes of the lower energy solar neutrinos arise only from vacuum oscillations. The transition from the matter-dominated oscillations within the Sun to the vacuum-dominated oscillations should occur near three MeV. This makes ^8B neutrinos the best choice when looking for a transition point within the energy spectrum. A second signature unique to oscillations arises from the effect of the terrestrial matter density on solar neutrino oscillations. This effect is tested directly by comparing solar neutrinos that pass long distances through the Earth at nighttime

to those which do not pass through the Earth during the daytime. Those neutrinos which pass through the Earth will generally have an enhanced electron neutrino content, leading to an increase in the nighttime electron elastic scattering rate. Super-K is sensitive to ^8B and hep solar neutrinos in the energy range around 4 to 18.7 MeV and precisely measures the neutrino interaction time. Super-K is therefore a good detector to search for both solar neutrino oscillation signatures.
Super-Kamiokande-IV data-taking began in September of 2008; the following results [110] includes data until February 2014, a total lifetime of 1664 days. Fig. 4.3 shows the ratio of data to prediction assuming no oscillation for pp, ^7Be and ^8B neutrinos. The SK-IV solar neutrino data determine the solar mixing angle as $\sin^2(\theta_{12}) = 0.327^{+0.026}_{-0.031}$ and the mass-squared splitting $\Delta m^2_{21} = 4.8^{+1.5}_{-0.8} \times 10^{-5} eV^2$ [110].

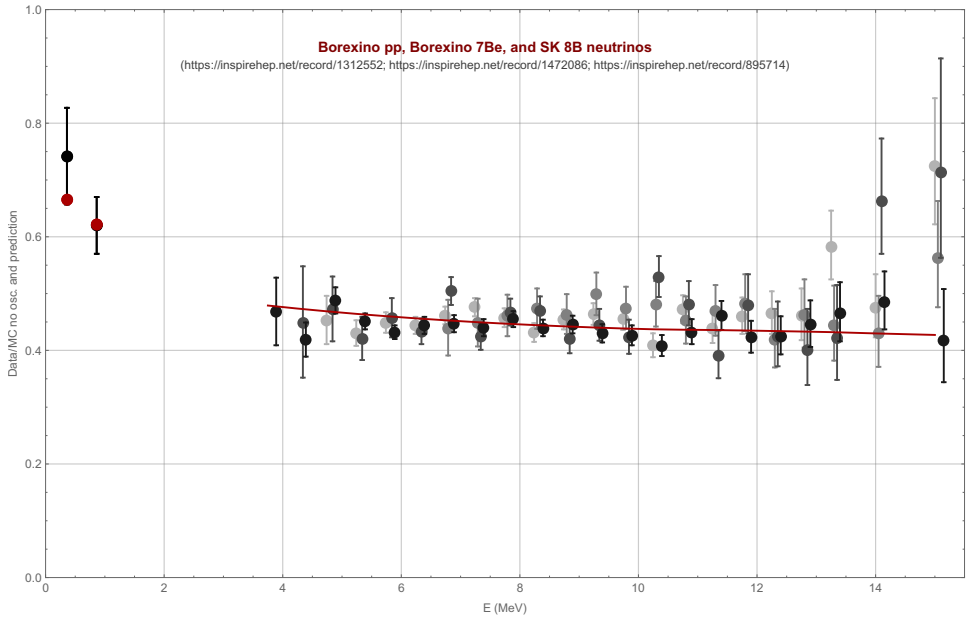

Figure 4.3: The ratio of data to prediction assuming no oscillation for pp, ^7Be and ^8B neutrinos. Black line refers to experimental data and red line to our prediction for the current global best fit points [5].

Atmospheric neutrinos

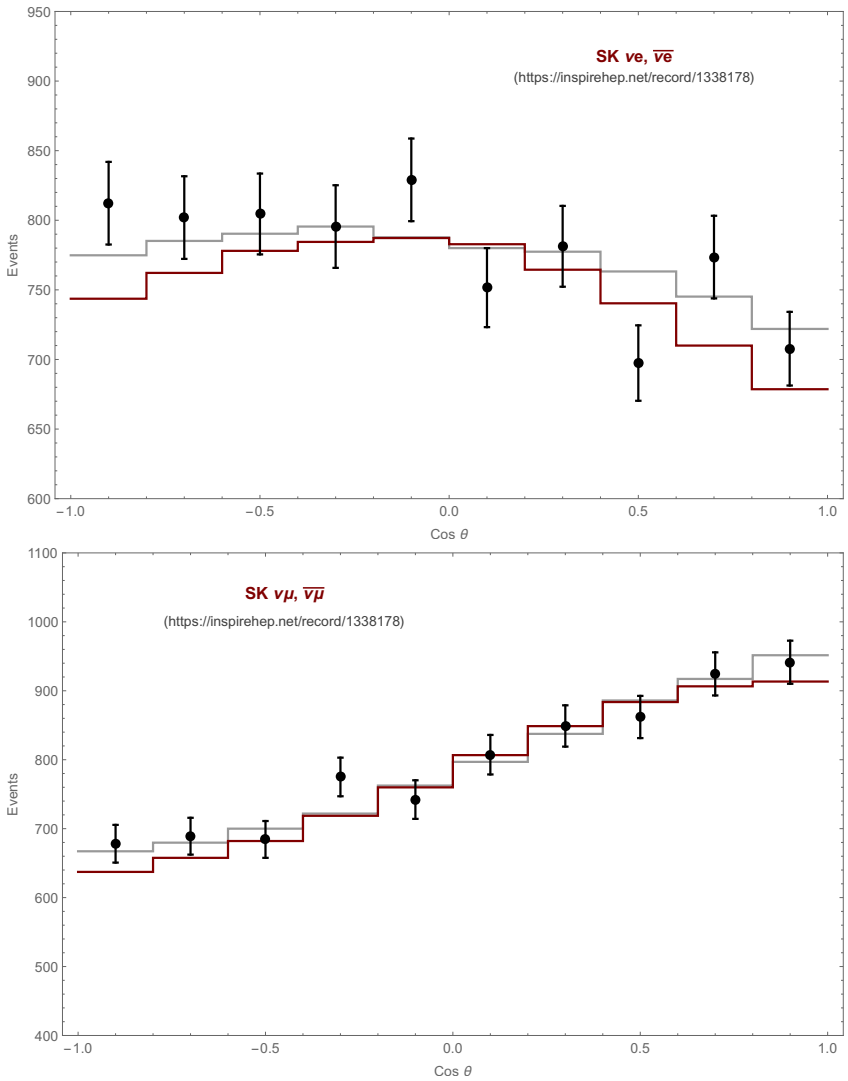

Figure 4.4: Zenith-angle θ distributions for multi-GeV atmospheric neutrino events based on 3.903 days of exposure of the Super-Kamiokande detector. Top panel: the distribution for e-like events. Bottom panel: the distribution for μ-like events. Black line refers to experimental data, grey line to the best fit points of Super-K as global [113] and red line to our prediction for the current global best fit points [5].

In the GeV/nucleon energy region, cosmic-ray particles consist mostly of protons, helium nuclei and a still-smaller fraction of heavier nuclei. These particles interact with the nuclei in the atmosphere high above the Earth. In these high-energy cosmic-ray interactions with nuclei, many pions (and, less abundantly, kaons) are produced. These pions decay to other particles. Similar decay processes occur for kaons and other particles. In this manner, neutrinos are produced. The flavor ratio of $\nu_\mu + \bar{\nu}_\mu$ to $\nu_e + \bar{\nu}_e$ below the GeV scale is approximately two, considering the dominance of the $\pi^\pm$ decay chains. This flux ratio is a good indicator of neutrino oscillations, given that it should deviate from the predicted ratio if neutrinos oscillate. Another important feature of the atmospheric neutrino flux is its up-down symmetry. A neutrino thus produced enters the Earth in a point with a zenith angle θ_{in} and should exit at a point with a zenith angle $\pi - \theta_{in}$. Because a cosmic ray enters the atmosphere at approximately the same rate at any position, there must be a neutrino that enters and exits at the same points with the same zenith angles. These two processes occur at equal rates insofar as the primary cosmic-ray fluxes in both positions are equal. Thus, the flux should be up-down symmetric. A comparison between the up-down asymmetry of the experimental data and the prediction of the expected flux, coming from Monte Carlo simulations, provided compelling evidence for neutrino oscillations and has been used to measure the neutrino mixing angle. The fig. 4.4 shows the zenith-angle θ distributions for multi-GeV atmospheric neutrino events.
The total number of atmospheric neutrino events observed in Super-Kamiokande between 1996 and 2012 (3.903 days) is $\sim$ 40.000. The Super-Kamiokande Collaboration performed a neutrino oscillation analysis by using these events.

4.4.1.4 Minos experiment

The MINOS experiment carries out precision measurements of neutrino oscillation via ν_μ disappearance. The main characteristic of this experiment is that for the first time two different data sets are used [114]: neutrinos produced in the NuMI accelerator [125] and those produced by cosmic ray interactions in the atmosphere. The accelerator provides a source of neutrinos with a fixed baseline and an energy spectrum that peaks at $L/E \sim 250$ km/GeV, close to the region where the ν_μ survival probabil-

ity reaches its first minimum. Atmospheric neutrinos are produced with a range of $E \sim (0.5 - 10^4)$ GeV and $L \sim (10 - 10^4)$ km. The combination of these two samples increases the precision of the oscillation measurements. Moreover, MINOS has the ability to separate neutrinos and antineutrinos on an event-by-event basis. The NuMI beam is produced at Fermilab by $120GeV$ protons striking a graphite target. This collision produces mesons and some of them decay to muons and neutrinos during their flight through a decay tunnel. The remaining protons and mesons are removed from the beam by an hadron absorber downstream of the decay region, the muons are absorbed by a rock shield while the neutrinos continue through it. The energy spectrum of the neutrino beam can be changed by varying the distance between the target and the hadron absorber. The data used in MINOS analysis were obtained using the low-energy beam configuration, in which the peak neutrino energy is 3.3 GeV [126]. By selectively focusing positive or negative pions and kaons, a ν_μ or $\bar{\nu}_\mu$ beam is produced. The MINOS experiment uses two detectors, called "near" and "far", to record the interactions of neutrinos in the NuMI beam. The near detector at Fermilab is used to characterize the neutrino beam and its interactions and is located about $1km$ from the primary proton beam target. The far detector performs similar measurements 735 km downstream. The focus of the experiment is to compare the rates, energies and topologies of events at the far detector with those at the near detector and from those comparisons determine the relevant oscillation parameters. The oscillations observed by MINOS are driven by the larger mass-squared difference Δm^2_{23} and are well described by an effective two flavor model with a single mass-squared difference and a mixing angle. A previous two flavor analysis yielded $\Delta m^2_{23} = 2.41^{+0.09}_{-0.10} 10^{-3}$ $\mathrm{eV}^2 and \sin^2(2\theta_{23}) = 0.950^{+0.035}_{-0.036}$ [114]. This result comes from the full MINOS data set collected over a period of 9 years.

4.4.1.5 T2K experiment

T2K (Tokai to Kamioka) [127] [128] is a long-baseline neutrino oscillation experiment that uses an intense muon neutrino beam to measure the mixing angle θ_{13} via the ν_e appearance [129] and the mixing angle θ_{23} and mass difference Δm^2_{23} via the ν_μ disappearance [130]. This experiment was made possible by the construction of the J-PARC high-intensity proton

accelerator at 295 km of distance from the Super-Kamiokande (SK) detector [131]. From the interaction of the 30 GeV proton beam extracted from J-PARC and a graphite target pions are generated and they quickly decay to muons and muons neutrinos. The neutrino/antineutrino beam is monitored at near detectors INGRID (on-axis) and ND280 (off-axis) placed at 280 m from the target and at the far detector (SK). The near detectors were constructed in order to reduce systematic uncertainties, they measure the number of muon neutrinos in the beam before any oscillation occurs. This measurement is used to predict the number of muon neutrinos that would be seen in the far detector if there were no oscillations. The main characteristic of this experiment is that it employs the off-axis method [132] to generate a narrow-band neutrino beam. The peak energy of the neutrino beam can be varied by changing the off-axis angle as illustred in the Fig. 1 of [133]. In this experiment, the off-axis angle is set at 2.5° so that the neutrino beam at SK has a peak energy at about 0.6 GeV, near the expected first oscillation maximum for $L \sim 300$ km. Since the energy spectrum changes depending on the off-axis angle, the neutrino beam direction has to be precisely monitored.
At 68% confidence level the analysis of combined measurements of muon neutrinos disappearence and electron neutrinos appearence gave a best fit at $\Delta m^2_{23} = 2.51^{+0.29}_{-0.25} 10^{-3} eV^2$ and $\sin^2(\theta_{23}) = 0.45^{+0.19}_{-0.07}$ [132].

4.4.1.6 DayaBay experiment

Nuclear reactors produce an intense and pure flux of $\bar{\nu}_e$'s, which is useful for esperimental searches for θ_{13} [116]. Reactor $\bar{\nu}_e$ are most commonly detected via inverse beta decay (IBD), $\bar{\nu}_e + p \rightarrow e^+ + n$, that consists of the capture of an electron anti-neutrino on a proton (hydrogen) resulting in the production of a positron and a neutron. The number of inverse beta-decay reactions is determined by counting the coincidence of the energy deposited by the positron (1 MeV to 8 MeV) followed by the energy released (8 MeV) from the neutron capture $\sim$ 30 ms later. Charge current interactions of $\bar{\nu}_\mu$ or $\bar{\nu}_\tau$ at these energies are forbidden by energy conservation, hence oscillation is observed as a disappearance of the expected $\bar{\nu}_e$ signal. The disappearance signal is most pronounced at the first oscillation minimum of the $\bar{\nu}_e$ survival probability. Based on existing accelerator and atmospheric

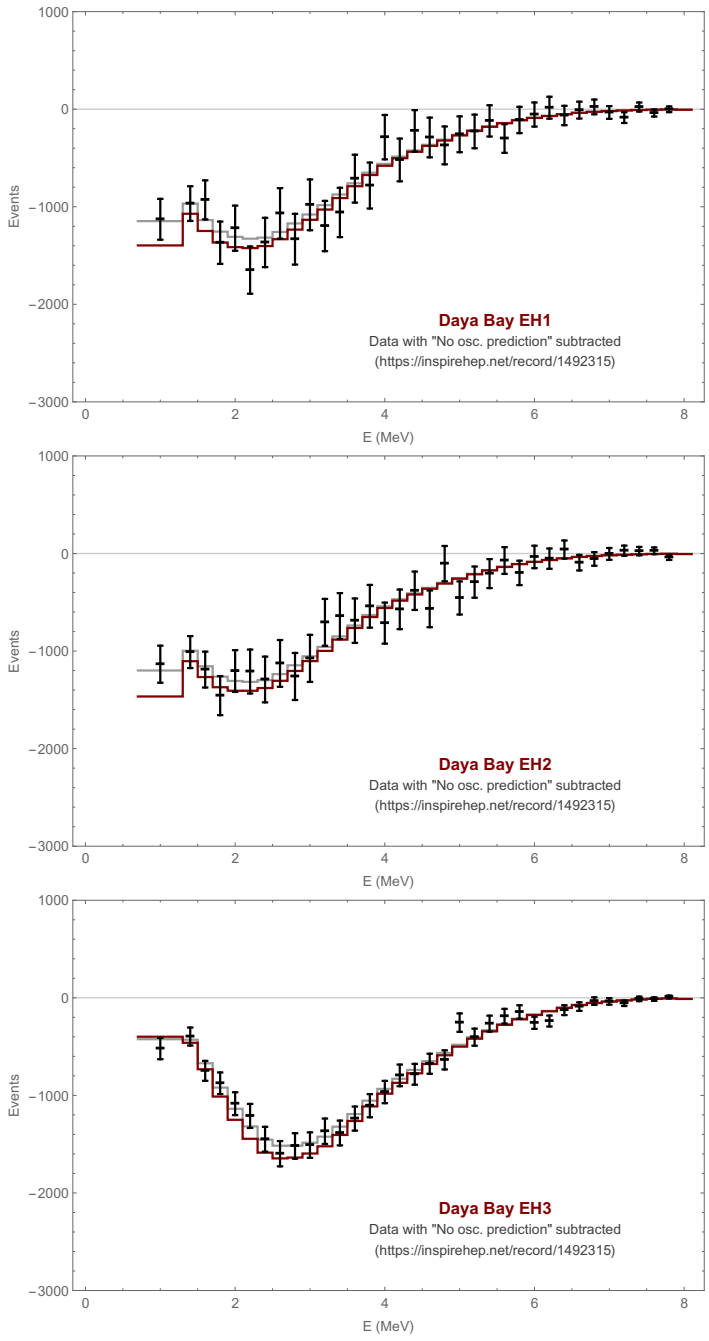

Figure 4.5: The ratio of data to prediction assuming no oscillation, with an arbitrary normalization. The spectra of the detectors in each experimental hall are combined: EH1 (top), EH2 (middle), and EH3 (bottom). Black line refers to experimental data, grey line to the best fit from the experiment and red line to our prediction for the current global best fit points.

ν_μ measurements of Δm^2_{32}, this corresponds to a distance $L_f \sim 1.6$ km for reactor $\bar{\nu}_e$ with a mean energy of ~ 4 MeV. Significant $\bar{\nu}_e$ disappearance in the near detectors would have reduced the overall sensitivity of the far-to-near comparison, so L_n was kept to ~ 500 m or less. The Daya Bay nuclear power complex is located in the city of Shenzhen, China. It consists of six 2.9 GWth pressurized water reactors and produced roughly $3.5 \times 10^{21} \bar{\nu}_e/s$. The Daya Bay experiment consists of three underground experimental halls (EHs) connected with horizontal tunnels, the two near halls (EH1 and EH2) and the far hall (EH3). Eight antineutrino detectors (ADs) are installed in the three halls, with two in EH1, two in EH2, and four in EH3. The locations of the experimental halls were determined to optimize sensitivity to θ_{13}.
From Dec. 4, 2011 to Jul. 28, 2015, the Daya Bay experiment measured the rate and energy spectrum of electron antineutrinos emitted and a total of $2.5 \times 10^6 \nu_e$ inverse beta decay interactions were observed. The unprecedented statistics of this sample allowed the most precise measurement of ν_e disappearance to date. Fig. 4.5 shows the ratio of the background-subtracted spectra for the ν_e candidate interactions to prediction assuming no oscillation. A relative comparison of the rates and positron energy spectra of the detectors located far ($\sim 1500 - 1950$ m) relative to those near the reactors ($\sim 350 - 600$ m) gave $\sin^2(2\theta_{13}) = 0.0841 \pm 0.0027(stat.) \pm 0.0019(syst.)$ [116]

4.4.1.7 Future experiment: JUNO

The Jiangmen Underground Neutrino Observatory (JUNO) [134], a 20 kton multi-purpose underground liquid scintillator detector, was proposed with the determination of the neutrino mass hierarchy as a primary physics goal. The detection of antineutrinos generated by a cluster of nuclear power plants allows the determination of the neutrino mass hierarchy at a $3 - 4\sigma$ significance with six years of running of JUNO. The measurement of the antineutrino spectrum with excellent energy resolution will also lead to the precise determination of the neutrino oscillation parameters $\sin^2\theta_{12}, \Delta m^2_{12}$ and Δm^2_{ee} to an accuracy of better than 1%, which will play a crucial role in the future unitarity test of the PMNS matrix. Meanwhile, JUNO can also provide us excellent opportunities to test the eV-scale sterile neutrino hy-

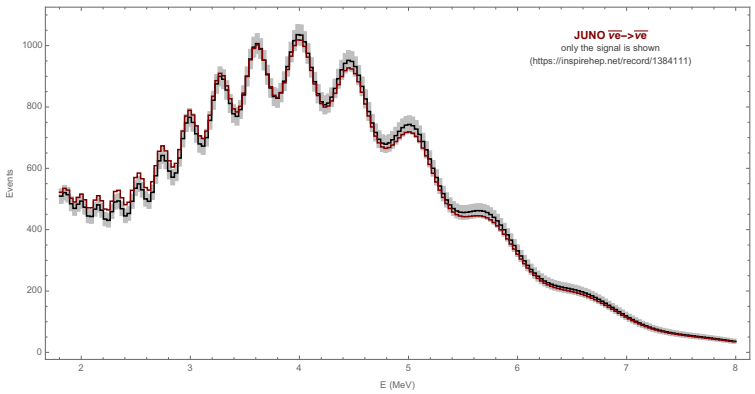

Figure 4.6: The number of simulated events as a function of the energy. Black line refers to experimental data, grey line to the best fit from the experiment and red line to our prediction for the current global best fit points. For more details see the text.

pothesis, using either radioactive neutrino sources or a cyclotron-produced neutrino beam. The JUNO detector is also sensitive to several other beyond-the-standard-model physics. Examples include the search for proton decay via the $p \to K^+ + \bar{\nu}$ decay channel, search for neutrinos resulting from dark-matter annihilation in the Sun, search for violation of Lorentz invariance via the sidereal modulation of the reactor neutrino event rate, and search for the effects of non-standard interactions.
The Juno experiment was proposed in 2008 to determine the neutrino mass hierarchy by detecting reactor antineutrinos from the Daya Bay nuclear power plant (NPP), thus formerly known as "Daya Bay II experiment". The mass hierarchy determination requires equal baselines from the detector to all reactor cores to avoid cancellation of the oscillation dephasing effect. Due to the complex and unclear layout of the future nuclear power plants in the neighborhood, the experiment was moved to Jiangmen city in Guangdong province in August 2012, and named as JUNO in 2013. The site location is optimized to have the best sensitivity for the mass hierarchy determination, which is at 53 km from both the Yangjiang and Taishan NPPs [135]. The neutrino detector is a liquid scintillator (LS) detector with a 20 kton fiducial mass, deployed in a laboratory 700 meter underground. The JUNO project was approved by Chinese Academy of Sciences in Febru-

ary 2013. Data taking is expected in 2020. Fig. 4.6 shows the number of events as a function of the energy. We produced a set of data that matches the theory, so χ^2 was zero.

4.4.2 Experimental data fit

We have seen that to construct quasi-Dirac neutrinos we can start from a theory with Dirac neutrinos to which we add new mass splitting and/or new mixing angles. Here we deal with the simplest case in which we add a mass splitting at a time to the standard three-generation context. The oscillation probabilities will therefore depend on a new parameter representing the quasi-Diracness of neutrino. Hence, we will show in detail that the quasi-Dirac theory fit the experimental data, in particular of KamLAND, MINOS and T2K and we will display the results of the limits derived on the parameter space from these three experiments separately. This will be useful to understand how data fit works before arriving at the next section where we will consider different scenarios and we will present the results obtained from a more complete analysis considering the combination of more experiments.
In this section we always have used a certain parametrization for the masses that we call *symmetric parametrization*: $m_i, m_{i+3} \to \sqrt{m_i^2 - \varepsilon_i^2/2}, \sqrt{m_i^2 + \varepsilon_i^2/2}$.

4.4.2.1 Correlation between KamLAND and the theoretical prediction

The data reported in [117] are based on a total live-time of 2991 days, collected between March 9, 2002 and November 20, 2012. This data set has been divided into three periods and we choose to compare our theoretical prediction with the experimental data collected in the first period (1486 days live-time), that means, to May 12, 2007. The last two periods in fact contain less data, this is a reflection of the fact that some reactors were switched off (in particular the third period was marked by the Fukushima nuclear accident in March 2011). So, we extracted the data from Fig. 1 in [65]. The positron energy (that is related to the neutrino one $E_\nu = E_p + 0.8$) range $[1.8, 9.0]$ MeV has been divided into 17 bins. To each bin corresponds the number of events experimentally measured (s_i) and the number of events

associated to the background (N_{bi}). The same picture shows the efficiency (ξ_i) of the detector as a function of the energy.
There are different types of backgrounds, in particular in Period I the dominant background is the $^{13}C(\alpha, n)^{16}O$ reaction, generated from the α-decay of ^{210}Po in the liquid scintillator; another contribution is due to the geoneutrinos flux produced by β-decays of the nuclei in the decay chains of ^{238}U and ^{232}Th within the earth and finally the accidental background.
The backgrounds are detailed in Table 1 of [117].
In principle, we considered the KamLAND proposal [118] in which in Table 3 one finds the event rate of no-oscillation coming from each reactor with a 100% of "live-time". Then, we saw that in [136] it is discussed that more reactors were added since the time of the KamLAND proposal and some values of thermal powers and distances were changed (see Table 1 of [136]). So we considered these data for our analysis. In the previous chapter we discussed the neutrino oscillation with the assumption of only two generations and we give the formula for the neutrino survival probability (see eq. 2.10). In order to improve the precision for our theoretical calculation the mean probability for each bin was calculated by choosing to subdivide it into $n = 5$ "sub-bins".

$$\begin{aligned} \bar{P} &= \frac{1}{n}\sum_{k=1}^{n} P_{k,\nu_e\to\nu_e}(E_p), \\ t_i &= \frac{1}{18}\sum_{j=1}^{18} \bar{P}_{i\nu_e\to\nu_e}(L_j)\cdot w_j \cdot \mathcal{N}_i(E_p), \end{aligned} \tag{4.21}$$

where $j = 1, ..., 18$ refers to the reactor distances from the detector and $i = 1, ..., 17$ the number of energy bins, $\mathcal{N}$ represents the reactor anti-neutrino spectrum [137] multiplied for the efficiency and normalized to the total number of events expected without oscillation N_{tot} and w_j the probability rate from each reactor of no oscillation:

$$\begin{aligned} \mathcal{N}(E_p) &= f(E_p)\cdot\sigma(E_p)\cdot\xi(E_p)\cdot N_{tot}, \\ w_j &= \frac{\mathcal{P}_j}{4\pi L^2}T_j, \end{aligned} \tag{4.22}$$

with $\mathcal{P}$ the thermal power of the nuclear power station and T the operating time.

With all this information we constructed the χ^2 where

$$\begin{aligned} e_i &= s_i - N_{bi} \\ \sigma^2 &= \sigma^2_{stat.} + \sigma^2_{syst.} = e_i + N_{bi}. \end{aligned} \tag{4.23}$$

We started by considering the standard oscillation to check if our calculation reproduces the same result as KamLAND analysis. This gives

$$\begin{aligned} \chi^2_{min} &= 16.1, \\ \Delta m^2_{12} &= 7.7^{+0.1}_{-0.2} \times 10^{-5} eV^2, \\ \sin^2(2\theta_{12}) &= 0.90^{+0.3}_{-0.4}. \end{aligned} \tag{4.24}$$

The ratio $\chi^2_{min}/n.d.f. \sim 1.07$ indicates that the standard oscillation theory agrees with the experimental data, moreover, one can see the values of Δm^2_{12} and $\sin^2(2\theta_{12})$ that minimize the χ^2 are in the 1σ region of the experimental data [65]. Then, we analyzed the quasi-Dirac case. Since KamLAND is sensitive to Δm^2_{12}, it will be sensitive to both ϵ^2_1 and ϵ^2_2. It means that two quasi-Dirac pairs can be constrained. We calculated the χ^2 for the KamLAND experimental data and the theoretical quasi-Dirac prediction in both cases:

$$\begin{aligned} \chi^2_{min}(\epsilon_1) &= 14.8, \\ \chi^2_{min}(\epsilon_2) &= 14.5. \end{aligned} \tag{4.25}$$

The ratio $\chi^2(\epsilon_i)/n_{d.o.f.}$ are $\sim$ 1.06 and $\sim$ 1.04 respectively. So, we can conclude that both theories, standard and quasi-Dirac, equally agree with the experimental data. There is no preference for either.

In Fig. 4.7 we display the allowed regions at $1\sigma, 2\sigma$ and 3σ in the $\sin^2(2\theta_{12}) - \Delta m^2_{12}$ plane (on the left) and $\epsilon^2_2 - \Delta m^2_{12}$ plane (on the right) marginalizing over ϵ^2_2 and $\sin^2(2\theta_{12})$ respectively. In Fig. 4.8 we display the allowed regions at $1\sigma, 2\sigma$ and 3σ in the $\sin^2(2\theta_{12}) - \Delta m^2_{12}$ plane (on the left) and $\epsilon^2_1 - \Delta m^2_{12}$ plane (on the right) marginalizing over ϵ^2_1 and $\sin^2(2\theta_{12})$ respectively. In particular, the plots show there exists, in both cases, a de-

$P_{\nu_e \to \nu_e}(\epsilon_1^2)$			
	Δm^2_{12}	$\sin^2(2\theta_{12})$	ϵ_1^2
b.f.p.	$7.7 \cdot 10^{-5} eV^2$	0.85	$4.0 \cdot 10^{-6} eV^2$
1σ	$[7.5, 7.8]10^{-5} eV^2$	$[0.77, 0.93]$	$[0.0, 5.3]10^{-6} eV^2$
2σ	$[7.4, 8.0]10^{-5} eV^2$	$[0.68, 0.97]$	$[0.0, 7.3]10^{-6} eV^2$
b.f.p.	$4.1 \cdot 10^{-5} eV^2$	0.95	$7.4 \cdot 10^{-5} eV^2$
1σ	$[3.4, 4.3]10^{-5} eV^2$	$[0.76, 1.00]$	$[7.2, 8.2]10^{-5} eV^2$
2σ	$[3.2, 4.4]10^{-5} eV^2$	$[0.53, 1.00]$	$[7.0, 8.4]10^{-5} eV^2$
$P_{\nu_e \to \nu_e}(\epsilon_2^2)$			
	Δm^2_{12}	$\sin^2(2\theta_{12})$	ϵ_2^2
b.f.p.	$7.7 \cdot 10^{-5} eV^2$	0.87	$7.9 \cdot 10^{-6} eV^2$
1σ	$[7.6, 7.8]10^{-5} eV^2$	$[0.83, 0.93]$	$[0.0, 1.3]10^{-5} eV^2$
2σ	$[7.4, 8.0]10^{-5} eV^2$	$[0.80, 0.97]$	$[0.0, 1.7]10^{-5} eV^2$
2σ	$[4.2, 4.4]10^{-5} eV^2$	$[0.98, 1.00]$	$[7.0, 7.5]10^{-5} eV^2$

Table 4.1: The best fit point and the 1σ and 2σ ranges of Δm^2_{12}, $\sin^2 2\theta_{12}$ and ϵ for both possible choices of ϵ_i and for both solutions found. The first block of values is related to the true minimum. In the second one we show for completeness the values related to the degenerate minimum. For more details see the text.

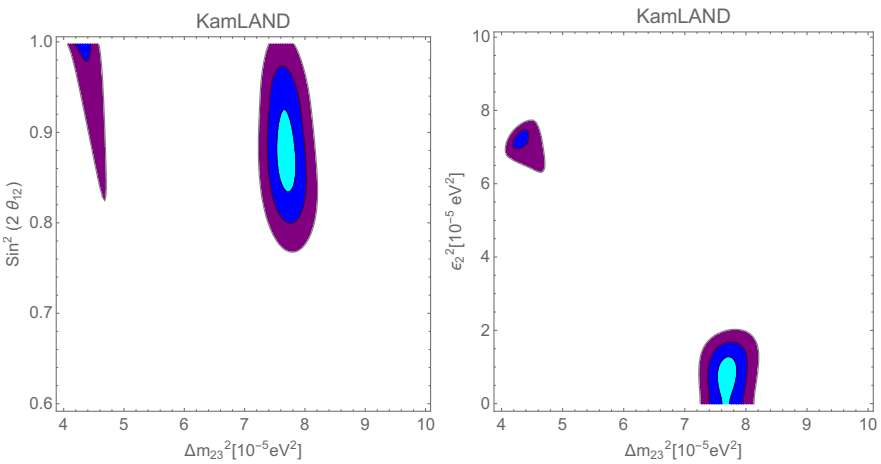

Figure 4.7: The χ^2 distribution where the theoretical number of events is due to $P_{\nu_e \to \nu_e}(\epsilon_2^2)$. Left panel: the $\sin^2(2\theta_{12})$ to Δm_{12}^2. Right panel: the ϵ_2^2 to Δm_{12}^2. The third parameter is marginalized over. The contours show the two-dimensional 68.27% (cyan), 95.45% (blue) and 99.73% (purple) confidence intervals.

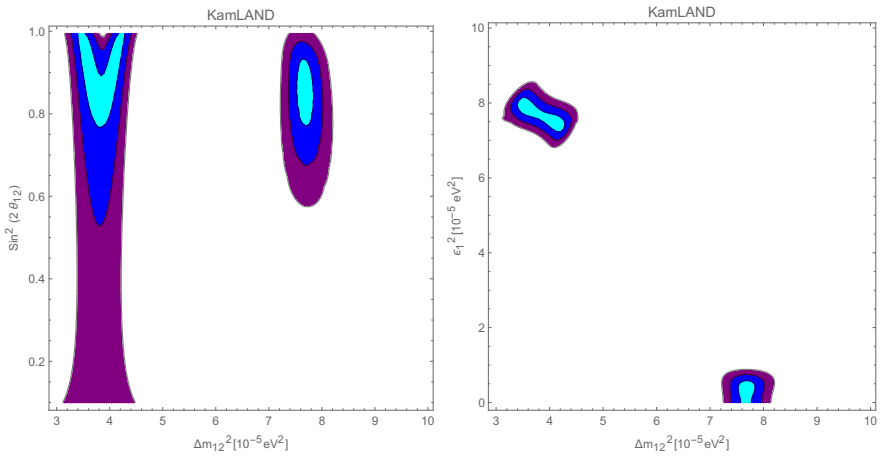

Figure 4.8: The χ^2 distribution where the theoretical number of events is due to $P_{\nu_\mu \to \nu_\mu}(\epsilon_3^2)$. Left panel: the $\sin^2(2\theta_{12})$ to Δm_{12}^2. Right panel: the ϵ_1^2 to Δm_{12}^2. The third parameter is marginalized over. The contours show the two-dimensional 68.27% (cyan), 95.45% (blue) and 99.73% (purple) confidence intervals.

generate minimum at 3σ with non-zero values of $\epsilon^2_{1,2}$. The table 4.1 shows the values of the parameters for both possible choices of ϵ_i and for the two different minima found. The limits of each parameter were calculated marginalizing over the other two. For both quasi-Dirac pairs, in the first block, the best fit point values of the standard parameters are in the 1σ region of the experimental data [65]. The second block show the values related to the degenerate minima. Their presence can be easily understood. As we can see from the table 4.1, they appear because the values of the ϵ_i are around the same value of the current best fit point of Δm^2_{12} [5]. When this happens, the value of Δm^2_{12} is smaller than ϵ_i and it is in contrast with the definition of the "Quasi-Dirac pairs". We will see that in the analysis done with combined experiments these degenerate minima disappear.

4.4.2.2 Correlation between MINOS and the theoretical prediction

We extracted the data from Fig. 1 in [114]. In general, the MINOS Collaboration did its analysis considering three events samples: contained-vertex muons, non-fiducial muons, and contained-vertex showers. The two muon samples are produced by ν_μ CC and $\bar{\nu}_\mu$ CC interactions. We took into account only the data coming from the contained-vertex muons sample produced by the ν_μ beam. It contains most of the events.
The figure reports number of events as a function of the neutrino energy. The energy range $(0-14)GeV$ was divided in 23 bins. In particular, for each bin, one finds the number of events experimentally measured, the number of events expected without oscillation (N_i), the number of events expected with oscillation.
With all this information we constructed the χ^2. We started considering the standard oscillation to check if that reproduces the same result as MINOS analysis, so

$$t_i \;=\; P_{i\nu_\mu\to\nu_\mu}\cdot N_i \tag{4.26}$$

Our results are:

$$\begin{aligned} \chi^2 &= 39.4, \\ \Delta m^2_{23} &= (2.36^{+0.07}_{-0.06}) \times 10^{-3} eV^2, \\ \sin^2(2\theta_{23}) &= (0.96 \pm 0.03), \end{aligned} \tag{4.27}$$

The ratio $\chi^2_{min}/n.d.f. \sim 1.9$ indicates that the standard oscillation theory agrees with the experimental data, moreover, one can see the values of Δm^2_{23} and $\sin^2(2\theta_{23})$ that minimize the χ^2 are in the 1σ region of the experimental data [114]. We calculated then the χ^2 for the MINOS experimental data and our theoretical quasi-Dirac prediction. Since MINOS is sensitive to Δm^2_{23}, consequently will be sensitive to ϵ^2_2 and ϵ^2_3. We did the analysis for both the quasi-Dirac pairs:

$$\begin{aligned} t_i(\epsilon_2) &= P_{i\nu_\mu \to \nu_\mu}(\epsilon_2) \cdot N_i, \\ t_i(\epsilon_3) &= P_{i\nu_\mu \to \nu_\mu}(\epsilon_3) \cdot N_i \end{aligned} \tag{4.28}$$

In particular, in order to improve the precision, we calculated the mean probability for each bin by choosing to subdivide it into $n = 20$ "sub-bins". After the χ^2 construction one calculates its minimum in order to find the best fit points and the parameters range. The result is:

$$\begin{aligned} \chi^2_{min}(\epsilon_2) &\sim 39.3, \\ \chi^2_{min}(\epsilon_3) &\sim 39.1. \end{aligned} \tag{4.29}$$

The values of the ratio $\chi^2(\epsilon_i)/n_{d.o.f.}$ are in both cases ~ 2.0. This indicates us that both standard and quasi-Dirac theories equally agree with the experimental data. There is no preference for either.

The table 4.2 shows the value of $\Delta m^2_{23}, \sin^2(\theta_{23})$ and ϵ for both the Quasi-Dirac cases. For each parameter the value is found marginalizing over the other two. Note that, of course we have not exactly reproduced the same results of MINOS experiment as we have worked with less data. However, our fit is only $1/2\sigma$ away, so we can conclude that our results agree with experimental measurements [114]. The results for the quasi-Dirac prediction are shown in Fig.4.9 where we display the allowed regions at $1\sigma, 2\sigma$ and 3σ in the $\epsilon^2_2 - \Delta m^2_{23}$ plane (on the left) and $\epsilon^2_2 - \sin^2(2\theta_{23})$ plane (on the right)

$P_{\nu_\mu \to \nu_\mu}(\epsilon_2^2)$			
	Δm^2_{23}	$\sin^2(2\theta_{23})$	ϵ_2^2
b.f.p.	$2.4 \cdot 10^{-3} eV^2$	0.96	$3.8 \cdot 10^{-4} eV^2$
1σ	$[2.3, 2.4] 10^{-3} eV^2$	$[0.87, 0.99]$	$[0.0, 1.0] 10^{-3} eV^2$
2σ	$[2.1, 2.7] 10^{-3} eV^2$	$[0.75, 1]$	$[0.0, 2.3] 10^{-3} eV^2$
$P_{\nu_\mu \to \nu_\mu}(\epsilon_3^2)$			
	Δm^2_{23}	$\sin^2(2\theta_{23})$	ϵ_3^2
b.f.p.	$2.3 \cdot 10^{-3} eV^2$	0.97	$8.7 \cdot 10^{-4} eV^2$
1σ	$[2.1, 2.3] 10^{-3} eV^2$	$[0.94, 0.99]$	$[0.0, 1.5] 10^{-3} eV^2$
2σ	$[1.9, 2.4] 10^{-3} eV^2$	$[0.91, 1.00]$	$[0.0, 1.8] 10^{-3} eV^2$

Table 4.2: The best fit point and the 1σ and 2σ ranges of Δm^2_{23}, $\sin^2 2\theta_{23}$ and ϵ_i.

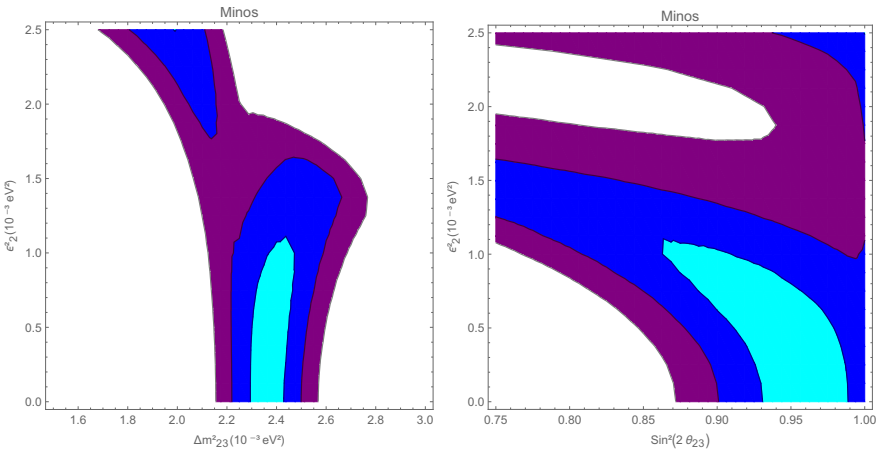

Figure 4.9: The χ^2 distribution where the theoretical number of events is due to $P_{\nu_\mu \to \nu_\mu}(\epsilon_2^2)$. Left panel: the ϵ_2^2 versus Δm^2_{23}. Right panel: the ϵ_2^2 versus $\sin^2(2\theta_{23})$. The third parameter is marginalized over. The contours show the two-dimensional 68.27% (cyan), 95.45% (blue), 99.73% (purple) confidence intervals.

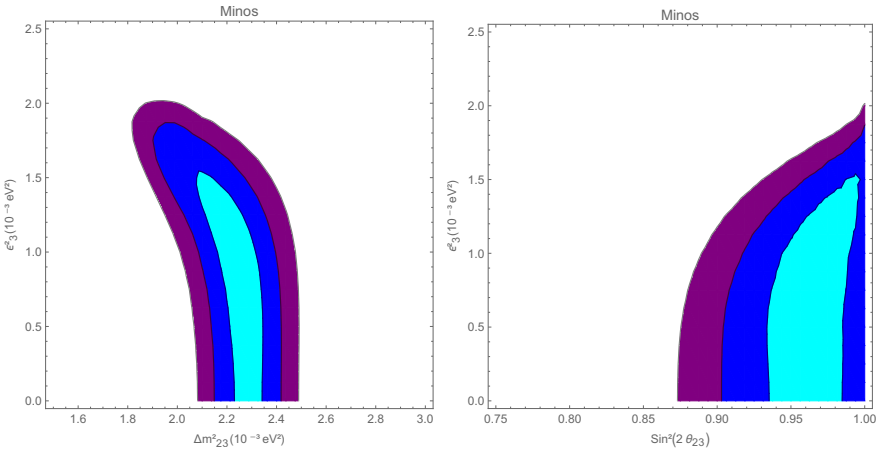

Figure 4.10: The χ^2 distribution where the theoretical number of events is due to $P_{\nu_\mu \to \nu_\mu}(\epsilon_3^2)$. Left panel: the ϵ_2^2 versus Δm^2_{23}. Right panel: the ϵ_2^2 versus $\sin^2(2\theta_{23})$. The third parameter is marginalized over. The contours show the two-dimensional 68.27% (cyan), 95.45% (blue), 99.73% (purple) confidence intervals.

marginalizing over $\sin^2(2\theta_{23})$ and Δm^2_{23} respectively. In Fig. 4.10 we display the allowed regions at $1\sigma, 2\sigma$ and 3σ in the $\epsilon_2^3 - \Delta m^2_{23}$ plane (on the left) and $\epsilon_3^2 - \sin^2(2\theta_{23})$ plane (on the right) marginalizing over $\sin^2(2\theta_{23})$ and Δm^2_{23} respectively.

4.4.2.3 Correlation between T2K and the theoretical prediction

T2K began operation in 2010 and was interrupted for one year by the Great East Japan Earthquake in 2011. The results reported in the previous section used data collected through 2013, as summerized in Table I of [115]. We extracted the data from the Figs.20 and 28 in [115].

In order to reproduce the curves of these figures we had to take into account the energy resolution (ΔE) of the far detector Super-K and we considered this expression as a function of the energy:

$$\Delta E \quad = \quad aE + b\sqrt{E} + c, \tag{4.30}$$

where E is the muon energy, then we constructed our theory

$$t_i = P_{i,\nu_\mu\to\nu_\mu}(E)\cdot N_i(E). \quad (4.31)$$

In principle P_i and N_i are calculated in different energy bins, for this reason we used an interpolating function to calculate the "N_i" in the same energy points of Fig.20 of [115]. The total number of bins is 29. In order to find the values of the parameters a, b and c we calculated the minimum of the χ^2 (see eq. 4.18): where $e_i = a_{iMC} - N_{b,ai}$ and $\sigma^2_{istat.} = a_{iMC}$. The result was:

$$\begin{aligned} a &= 0.01, \\ b &= 0.07, \\ c &= 0.02. \end{aligned} \quad (4.32)$$

Then we used a probability density function to calculate the weighted average of the survival probability:

$$w = \frac{1}{\sqrt{2\pi}\sigma} e^{-\frac{(x-E)^2}{2\sigma^2}}, \quad (4.33)$$

where $\sigma = \Delta E/E$. We sub-divided each bin in 21 "sub-bins" by varying the value of x from $E-2\sigma$ to $E+2\sigma$ for a number of step equal to $\sigma/5$. For each point we calculated the weight (w) and the weighted average probability:

$$\mathcal{P}_{\nu_\mu\to\nu_\mu} = \frac{\sum_{j=1}^{21} P_{\nu_\mu\to\nu_\mu}(x_j)\cdot w_j}{\sum_{j=1}^{21} w_j}, \quad (4.34)$$

and finally

$$th_i = N_i \cdot \mathcal{P}_{\nu_\mu\to\nu_\mu}. \quad (4.35)$$

With all this information we constructed the χ^2 and started our analysis where

$$\begin{aligned} e_i &= d_i - N_{b,di} \\ \sigma^2 &= (1.7)d_i + N_{d,ai}. \end{aligned} \quad (4.36)$$

To the systematic error $N_{d,ai}$ we added a small error due to the uncertainties in our theoretical calculation. The number 1.7 was inferred by us such that our simulation reproduces the allowed parameter ranges for the standard oscillation parameters, determined by T2K.
We started considering the standard oscillation to check if that reproduces the same results as T2K analysis. Our results are:

$$\begin{aligned} \chi^2 &= 24.7, \\ \Delta m^2_{23} &= 2.50^{+0.05}_{-0.10} \times 10^{-3} eV^2, \\ \sin^2(2\theta_{23}) &= 1.000_{-0.001} \end{aligned} \tag{4.37}$$

The ratio $\chi^2_{min}/n.d.f. \sim 0.9$ indicates that the standard oscillation theory agrees with the experimental data, moreover, one can see the values of Δm^2_{23} and $\sin^2(2\theta_{23})$ that minimize the χ^2 are in the 1σ region of the experimental data [132]. Then we analyzed the quasi-Dirac case. Since T2K is sensitive to Δm^2_{23}, it will be sensitive to both ϵ_2^2 and ϵ_3^2. It means that two quasi-Dirac pairs can be constrained. We calculated the χ^2 for the T2K experimental data and the theoretical quasi-Dirac prediction in both cases:

$$\begin{aligned} \chi^2_{min}(\epsilon_2) &= 21.4 \quad , \\ \chi^2_{min}(\epsilon_3) &= 22.8 \quad . \end{aligned} \tag{4.38}$$

Since $\chi^2(\epsilon_i)/n_{d.o.f.}$ are ~ 0.8 and ~ 0.9 respectively we can conclude that the quasi-Dirac theory equally agree with the experimental data as the standard theory. There is no preference for either.

The table 4.3 shows the value of $\Delta m^2_{23}, \sin^2(\theta_{23})$ and ϵ_i for both the quasi-Dirac cases. For each parameter the value is found marginalizing over the other two. The values found for the standard parameters are inside the 1σ region of the experimental data [132]. The results of the quasi-Dirac prediction are shown in Fig. 4.11 where we display the allowed regions at $1\sigma, 2\sigma$ and 3σ in the $\sin^2(2\theta_{23}) - \Delta m^2_{23}$ plane (on the left) and $\epsilon_2^2 - \Delta m^2_{23}$ plane (on the right) marginalizing over ϵ_2^2 and $\sin^2(2\theta_{23})$ respectively. In Fig. 4.12 we display the allowed regions at $1\sigma, 2\sigma$ and 3σ in the $\sin^2(2\theta_{23}) - \Delta m^2_{23}$ plane (on the left) and $\epsilon_3^2 - \Delta m^2_{23}$ plane (on the right) marginalizing over ϵ_3^2 and $\sin^2(2\theta_{23})$ respectively.

$P_{\nu_\mu \to \nu_\mu}(\epsilon_2^2)$			
	Δm^2_{23}	$\sin^2(2\theta_{23})$	ϵ_2^2
b.f.p.	$2.6 \cdot 10^{-3} eV^2$	0.99	$1.1 \cdot 10^{-3} eV^2$
1σ	$[2.4, 2.7]10^{-3} eV^2$	$[0.94, 1.00]$	$[0.7, 1.4]10^{-3} eV^2$
2σ	$[2.3, 2.9]10^{-3} eV^2$	$[0.87, 1.00]$	$[0.0, 1.8]10^{-3} eV^2$
$P_{\nu_\mu \to \nu_\mu}(\epsilon_3^2)$			
	Δm^2_{23}	$\sin^2(2\theta_{23})$	ϵ_3^2
b.f.p.	$2.5 \cdot 10^{-3} eV^2$	1.0	$1.0 \cdot 10^{-3} eV^2$
1σ	$[2.4, 2.7]10^{-3} eV^2$	$[0.996, 1.000]$	$[0.5, 1.6]10^{-3} eV^2$
2σ	$[2.3, 2.9]10^{-3} eV^2$	$[0.999, 1.000]$	$[0.0, 2.0]10^{-3} eV^2$

Table 4.3: The best fit point and the 1σ and 2σ ranges of Δm^2_{23}, $\sin^2 2\theta_{23}$ and ϵ_i.

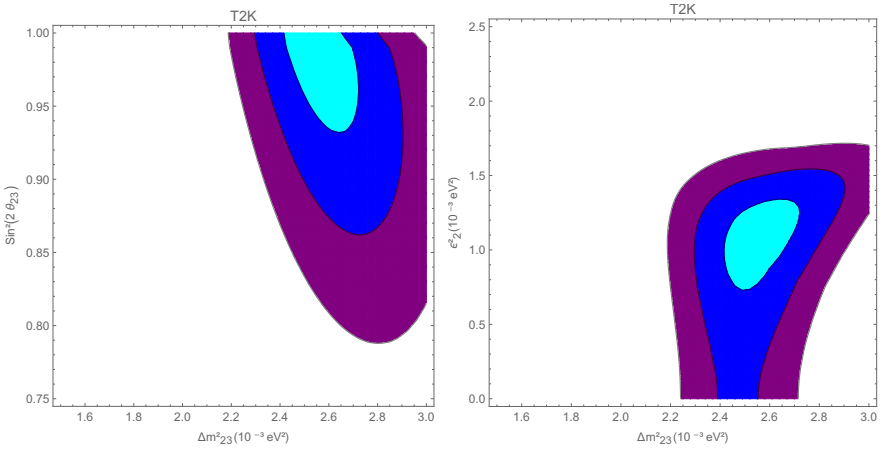

Figure 4.11: The χ^2 distribution where the theoretical number of events is due to $P_{\nu_\mu \to \nu_\mu}(\epsilon_2^2)$. Left panel: the $\sin^2(2\theta_{23})$ to Δm^2_{23}. Right panel: the ϵ_2^2 to Δm^2_{23}. The third parameter is marginalized over. The contours show the two-dimensional 68.27% (cyan), 95.45% (blue) and 99.73% (purple) confidence intervals.

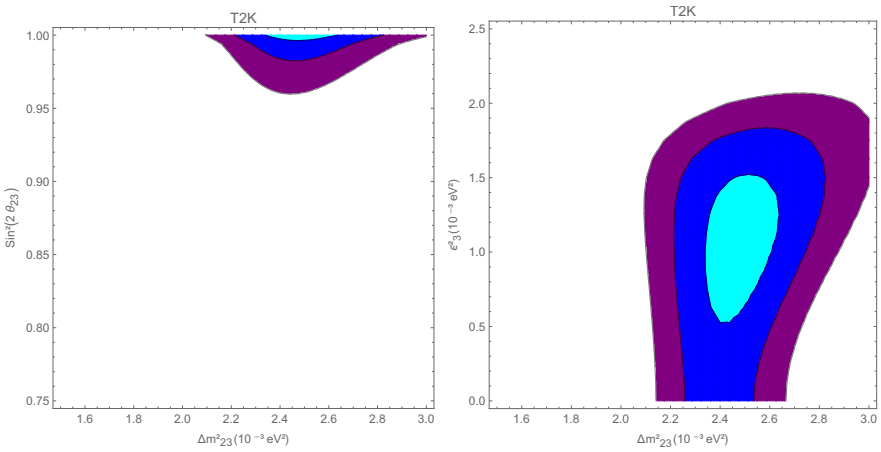

Figure 4.12: The χ^2 distribution where the theoretical number of events is due to $P_{\nu_\mu \to \nu_\mu}(\epsilon_3^2)$. Left panel: the $\sin^2(2\theta_{23})$ to Δm^2_{23}. Right panel: the ϵ_2^2 to Δm^2_{23}. The third parameter is marginalized over. The contours show the two-dimensional 68.27% (cyan), 95.45% (blue) and 99.73% (purple) confidence intervals.

4.5 Current experimental limits and future prospects

In this section we present the constraints on the quasi-Dirac neutrino parameters imposed by current neutrino oscillation data. In particular, differently from the previous section, the results obtained here come from the combination of various experiments. We also briefly discuss our expectation from the future JUNO experiment.

As discussed, the full parameter space for a system of 3 pairs of QD neutrinos has 30 free parameters: Two independent Δm^2_{ij} plus one overall mass scale, three ε_i^2, twelve angles and twelve phases. Even discounting the five Majorana phases and the overall mass scale, which can not be probed in oscillation experiments, the remaining number of parameters is much too large to fit simultaneously.

Nearly all experimental data, on the other hand, is consistent with the standard picture of only three active neutrino species participating in os-

cillations [5], i.e. two mass squared differences ($\Delta m^2_{\rm Atm}$ and $\Delta m^2_{\odot}$), three mixing angles (θ_{23}, θ_{12} and θ_{13}) plus one phase (δ) are sufficient to describe the data. As mentioned in the introduction to this Chapter, there are also some hints for sterile neutrinos with a mass scale of the order of $\Delta m^2 \sim \mathcal{O}(\text{eV})$ [107, 108]. However, all these hints are at most of the order of $(2-3)\ \sigma$, we will thus not take them into account in the following. Instead, since the standard three generation picture seems to describe the data well, we will consider "small" perturbations and derive limits on particular combinations of non-standard parameters.

In order to deal effectively with the large number of parameters controlling quasi-Dirac neutrino oscillations, we will consider two simplified scenarios:

1. First, we take one non-zero ε_i at a time. In these one-parameter extensions, very stringent limits on ε_i are found, in agreement with earlier analysis, see for example [86, 87]. We then extend this analysis to two new parameters: One mass splitting plus one new angle. This second step allows us to identify "blind spots" in the oscillation experiments, i.e. degenerate minima in particular directions in parameter space, where limits on mass splittings are much worse than in the one parameter fits. We then discuss a particular parametrization of these degenerate directions in parameter space, where the effects of ε_i can be decoupled from oscillation experiments nearly completely.

2. In the second setup, we discuss the limit where mass splittings are too small to be measured in oscillation experiments, hence there are just angles and phases of Ω to deal with. In this situation, it can be shown that from the 24 parameters in Ω only 13 combinations enter the oscillation probabilities of active neutrinos. Moreover, since there is only very limited information on oscillations involving ν_τ, we can in practice restrict ourselves to experiments involving ν_e's and ν_μ's. There are then only 7 combinations of the 24 angles θ_{ij} and phases ϕ_{ij} which appear in the oscillation probabilities. We discuss the construction of these 7 quantities, the current constraints and possible tests for quasi-Dirac neutrinos in this limit.

In our fits, to determine the allowed ranges of model parameters, we use the χ^2 method that we discussed in section 4.3. We take statistical and

systematic errors from the experimental publications, to which we added a further (small) systematic error for the uncertainties in our theoretical calculations. This latter systematic error was chosen such that our simulations reproduce the allowed parameter ranges for the standard oscillation parameters, determined by the respective experiment, within typically (1-1.5) σ c.l. ranges. Note that we do not attempt to do a precision global fit for standard neutrino oscillation parameters. Rather, we consider reproducing the experimental results for the standard case as a test for the reliability of our derived limits.

4.5.1 Limits on mass splittings ε_i

4.5.1.1 One parameter limits

We will first discuss limits derived on ε_i assuming one $\varepsilon_i \neq 0$ at a time and taking all non-standard angles to be zero. Table (4.4) shows limits on ε_i^2 and the corresponding experimental data sets used to derive the limits.

Experiment	ε_1^2 [eV^2]	ε_2^2 [eV^2]	ε_3^2 [eV^2]
KamLAND	$7.7(3.4) \times 10^{-6}$	$1.7(1.0) \times 10^{-5}$	–
Solar + KamLAND	$1.7(1.3) \times 10^{-11}$	$1.7(1.5) \times 10^{-11}$	–
DayaBay + MINOS + T2K	–	$1.5(0.9) \times 10^{-4}$	$1.3(0.074) \times 10^{-3}$
Super-K + DayaBay + MINOS + T2K	–	$1.9(1.8) \times 10^{-5}$	$1.2(1.1) \times 10^{-5}$
JUNO	$1.7(0.07) \times 10^{-5}$	$2.3(0.09) \times 10^{-5}$	$6.0(2.2) \times 10^{-5}$

Table 4.4: 95 % upper limits on ε_i^2 derived from different experimental data sets. Two numbers are given for each case; the first one is the limit obtained marginalizing over two standard oscillation parameters (see text), the second (in brackets) is the limit obtained for the best fit point value of the standard oscillation parameters. For a discussion see text.

For each case listed in table (4.4), we have calculated the upper limits on the ε_i^2 twice: (a) marginalizing over two of the standard neutrino oscillation parameters and (b) for the best fit point value of the standard parameters. Marginalization over standard oscillation parameters leads to less stringent limits. However, the importance of this marginalization procedure differs widely for different experiments. For example, in the case of KamLAND, bounds on ε_1^2 of the order of roughly 10^{-5} are derived marginalizing over the

allowed ranges of $\Delta m^2_\odot$ and $\sin^2\theta_{12}$, while for the best fit values of these last two parameters, the limits are more stringent by "only" roughly a factor 2.

As the table shows, the strongest constraints on ε_1^2 and ε_2^2 come from solar neutrino data. This is easily understood from fig. (4.13), which shows the electron neutrino survival probability as a function of neutrino energy for different values of ε_2^2 and for the best fit values of the standard solar oscillation parameters. For low values of neutrino energies, vacuum oscillations dominate and so very small ε_2^2 can be probed up to a scale essentially determined by the Earth-Sun distance ($\sim 10^{-12,-11}$ eV^2). Note that a non-zero ε_2^2 reduces P_{ee}, but this reduction could be hidden in the relatively large error bar of the low-energy measurements.[6] Nevertheless, at higher neutrino energies, a similar reduction of P_{ee} is produced due to matter effects in the sun. Since Super-K data provides a very accurate measurement of P_{ee} at these higher energies, one can rule out values of ε_2^2 which can not be excluded by the Borexino measurements alone. The situation is very similar for ε_1^2: limits on ε_1^2 and ε_2^2 are then of the order of 10^{-11} eV^2 if we take the best fit values of the standard solar oscillation parameters; slightly less stringent numbers are obtained when marginalizing over the standard parameter uncertainties.

Solar neutrino experiments have essentially no sensitivity to ε_3^2. This is simply due to the smallness of θ_{13} ($\sin^2\theta_{13} \simeq 0.0215$ [5]). Thus, we have to rely on experiments testing the atmospheric scale to derive limits on ε_3^2. Table (4.4) quotes numbers for two cases.

In the first scenario, we have combined data from DayaBay [116], T2K [115] and MINOS [114]: DayaBay fixes most accurately θ_{13}, while both MINOS and T2K measure $\Delta m^2_{\rm Atm}$ with rather small errors. Here, the limit on ε_2^2 is (not surprisingly) less stringent than the one derived from KamLAND (or solar). Depending on whether or not $\Delta m^2_{\rm Atm}$ and $\sin^2\theta_{23}$ are used at their best fit value or marginalized over, we get very different limits on ε_3^2. This is due to the fact that when scanning over the standard oscillation parameters, the χ^2 function has two almost degenerate minima: one for small values of ε_3^2 and another for ε_3^2 of the order 10^{-3} eV^2. However, as the table also shows (second case), this non-standard solution is excluded,

[6] Due to the annual variation of the Earth-Sun distance, for values of ε_2^2 larger than $\sim 10^{-10,-9}$ eV^2, the oscillations are averaged over, so only an overall reduction of survival probability is seen.

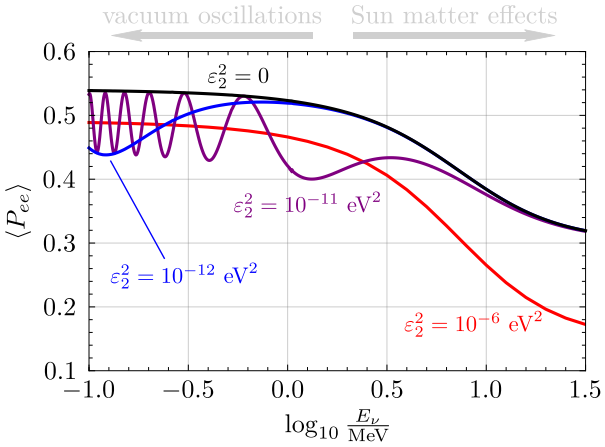

Figure 4.13: Solar neutrino survival probability as a function of neutrino energy, for different choices of ε_2^2. Solar angle and mass splitting have been fixed at their best fit values in this plot [5].

once we add Super-K atmospheric neutrino sub-GeV data to the fit. With the combination of these four experiments limits on ε_2^2 and ε_3^2 are again of order 10^{-5} eV^2.

In the last line of table (4.4) we give our forecast of the sensitivity of the planned experiment JUNO [134]. JUNO will measure $\Delta m^2_\odot$ and Δm^2_{Atm} very precisely and thus it will also be able to derive limits on any ε_i^2. However, our results indicate that, despite being a very precise experiment, JUNO will not lead to a major improvement over existing limits on ε_i^2. Here, it is important to stress that limits using the best fit point and limits marginalizing over standard parameter uncertainties are very different. This can be traced back again to a near-degeneracy in the χ^2-function: For ϵ_i^2 of the order of Δm^2_{ij} one has two only slightly different oscillation lengths contributing in the fit, which can give a better description than a single oscillation length.

In summary, strong limits on mass splittings can be derived from atmospheric and solar neutrino data ($\varepsilon_3^2 \sim \mathcal{O}(10^{-5})$ eV^2 and $\varepsilon_{1,2}^2 \sim \mathcal{O}(10^{-11})$ eV^2, respectively) in the case where no other extra parameter is added to the standard neutrino oscillation picture.

4.5.1.2 Two parameter case

While the discussion in the previous subsection seems to show that constraints on QD mass splittings are very stringent, we will now see that this conclusion is valid only under the assumption that no other non-standard parameter is different from zero.

As a simple example, consider the electron neutrino survival probability at distances short enough that the effects of $\Delta m^2_{\odot}$ can be neglected.[7] We shall consider the particular example of a non-zero ε_3^2 and a non-zero θ_{16} angle, defined in section 4.2. One finds that

$$P_{ee} = 1 - 2c_{13}^2 c_{16}^2 \Big(\Delta m^-_{ee} (s_{16} + c_{16} s_{13})^2 + \Delta m^+_{ee} (s_{16} - c_{16} s_{13})^2 \Big) \,, \qquad (4.39)$$

where c_{ij} and s_{ij} are short-hands for $\cos\theta_{ij}$ and $\sin\theta_{ij}$ and

$$\Delta m^{\pm}_{ee} \equiv c_{12}^2 \sin^2 \left[\frac{L}{4E} \left(\Delta m^2_{31} \pm \varepsilon_3^2/2 \right) \right] + s_{12}^2 \sin^2 \left[\frac{L}{4E} \left(\Delta m^2_{32} \pm \varepsilon_3^2/2 \right) \right] . \qquad (4.40)$$

It is straightforward to see that the above expression for the neutrino survival probability remains (nearly) unchanged if we swap θ_{13} by θ_{16}. This is true up to very small terms proportional to $\Delta(P_{ee}) \propto (\Delta m^-_{ee} - \Delta m^+_{ee})(c_{13} - c_{16}) s_{13} s_{16}$. More specifically, in the limit where $\Delta m^{\pm}_{ee}$ have the same value, P_{ee} is only a function of the combination $\sin^2\theta_{13} + \sin^2\theta_{16}$. Thus, there will be a near-degeneracy of the relevant χ^2 function involving these two angles, and so values (or limits) derived for one of these parameters, without varying the other, will be misleading.

There is, however, another more interesting degeneracy associated to eq. (4.39). As in the previous section, in calculating this expression we have used the symmetric parametrization. Choosing $\sin\theta_{13} = \tan\theta_{16}$, the second term inside the bracket in eq. (4.39) vanishes (this choice corresponds to $\Omega_{e6} = 0$). So, by adjusting Δm^2_{31} and ε_3^2 we can keep $\Delta m^2_{31} - \varepsilon_3^2/2$ constant and equal to the best fit point value of $\Delta m^2_{\rm Atm}$, in which case there will be no upper limit on ε_3^2 itself coming from the electron neutrino survival experiments.

[7] To a good approximation, this is the situation in the DayaBay experiment.

Note that we could have defined $m_i, m_{i+3} \to m_i, \sqrt{m_i^2 + \varepsilon_i^2}$.[8] We call this the *asymmetric parametrization*. Rewriting eq. (4.39) with this parametrization, the first term inside the bracket would not depend on ε_3^2 at all, so it becomes obvious that for the choice of $\sin\theta_{13} = \tan\theta_{16}$ all dependence of P_{ee} on ε_3^2 disappears. Fig. (4.14) shows these parameter degeneracies in the space $(\varepsilon_3^2, \sin^2\theta_{13}, \sin^2\theta_{16})$, using only the DayaBay data (on the left column). The underlying scan was done in the asymmetric parametrization, which is numerically simpler to implement. The plot in the upper and middle panel show clearly that there is no upper limit on ε_3^2 in this scan. The lower plot shows the degeneracy in parameter space under the exchange of $\theta_{13} \leftrightarrow \theta_{16}$.

We can break this particular degeneracy in parameter space, by adding more experiments. T2K measures two probabilities: (a) The muon neutrino survival probability, $P_{\mu\mu}$, and (b) the electron neutrino appearance probability, $P_{\mu e}$, both at values of L/E which give access to the atmospheric neutrino mass scale, Δm^2_{Atm}. If the only non-standard angle different from zero is θ_{16}, then $P_{\mu\mu}$ will not depend on θ_{16} at all, while $P_{\mu e}$ will have θ_{16}-dependence which is different from the one of P_{ee}. Thus, adding T2K data to the scan is enough to break the degeneracy in $\theta_{13} \leftrightarrow \theta_{16}$ hence an upper limit on ε_3^2 reappears. The middle column of fig. (4.14) illustrates this point; it shows the results of a combined scan over ε_3^2, $\sin^2\theta_{13}$ and $\sin^2\theta_{16}$ for DayaBay plus T2K data. By comparison of the right with the middle column of fig. (4.14), one can clearly see that the addition of Super-K data generates a strong upper limit on ε_3^2, for this particular choice of parameter subspace.

Given these results, one might wonder if there are particular directions in parameter space for which oscillation experiments become completely blind to QD neutrino mass splittings. Recall that the blind (or: degenerate) direction discussed above for P_{ee} corresponds to the particular choice of $\Omega_{e6} = 0$. In a similar way, for example, $P_{\mu\mu}$ would loose any sensitivity to ε_3^2 if $\Omega_{\mu 6} = 0$. Thus, with some special choice of θ_{16} and θ_{26} such that both Ω_{e6} and $\Omega_{\mu 6}$ are zero at the same time, one can indeed make DayaBay and T2K blind to variations of ε_3^2.

[8] Numerically this leads to the same limits on ε_i^2, as long as the mass splitting is much smaller than the relevant Δm^2_{ij} (i.e., the solar or atmospheric scale).

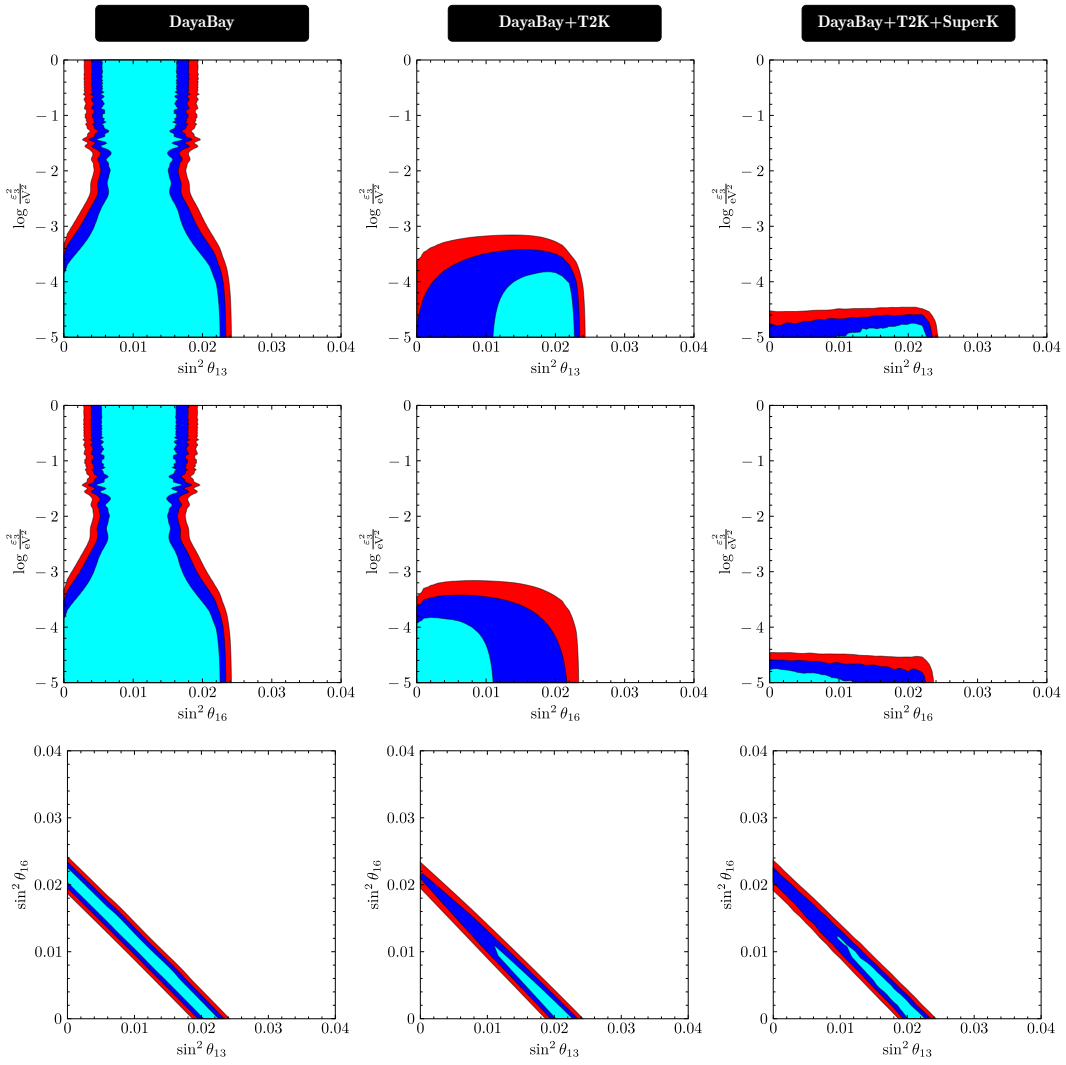

Figure 4.14: Allowed parameter ranges for ε_3^2, $\sin^2\theta_{13}$ and $\sin^2\theta_{16}$ for different experiments. The parameter planes always marginalize over the parameter not shown and all calculations used the best fit point value for $\Delta m^2_{\mathrm{Atm}}$. In the plots on the left only DayaBay data is taken into account; the middle panel combines DayaBay with T2K and the panel to the right shows the combination of DayaBay, T2K with Super-K atmospheric neutrino data. The different coloured regions present the 1, 2 and 3 σ c.l. allowed regions (cyan, blue and red). For discussion see text.

While it is possible, in principle, to calculate the combination of angles θ_{ij} and phases ϕ_{ij} (defined in section (4.2)) associated to these blind directions, in the following we will consider a simpler alternative. Consider a unitary rotation of the columns i and $i+3$ of the mixing matrix Ω. Since we are not interested in column phases, such a rotation is governed by just two parameters (φ_i and β_i):

$$\begin{pmatrix} \vdots & \vdots \\ \text{col. } i \text{ of } \Omega & \text{col. } i+3 \text{ of } \Omega \\ \vdots & \vdots \end{pmatrix} \rightarrow \begin{pmatrix} \vdots & \vdots \\ \text{col. } i \text{ of } \Omega & \text{col. } i+3 \text{ of } \Omega \\ \vdots & \vdots \end{pmatrix} \begin{pmatrix} \cos\varphi_i & e^{i\beta_i}\sin\varphi_i \\ -e^{-i\beta_i}\sin\varphi_i & \cos\varphi_i \end{pmatrix} \tag{4.41}$$

Now, recall that in the Dirac limit (see eq. (4.11)) the columns i and $i+3$ of the mixing matrix Ω are proportional to each other, $\Omega_{\alpha,i} = -i\Omega_{\alpha,i+3} = V_{\alpha,i}/\sqrt{2}$. This means that applying the (φ_i, β_i) transformation to the Dirac neutrino mixing matrix and, without loss of generality setting $\beta_i = 0$, we obtain:

$$\begin{pmatrix} \vdots & \vdots \\ \Omega_{\alpha,i} & \Omega_{\alpha,i+3} \\ \vdots & \vdots \end{pmatrix} = \begin{pmatrix} \vdots & \vdots \\ \frac{\cos\varphi_i+\sin\varphi_i}{\sqrt{2}} V_{\alpha,i} & i\frac{\cos\varphi_i-\sin\varphi_i}{\sqrt{2}} V_{\alpha,i} \\ \vdots & \vdots \end{pmatrix}. \tag{4.42}$$

From the last of these equations it can be seen that the i'th column (the $(i+3)$'th column) of Ω vanishes, if one chooses $\varphi_i = 3\pi/4$ ($\varphi_i = \pi/4$).

Fig. (4.15) shows a scan over the allowed parameter space in the plane $(\varepsilon_3^2, \varphi_3)$ using DayaBay, T2K, MINOS and Super-K atmospheric neutrino data. In agreement with the above discussion, there is a blind spot where no limit on ε_3^2 exist. This blind direction corresponds to the choice of $\varphi_3 =$

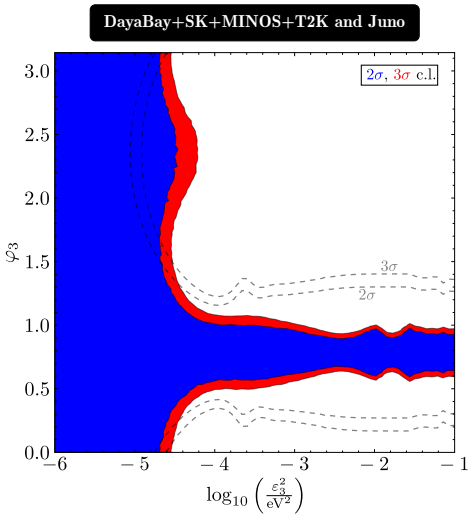

Figure 4.15: Allowed parameter space in the plane $(\varepsilon_3^2, \varphi_3)$ using DayaBay, T2K, MINOS and Super-K atmosheric neutrino data. The coloured plane shows the 2 and 3 σ c.l. allowed regions (blue and red). The dashed lines show the expected limits for JUNO. The asymmetric parametrization of the mass splitting $(m_3, \sqrt{m_3^2 + \varepsilon_3^2})$ was used, so for $\varphi_3 = \pi/4$ there is no sensitivity to ε_3^2.

$\pi/4$.[9] Fig. (4.15) also shows that the addition of JUNO data can lead only to a marginally improved limit.

We now turn to a discussion of ε_1^2 and ε_2^2. For these two parameters, again solar neutrino physics provides the most important constraints. As above for ε_3^2, we can define a rotation angle φ_1 (φ_2) between the columns 1 and 4 (2 and 5) of the mixing angle which will mitigate the effects of a non-zero ε_1^2 (ε_2^2). Fig. (4.16) shows the P_{ee} probability for solar neutrinos as a function of neutrino energy for two different values of ε_2^2 and various values of φ_2.[10] The results for ε_1^2 and φ_1 are completely analogous. As the figure shows, for $\varphi_2 = \pi/4$ again the effects of ε_2^2 completely decouple from the oscillation probability.

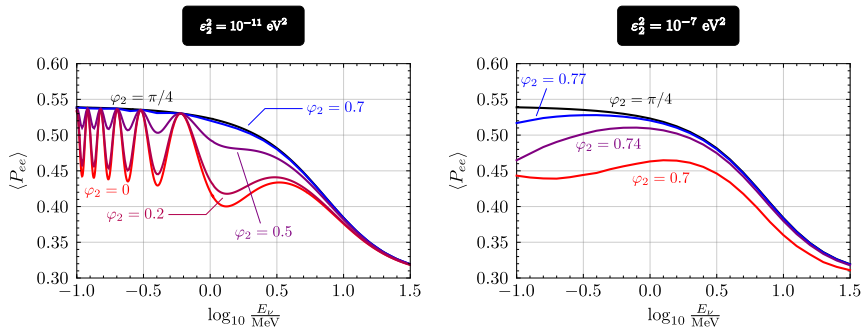

Figure 4.16: Average solar neutrino survival probability as a function of neutrino energy, for different choices of φ_2 and two different values of ε_2^2 and φ_2.

Fig. (4.17) shows the allowed parameter space in the two planes $(\varphi_1, \varepsilon_1^2)$ and $(\varphi_2, \varepsilon_2^2)$ using solar data and combining solar data with KamLAND. These plots have been calculated using the best fit point values for $\Delta m^2_\odot$ and $\sin^2\theta_{12}$ from the global fit [5]. The plots show in all cases that there

[9] Shifting ε_3^2 one could alternatively define $(\sqrt{m_3^2 + \varepsilon_3^2}, m_3)$. In that case, the blind spot occurs at $\varphi_3 = 3\pi/4$ instead.

[10] This probability is averaged over the variations of the Earth-Sun distance, and neutrino production point inside the Sun.

exists a slight preference, between (2-2.5) σ in all cases, for non-zero values of ε_i^2. Note that the preferred solution of the solar data in the region of $\varphi_1 \sim 3/4\pi$ and $\varepsilon_1^2 \sim (10^{-4.5} - 10^{-4})$ is ruled out by KamLAND. However, even combining solar and KamLAND data some preference for non-zero ε_i^2 of the order of very roughly $10^{-10.5}$ eV^2 remains.

We have traced back this preference for non-zero mass splittings in solar data to the well-known difference in the best fit points from $\Delta m^2_\odot$ in solar and KamLAND data. As can be seen also in the latest global fits [5], solar data prefers a $\Delta m^2_\odot$ around $(4-5) \times 10^{-5}$ eV^2, while KamLAND prefers $\Delta m^2_\odot \simeq 7.6 \times 10^{-5}$ eV^2. This tension between the two data sets is roughly of the order of 2 σ, with the error bar dominated by the larger error on $\Delta m^2_\odot$ in the solar data set. We have therefore recalculated the constraints on $(\varphi_1, \varepsilon_1^2)$ from solar data for a value of $\Delta m^2_\odot = 4 \times 10^{-5}$ eV^2. Fig. (4.18) shows the results of such a scan. As can be seen, in this calculation there is no longer any preference for a non-zero value of ε_1^2.

Note that such a low value of $\Delta m^2_\odot$ is ruled out by many σ from the KamLAND data. Thus, a small non-zero mass splitting could provide, in principle, a solution for the observed tension between solar and KamLAND data.

In summary, by introducing one mass splitting at a time, we extracted bounds for the pairs of parameters $(\varepsilon_i, \varphi_i)$, $i = 1, 2, 3$. In the limit where φ_i is $(2 \pm 1)/4\pi$, one column of the mixing matrix vanishes and therefore the mass splitting ε_i becomes unobservable. For this reason, one expects that for reasonably large values of ε_i there must be tight limits on $|\varphi_i - (2 \pm 1)/4\pi|$, meaning that φ_i has to be quite far from the Dirac limit ($\varphi_i = 0$). On the other hand, for a small enough value of the mass splitting ε_i, the associated oscillation length eventually become larger than the baseline of the relevant experiments, and in that case φ_i becomes unconstrained.

4.5.2 Quasi-Dirac neutrinos in the limit $\varepsilon_i \to 0$

If masses are degenerate as in eq. (4.10), then the oscillation probability formula will not change under unitary rotations of the columns i and $i+3$

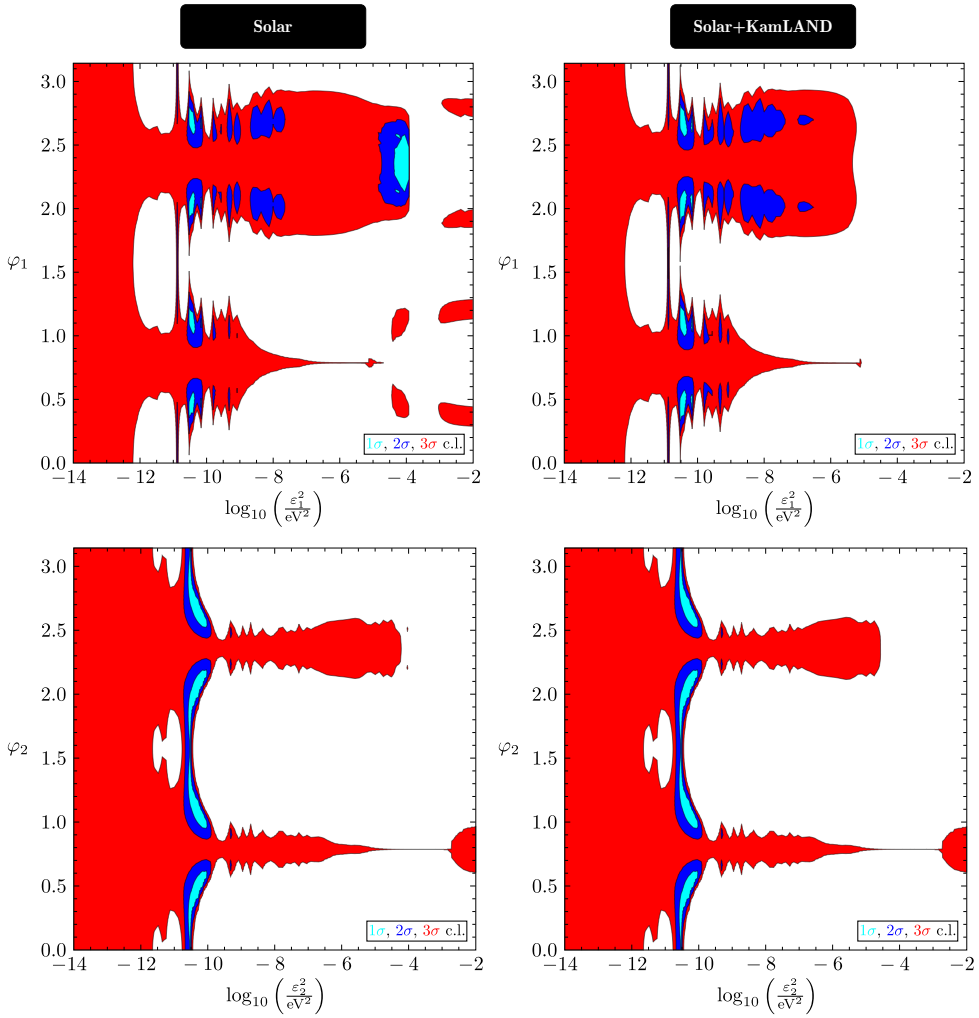

Figure 4.17: Allowed parameter range in the space $\varphi_1, \varepsilon_1^2$ (top) and $\varphi_2, \varepsilon_2^2$ (bottom). To the left: Solar data, to the right solar data + KamLAND. This plot uses the best fit point values for $\Delta m^2_\odot$ and $\sin^2\theta_{12}$ from the global fit. This combination of data shows a slight preference for a non-zero value of the mass splitting, for a discussion see text.

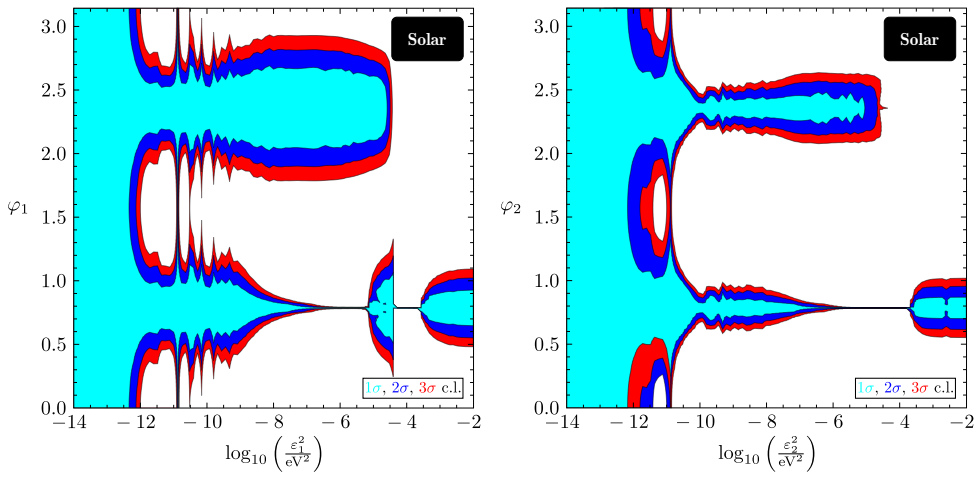

Figure 4.18: Allowed parameter range in the space $\varphi_1, \varepsilon_1^2$ (left) and $\varphi_2, \varepsilon_2^2$ (right) from solar data, using $\Delta m^2_{\odot} = 4 \times 10^{-5}$ eV^2.

of the mixing matrix, see eq. (4.41). In other words,

$$\begin{pmatrix} \vdots & \vdots \\ \text{col. } i \text{ of } \Omega & \text{col. } i+3 \text{ of } \Omega \\ \vdots & \vdots \end{pmatrix} \rightarrow \begin{pmatrix} \vdots & \vdots \\ \text{col. } i \text{ of } \Omega & \text{col. } i+3 \text{ of } \Omega \\ \vdots & \vdots \end{pmatrix} U(i) \tag{4.43}$$

for unitary matrices $U(i)$ $(i = 1, 2, 3)$ leaves $P(\nu_\alpha \rightarrow \nu_\beta)$ unchanged. Hence, there is a $U(2)^3$ redundancy in our description of Ω, and in turn this means that out of the 24 parameters describing the mixing matrix, oscillation experiments are only sensitive to 13.[11] This number is further reduced to

[11]The counting goes as follows: each $U(2)$ describes 4 redundancies in the parameters, hence there is a total of 12 redundancies in $U(2)^3$. However, one of them corresponds to the irrelevance of multiplying Ω by an overall phase; that was already taken care of when

7 if we ignore tau neutrinos. In this latter case the oscillation probabilities can be written as:

$$P\left(\nu_e \to \nu_e\right) = 1 + \left(1 - X_1 - X_2\right) X_2 \mathcal{A}_{12} + \left(1 - X_1 - X_2\right) X_1 \mathcal{A}_{13} + X_1 X_2 \mathcal{A}_{23} \tag{4.44}$$

$$P\left(\nu_\mu \to \nu_\mu\right) = 1 + \left(1 - X_3 - X_4\right) X_4 \mathcal{A}_{12} + \left(1 - X_3 - X_4\right) X_3 \mathcal{A}_{13} + X_3 X_4 \mathcal{A}_{23}\,, \tag{4.45}$$

$$\begin{aligned} P\left(\nu_e \to \nu_\mu\right) = &- \left(X_6 + \mathrm{Re}X_7\right) \mathcal{A}_{12} - \left(X_5 + \mathrm{Re}X_7\right) \mathcal{A}_{13} + \mathrm{Re}X_7 \mathcal{A}_{23}| \\ &+ \mathrm{Im}X_7 \left(\mathcal{B}_{12} - \mathcal{B}_{13} + \mathcal{B}_{23}\right)\,, \end{aligned} \tag{4.46}$$

with the oscillating factors $\mathcal{A}_{ij} \equiv -4\sin^2\left[\left(m_i^2 - m_j^2\right) L/\left(4E\right)\right]$ and $\mathcal{B}_{ij} \equiv 2\sin\left[\left(m_i^2 - m_j^2\right) L/\left(2E\right)\right]$ and the 7 parameters X_i defined as follows:

$$X_1 \equiv \left|\Omega_{e3}\right|^2 + \left|\Omega_{e6}\right|^2\,,\; X_2 \equiv \left|\Omega_{e2}\right|^2 + \left|\Omega_{e5}\right|^2\,, \tag{4.47}$$

$$X_3 \equiv \left|\Omega_{\mu 3}\right|^2 + \left|\Omega_{\mu 6}\right|^2\,,\; X_4 \equiv \left|\Omega_{\mu 2}\right|^2 + \left|\Omega_{\mu 5}\right|^2\,, \tag{4.48}$$

$$X_5 \equiv \left|\Omega_{e3}\Omega_{\mu 3}^* + \Omega_{e6}\Omega_{\mu 6}^*\right|^2\,,\; X_6 \equiv \left|\Omega_{e2}\Omega_{\mu 2}^* + \Omega_{e5}\Omega_{\mu 5}^*\right|^2\,, \tag{4.49}$$

$$X_7 \equiv \left(\Omega_{e3}\Omega_{\mu 3}^* + \Omega_{e6}\Omega_{\mu 6}^*\right)\left(\Omega_{e2}^*\Omega_{\mu 2} + \Omega_{e5}^*\Omega_{\mu 5}\right)\,. \tag{4.50}$$

As a side remark, we would like to point out here that a similar approach could, in principle, be used in the presence of one ε_i: in this case, instead of 7, there would be 9 combinations of angles and phases to take into account.[12]

row phases were removed from the mixing matrix. Hence we are left with 24-12+1 real parameters which affect the neutrino oscillation probabilities if no ε_i's are introduced.

[12]Consider a non-zero ε_1 (for $\varepsilon_{i=2,3} \neq 0$, the changes to the following expressions are trivial). Then the $P\left(\nu_e \to \nu_e\right)$, $P\left(\nu_e \to \nu_\mu\right)$ and $P\left(\nu_\mu \to \nu_\mu\right)$ probabilities depend only on the following quantities:

$$\widehat{X}_1 \equiv \left|\Omega_{e3}\right|^2 + \left|\Omega_{e6}\right|^2\,,\; \widehat{X}_2 \equiv \left|\Omega_{e2}\right|^2 + \left|\Omega_{e5}\right|^2\,,\; \widehat{X}_3 \equiv \left|\Omega_{e1}\right|^2\,, \tag{4.51}$$

$$\widehat{X}_4 \equiv \left|\Omega_{\mu 3}\right|^2 + \left|\Omega_{\mu 6}\right|^2\,,\; \widehat{X}_5 \equiv \left|\Omega_{\mu 2}\right|^2 + \left|\Omega_{\mu 5}\right|^2\,,\; \widehat{X}_6 \equiv \left|\Omega_{\mu 1}\right|^2\,, \tag{4.52}$$

$$\widehat{X}_7 \equiv \left|\Omega_{e3}\Omega_{\mu 3}^* + \Omega_{e6}\Omega_{\mu 6}^*\right|^2\,,\; \arg\left(\widehat{X}_8\right) \equiv \arg\left(\Omega_{e1}\Omega_{\mu 1}^*\Omega_{e4}^*\Omega_{\mu 4}\right)\,, \tag{4.53}$$

$$\arg\left(\widehat{X}_9\right) \equiv \arg\left[\Omega_{e1}\Omega_{\mu 1}^*\left(\Omega_{e2}^*\Omega_{\mu 2} + \Omega_{e5}^*\Omega_{\mu 5}\right)\right]\,. \tag{4.54}$$

Note that the X_i defined above can take any value in our framework, provided that the following constraints are obeyed:

1. the first six X_i are non-negative real numbers;
2. neither $X_1 + X_2$ nor $X_3 + X_4$ can be larger than 1;
3. $X_5 \leq X_1 X_3$ and $X_6 \leq X_2 X_4$;
4. the norm of X_7 is fixed by X_5 and X_6 ($|X_7|^2 = X_5 X_6$), so even though X_7 is a complex parameter, only $\arg(X_7)$ is an independent degree of freedom;
5. $X_5 + X_6 + 2\cos[\arg(X_7)]\sqrt{X_5 X_6}$ cannot be bigger than $(1 - X_1 - X_2)(1 - X_3 - X_4)$.

These conditions are a consequence of the definitions of the X_i and the fact that the rows of the mixing matrix Ω are orthonormal ($\Omega\Omega^\dagger = 1$). Taking them into account, we are able to pick out all valid points in the X_i parameter space, without ever referencing back to specific entries of the mixing matrix.

For reference, the values of these X_i parameters in the Dirac limit as a function of the standard θ_{12}, θ_{13}, θ_{23} and δ parameters (see eq. (4.15)) are the following:

$$X_1 = \sin^2\theta_{13}\,,\; X_2 = \sin^2\theta_{12}\cos^2\theta_{13}\,,\; X_3 = \cos^2\theta_{13}\sin^2\theta_{23}\,, \tag{4.55}$$

$$X_4 = \sin^2\theta_{12}\sin^2\theta_{13}\sin^2\theta_{23} + \cos^2\theta_{12}\cos^2\theta_{23} - \frac{1}{2}\sin 2\theta_{12}\sin 2\theta_{23}\sin\theta_{13}\cos\delta\,, \tag{4.56}$$

$$X_5 = X_1 X_3\,,\; X_6 = X_2 X_4\,, \tag{4.57}$$

$$X_7 = \sin\theta_{12}\sin\theta_{13}\cos^2\theta_{13}\sin\theta_{23}\left(-\sin\theta_{12}\sin\theta_{13}\sin\theta_{23} + e^{-i\delta}\cos\theta_{12}\cos\theta_{23}\right)\,. \tag{4.58}$$

Using $\Delta m^2_{\rm Atm} = 2.55 \times 10^{-3}$ eV and $\Delta m^2_{\odot} = 7.56 \times 10^{-5}$, we performed a 7-dimensional scan over all X_i. Electron neutrino survival data from at KamLAND, DayaBay, SuperK and Borexino was used, together with muon neutrino survival data at MINOS and T2K and $\nu_\mu \to \nu_e$ T2K data. The allowed values in the planes (X_1, X_2), (X_3, X_4) and (X_5, X_6) are shown in

fig. (4.19). The marginalized χ^2 function for $X_{1,\cdots,6}$ is shown in fig. (4.20); the marginalized $\chi^2\left[\arg\left(X_7\right)\right]$ function is not shown as it is essentially flat from 0 to 2π.

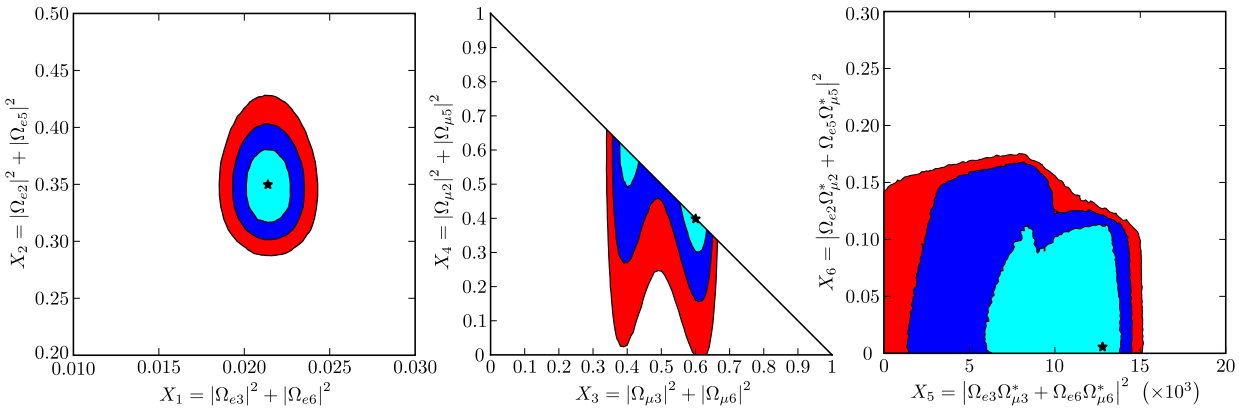

Figure 4.19: One, two and three σ regions in the (X_1, X_2), (X_3, X_4) and (X_5, X_6) which are allowed by electron neutrino survival data from at KamLAND, DayaBay, SuperK and Borexino, muon neutrino survival data at MINOS and T2K and muon to electron transition data from T2K. This plots were obtained from a 7-dimensional scan of the X_i defined in eqs. (4.47)–(4.50) and marginalizing over 5 variables.

Overall, the bounds on these 7 parameters are broadly consistent with the standard three neutrino oscillation picture. In other words, by substituting in expressions (4.55)–(4.58) the numbers obtained for θ_{12}, θ_{13}, θ_{23} and δ from global fits [5], we get values for the X_i roughly in agreement with figs. (4.19) and (4.20). In order to see clearly that current data is consistent with the Dirac limit, note that in this latter case there are only 4 independent parameters. Thus, it follows that the standard three neutrino oscillation picture must correspond to three relations among the 7 X_i. These are

$$X_5 = X_1 X_3\,, \tag{4.59}$$

$$X_6 = X_2 X_4\,, \tag{4.60}$$

$$\mathrm{Re}\left(X_7\right) = \frac{1}{2}\left(1 - X_1 - X_2 - X_3 - X_4 + X_1 X_4 + X_2 X_3\right)\,, \tag{4.61}$$

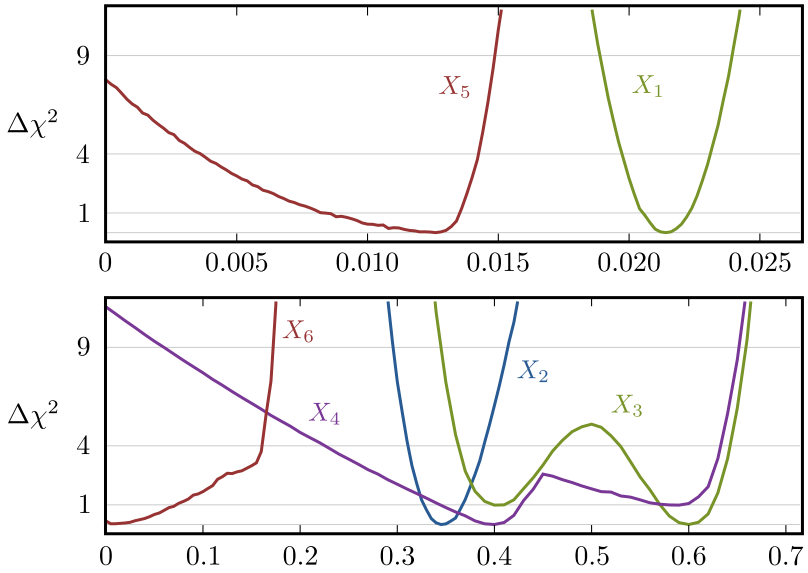

Figure 4.20: Marginalized $\Delta\chi^2$ values for the variables $X_{1,\dots,6}$ defined in eqs. (4.47)–(4.50). The χ^2 function for X_7 is essentially flat. These parameters are a function of the entries of the mixing matrix only; no mass splittings ε_i were considered.

and from fig. (4.21) one can see that oscillation data is compatible with each of these equalities within $\sim 1\sigma$. The three together are disfavored only at $\min(\chi^2_{\text{Dirac}}) - \min(\chi^2) = 1.9$ so, assuming no mass splittings ε_i, there is currently no significant indication for quasi-Dirac neutrinos.

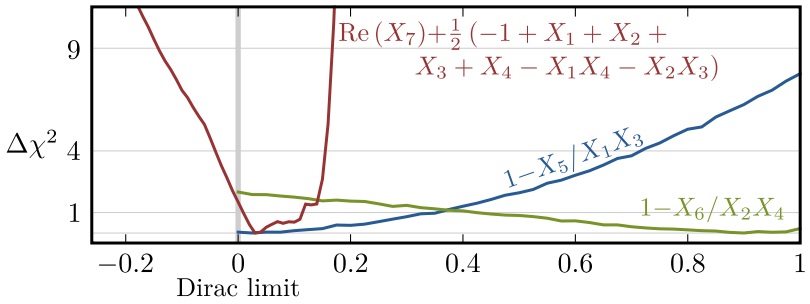

Figure 4.21: $\Delta\chi^2$ functions for the three combinations of parameters which, when equal to 0 simultaneously, signal the Dirac limit (see eq. (4.61)).

We would like to point out that even in the absence of new mass scales, quasi-Dirac neutrinos can, in principle, be distinguished from some other scenarios through oscillation experiments. In particular, consider 3 active neutrinos and a non-unitary 3×3 mixing matrix V. The oscillation probabilities are then given by the expressions

$$P(\nu_e \to \nu_e) = F\left(J^{12}_{ee}, J^{13}_{ee}, J^{23}_{ee}\right) + J^{12}_{ee}\mathcal{A}_{12} + J^{13}_{ee}\mathcal{A}_{13} + J^{23}_{ee}\mathcal{A}_{23}\,, \tag{4.62}$$

$$P(\nu_\mu \to \nu_\mu) = F\left(J^{12}_{\mu\mu}, J^{13}_{\mu\mu}, J^{23}_{\mu\mu}\right) + J^{12}_{\mu\mu}\mathcal{A}_{12} + J^{13}_{\mu\mu}\mathcal{A}_{13} + J^{23}_{\mu\mu}\mathcal{A}_{23}\,, \tag{4.63}$$

$$\begin{aligned} P(\nu_e \to \nu_\mu) = {} & F'\left(J^{12}_{ee}, J^{13}_{ee}, J^{23}_{ee}, J^{12}_{\mu\mu}, J^{13}_{\mu\mu}, J^{23}_{\mu\mu}, J^{12}_{e\mu}, J^{13}_{e\mu}, J^{23}_{e\mu}\right) \\ & + \mathrm{Re}\left(J^{12}_{e\mu}\right)\mathcal{A}_{12} + \mathrm{Re}\left(J^{13}_{e\mu}\right)\mathcal{A}_{13} + \mathrm{Re}\left(J^{23}_{e\mu}\right)\mathcal{A}_{23} \\ & + \mathrm{Im}\left(J^{12}_{e\mu}\right)\mathcal{B}_{12} + \mathrm{Im}\left(J^{13}_{e\mu}\right)\mathcal{B}_{13} + \mathrm{Im}\left(J^{23}_{e\mu}\right)\mathcal{B}_{23}\,, \end{aligned} \tag{4.64}$$

where $J^{ij}_{\alpha\beta} = V^*_{\alpha i}V^*_{\beta j}V_{\beta i}V_{\alpha j}$. The exact form of the functions F and F' which control the 0-distance neutrino behavior is not important for the present discussion. The more important point is that with a non-unitary V one can have an oscillatory behavior which is impossible to reproduce with quasi-Dirac neutrinos, and vice-versa.

For example, the $\mathcal{B}_{ij}$ coefficients in $P(\nu_e \to \nu_\mu)$ do not need to be related for a non-unitary V, while for quasi-Dirac neutrinos they must be the same (up to a minus sign — see eq. (4.46)). On the other hand, note that from the J^{ij}_{ee} and $J^{ij}_{\mu\mu}$ one can extract the modulus of the absolute value of all $J^{ij}_{e\mu}$, hence by measuring $P(\nu_e \to \nu_e)$ and $P(\nu_\mu \to \nu_\mu)$, as well as the coefficients $\mathcal{B}_{ij}$ in $P(\nu_e \to \nu_\mu)$, the coefficients of the oscillatory factors $\mathcal{A}_{ij}$ in $P(\nu_e \to \nu_\mu)$ are fixed for a non-unitary V (up to $\pm$ signs). However, for quasi-Dirac neutrinos no such constraint exists. So, with this short theoretical argument, one can conclude that in principle these two non-standard neutrino scenarios can be distinguished through oscillation experiments.

In conclusion, in this Chapter we focus on light active neutrinos. We constructed three pairs of quasi-Dirac neutrinos and we derived the constraints on these quasi-Dirac neutrino parameters imposed by some neutrino oscillation experiments. We saw that to describe three generations of quasi-Dirac neutrinos we need a total of 6 masses, 12 angles and 12 phases. The number of parameters is too large to be analyzed simultaneously so we considered some special cases: one parameter extension in which we found limits on the mass splittings, two parameters extension (one mass splitting and one new angle) where we found degeneracies for which it was impossible derive some limits from a single experiment and finally, we considered the limit where the mass splittings are null and we considered just angles and phases. We found that the current data is consistent with the Dirac scenario. We expect that next experiments, in particular DUNE, provide more sensitive probes for this particular setup of quasi-Dirac neutrinos.

Chapter 5

High-dimensional neutrino masses

In this Chapter, based on [138] we study high-dimensional tree-level diagrams for Majorana neutrino masses. We treat systematically all possible topologies for the deconstruction of the $d = 9$, $d = 11$ and $d = 13$ operators. We identify all the "genuine" diagrams, which for us are those diagrams that can give the leading contribution to the neutrino mass matrix, without the use of extra (discrete or flavour) symmetries. We discuss this requirement in more detail in section 5.2.3. The Chapter is organized as follows. After an initial discussion on the topic in which we show the main motivation, in section 5.2 we set up our notation and briefly discuss neutrino mass generation at lower dimensions. This is necessary to clearly define what we mean by "genuine" models. Section 5.3 then contains the central piece of our work. We explain our methods, discuss topologies and list and briefly discuss the genuine models. Finally, in section 5.4 we briefly discuss how experimental data on neutrino masses and mixing can be easily fitted with these high-dimensional models.

5.1 Motivation

The Weinberg operator is the lowest dimensional non-renormalizable operator that one can write down with only standard model (SM) fields [6]. It violates lepton number by two units and thus, once the electro-weak

symmetry is broken, Majorana neutrino masses are generated. The observed smallness of the neutrino masses is then usually attributed to the large value of the scale of lepton number violation (LNV), typically $\Lambda \sim (10^{14} - 10^{15})$ GeV. This is the essence of the seesaw mechanism [22, 25, 139–147]. While simple and elegant, the large mass scale involved in this argument makes direct tests of the classical seesaw impossible.

There exist, however, many possibilities to explain the smallness of the observed neutrino masses with lower LNV scales. For Majorana neutrinos one can write in general [9]

$$m_\nu \propto \epsilon \cdot \left(\frac{1}{16\pi^2}\right)^n \cdot \left(\frac{v}{\Lambda}\right)^{d-5} \cdot \frac{v^2}{\Lambda}. \tag{5.1}$$

Here, v stands for the standard model vacuum expectation value (vev), d is the dimension of the operator, n stands for the number of loops at which neutrino masses are generated. ϵ expresses symbolically the additional suppression of lepton number violation that might arise in particular constructions, such as for example the inverse seesaw mechanism [8]. Finally, in addition, small Yukawa or scalar couplings, not shown explicitly in Eq. (5.1), could lead to smaller than expected neutrino masses.

Equation (5.1) can be used to estimate the typical scale Λ, for which the observed neutrino masses could be explained for a given d and n. Fig. 5.1 illustrates this estimate. Here, $\mathcal{O}_5$ at tree-level corresponds to the classical seesaw mechanism. Note that for $\mathcal{O}_5$ at tree-level (1-loop level) Yukawa couplings of order $\mathcal{O}(10^{-6})$ ($\mathcal{O}(10^{-3})$) would be needed to obtain a scale as low as $\Lambda \simeq 1$ TeV. In this figure we also show the estimated reach for three colliders. The LEP line reflects that no electrically charged particle coupled to SM fermions with masses below roughly 100 GeV can exist, after the negative searches performed at the LEP collider [148]. The horizontal grey band indicates a very rough estimate of the reach of the LHC: The lower edge of the band is a more conservative estimate (pair production of charged particles), while the upper edge is roughly the reach of the LHC for particles produced in s-channel diagrams and/or with colour. For $d = 9$ and larger one expects that LHC experiments will cover an important part of the available parameter space of these models. We also show as a dashed line a rough estimate of the reach of a hypothetical $\sqrt{s} = 100$ TeV collider, here called FCC. Thus, neutrino mass models generated at $d = 9$ and higher

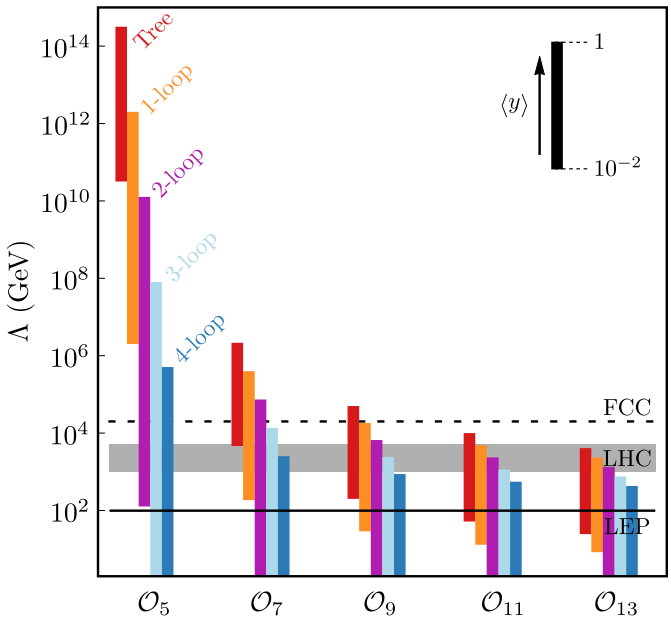

Figure 5.1: The typical energy scales (Λ) for which a neutrino mass model with a given dimension and number of loops (d, n) can explain correctly the observed sub-eV neutrino masses. Operators start at $d = 5$, corresponding to the Weinberg operator. Energy ranges have been estimated using average couplings $\langle y \rangle$ in the range of $[0.01, 1]$.

should be testable in the near future. This simple argument forms the main motivation for our study.

Before presenting our analysis at $d = 9, d = 11$ and $d = 13$, let us briefly mention that, of course, many authors have studied neutrino mass models beyond the simplest tree-level seesaw, for a recent review see for example [149]. The Zee model [150], or the Zee-Babu model [146, 151, 152] are early examples of 1-loop and 2-loop realizations of the Weinberg operator. A systematic analysis of possible neutrino mass models at $d = 5$ and 1-loop can be found in Ref. [9], for a general analysis of $d = 5$ models at 2-loop see Ref. [10]. For the 3-loop case, there exist some well-known models in the literature [153, 154]; a complete study of 3-loop neutrino masses at

$d = 5$ can be found in Ref. [11]. Neutrino masses at $d = 7$ level have also been studied. A systematic analysis at tree-level was done in Ref. [12]. At $d = 7$ tree-level there is only one genuine (in our sense) tree-level neutrino mass model, which was first discussed in Ref. [155]; we will call it the BNT model below. A general analysis of $d = 7$ neutrino masses at 1-loop order was recently presented in Ref. [13, 14].

Then there are also some papers on $d = 9$ (and higher) neutrino mass models, see Refs. [156–161]. We will come back to these papers briefly in Sec. 5.2, where we discuss the main differences between their results and our present work. We mention in passing also the model presented in Ref. [162], which uses a scalar septet to construct a model giving $d = 13$ neutrino masses at 1-loop. Note, however, that this model is not genuine in our sense, since it uses a Z_2 symmetry to eliminate the $d = 5$ seesaw contribution.

5.2 Preliminaries

In this section we briefly go over some basic facts about $d = 5$ and $d = 7$ neutrino masses. This will be useful later, when we discuss genuine higher dimensional models, since those models can give the dominant contribution to the neutrino mass matrix only if $d = 5$ and $d = 7$ contributions are absent. We will use the following notation. A $SU(2)_L$ multiplet with hypercharge Y is denoted as $\mathbf{R}_Y$, to which we add the superscript F or S for fermion or scalar, respectively. Thus, for example $\mathbf{5}_0^F$ is a hypercharge-less fermionic quintuplet.

5.2.1 Tree level $d = 5$ and $d = 7$

The $d = 5$ Weinberg operator can be generated at tree-level in exactly three different ways [163]. In the literature these are known as seesaw type-I, type-II and type-III. Type-I is the standard contribution due to right-handed neutrino ν_R (or $\mathbf{1}_0^F$ in our notation). The Majorana mass term for ν_R is the origin of lepton number violation. Type-III seesaw replaces $\mathbf{1}_0^F$ by $\mathbf{3}_0^F$ [147], which is a field usually denoted as Σ in the literature. Finally, for type-II seesaw one introduces $\mathbf{3}_1^S \equiv \Delta$. In this latter case, the presence of

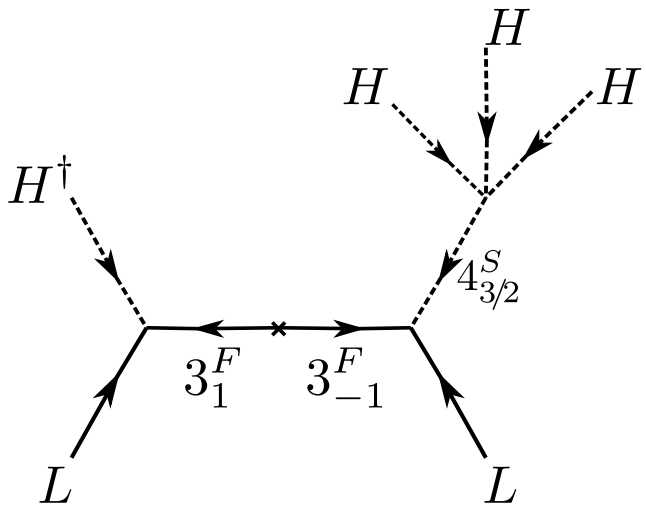

Figure 5.2: The genuine tree-level diagram for $d = 7$ [155]. At least two beyond-the-SM particles are needed for higher dimensional operators.

both the Yukawa coupling $L\Delta L$ and the scalar coupling $H\Delta^\dagger H$, leads to lepton number violation.

At $d = 7$ one already finds five different topologies [12]. However, one of these can not lead to any renormalizable neutrino mass model, while for three more topologies the diagrams always contain necessarily one of the $d = 5$ seesaw mediators. The only diagram for which the $d = 5$ tree-level seesaw is absent without the need of additional symmetries was first discussed in Ref. [155]. This model contains two new particles, $\mathbf{3}^F_1$ and $\mathbf{4}^S_{3/2}$, as shown in Fig. 5.2.

A few comments might be in order at this point. As Fig. 5.2 indicates, two Weyl fermions are actually needed to generate the diagram: $\mathbf{3}^F_1$ and its vector partner $\mathbf{3}^F_{-1}$. Without the mass term $m_{\mathbf{3}^F_1}\mathbf{3}^F_1\mathbf{3}^F_{-1}$ there would not be any source of lepton number violation in the model and, thus, no Majorana masses for the light, active neutrinos could be generated. We have therefore shown this mass insertion explicitly in Fig. 5.2. In many of the diagrams in the rest of this Chapter, on the other hand, for a more compact presentation, we do not explicitly show the vector partners. However, we stress that in all of our tree-level models all exotic fermions must necessarily be of vector-type or Majorana fermions. Also, while at $d = 5$ one new particle is sufficient

for each of the three seesaws, at $d = 7$ we already need two different fields (three if one counts the vector fermion as two distinct Weyl fermions) for a genuine model.

5.2.2 1-loop $d = 5$ and $d = 7$ diagrams

The authors of Ref. [9] systematically analyzed all 1-loop $d = 5$ topologies. In total, there are 6 topologies, but only two of them (called T-1 and T-3) can yield genuine models in our sense. These lead to four different diagrams, shown in Fig. 5.3. T-1-ii corresponds to the diagram of the well-known Zee model [150], an example for T-3 is the scotogenic model [164]. Note also that in all 1-loop diagrams at least two beyond-the-SM fields are needed.

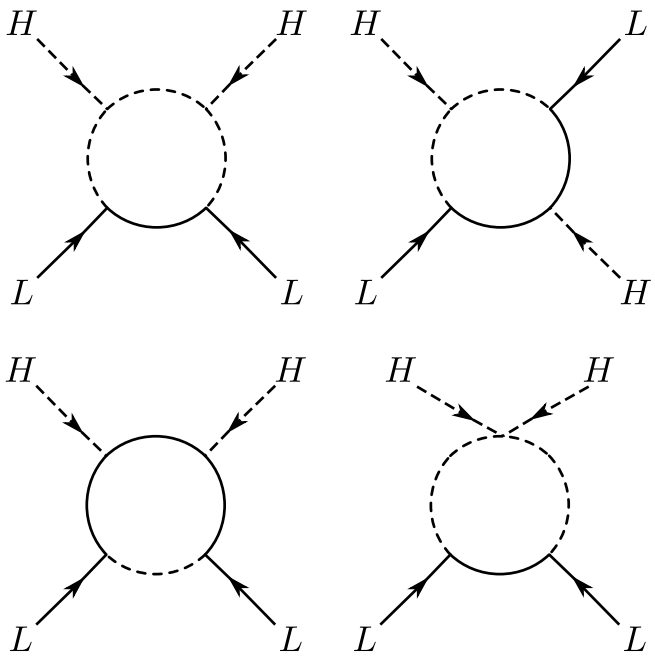

Figure 5.3: The four genuine 1-loop $d = 5$ neutrino mass diagrams [9]. In the top panel we show the T-1-i diagram on the left and the T-1-ii diagram on the right. In the bottom panel, the T-1-iii diagram on the left and the T-3 diagram on the right.

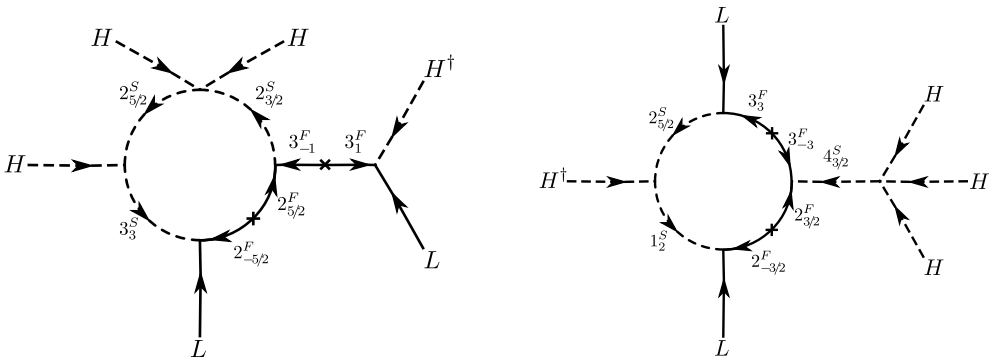

Figure 5.4: Two examples for genuine 1-loop $d = 7$ diagrams. These examples have been chosen since they contain the smallest representations, for which genuine 1-loop $d = 7$ diagrams can be constructed.

In contrast to tree-level diagrams, discussed above, for 1-loop diagrams the representation and hypercharges of the internal particles are not uniquely fixed. Since both L and H are $SU(2)_L$ doublets, the two internal particles they meet in a trilinear vertex must transform as $(\mathbf{N})^{S/F}_{Y}$ and $(\mathbf{N+1})^{S/F}_{Y\pm1/2}$, for some unconstrained $\mathbf{N}$ and Y.[1] This leads to a series of possible models at 1-loop, if one allows for larger $SU(2)$ representations and hypercharges.

At $d = 7$ 1-loop one finds already 48 different topologies, from which, however, only 8 can lead to genuine models [13]. The analysis of Ref. [13] shows that there is only one diagram in which the largest internal representation can be as small as a triplet, while there are a further 22 diagrams, with at least one quadruplet. We will not repeat here all the diagrams for brevity and instead show in Fig. 5.4 just two examples.

Figure 5.4 shows on the left the model with only triplets, while the diagram on the right is an example of a model with exactly one quadruplet. The exotic particles external to the loop in these example models are $\mathbf{3}^F_1$ (left

[1] Although less important for us, we mention that differently from the tree-level realizations, internal particles in the loops can also be coloured. In analogy to what happens for the $SU(2)$ quantum numbers, since L and H are both colorless, the two internal particles which they meet in a trilinear vertex must transform as $\mathbf{R}$ and $\bar{\mathbf{R}}$ under $SU(3)_C$, with $\mathbf{R}$ being arbitrary.

diagram) and $\mathbf{4}^S_{3/2}$ (right diagram). These two particles can not be present in 1-loop $d = 7$ models at the same time, otherwise one generates the $d = 7$ tree-level diagram of the BNT model. Again, as in the case of $d = 5$ 1-loop, one can build series of models allowing for larger representations and/or hypercharges for the particles in the loop. Also, from the fact that H and L have fixed quantum numbers, one can derive a set of conditions on the possible combinations of representations and hypercharges for the internal particles. The exact conditions, however, depend on the type of diagram under consideration. Note that most 1-loop $d = 7$ diagrams need five new particles (more, if one counts the vector partners of the fermions as extra degrees of freedom), although for special values of the quantum numbers four new fields are enough.

5.2.3 Genuineness

In this subsection we want to discuss our concept of "genuineness" for neutrino mass models in somewhat more detail. In short, we consider a model genuine at dimension d, if all lower dimensional contributions are automatically absent, without the need for additional symmetries beyond those of the standard model group.

However, one aspect of higher-dimensional neutrino mass models needs to be considered first. There is a single $\Delta L = 2$ neutrino mass operator of dimension d, which is always of the following form:[2]

$$\mathcal{O}^d \propto LLHH(H^\dagger H)^{(d-5)/2}\,, \tag{5.2}$$

[2]Invariance under $SU(2)$ forces the operator dimension d to be odd. Note also that $\mathcal{O}^d$ in eq. (5.2) contains $d - 1 \equiv 2n$ doublets of $SU(2)$, and in general the product of multiple doublets is expected to have many independent contractions. Indeed, it seems that the number of singlets in the product of $2n$ doublets is given by the Catalan numbers $C(n) \equiv (2n)!/\left[(n+1)!n!\right]$, hence for $d = 13$ (i.e. $n = 6$) we might had expected 132 different contractions of the $SU(2)$ indices. Yet, we note that there is a single Higgs field, so all $(d-1)/2$ copies of H must be contracted symmetrically; the same is true for the $(d-5)/2$ copies of H^*. And it is not complicated to see that for a given d, there is always one—and only one—contraction with this property; all the others are therefore identically 0. See also Ref. [165].

with the $SU(2)$ indices of each pair LH outside the brackets contracted with the anti-symmetric real tensor ϵ_{ab}, and each pair $H^\dagger H$ inside the brackets contracted with the δ_{ab} tensor.

The very same operators will always lead to lower order loop models:[3]

$$\frac{1}{\Lambda^{(d-4)}} LLHH(H^\dagger H)^{(d-5)/2} \to \frac{1}{16\pi^2}\frac{1}{\Lambda^{(d-6)}} LLHH(H^\dagger H)^{(d-7)/2} \qquad (5.3)$$

In the SM, where there is only one Higgs doublet, such loops can not be forbidden by postulating some symmetry. [4] One can straightforwardly estimate that such a loop contribution will become more important than the tree-level one if $(\Lambda/v) \gtrsim 4\pi$. This means $\Lambda \lesssim 2$ TeV is required for the d-dimensional tree-level contribution to dominate over the $(d-2)$ dimensional 1-loop one. Since this is unavoidable in the SM, $d \geq 7$ tree-level model of neutrino mass *must have new particles below 2 TeV*, otherwise loop contributions will dominate the neutrino mass matrix. Note that this "upper limit" is more stringent than the estimates for the typical scales Λ shown in Fig. 5.1.

In loop calculations usually there appear both finite and infinite loop integrals. However, in a renormalizable theory, infinite contributions are canceled by counter-terms, implying that there are lower order contributions to the same operator. Thus, all models with diagrams requiring renormalization are not genuine in our sense. On the other hand, diagrams associated to finite loop integrals only, can lead to genuine models. One should distinguish two different scenarios: Models in which lower order contributions are absent automatically, and models which forbid lower order contributions with the help of an extra symmetry. We consider only the former class of models genuine.

Let us discuss the second scenario with one concrete and well-known example: the scotogenic model [164]. Here, the right-handed neutrino is assumed to be odd under a Z_2 and a new scalar doublet (odd under the

[3] Diagrammatically, this does not mean that one can close every pair of H,H^* external lines. However, there will always be at least one such pairs of lines which can be closed.

[4] For this reason, the authors of Ref. [12] considered a two-Higgs doublet extension of the SM. Assigning different charges to the two doublets under a new Z_n makes it possible to forbid loop contributions. Note, however, that these additional symmetries are spontaneously broken by the doublet vevs.

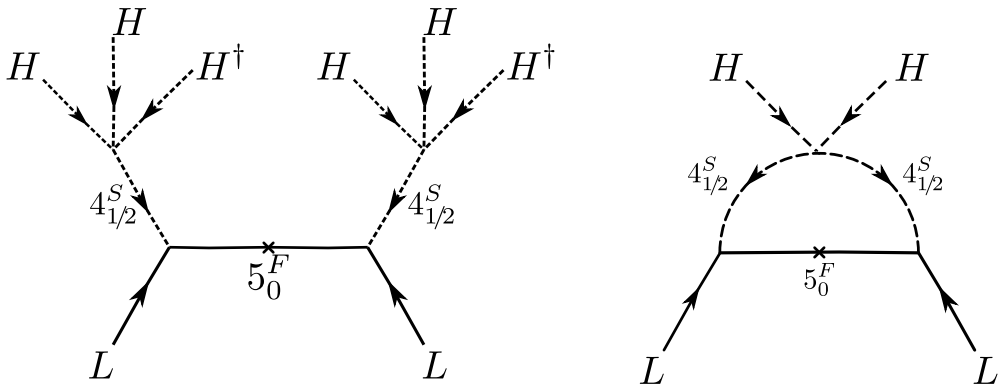

Figure 5.5: One example of a "non-genuine" $d = 9$ diagram, to the left. Connecting the two quadruplet scalars, as shown on the right, leads to a 1-loop diagram at $d = 5$.

Z_2 as well) is added to the model. Thus, there is no $d = 5$ tree-level contribution from the SM Higgs and the 1-loop contribution can dominate. The resulting 1-loop integral is finite and thus, technically, no tree-level neutrino mass term is needed. Let us stress that while we do not consider such a construction to be "genuine" in our sense, such neutrino mass models are of course perfectly valid and phenomenologically interesting models.

However, we also want to mention that such a construction relies on the assumption that the new scalars in these models do not acquire a vacuum expectation values. Of course, adding some discrete symmetry to the model does not guarantee, by itself, the absence of a vev. Rather, a non-zero vev for the exotic scalar(s) would break the discrete symmetry spontaneously, leading to an unwanted tree-level neutrino mass term and thus usually (but not always) vevs are to be avoided. This can be achieved with an appropriate choice of parameter values in the scalar potential. (In the scotogenic model essentially it corresponds to imposing the condition that the mass squared parameter of the new scalar doublet is positive, $\mu_D^2 > 0$.)

For concreteness, let us now consider a particular example model for a $d = 9$ tree-level diagram. The model presented in Ref. [157] contains two new fields: $\mathbf{4}^S_{1/2}$ and $\mathbf{5}^F_0$. This model is non-genuine in our definition. [5]

[5]The same model was discussed also in Ref. [161].

The model generates a $d = 9$ tree-level diagram, see fig. (5.5) on the left, via the four scalar vertex $\lambda_4(\mathbf{4}^S_{1/2})^\dagger H H H^\dagger$.[6] Connecting the two quadruplet scalars via a quartic interaction $\lambda_5(\mathbf{4}^S_{1/2})^\dagger(\mathbf{4}^S_{1/2})^\dagger H H$ allows one to draw the 1-loop $d = 5$ diagram on the right. The loop integral is finite, just as in the scotogenic model. Assuming the masses of $\mathbf{4}^S_{1/2}$ and $\mathbf{5}^F_0$ to be roughly of order Λ the ratio of the contributions of the two diagrams can be estimated as

$$R(\text{tree/loop}) \propto \frac{\lambda_4^2}{\lambda_5}\left(\frac{v_{SM}}{\Lambda}\right)^4, \tag{5.4}$$

i.e. the tree-level will be less important than the loop for scales Λ bigger than roughly $\Lambda \simeq 600\sqrt{\lambda_4}/(\lambda_5)^{1/4}$ GeV. Note that, since $\mathbf{4}^S_{1/2}$ contains one doubly charged component, the LHC searches on same-sign dileptons [166] should apply. Thus, one can estimate that the current lower limits on the mass of $\mathbf{4}^S_{++}$ should be in the range of roughly [500,650] GeV, depending on the final state lepton generation [14].

Similar comments apply to the models presented in Refs. [156, 158–160]. Reference [156] introduces $\mathbf{5}^F_1$, $\mathbf{4}^S_{3/2}$ and $\mathbf{4}^S_{1/2}$. The model has a a 1-loop diagram of type T_3, just as in the example of Ref. [157] discussed above. Reference [158] introduces the idea of a "cascade seesaw". Essentially here the author discusses that models such as [157] can be generalized to yield $d = 9$, $d = 13$ and higher, by using larger and larger multiplets. References [159, 160] discusses different seesaw models at $d = 7$ and $d = 9$. However, this analysis considers only one exotic fermion (and two new scalars) in each model. None of the models in Refs. [159, 160] is genuine in our sense.

5.3 Classification and results

The basic steps in the procedure are similar for $d = 9$, $d = 11$ and $d = 13$. At each d we first generate all possible topologies via a computer code based on known algorithms [167]. Once these are obtained, we find all diagrams simply by labeling each line as a fermion or a scalar in all possible ways, and ensuring that one obtains fermion-fermion-scalar, scalar-scalar-scalar and scalar four-point vertices only. From these (large) lists of diagrams one

[6] λ_4 will lead to an induced vev for $\mathbf{4}^S_{1/2}$ even if the mass squared parameter $m^2_{S_4}$ is positive.

can construct all models by searching for every allowed combination of L, H and $H^\dagger$ in the outer legs of the diagrams. From these lists we then eliminate every model, which is non-genuine in our definition. We will not show all possible topologies and diagrams here for brevity. The complete lists can be found at renatofonseca.net/high-dim-neutrino-masses.php.

5.3.1 Dimension 9 ($d = 9$)

We start the discussion with $d = 9$. Figure 5.6 shows all 18 topologies from which one can build valid neutrino mass diagrams with renormalizable vertices only. There is one more topology (not shown), with 8 external lines and no loops, but it requires three 4-point vertices, hence it will lead only to non-renormalizable models. The 18 topologies which we do show generate a total of 66 diagrams. However, all except four topologies lead only to diagrams that necessarily have a tree-level neutrino mass at either $d = 5$ or $d = 7$. Diagrams from two more topologies will always also generate 1-loop $d = 5$ diagrams hence, in the end, only topologies T_1 and T_5 yield diagrams that are genuine in our sense. But not all diagrams obtained from T_1 and T_5 are genuine either; the only ones which are genuine can be seen in Fig. 5.7.

Consider first the diagram on the left hand side of Fig. 5.7. It contains only three new fermions, $\mathbf{3}^F_1$, $\mathbf{4}^F_{1/2}$ and $\mathbf{5}^F_0$, together with their vector partners, and no exotic scalar. This is the minimal genuine model at $d = 9$. Its Lagrangian is given by:

$$\mathcal{L} = \mathcal{L}_{SM} + \mathcal{L}_{Yuk} + \mathcal{L}_{mass}, \tag{5.5}$$

where

$$\begin{aligned}\mathcal{L}_{Yuk} = {} & Y_\nu\, L \cdot \mathbf{3}^F_1 H^\dagger + \overline{Y}_{\mathbf{34}}\, \mathbf{3}^F_{-1} \cdot \mathbf{4}^F_{1/2} H + Y_{\mathbf{34}}\, \mathbf{3}^F_1 \cdot \mathbf{4}^F_{-1/2} H^\dagger \\ & + \overline{Y}_{\mathbf{45}}\, \mathbf{4}^F_{1/2} \cdot \mathbf{5}^F_0 H^\dagger + Y_{\mathbf{45}}\, \mathbf{4}^F_{-1/2} \cdot \mathbf{5}^F_0 H\end{aligned} \tag{5.6}$$

and

$$\mathcal{L}_{mass} = M_{\mathbf{3}} \mathbf{3}^F_1 \mathbf{3}^F_{-1} + M_{\mathbf{4}} \mathbf{4}^F_{1/2} \mathbf{4}^F_{-1/2} + M_{\mathbf{5}} \mathbf{5}^F_0 \mathbf{5}^F_0. \tag{5.7}$$

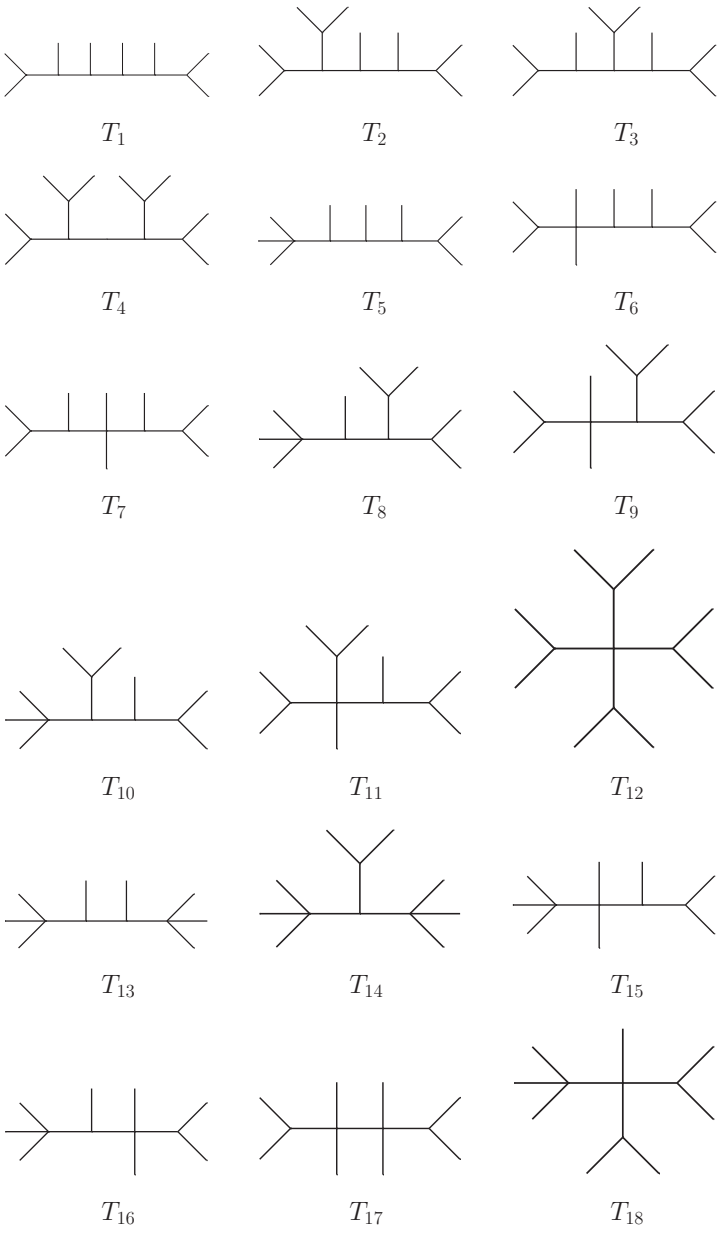

Figure 5.6: The 18 topologies at $d = 9$ level that can give renormalizable diagrams.

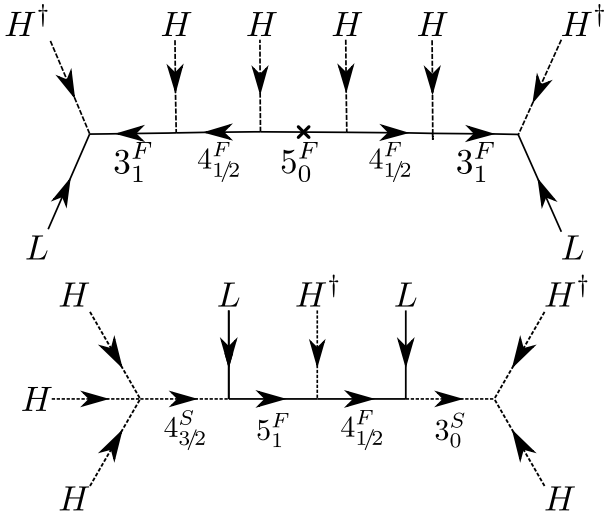

Figure 5.7: The two genuine diagrams at $d = 9$.

The light neutrino mass can be estimated in seesaw approximation (for one generation) as:

$$m_\nu \simeq Y_\nu^2 \overline{Y}^2_{\mathbf{34}} Y^2_{\mathbf{45}} \frac{v^6_{SM}}{M^2_{\mathbf{3}} M^2_{\mathbf{4}} M_{\mathbf{5}}} \tag{5.8}$$

For masses of the order of $\mathcal{O}(1-2)$ TeV, Yukawas of the order of $(0.03-0.04)$ will reproduce the scale of the atmospheric neutrinos, $m_\nu \simeq \sqrt{\Delta(m^2_{Atm})} \simeq 0.05$ eV. For a more detailed fit of neutrino masses and angles, see the appendix.

The diagram on the right hand side of Fig. 5.7 contains two exotic scalars and two exotic fermions. We give only the part of the Lagrangian relevant for the calculation of the neutrino mass,

$$\begin{aligned}\mathcal{L} \propto\ & \lambda_4 HHH(\mathbf{4}^S_{3/2})^\dagger + \mu_3 \mathbf{3}^S_0 HH^\dagger + m^2_4 |\mathbf{4}^S_{3/2}|^2 + m^2_3 |\mathbf{3}^S_0|^2 \\ & + Y_{5L} L \cdot \mathbf{5}^F_{-1} \mathbf{4}^S_{3/2} + Y_{45} \mathbf{4}^F_{-1/2} \cdot \mathbf{5}^F_1 H^\dagger + Y_{4L} L \cdot \mathbf{4}^F_{1/2} (\mathbf{3}^S_0)^\dagger \\ & + M_{\mathbf{5_1}} \mathbf{5}^F_{-1} \mathbf{5}^F_1 + M_{\mathbf{4}} \mathbf{4}^F_{-1/2} \mathbf{4}^F_{1/2}.\end{aligned} \tag{5.9}$$

Again in seesaw approximation and for one generation we can roughly estimate the size of the neutrino mass generated by this model as,

$$m_\nu \simeq Y_{5L} Y_{4L} Y_{45} \lambda_4 \frac{\mu_3 v_{SM}^6}{M_{\mathbf{5_1}} M_{\mathbf{4}} m_4^2 m_3^2}. \tag{5.10}$$

With all mass parameters equal to 1 TeV, $\mu_3 = M_{\mathbf{5_1}} = M_{\mathbf{4}} = m_4 = m_3 = 1$ TeV, and for $\lambda_4 = Y_{5L} = Y_{4L} = Y_{45} = \mathcal{O}(10^{-2})$ this gives roughly 0.3 eV. A more detailed description on how all neutrino data can be fitted in this model is deferred to the appendix.

5.3.2 Dimension 11 ($d = 11$)

At $d = 11$ we find 92 topologies, which generate a total of 504 diagrams. It is not very instructive to discuss in detail all the topologies and diagrams, as the methodology for eliminating non-genuine models is the same as for the $d = 9$ case. The only two genuine diagrams are shown in Fig. 5.8, and they are based on very similar models. The diagram on the right contains five new particles, four of which are also present in the diagram on the left. Thus, the model for the right diagram always produces also the diagram on the left. Unsurprisingly, at $d = 11$ genuine diagrams require at least four different beyond-SM particles and large representations: At least two different quintuplets are needed and the model shown in the right diagram of Fig. 5.8 requires in addition a sextuplet.

Again, we write down only the part of the Lagrangian relevant for estimating the neutrino mass,

$$\begin{aligned}\mathcal{L} \propto\ & \lambda_{55} \mathbf{5}^S_{-2} \mathbf{5}^S_1 HH + \lambda_{53} \mathbf{5}^S_{-1} \mathbf{3}^S_0 HH + \mu_{61} \mathbf{5}^S_1 \mathbf{6}^S_{-3/2} H + \mu_{62} \mathbf{5}^S_{-2} \mathbf{6}^S_{3/2} H \\ & + \mu_3 \mathbf{3}^S_0 H H^\dagger + m_3^2 |\mathbf{3}^S_0|^2 + m_{5_1}^2 |\mathbf{5}^S_1|^2 + m_{5_2}^2 |\mathbf{5}^S_2|^2 + m_6^2 |\mathbf{6}^S_{3/2}|^2 \\ & + Y_\nu L \cdot \mathbf{3}^F_1 H^\dagger + Y_3 \mathbf{3}^F_{-1} \cdot \mathbf{3}^F_{-1} \mathbf{5}^S_2 + M_{\mathbf{3}} \mathbf{3}^F_{-1} \mathbf{3}^F_1 .\end{aligned} \tag{5.11}$$

A simple estimate for the neutrino mass from the left diagram in Fig. 5.8 gives:

$$m_\nu \simeq Y_\nu^2 Y_3 \lambda_{55} \lambda_{53} \frac{\mu_3 v_{SM}^8}{M_{\mathbf{3}}^2 m_3^2 m_{5_2}^2 m_{5_2}^2} \tag{5.12}$$

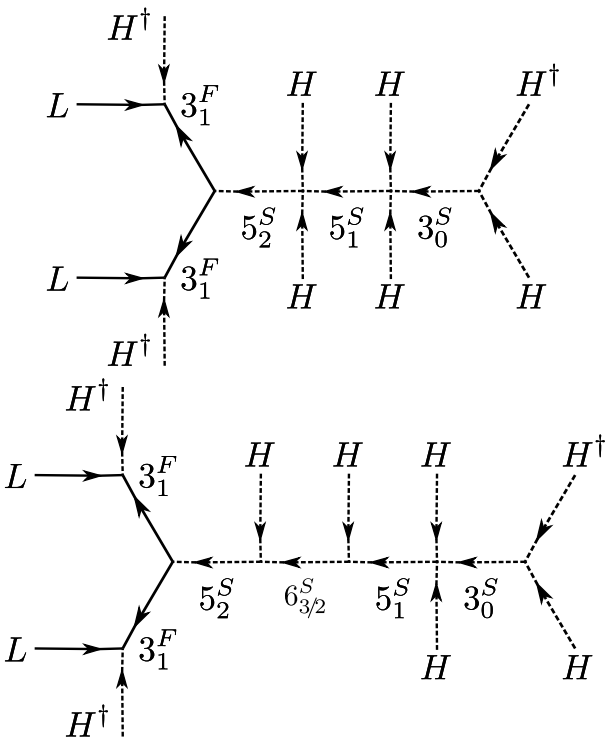

Figure 5.8: The two genuine diagrams at $d = 11$. Note that the fields on the right-hand side diagram always produce the diagram on the left-hand side.

For a new physics scale of $\Lambda = 1$ TeV and all dimensionless couplings order 0.05 one finds again a neutrino mass of order 0.3 eV. As is also the case for the second of our $d = 9$ models, the dimensionful scalar coupling μ_3 can be a source of additional neutrino mass suppression. For $\mu \simeq 100$ keV and all dimensionless couplings $\mathcal{O}(1)$ ($\Lambda = 1$ TeV) one finds $m_\nu \sim \mathcal{O}(0.1)$ eV.

A straightforward calculation shows that the diagram on the right gives a neutrino mass of roughly the same numerical value, if $(\mu_{61}\mu_{62})/m_6^2 \simeq \lambda_{55}$. Thus, the diagram on the left is the dominant one, if either μ_{61} or μ_{62} (or both) are very small relative to the new physics scale Λ. On the other hand, for $\lambda_{55} \ll 1$ the opposite situation is found.

5.3.3 Dimension 13 ($d = 13$)

At $d = 13$ there are 576 topologies and 4199 diagrams. One has to delete not only all models that lead to a tree level $d = 5$, $d = 7$, $d = 9$ and $d = 11$ diagram, as well as a 1-loop $d = 5$ or $d = 7$ diagram, but also all models with a 1-loop $d = 9$ diagram. The last cut drastically reduces again the list of genuine models: without it nearly 50 different diagrams remain, while after this cut only 2 genuine tree-level diagrams at $d = 13$ remain.

Figure 5.9 shows the two remaining genuine diagrams. Unsurprisingly, more fields and larger representations are needed in these diagrams. The largest representation is now a $SU(2)_L$ septet. There is a total of six model variations that one can find for these two diagrams. In addition to the four models shown, one can construct two more model variations for the first diagram (top row): Replace either one or both of the $\mathbf{4}^F_{3/2}$ by a $\mathbf{4}^F_{1/2}$ (rearranging H and $H^\dagger$ correspondingly). Note that the models with $\mathbf{4}^F_{1/2}$ are only genuine with a $\mathbf{7}^F_0$.

Let us discuss first briefly the models corresponding to the diagram in the top row. These models contain only new fermions, but no exotic scalars, and are very similar to each other. The models shown contain five new fermions. As mentioned above, there are two more variations containing a $\mathbf{4}^F_{1/2}$. Comparing these fermion-only models with the simplest $d = 9$ model, one sees that higher dimensional fermion-only diagrams ($d = 17, 21$ etc.) could be straightforwardly found, following the same construction principles.

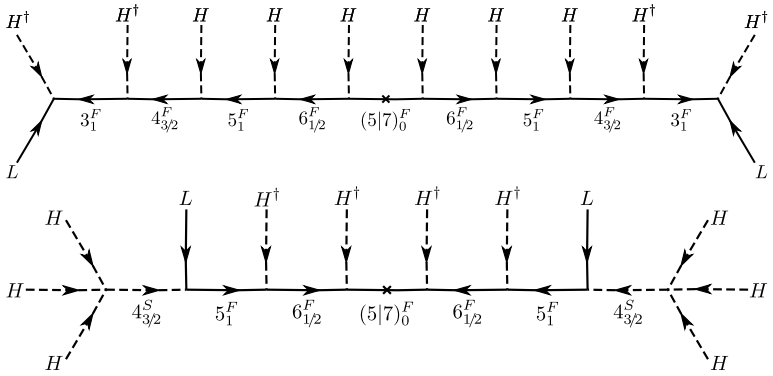

Figure 5.9: The two genuine diagrams at $d = 13$ can be realized in a total of 6 models. It is possible to have either a $\mathbf{5}_0^F$ or a $\mathbf{7}_0^F$ in the middle. Furthermore, two extra models are obtained from the top diagram by rearranging appropriately the external H's and $H^\dagger$'s and replacing either one or both of the internal $\mathbf{4}_{3/2}^F$ correspondingly by a $\mathbf{4}_{1/2}^F$. Note also that these two extra models (not represented above) with the field $\mathbf{4}_{1/2}^F$ need $\mathbf{7}_0^F$ in the middle of the diagram in order to be genuine.

We will not write down the complete Lagrangian for these $d = 13$ models for brevity. The neutrino mass is estimated for these models to be of order $m_\nu \simeq Y^{10}\frac{v^{10}}{\Lambda^9}$, where Y stands symbolically for the Yukawa couplings in the diagrams and we assumed for simplicity that all masses are of order Λ. Yukawa couplings now have to be of order $\mathcal{O}(0.3)$ (with $\Lambda = 1$ TeV) for a neutrino mass $m_\nu \simeq (0.1 - 0.2)$ eV.

The remaining $d = 13$ models in the bottom row of Fig. 5.9 need four exotic fields, one of them needs to be an exotic scalar. Again, a fermionic septet is the largest $SU(2)_L$ representation. Since in these models, some of the Yukawa couplings from the fermion-only models are replaced by four-point scalar couplings, slightly smaller couplings, say $\mathcal{O}(0.2)$, are needed here to achieve $m_\nu \simeq (0.1 - 0.2)$ eV. We close this subsection by stating again that all $d = 13$ models can easily fit all measured neutrino mass squared differences and angles.

5.4 Neutrino mass and angle fits

Above we gave simple estimates for the typical parameter choices that generate a neutrino mass scale large enough to explain the atmospheric neutrino oscillations. However, in all the models presented in this Chapter it is actually easy to fit all angles and masses simultaneously. For the current status of oscillation data see, for example, the recently updated global fit [5]. Here we briefly discuss how tree-level neutrino mass models can be fitted to oscillation data.

We can divide all models discussed above into just two classes: (i) models in which only one type of exotic fermion couples to the outside leptons, for example the $d = 9$ model shown in Fig. 5.6 on the left. And, (ii) models in which two different fermions can couple to the leptons, for example the $d = 9$ model in Fig. 5.6 on the right.

We start with case (i). First, recall that neutrino oscillations require at least two neutrino masses to be non-zero. For models of case (i) there will be one non-zero neutrino mass for each copy of exotic fermions coupling to the leptons. Assuming there are three copies of these exotic fermions one can then use a slight modification of the well-known Casas-Ibarra parametrization [31] that makes it possible to fit neutrino data for an ordinary seesaw ($d = 5$ tree-level). In the simplest seesaw, the light neutrino mass matrix is approximately given by

$$m_\nu = -m_D^T (\hat{M}_R)^{-1} m_D, \tag{5.13}$$

where m_D is the Dirac mass term for neutrinos and $\hat{M}_R$ is the diagonal matrix of the heavy neutrino eigenvalues. Diagonalizing the light neutrino mass matrix with a matrix V_L and solving Eq. (5.13) for m_D one finds [31]

$$m_D = i\sqrt{\hat{M}_R}\mathcal{R}\sqrt{\hat{m}_\nu}V_L^\dagger \tag{5.14}$$

$\mathcal{R}$ is a matrix of three complex angles, with $\mathcal{R}^T\mathcal{R} = 1$, left undetermined when solving Eq. (5.13). V_L contains the measured neutrino angles and Dirac CP-phase δ and $\hat{m}_\nu$ is the diagonal matrix of the light neutrino eigenvalues.

The derivation of Eq. (5.14) relies on the fact that in the standard model augmented with a simple seesaw one can always perform a basis change,

such that M_R, the mass matrix for the right-handed neutrinos, is diagonal. In the higher dimensional neutrino mass models, discussed in this Chapter, for the effective neutrino mass, see Eq. (5.13), we have to replace M_R by a product of matrices. For example for the $d = 9$ model one finds:

$$M_R^{-1} \to M_{eff}^{-1} = \hat{M}_3^{-1} m_{34}^T \hat{M}_4^{-1} m_{45}^T \hat{M}_5^{-1} m_{45} \hat{M}_4^{-1} m_{34} \hat{M}_3^{-1}. \tag{5.15}$$

Basis changes can be used to diagonalize the vector-like mass terms—but not the "Dirac"-like mass terms m_{ij} at the same time. M_{eff} is a complex symmetric matrix and can be diagonalized with a matrix U, containing in general 3 angles and 3 phases. For arbitrary choices of the parameters entering the various matrices in Eq. (5.15) one can find U numerically and then use Eq. (5.14) to determine the correct choice of m_D, using the simple replacement:

$$\sqrt{\hat{M}_R} \to U^\dagger \sqrt{\hat{M}_{eff}}. \tag{5.16}$$

For other models of the same type the form of M_{eff} may change, but the procedure for the neutrino fit is completely analogous.

For case (ii) one can do a neutrino fit using only one copy of each of the two exotic fermions coupling to leptons. Let $\vec{h}^1$ and $\vec{h}^2$ be the two Yukawa vectors coupling exotic fermions to standard model leptons in any given model of this type. Then, schematically, one finds a neutrino mass matrix given by:

$$(m_\nu)_{\alpha\beta} = c(h_\alpha^1 h_\beta^2 + h_\beta^1 h_\alpha^2) \tag{5.17}$$

Here, c is a constant with dimension of mass. For example, in the $d = 9$ model shown on the right of Fig. 5.7, c is given by $c = Y_{45}\lambda_4 \frac{\mu_3 v_{SM}^6}{M_{\mathbf{5_1}} M_{\mathbf{4}} m_4^2 m_3^2}$. The matrix in Eq. (5.17) has determinant zero. Thus, it can be solved analytically using only quadratic equations. Let $|\vec{h}^i|$ be the absolute value of the vector $\vec{h}^i$. Then the two non-zero of eigenvalues Eq. (5.17) are given by:

$$m_{\nu_{2,3}} = c\Big(\vec{h}^1 \cdot \vec{h}^2 \mp |\vec{h}^1||\vec{h}^2|\Big). \tag{5.18}$$

Neutrino angles, on the other hand, depend only on ratios of entries in the Yukawa vectors. Although also the eigenvectors can be found analytically, neutrino angles are fitted most easily numerically. We calculate m_ν from the measured Δm_{ij}^2 and θ_{ij}. Then, for any choice of the parameters en-

tering c, we can choose one entry in the two Yukawa vectors freely, say for example h^1_1, and numerically solve five entries of the matrix in Eq. (5.17) for five independent entries in m_ν. Note that, since c itself can contain small parameters (for example, all of Y_{45}, λ_4 and μ_3 can be small), one needs to check that the resulting Yukawa vectors have entries which are perturbative.

We close this short section with a comment. In certain limits, the two types of models can be fitted with both procedures described above. For example, a model in class (ii) could have 3 copies of both exotic fermions. If $\vec{h}^1 \propto \vec{h}^2$ for the three pairs of vectors, one can also use the modified Casa-Ibarra procedure to find solutions fitting all data.

Summarizing, in this Chapter we have discussed the systematic deconstruction of the $d = 9$, $d = 11$ and $d = 13$ neutrino mass operators at tree-level. We have presented the list of all the genuine topologies, diagrams and models found for these operators. In particular, 18 topologies, 66 diagrams and 2 models at $d = 9$ level; 92 topologies, 504 diagrams and 2 models at the $d = 11$ level, and finally 576 topologies, 4199 diagrams and 6 models at $d = 13$.

Chapter 6

Conclusions

This thesis focuses on two research topics. The first one is the "quasi-diracness" of neutrinos. In general, neutrinos can have lepton number violating (Majorana) and lepton number conserving (Dirac) mass terms. If the lepton number violating mass terms are smaller than the lepton number preserving ones, neutrinos are *quasi-Dirac* particles. The second one is the generation of neutrino masses from high dimensional operators and the cataloging of the genuine neutrino diagrams. The word "genuine" here refers to those diagrams which provide the dominant contribution to the neutrino mass matrix, assuming no extra symmetries beyond the standard model ones. Beyond the study of the literature concerning the topics presented in the previous Chapters, the work has been carried out both with analytical and numerical tools, such as MATHEMATICA and FORTRAN codes. In this chapter we will summarize the main results achieved.

In the third Chapter, we have discussed signals of lepton number violation that could originate in scenarios with quasi-Dirac neutrinos. In particular, we focused on the ratio of same-sign to opposite-sign dilepton events R_{ll}, which is the most promising LNV observable for experimental searches at the LHC. It is well known that if the dilepton events originate from production/decays of heavy Majorana neutrinos, then $R_{ll} = 1$ is expected. We have shown that in the quasi-Dirac case, in the regime in which the mass splitting ΔM between the pair of heavy RH neutrino resonances becomes of the order of their widths, any value within the interval $R_{ll} \in [0, 1]$ is pos-

sible, and $R_{ll} = 0$ is approached in the limit $\Delta M/\Gamma \to 0$ which defines the pure Dirac limit of the quasi-Dirac neutrino pair. It is then clear that an experimental result $R_{ll} < 1 (\neq 0)$ could provide valuable information about the mechanism of generation of the light neutrino masses. We stress that our main result on R_{ll} does not depend on the particular model realization of the quasi-Dirac neutrino scenario (other features, as for example the total event rate for heavy neutrino production, obviously do depend on the specific model). For definiteness we have carried out our discussion in the framework of a LR symmetric model equipped with an inverse seesaw mechanism, since this setup appears to be of prominent experimental interest in view of the ongoing searches for signals of LNV and of RH neutrinos at the LHC. In discussing the LHC phenomenology, we have pointed out that specific values of $R_{ll} \neq 0, 1$ can be correlated with special features of observables in the decay modes of the heavy neutrinos, and this correlation can help to test the scenario. Last but not least, in developing our analysis we have introduced a new parametrization of the inverse seesaw which allows to scan the parameter space of the fundamental theory while automatically respecting all the phenomenological constraints of the low energy effective theory. The use of this parametrization has proven to be very convenient in carrying out our numerical study.

In the fourth Chapter we discussed the phenomenology of quasi-Dirac neutrino oscillations. Phenomenologically, this corresponds to the existence of three pairs of neutrinos with slightly different masses, hence oscillation experiments are sensitive not only to the usual solar and atmospheric mass scales, but also to three small mass splittings ε_i. Furthermore, for quasi-Dirac neutrinos there are more than 3+1 angles and phases to be considered. In this Chapter, we have analyzed the constraints on these quasi-Dirac neutrino parameters imposed by current neutrino oscillation data and also briefly discussed the potential of the future JUNO experiment to improve upon existing constraints. We have discussed a fully general parametrization of the lepton sector for three generations of quasi-Dirac neutrinos. In addition to the charged lepton masses, there is a total of 6 masses, 12 angles and 12 phases. Oscillation experiments are not sensitive to the overall neutrino mass scale nor to 5 of the phases (which are of the Majorana type). Hence we are left with a 24-dimensional model space, compared to the six-dimensional space for an ordinary three generation case ($\Delta m^2_\odot$,

$\Delta m^2_{\rm Atm}$, θ_{12}, θ_{13}, θ_{23} and δ). It is numerically too costly to handle such a large number of parameters at the same time, hence we analyzed several different special cases. First, we took a single mass splitting $\varepsilon_i^2 \neq 0$. If we split two neutrinos with mass m_i into a quasi-degenerate pair of particles with masses $\sqrt{m_i^2 - \varepsilon_i^2/2}$ and $\sqrt{m_i^2 + \varepsilon_i^2/2}$ then a new oscillation length $L \propto 1/\varepsilon_i^2$ appears which is associated to the conversion of active to sterile neutrinos. Very stringent limits on ε_i^2 in such one parameter extensions can be derived, of the order of 10^{-11} eV^2 for $\varepsilon^2_{1,2}$ (from solar neutrino data) and 10^{-5} eV^2 for ε^2_3 (dominated by Super-K atmospheric neutrino data). Next, we considered the case when one mass splitting and one of the non-standard angles are allowed to take non-zero values at the same time. As we have shown, in this situation degeneracies of the χ^2 function can occur, implying that from a single experiment in many cases it will no longer be possible to derive meaningful limits on individual parameters. These degeneracies can be resolved by considering data from more than one experiment, accessing different $P\left(\nu_\alpha \to \nu_\beta\right)$. We then considered the possibility of nullifying the effects of the ε_i completely by changing some particular combinations of the angles θ_{ij} of our parametrization. Instead of pursuing the exact form of these rather complex parameter combinations, we discussed a simpler definition, describing 3 angles φ_i associated to rotations between the columns i and $i+3$ of the quasi-Dirac mixing matrix, such that in the limit where these angles are equal to $\pi/4$ $(3\pi/4)$ the $i+3(i)$ column of the mixing matrix vanishes and hence the associated neutrino mass disappears from the oscillation probability formula. We stress that for these particular parameter combinations no limits on the ε_i can be derived from oscillation experiments. The regions in the planes $(\varepsilon_i, \varphi_i)$ which are allowed by various experiments are shown in figs. (4.15) and (4.17). In this context, it is interesting to note that the tension between the value of the solar mass scale preferred by global fits ($\sim 7.6 \times 10^{-3}$ eV^2) and the lower one preferred by solar data ($\sim 4 \times 10^{-3}$ eV^2) might be resolved by a non-zero value for either ε_1 or ε_2. Lastly, we considered the possibility that the mass splittings ε_i are too small to be measured in oscillation experiments. Even in this scenario, one can have departures from the lepton-number-conserving Dirac scenario due to the new angles θ_{ij} (and phases ϕ_{ij}). As mentioned above, there is a large number of such parameters. However, it can be shown that with 3 pairs of neutrinos with the same mass, oscillations will only depend on a

total of 13 combinations of angles and phases. Additionally, if we focus just on electron and muon neutrinos, this number is further reduced to 7, corresponding to 6 angles and 1 phase. In the text we called these parameter combinations $X_{1\ldots7}$ and stressed that they can not be identified with θ_{12}, θ_{13}, θ_{23} nor δ, as these quantities by themselves are not physical. Instead, the 7 X_i correspond to combinations of these and additional θ_{ij} angles and ϕ_{ij} phases. We made a 7-dimensional scan of these X_i parameters in the absence of mass splittings. Their exact definitions, as well as the limits imposed on them by current data can be found there. Crucially, for Dirac neutrinos there are only 4 parameters. Hence the Dirac limit corresponds to 3 relations among the 7 X_i. By testing these relations, we find that $\min(\chi^2_{\text{Dirac}}) - \min(\chi^2) = 1.9$, i.e. current data is compatible with the Dirac scenario. Progress on tests for quasi-Diracness can be made in the future with a more precise measurement of $P(\nu_e \to \nu_\mu)$ and $P(\nu_\mu \to \nu_\mu)$. Thus, more statistics taken in T2K, MINOS+ or NOνA and, in particular, the future precise measurements possible at DUNE should provide more sensitive probes for this particular setup of quasi-Dirac neutrinos without new mass scales.

In the fifth Chapter, we have discussed the systematic deconstruction of the $d = 9$, $d = 11$ and $d = 13$ neutrino mass operators at tree-level. We have found all genuine neutrino mass tree-level diagrams for these operators. Very few genuine models can be constructed, despite the fact that the number of possible topologies increases rapidly with the dimension of the operator. With renormalizable vertices, one can build 18 topologies and 66 diagrams at $d = 9$ level; these numbers increase to 92 topologies and 504 diagrams at the $d = 11$ level, and finally at $d = 13$ one finds 576 topologies and 4199 diagrams. From all of these, we find only 10 genuine models: 2 models at $d = 9$ and $d = 11$ each, and 6 models at $d = 13$. We have discussed how our definition of a genuine mass model requires that all these high-dimensional models use large $SU(2)_L$ representations. For example, both of the two $d = 9$ models require quadruplets and quintuplets. On the other hand, for some $d = 13$ models scalar septets are needed. These high-dimensional models require not only larger representations but also more of them: Three new particles are sufficient for one of the two $d = 9$ models, while for $d = 11$ ($d = 13$) already four (five) exotic fields are needed. Thus, models become necessarily more baroque with larger dimensions. This fact,

together with the rather low new physics scale required by the high dimensionality of the operators, makes these models testable at accelerator experiments and also in searches for lepton flavour violation.

Appendix A

1 Neutrino-antineutrino oscillations

In this appendix we give the correct mathematical description of neutrino-antineutrino oscillations. We show in detail the calculation done to get the result obtained in Chapter 3. We start by defining the Dirac and the Majorana fields both for massless and for massive particles. We calculate, in one generation, the transition probability both for a left-handed neutrino to a left-handed neutrino and for a left-handed neutrino to a right-handed neutrino. Then, we consider an example with two neutrino states and we calculate the neutrino-neutrino and neutrino-antineutrino transitions. We will see that the last one only is possible for Majorana neutrinos. If the mass difference is different from 0, the two states are Majorana states. If the mass difference is equal to 0, the two states form a Dirac pair and the transition can not happen. In the final section we do the same for the inverse see-saw obtaining the same result as in the previous example. All the basic definitions and the notation for spinors are taken from [168].

1.1 Description of massless neutrinos

If only the left-handed field ν_L participates in the weak interaction, it cannot be distinguished experimentally whether the Majorana or the Dirac description is correct. For this it would be necessary to check whether the terms which occur in the non-interacting component $\hat{\nu}_R$ are independent of those in $\hat{\nu}_L$ (Dirac), or whether they are associated to each other by charge conjugation (Majorana). This requires a helicity flip that occurs only for massive particles. Nevertheless we start to give all the definitions

for massless particles to arrive, step by step, at the complete formalism for massive particles.

In the case of massless fermions only two of the four basis Dirac spinors, which occur for massive fermions, are linearly independent. For example we may choose the eigenspinors $u^0_\pm$ (the apex "0" is related to the particles without mass) of the helicity operator $\mathcal{H} = \vec{\sigma} \cdot \vec{p}/|\vec{p}|$ as a basis:

$$u^0_+ = iv^0_- = \sqrt{E} \begin{pmatrix} \chi_+ \\ \chi_+ \end{pmatrix}, \tag{1}$$

$$u^0_- = iv^0_+ = \sqrt{E} \begin{pmatrix} \chi_- \\ -\chi_- \end{pmatrix}, \tag{2}$$

where χ_+, χ_- are eigenstates of the helicity operator

$$\mathcal{H}\chi_+ = \chi_+, \tag{3}$$

$$\mathcal{H}\chi_- = -\chi_-. \tag{4}$$

The explicit form of $\chi_\pm$ dependes on the momentum $\vec{p}$, but it is not important in our discussion here. The spinors $u^0_\pm$ have a defined chirality. If we define the left- and right-handed projections of a spinor u by

$$u_L = \frac{1}{2}(1 - \gamma_5)u, \tag{5}$$

$$u_R = \frac{1}{2}(1 + \gamma_5)u, \tag{6}$$

then we have

$$u^0_L = \frac{1}{2}(1 - \gamma_5)u^0_-, \tag{7}$$

$$u^0_R = \frac{1}{2}(1 + \gamma_5)u^0_+. \tag{8}$$

In the case of the spinors v of the antiparticles:

$$v^0_L = \frac{1}{2}(1 + \gamma_5)v^0_- \tag{9}$$

$$v^0_R = \frac{1}{2}(1 - \gamma_5)u^0_+ \tag{10}$$

Consequently chirality and helicity are identical for massless fermions. Note that the left-handed particle spinor u_L is projected out by the operator $(1-\gamma_5)/2$ and the left-handed antiparticle spinor v_L is projected out by the operator $(1+\gamma_5)/2$:

$$u_L^0 = u_-^0 = iv_+^0 = iv_R^0 \quad (11)$$
$$u_R^0 = u_+^0 = iv_-^0 = iv_L^0 \quad (12)$$

Thus the spinor u_L^0 describes both a left-handed particle and a right-handed antiparticle.

A Dirac field for a massless neutrino $\nu^D(x)$ has the form

$$\nu^D(x) = \frac{1}{\sqrt{V}} \int \frac{d^3p}{\sqrt{2E}} (b_{\nu_L} u_L^0 e^{-ipx} + d_{\bar{\nu}_R}^\dagger v_R^0 e^{ipx} + b_{\nu_R} u_R^0 e^{-ipx} + d_{\bar{\nu}_L}^\dagger v_L^0 e^{ipx}). \quad (13)$$

The operator $b_{\nu_L}(b_{\nu_R})$ annihilates a left-handed (right-handed) neutrino, whilst $d_{\bar{\nu}_R}^\dagger(d_{\bar{\nu}_L}^\dagger)$ creates a right-handed (left-handed) antineutrino. For clarity we introduce the quantities

$$\hat{\nu}_L^D(p,x) = (b_{\nu_L} u_L^0 e^{-ipx} + d_{\bar{\nu}_R}^\dagger v_R^0 e^{ipx}), \quad (14)$$
$$\hat{\nu}_R^D(p,x) = (b_{\nu_R} u_R^0 e^{-ipx} + d_{\bar{\nu}_L}^\dagger v_L^0 e^{ipx}). \quad (15)$$

With these operators the field $\nu^D(p,x)$ is given by

$$\nu^D(x) = \frac{1}{\sqrt{V}} \int \frac{d^3p}{\sqrt{2E}} (\hat{\nu}_L^D(p,x) + \hat{\nu}_R^D(p,x)). \quad (16)$$

Note that the operator $\hat{\nu}_L^D(p,x)$ describes "known" particles: the left-handed neutrino and the right-handed antineutrino. The $\hat{\nu}_R^D(p,x)$ describes "hypothetical" particles: the right-handed neutrino and the left-handed antineutrino.

Now we assume that the neutrino and the antineutrino are identical in a way defined below. We find:

$$\hat{\nu}_L^M(p,x) = (c_{\nu_L} u_L^0 e^{-ipx} + c_{\bar{\nu}_R}^\dagger v_R^0 e^{ipx}) \quad (17)$$
$$\hat{\nu}_R^M(p,x) = (c_{\nu_R} u_R^0 e^{-ipx} + c_{\bar{\nu}_L}^\dagger v_L^0 e^{ipx}). \quad (18)$$

Here the operator $\hat{\nu}_R^M(p,x)$ contains no new degrees of freedom, but the particle operators which it involves are the hermitian conjugates of those of $\hat{\nu}_L^M(p,x)$. The neutrino field defined in this way contains only two degrees of freedom: $c_{\nu_L}u_L^0$ and $c_{\nu_R}u_R^0$ and one can do the follow identification:

$$c_{\nu_L} = \frac{b_{\nu_L} + d_{\bar{\nu}_L}}{\sqrt{2}} \tag{19}$$

$$c_{\nu_R} = \frac{b_{\nu_R} + d_{\bar{\nu}_R}}{\sqrt{2}}. \tag{20}$$

In this description the neutrino field is given by

$$\nu^M(x) = \frac{1}{\sqrt{V}} \int \frac{d^3p}{\sqrt{2E}} (\hat{\nu}_L^M(p,x) + \hat{\nu}_R^M(p,x)). \tag{21}$$

Such a neutrino is called a Majorana neutrino. The Majorana field has the following important charge conjugation property:

$$(\nu^M)^C = \eta_C \nu^M, \tag{22}$$

where $\eta_C = 1$. Thus the Majorana field is the charge conjugate to itself, which expresses the indistinguishability of particles and antiparticles, and it can be written as $\nu^M = \nu_L + \nu_R^C$. The behaviour of the spinors u and v under charge conjugation is interesting:

$$u(p,s) \rightarrow u^C(p,s) = i\gamma^2\gamma^0\bar{u}^T(p,s) = v(p,s) \tag{23}$$

$$v(p,s) \rightarrow v^C(p,s) = i\gamma^2\gamma^0\bar{v}^T(p,s) = u(p,s). \tag{24}$$

1.2 Massive neutrinos

Our considerations for Dirac and Majorana neutrinos in the last paragraph refer to the case of massless neutrinos. Now we discuss the modifications necessary to include the possibility of massive neutrinos. Let's

consider the spinors for massive fermions

$$u_\pm(p) = \sqrt{E+m}\begin{pmatrix} \chi_\pm \\ \frac{\vec{\sigma}\vec{p}}{E+m}\chi_\pm \end{pmatrix} = \sqrt{E+m}\begin{pmatrix} \chi_\pm \\ \frac{|\vec{p}|}{E+m}\chi_\pm \end{pmatrix} \quad (25)$$

$$v_\pm(p) = -i\sqrt{E+m}\begin{pmatrix} \frac{|\vec{\sigma}\vec{p}|}{E+m}\chi_\mp \\ \chi_\mp \end{pmatrix} \quad (26)$$

We may define the left-handed component of a spinor also for massive fermions by the projection operator $(1-\gamma_5)/2$:

$$\begin{aligned} u_L(p) &= \frac{1}{2}(1-\gamma_5)u(p) \\ &= \frac{1}{2}(1-\gamma_5)\sqrt{E+m}\begin{pmatrix} \chi_s \\ \frac{\vec{\sigma}\vec{p}}{E+m}\chi_s \end{pmatrix} \\ &= \frac{1}{2}\sqrt{E+m}\begin{pmatrix} \chi_s - \frac{\vec{\sigma}\vec{p}}{E+m}\chi_s \\ \frac{\vec{\sigma}\vec{p}}{E+m}\chi_s - \chi_s \end{pmatrix} \\ &\neq u_-(p). \end{aligned} \quad (27)$$

But here, $u_L(p,s)$ is not a solution of the Dirac equation, and the two-spinor $\chi_s - \vec{\sigma}\vec{p}/(E+m)\chi_s$ which occur in u_L is not an eigenstate of the operator $\mathcal{H}$. Thus the chirality defined by the operators $(1\pm\gamma_5)/2$ is a quantum number conserved only for massless particles. The eigenspinors $u_\pm$ for massive fermions may be decomposed, as shown below for u_-, into components of defined handedness:

$$\begin{aligned} u_-(p) &= P_L u_-(p) + P_R u_-(p) \\ &= \frac{1}{2}\sqrt{E+m}\left\{\begin{pmatrix} I & -I \\ -I & I \end{pmatrix}\begin{pmatrix} \chi_- \\ \frac{|\vec{p}|}{E+m}\chi_- \end{pmatrix} + \begin{pmatrix} I & I \\ I & I \end{pmatrix}\begin{pmatrix} \chi_- \\ \frac{|\vec{p}|}{E+m}\chi_- \end{pmatrix}\right\} \\ &= \frac{1}{2}\sqrt{E+m}\left\{\begin{pmatrix} \chi_- + \frac{|\vec{p}|}{E+m}\chi_- \\ -\chi_- - \frac{|\vec{p}|}{E+m}\chi_- \end{pmatrix} + \begin{pmatrix} \chi_- - \frac{|\vec{p}|}{E+m}\chi_- \\ \chi_- - \frac{|\vec{p}|}{E+m}\chi_- \end{pmatrix}\right\} \\ &= \frac{1}{2}\sqrt{E+m}\left(1+\frac{|\vec{p}|}{E+m}\right)\begin{pmatrix} \chi_- \\ -\chi_- \end{pmatrix} + \left(1-\frac{|\vec{p}|}{E+m}\right)\begin{pmatrix} \chi_- \\ \chi_- \end{pmatrix}. \end{aligned} \quad (28)$$

Then from the relation $\chi_-(\vec{p}) = \chi_+(-\vec{p})$ we have:

$$\begin{aligned} u_-(p) &= \frac{1}{2}\left\{\left(1+\frac{|\vec{p}|}{E+m}\right)u_-^0(\vec{p}) + \left(1-\frac{|\vec{p}|}{E+m}\right)u_+^0(-\vec{p})\right\} \\ &= \alpha u_L^0(\vec{p}) + \beta u_R^0(-\vec{p}), \end{aligned} \tag{29}$$

and by doing the same for the spinor $u_+(p)$, they can be written in a more compact way

$$u_-(p) = \alpha u_L^0(\vec{p}) + \beta u_R^0(-\vec{p}) \tag{30}$$

$$u_+(p) = \alpha u_R^0(\vec{p}) + \beta u_L^0(-\vec{p}). \tag{31}$$

where

$$\alpha = \frac{1}{2}\left(1+\frac{|\vec{p}|}{E+m}\right) \tag{32}$$

$$\beta = \frac{1}{2}\left(1-\frac{|\vec{p}|}{E+m}\right) \tag{33}$$

for $m << E$. Another interesting limit is $\vec{p} \to 0$, to analyze the on-shell particle decay. In this limit

$$\begin{aligned} u_-(p) &= P_L u_-(p) + P_R u_-(p) \\ &= \frac{1}{2}\sqrt{2E}\left\{\begin{pmatrix} I & -I \\ -I & I \end{pmatrix}\begin{pmatrix} \chi_- \\ 0 \end{pmatrix} + \begin{pmatrix} I & I \\ I & I \end{pmatrix}\begin{pmatrix} \chi_- \\ 0 \end{pmatrix}\right\} \\ &= \frac{1}{2}\sqrt{2E}\begin{pmatrix} \chi_- \\ -\chi_- \end{pmatrix} + \begin{pmatrix} \chi_- \\ \chi_- \end{pmatrix} \\ &= \frac{1}{\sqrt{2}}\left(u_L^0(\vec{p}) + u_R^0(-\vec{p})\right). \end{aligned} \tag{34}$$

Let's concentrate on the Majorana case. We have all the elements to write the Majorana neutrino field with mass by modifying the equations (17) and (18) by adding the "false" chirality component that appears in the equations

(30) and (31) (the superscript "0" is omitted):

$$\begin{aligned}
\hat{\nu}_L^M(p,x) &= (\alpha c_{\nu_L} u_L(\vec{p}) e^{i\vec{p}\vec{x}} + \beta c_{\nu_R} u_R(\vec{p}) e^{-i\vec{p}\vec{x}}) e^{-iEt} + \\
&+ (\alpha c^\dagger_{\nu_R} v_R(\vec{p}) e^{-i\vec{p}\vec{x}} + \beta c^\dagger_{\nu_L} v_L(\vec{p}) e^{i\vec{p}\vec{x}}) e^{iEt} \qquad (35) \\
\hat{\nu}_R^M(p,x) &= (\alpha c_{\nu_R} u_R(\vec{p}) e^{i\vec{p}\vec{x}} + \beta c_{\nu_L} u_L(\vec{p}) e^{-i\vec{p}\vec{x}}) e^{-iEt} + \\
&+ (\alpha c^\dagger_{\nu_L} v_L(\vec{p}) e^{-i\vec{p}\vec{x}} + \beta c^\dagger_{\nu_R} v_R(\vec{p}) e^{i\vec{p}\vec{x}}) e^{iEt}. \qquad (36)
\end{aligned}$$

It follows that $\nu_L^M(\nu_R^M)$ can create and destroy one and the same eigenstate.

1.3 $\nu_L - \nu_R$ transition

In this section we want to take into account the transition of a left-handed neutrino into itself and into a right-handed neutrino by showing that thanks to the "false" chirality the last one is different from 0. Let's start from the construction of Majorana neutrino states:

$$\begin{aligned}
|\nu_L(0)> &= (\alpha c^\dagger_{\nu_L} u^\dagger_L(\vec{p}) + \beta c^\dagger_{\nu_R} u^\dagger_R(-\vec{p}))|0> \qquad (37) \\
|\nu_L(x)> &= (\alpha c^\dagger_{\nu_L} u^\dagger_L(\vec{p}) e^{-i\vec{p}\vec{x}} + \beta c^\dagger_{\nu_R} u^\dagger_R(\vec{p}) e^{i\vec{p}\vec{x}}) e^{iEt}|0> \qquad (38) \\
|\nu_R(x)> &= (\alpha c^\dagger_{\nu_R} u^\dagger_R(\vec{p}) e^{-i\vec{p}\vec{x}} + \beta c^\dagger_{\nu_L} u^\dagger_L(\vec{p}) e^{i\vec{p}\vec{x}}) e^{iEt}|0> . \qquad (39)
\end{aligned}$$

the $\nu_L - \nu_L$ transition will be

$$\begin{aligned}
< \nu_L(x)|\nu_L(0) > &= < 0|(\alpha c_{\nu_L} u_L(\vec{p}) e^{i\vec{p}\vec{x}} + \beta c_{\nu_R} u_R(\vec{p}) e^{-i\vec{p}\vec{x}}) e^{-iEt} \cdot \\
&\cdot (\alpha c^\dagger_{\nu_L} u^\dagger_L(\vec{q}) + \beta c^\dagger_{\nu_R} u^\dagger_R(-\vec{q}))|0 >= \\
&= \alpha^2 \delta^{(3)}(\vec{p} - \vec{q}) u_L(\vec{p}) u^\dagger_L(\vec{q}) e^{-iEt} e^{+i\vec{p}\vec{x}} \\
&+ \beta^2 \delta^{(3)}(\vec{p} + \vec{q}) u_R(\vec{p}) u^\dagger_R(-\vec{q}) e^{-iEt} e^{-i\vec{p}\vec{x}}) = \\
&= \alpha^2 e^{-iEt} e^{i\vec{q}\vec{x}} + \beta^2 e^{-iEt} e^{i\vec{q}\vec{x}}, \qquad (40) \\
| < \nu_L(x)|\nu_L(0) > |^2 &= (\alpha^2 + \beta^2)^2. \qquad (41)
\end{aligned}$$

The $\nu_L - \nu_R$ transition will be

$$| < \nu_R(x)|\nu_L(0) > |^2 = 4(\alpha\beta)^2. \qquad (42)$$

For a Majorana neutrino $\bar{\nu}_L = [(\nu_L)^c]^T C = [(\nu^c)_R]^T C \equiv \nu_R$ due to the Majorana condition $\nu^c \equiv \nu$ and, in the same way, $\bar{\nu}_R = \nu_L$, then obviously

$$| < \bar{\nu}_L(x)|\nu_L(0) > |^2 = | < \nu_R(x)|\nu_L(0) > |^2, \quad (43)$$
$$| < \bar{\nu}_R(x)|\nu_L(0) > |^2 = | < \nu_L(x)|\nu_L(0) > |^2. \quad (44)$$

In order to get the sum of the two probabilities equal to 1 we have to normalize them (we are considering the Majorana case)

$$(\alpha^2 + \beta^2) \rightarrow (\alpha'^2 + \beta'^2) = \frac{(\alpha^2 + \beta^2)}{\sqrt{(\alpha^2 + \beta^2)^2 + (2\alpha\beta)^2}} \quad (45)$$
$$(2\alpha\beta) \rightarrow (2\alpha'\beta') = \frac{(2\alpha\beta)}{\sqrt{(\alpha^2 + \beta^2)^2 + (2\alpha\beta)^2}}. \quad (46)$$

By considering the definition of α and β, if we take the limit $m << E$ through a series expansion in m/E we get

$$| < \nu_L(x)|\nu_L(0) > |^2 = (\alpha'^2 + \beta'^2)^2 \sim 1 - \frac{m^2}{E^2} + \mathcal{O}\left[\frac{m^2}{E^2}\right]^3 \quad (47)$$
$$| < \nu_R(x)|\nu_L(0) > |^2 = (2\alpha'\beta')^2 \sim \frac{m^2}{E^2} + \mathcal{O}\left[\frac{m^2}{E^2}\right]^3, \quad (48)$$

and in the limit of $\vec{p} \rightarrow 0$

$$| < \bar{\nu}_R(x)|\nu_L(0) > |^2 = | < \nu_L(x)|\nu_L > |^2 = (\alpha'^2 + \beta'^2)^2 \rightarrow \frac{1}{2} \quad (49)$$
$$| < \bar{\nu}_L(x)|\nu_L(0) > |^2 = | < \nu_R(x)|\nu_L(0) > |^2 = (2\alpha'\beta')^2 \rightarrow \frac{1}{2}. \quad (50)$$

Let's focus now on Dirac neutrino states. The two Dirac operators (14), (15) are corrected from the "false" chirality in this way

$$\begin{aligned} \hat{\nu}_L^D(p,x) &= \alpha b_{\nu_L} u_L e^{i\vec{p}\vec{x}} e^{-iEt} + \beta b_{\nu_R} u_R e^{-i\vec{p}\vec{x}} e^{-iEt} \\ &+ \alpha d^\dagger_{\bar{\nu}_R} v_R e^{-i\vec{p}\vec{x}} e^{iEt} + \beta d^\dagger_{\bar{\nu}_L} v_L e^{i\vec{p}\vec{x}} e^{iEt}, \quad (51) \\ \hat{\nu}_R^D(p,x) &= \alpha b_{\nu_R} u_R e^{i\vec{p}\vec{x}} e^{-iEt} + \beta b_{\nu_L} u_L e^{-i\vec{p}\vec{x}} e^{-iEt} \\ &+ \alpha d^\dagger_{\bar{\nu}_L} v_L e^{-i\vec{p}\vec{x}} e^{iEt} + \beta d^\dagger_{\bar{\nu}_R} v_R e^{i\vec{p}\vec{x}} e^{iEt} \quad (52) \end{aligned}$$

and we are able to construct left and right neutrino states:

$$|\nu_L^D(x)> = \left(\alpha b^\dagger_{\nu_L} u^\dagger_L e^{-i\vec{p}\vec{x}} e^{iEt} + \beta b^\dagger_{\nu_R} u^\dagger_R e^{i\vec{p}\vec{x}} e^{iEt}\right)|0>, \quad (53)$$

$$|\nu_R^D(x)> = \left(\alpha b^\dagger_{\nu_R} u^\dagger_R e^{-i\vec{p}\vec{x}} e^{iEt} + \beta b^\dagger_{\nu_L} u^\dagger_L e^{i\vec{p}\vec{x}} e^{iEt}\right)|0>, \quad (54)$$

so that

$$|<\nu_L(x)|\nu_L(0)>|^2 = (\alpha^2+\beta^2)^2, \quad (55)$$

$$|<\nu_L(x)|\nu_R(0)>|^2 = 4(\alpha\beta)^2. \quad (56)$$

Again we can normalize like in the Majorana case and we get exactly the same result. There exist a $\nu_L - \nu_R$ transition different from 0 for a Dirac massive neutrino too. The difference from the Majorana case is that for a Dirac neutrino $\bar{\nu}_L \neq \nu_R$ and in particular

$$<\bar{\nu}_L(x)|\nu_L(0)>=<\bar{\nu}_R(x)|\nu_L(0)>=<\bar{\nu}_R(x)|\nu_R(0)>=<\bar{\nu}_L(x)|\nu_R(0)>=0, \quad (57)$$

because of the relations between the operators b_ν and $d_{\bar{\nu}}$

$$\left\{b_r(\vec{p}), d_s^\dagger(\vec{q})\right\} = \left\{d_r(\vec{p}), b_s^\dagger(\vec{q})\right\} = 0. \quad (58)$$

1.4 Neutrino-antineutrino transition in the see-saw

In this section we present an example with two massive neutrinos and we only deal with Majorana neutrinos. In particular, we are interested to study the behavior of heavy neutrinos that propagate and decay into massive particles. We will start by writing the neutrinos states and then we will calculate all the possible transitions. At first, we will consider the most simple case of neutrinos at rest, namely, $\vec{p}=0$; then we will deal with the more realistic case with $\vec{p}\neq 0$. We define for the following expressions $\nu_R^c \equiv (\nu^c)_R$ and $\nu_L^c \equiv (\nu^c)_L$. Let's consider the following Lagrangian density:

$$-\mathcal{L}_m = \frac{1}{2}(\bar{\nu}_L \bar{\nu}_L^c) \begin{pmatrix} m_1^M & m^D \\ m^D & m_2^M \end{pmatrix} \begin{pmatrix} \nu_R^c \\ \nu_R \end{pmatrix} + h.c. \quad (59)$$

By using a unitary transformation U which diagonalizes the mass matrix we can write:

$$-\mathcal{L}_m = \frac{1}{2}(\bar{\nu}_L \bar{\nu}_L^c) U^{-1} U \begin{pmatrix} m_1^M & m^D \\ m^D & m_2^M \end{pmatrix} U^{-1} U \begin{pmatrix} \nu_R^c \\ \nu_R \end{pmatrix} + h.c. \quad (60)$$

with

$$U = \begin{pmatrix} \cos\theta & \sin\theta \\ -\sin\theta & \cos\theta \end{pmatrix}. \quad (61)$$

The fields written in terms of the eigenstates are

$$\begin{aligned} |\nu_L^c> &= \cos\theta|\nu_{1L}> - \sin\theta|\nu_{2L}> & (62)\\ |\nu_L> &= \sin\theta|\nu_{1L}> + \cos\theta|\nu_{2L}> & (63)\\ |\nu_R^c> &= \cos\theta|\nu_{1R}> - \sin\theta|\nu_{2R}> & (64)\\ |\nu_R> &= \sin\theta|\nu_{1R}> + \cos\theta|\nu_{2R}> . & (65) \end{aligned}$$

Now we should be able to calculate the neutrino-neutrino and the neutrino-antineutrino transitions. Following the same procedure as in one generation case, one finds

$$\begin{aligned} |\nu_L(x)> &= \cos\theta(\alpha_1 c^\dagger_{\nu_{1L}} u^\dagger_{1L}(\vec{p}_1) e^{-i\vec{p}_1\vec{x}} + \beta_1 c^\dagger_{\nu_{1R}} u^\dagger_{1R}(-\vec{p}_1) e^{i\vec{p}_1\vec{x}}) e^{iE_1 t}|0> \\ &- \sin\theta(\alpha_2 c^\dagger_{\nu_{2L}} u^\dagger_{2L}(\vec{p}_2) e^{-i\vec{p}_2\vec{x}} + \beta_2 c^\dagger_{\nu_{2R}} u^\dagger_{2R}(-\vec{p}_2) e^{i\vec{p}_2\vec{x}}) e^{iE_2 t}|0>, \\ |\nu_L^c(x)> &= \sin\theta(\alpha_1 c^\dagger_{\nu_{1L}} u^\dagger_{1L}(\vec{p}_1) e^{-i\vec{p}_1\vec{x}} + \beta_1 c^\dagger_{\nu_{1R}} u^\dagger_{1R}(-\vec{p}_1) e^{i\vec{p}_1\vec{x}}) e^{iE_1 t}|0> \\ &+ \cos\theta(\alpha_2 c^\dagger_{\nu_{2L}} u^\dagger_{2L}(\vec{p}_2) e^{-i\vec{p}_2\vec{x}} + \beta_2 c^\dagger_{\nu_{2R}} u^\dagger_{2R}(-\vec{p}_2) e^{i\vec{p}_2\vec{x}}) e^{iE_2 t}|0>, \\ |\nu_R(x)> &= \sin\theta(\alpha_1 c^\dagger_{\nu_{1R}} u^\dagger_{1R}(\vec{p}_1) e^{-i\vec{p}_1\vec{x}} + \beta_1 c^\dagger_{\nu_{1L}} u^\dagger_{1L}(-\vec{p}_1) e^{i\vec{p}_1\vec{x}}) e^{iE_1 t}|0> \\ &+ \cos\theta(\alpha_2 c^\dagger_{\nu_{2R}} u^\dagger_{2R}(\vec{p}_2) e^{-i\vec{p}_2\vec{x}} + \beta_2 c^\dagger_{\nu_{2L}} u^\dagger_{2L}(-\vec{p}_2) e^{i\vec{p}_2\vec{x}}) e^{iE_2 t}|0>, \\ |\nu_R^c(x)> &= \cos\theta(\alpha_1 c^\dagger_{\nu_{1R}} u^\dagger_{1R}(\vec{p}_1) e^{-i\vec{p}_1\vec{x}} + \beta_1 c^\dagger_{\nu_{1L}} u^\dagger_{1L}(-\vec{p}_1) e^{i\vec{p}_1\vec{x}}) e^{iE_1 t}|0> \\ &- \sin\theta(\alpha_2 c^\dagger_{\nu_{2R}} u^\dagger_{2R}(\vec{p}_2) e^{-i\vec{p}_2\vec{x}} + \beta_2 c^\dagger_{\nu_{2L}} u^\dagger_{2L}(-\vec{p}_2) e^{i\vec{p}_2\vec{x}}) e^{iE_2 t}|0> \quad (66) \end{aligned}$$

and

$$\begin{aligned} <\nu_L(x)|\nu_L(0)> &= \cos^2\theta(\alpha_1^2+\beta_1^2)e^{-ip_1 x} + \sin^2\theta(\alpha_2^2+\beta_2^2)e^{-ip_2 x}, & (67)\\ <\nu_L^c(x)|\nu_L(0)> &= \cos\theta\sin\theta((\alpha_1^2+\beta_1^2)e^{-ip_1 x} - (\alpha_2^2+\beta_2^2)e^{-ip_2 x}). & (68) \end{aligned}$$

In the limit $\vec{p}_1 = \vec{p}_2 = 0$, we already know $\alpha_1 = \beta_1 = \alpha_2 = \beta_2 = 1/\sqrt{2}$, eq. (34):

$$
\begin{aligned}
|<\nu_L(x)|\nu_L(0)>|^2 &= \cos^4\theta + \sin^4\theta + 2\cos^2\theta\sin^2\theta\cos(\Delta m t), \quad (69)\\
|<\nu_L^c(x)|\nu_L(0)>|^2 &= 2\cos^2\theta\sin^2\theta(1-\cos(\Delta m t)). \quad (70)
\end{aligned}
$$

We can follow the same reasoning for the other two possible transitions:

$$
\begin{aligned}
<\nu_R^c(x)|\nu_L(0)> &= 2\alpha_1\beta_1(\cos^2\theta e^{-ip_1 x} + \sin^2\theta e^{-ip_2 x}), \quad (71)\\
|<\nu_R^c(x)|\nu_L(0)>|^2 &= |<\nu_L(x)|\nu_L(0)>|^2, \quad (72)\\
<\nu_L^c(x)|\nu_L(0)> &= 2\alpha_1\beta_1\cos\theta\sin\theta(e^{-ip_1 x} - e^{-ip_2 x}), \quad (73)\\
|<\nu_L^c(x)|\nu_L(0)>|^2 &= |<\nu_L^c(x)|\nu_L(0)>|^2. \quad (74)
\end{aligned}
$$

By normalizing the four probabilities we get

$$
\begin{aligned}
|<\nu_R^c(x)|\nu_L(0)>|^2 &= |<\nu_L(x)|\nu_L(0)>|^2 = \\
&= \frac{1}{2}\left(\cos^4\theta + \sin^4\theta + 2\cos^2\theta\sin^2\theta\cos(\Delta m t)\right), \quad (75)\\
|<\nu_R(x)|\nu_L(0)>|^2 &= |<\nu_L^c(x)|\nu_L(0)>|^2 = \\
&= \cos^2\theta\sin^2\theta(1-\cos(\Delta m t)). \quad (76)
\end{aligned}
$$

Note the difference from the one generation case: now we have to take into account four probabilities because although $|<\nu_R^c(x)|\nu_L(0)>|^2 = |<\nu_L(x)|\nu_L(0)>|^2$ and $|<\nu_R(x)|\nu_L(0)>|^2 = |<\nu_L^c(x)|\nu_L(0)>|^2$ the neutrinos states are different from each other. If $\Delta m \to 0$

$$
|<\nu_L^c(x)|\nu_L(0)>|^2 = |<\nu_R(x)|\nu_L(0)>|^2 = 0. \quad (77)
$$

$\Delta m = 0$ means that the two states are degenerates and form a Dirac pair. There is no probability to find an antineutrino in the final state. Let's

explore the limit $\vec{p}_1 = \vec{p}_2 \equiv \vec{p} \neq 0$:

$$\alpha_1 = \frac{1}{2}\left(1 + \frac{|\vec{p}|}{E_1 + m_1}\right), \tag{78}$$

$$\beta_1 = \frac{1}{2}\left(1 - \frac{|\vec{p}|}{E_1 + m_1}\right), \tag{79}$$

$$\alpha_2 = \frac{1}{2}\left(1 + \frac{|\vec{p}|}{E_2 + m_2}\right), \tag{80}$$

$$\beta_2 = \frac{1}{2}\left(1 - \frac{|\vec{p}|}{E_2 + m_2}\right), \tag{81}$$

Let's concentrate on the terms $\alpha_1^2+\beta_1^2$ and $\alpha_2^2+\beta_2^2$; we know $E_1 = \sqrt{p^2 + m_1^2}$, $E_2 = \sqrt{p^2 + m_2^2}$. Let's define $m_1 = \bar{M} - \Delta m/2$ and $m_2 = \bar{M} + \Delta m/2$. By doing a power series expansion in $\vec{p}$ and stopping the series to the order $\mathcal{O}(p^2)$ we get

$$\alpha_1^2 + \beta_1^2 = \frac{1}{2}\left(1 + \frac{\vec{p}^2}{4(\bar{M} - \frac{\Delta m}{2})^2}\right), \tag{82}$$

$$\alpha_2^2 + \beta_2^2 = \frac{1}{2}\left(1 + \frac{\vec{p}^2}{4(\bar{M} + \frac{\Delta m}{2})^2}\right), \tag{83}$$

and by doing a series expansion in Δm and stopping the series at order $\mathcal{O}(\Delta m)$

$$\alpha_1^2 + \beta_1^2 = \frac{1}{2}\left(1 + \frac{\vec{p}^2}{4\bar{M}^2} + \frac{\vec{p}^2}{4\bar{M}^2}\frac{\Delta m}{\bar{M}}\right), \tag{84}$$

$$\alpha_2^2 + \beta_2^2 = \frac{1}{2}\left(1 + \frac{\vec{p}^2}{4\bar{M}^2} - \frac{\vec{p}^2}{4\bar{M}^2}\frac{\Delta m}{\bar{M}}\right). \tag{85}$$

So the probabilities for $\nu_L(x) - \nu_L(0)$ and $\nu_L^c(x) - \nu_L(0)$ are

$$\begin{aligned} |<\nu_L(x)|\nu_L(0)>|^2 &\sim \frac{1}{4}\left(1+\frac{p^2}{2\bar{M}^2}\right)\left(\cos^4\theta+\sin^4\theta+2\cos^2\theta\sin^2\theta\cos(\Delta m t)\right) \\ &+ \frac{\Delta m p^2}{8\bar{M}^3}\left(\cos^4\theta-\sin^4\theta\right) \qquad (86) \\ |<\nu_L^c(x)|\nu_L(0)>|^2 &\sim \frac{1}{2}\left(1+\frac{p^2}{2\bar{M}^2}\right)(\cos^2\theta\sin^2\theta(1-\cos(\Delta m t))). \qquad (87) \end{aligned}$$

We can follow the same reasoning for the other two possible transition:

$$\begin{aligned} <\nu_R^c(x)|\nu_L(0)> &= \cos^2\theta(2\alpha_1\beta_1)e^{-ip_1x}+\sin^2\theta(2\alpha_2\beta_2)e^{-ip_2x} \qquad (88) \\ <\nu_R(x)|\nu_L(0)> &= \cos\theta\sin\theta(2\alpha_1\beta_1)e^{-ip_1x}-(2\alpha_2\beta_2)e^{-ip_2x}. \qquad (89) \end{aligned}$$

Again, let us concentrate on the terms $2\alpha_1\beta_1$ and $2\alpha_2\beta_2$; through a power series expansion in $\vec{p}$ and stopping the series at order $\mathcal{O}(p^2)$ we get

$$\begin{aligned} 2\alpha_1\beta_1 &= \frac{1}{2}\left(1-\frac{\vec{p}^2}{4(\bar{M}-\frac{\Delta m}{2})^2}\right), \qquad (90) \\ 2\alpha_2\beta_2 &= \frac{1}{2}\left(1-\frac{\vec{p}^2}{4(\bar{M}+\frac{\Delta m}{2})^2}\right), \qquad (91) \end{aligned}$$

and by doing a series expansion in Δm and stopping the series at order $\mathcal{O}(\Delta m)$

$$\begin{aligned} 2\alpha_1\beta_1 &= \frac{1}{2}\left(1-\frac{\vec{p}^2}{4\bar{M}^2}-\frac{\vec{p}^2}{4\bar{M}^2}\frac{\Delta m}{\bar{M}}\right), \qquad (92) \\ 2\alpha_2\beta_2 &= \frac{1}{2}\left(1-\frac{\vec{p}^2}{4\bar{M}^2}+\frac{\vec{p}^2}{4\bar{M}^2}\frac{\Delta m}{\bar{M}}\right). \qquad (93) \end{aligned}$$

So the probabilities for $\nu_R^c(x) - \nu_L(0)$ and $\nu_R - \nu_L(0)$ are

$$
\begin{aligned}
|<\nu_R^c(x)|\nu_L(0)>|^2 &\sim \frac{1}{4}\left(1-\frac{p^2}{2\bar{M}^2}\right)\left(\cos^4\theta+\sin^4\theta+2\cos^2\theta\sin^2\theta\cos(\Delta m t)\right) \\
&- \frac{\Delta m p^2}{8\bar{M}^3}\left(\cos^4\theta-\sin^4\theta\right), \qquad (94)\\
|<\nu_R(x)|\nu_L(0)>|^2 &\sim \frac{1}{2}\left(1-\frac{p^2}{2\bar{M}^2}\right)(\cos^2\theta\sin^2\theta(1-\cos(\Delta m t))). \qquad (95)
\end{aligned}
$$

By normalizing the four probabilities we finally get

$$
\begin{aligned}
|<\nu_L(x)|\nu_L(0)>|^2 &\sim \frac{1}{2}\left(1+\frac{p^2}{2\bar{M}^2}\right)\left(\cos^4\theta+\sin^4\theta+2\cos^2\theta\sin^2\theta\cos(\Delta m t)\right) \\
&+ \frac{\Delta m p^2}{8\bar{M}^3}\left(\cos^4\theta-\sin^4\theta\right) \qquad (96)\\
|<\nu_L^c(x)|\nu_L(0)>|^2 &\sim \left(1+\frac{p^2}{2\bar{M}^2}\right)(\cos^2\theta\sin^2\theta(1-\cos(\Delta m t))) \qquad (97)\\
|<\nu_R^c(x)|\nu_L(0)>|^2 &\sim \frac{1}{2}\left(1-\frac{p^2}{2\bar{M}^2}\right)\left(\cos^4\theta+\sin^4\theta+2\cos^2\theta\sin^2\theta\cos(\Delta m t)\right) \\
&- \frac{\Delta m p^2}{8\bar{M}^3}\left(\cos^4\theta-\sin^4\theta\right) \qquad (98)\\
|<\nu_R(x)|\nu_L(0)>|^2 &\sim \left(1-\frac{p^2}{2\bar{M}^2}\right)(\cos^2\theta\sin^2\theta(1-\cos(\Delta m t))). \qquad (99)
\end{aligned}
$$

Note that if $\Delta m = 0$ again $|<\nu_L^c(x)|\nu_L(0)>|^2 = |<\nu_R(x)|\nu_L(0)>|^2 = 0$ and there is a term proportional to p^2 that increases the transition probability $|<\nu_L(x)|\nu_L(0)>|^2$ and decreases $|<\nu_R^c(x)|\nu_L(0)>|^2$. This express that the more relativistic the neutrino, the smaller the probability to find the neutrino with wrong helicity.

1.5 Neutrino-antineutrino oscillation in the Inverse See-Saw

We write the inverse see-saw matrix for one generation, in the interaction basis $N' = \{\nu_L, N_R, S\}$ as:

$$M = \begin{pmatrix} 0 & m_D & 0 \\ m_D & 0 & M_R \\ 0 & M_R & \mu \end{pmatrix}$$

In the gauge field basis, ν_L is the standard (mainly light eigenstate) L-handed neutrino, N_R is the neutral member of the $SU(2)_R$ doublet, and S is a gauge singlet fermion equipped with a Majorana mass term μ. In the following we are interested only in the heavy sector. For $M_R \sim TeV$ we get one light eigenvalue $m_\nu \sim 1eV$ for $\epsilon \sim 10{-}3$ [i.e. $m_D \sim GeV$] and $\eta \sim 10^{-6}$ [i.e. $\mu \sim MeV$]. The mass matrix M is symmetric and thus can be factorized as:

$$\mathcal{M} = V^\dagger M V^* \tag{100}$$
$$V = W\phi \tag{101}$$
$$\phi = diag(1, i, 1) \tag{102}$$

with $\mathcal{M}$ diagonal with real and positive eigenvalues, W unitary, and ϕ a matrix of phases such that (in the present 3×3 case) V has real entries and is thus an orthogonal matrix. Since $\epsilon, \eta << 1$ the diagonalization can be performed perturbatively, and yields the eigenvalues:

$$M \approx M_R diag\left(0, 1 - \frac{1}{2}\eta, 1 + \frac{1}{2}\eta\right) \tag{103}$$

in which we have carried out an expansion up $\mathcal{O}(\eta\epsilon^2)$ and after that we have set $\epsilon^2 \to 0$. Note that at this order the mass splitting between the two heavy eigenvalues is $\Delta M = M_2 - M_1 \sim M_R\eta$ as expected. The matrix V reads

$$W = \begin{pmatrix} 1 & \frac{\epsilon}{\sqrt{2}} & \frac{\epsilon}{\sqrt{2}} \\ 0 & -\frac{1}{\sqrt{2}}\left(1 + \frac{\eta}{4}\right) & \frac{1}{\sqrt{2}}\left(1 - \frac{\eta}{4}\right) \\ -\epsilon & \frac{1}{\sqrt{2}}\left(1 - \frac{\eta}{4}\right) & \frac{1}{\sqrt{2}}\left(1 + \frac{\eta}{4}\right) \end{pmatrix}$$

again with $\epsilon^2 \to 0$. So

$$V = \begin{pmatrix} 1 & \frac{i\epsilon}{\sqrt{2}} & \frac{\epsilon}{\sqrt{2}} \\ 0 & -\frac{i}{\sqrt{2}}\left(1+\frac{\eta}{4}\right) & \frac{1}{\sqrt{2}}\left(1-\frac{\eta}{4}\right) \\ -\epsilon & \frac{i}{\sqrt{2}}\left(1-\frac{\eta}{4}\right) & \frac{1}{\sqrt{2}}\left(1+\frac{\eta}{4}\right) \end{pmatrix}$$

Let us define the mass eigenstates basis as $N = \{N_0, N_1, N_2\}$, then $N_R = V_{i\alpha} N_i$:

$$|N_R(0)> = \frac{1}{\sqrt{2}}\left[-i(1+\frac{\eta}{4})|N_1(0)> +(1-\frac{\eta}{4})|N_2(0)>\right], \quad (104)$$

$$|S(0)> = \frac{1}{\sqrt{2}}\left[i(1-\frac{\eta}{4})|N_1(0)> +(1+\frac{\eta}{4})|N_2(0)>\right]. \quad (105)$$

Let us consider the limit of $\vec{p}_1 = \vec{p}_2 = \vec{p} \to 0$ and let's write the time evolution equation for the two states:

$$|N_R(t)> = \frac{1}{\sqrt{2}}\left[-i(1+\frac{\eta}{4})e^{im_1 t}|N_1(0)> +(1-\frac{\eta}{4})e^{im_2 t}|N_2(0)>\right], \quad (106)$$

$$|S(t)> = \frac{1}{\sqrt{2}}\left[i(1-\frac{\eta}{4})e^{im_1 t}|N_1(0)> +(1+\frac{\eta}{4})e^{im_2 t}|N_2(0)>\right]. \quad (107)$$

Note that, in the limit of $\eta \to 0$ the two states are normalized and, moreover, they are written in terms of the same eigenstates. It is easy to verify that

$$|< S(t)|N_R(0)>|^2 = \frac{1}{4}(1-\cos\mu t). \quad (108)$$

We can do the same reasoning for $\bar{N}_R(0)$. Let us define the mass eigenstates basis as $\bar{N} = \left\{\bar{N}_0, \bar{N}_1, \bar{N}_2\right\}$, then $\bar{N}_R = V^{\star}_{i\alpha}\bar{N}_i$. We get

$$|\bar{N}_R(0)> = \frac{1}{\sqrt{2}}\left[i(1+\frac{\eta}{4})|\bar{N}_1(0)> +(1-\frac{\eta}{4})|\bar{N}_2(0)>\right]. \quad (109)$$

Now we are interested to calculate the $\bar{N}_R(t) - N_R$ transition, so by remembering the equation of the Majorana fields we can write

$$\begin{aligned} |N_R(t)> &= \frac{1}{\sqrt{2}}[-i(1+\frac{\eta}{4})\left(\alpha_1 c^\dagger_{N_{1R}} u^\dagger_{1R}(\vec{p}) + \beta_1 c^\dagger_{N_{1L}} u^\dagger_{1L}(\vec{p})\right) e^{im_1 t}|0> \\ &+ (1-\frac{\eta}{4})\left(\alpha_2 c^\dagger_{N_{2R}} u^\dagger_{2R}(\vec{p}) + \beta_2 c^\dagger_{N_{2L}} u^\dagger_{2L}(\vec{p})\right) e^{im_2 t}]|0> \qquad (110) \\ |\bar{N}_R(t)> &= \frac{1}{\sqrt{2}}[i(1+\frac{\eta}{4})\left(\alpha_1 c^\dagger_{N_{1L}} u^\dagger_{1L}(\vec{p}) + \beta_1 c^\dagger_{N_{1R}} u^\dagger_{1R}(\vec{p})\right) e^{im_1 t}|0> \\ &+ (1-\frac{\eta}{4})\left(\alpha_2 c^\dagger_{N_{2L}} u^\dagger_{2L}(\vec{p}) + \beta_2 c^\dagger_{N_{2R}} u^\dagger_{2R}(\vec{p})\right) e^{im_2 t}]|0> \qquad (111) \end{aligned}$$

in the limit of $\vec{p}_1 = \vec{p}_2 = \vec{p} \to 0$, $\alpha_1 = \alpha_2 = \beta_1 = \beta_2 = \frac{1}{\sqrt{2}}$ (eq. (34)), we get

$$\begin{aligned} < \bar{N}_R(t)|N_R(0)> &= \frac{1}{2}\left[-(1+\frac{\eta}{4})^2 e^{im_1 t} + (1-\frac{\eta}{4})^2 e^{im_2 t}\right](2\alpha_1\beta_1), \qquad (112) \\ |< \bar{N}_R(t)|N_R(0)>|^2 &= \frac{1}{4}[(1+\frac{\eta}{4})^4 + (1-\frac{\eta}{4})^4 \\ &- (1+\frac{\eta}{4})^2(1-\frac{\eta}{4})^2 \cdot \\ &\cdot \quad (e^{i(m_1-m_2)t} + e^{-i(m_1-m_2)t})](2\alpha_1\beta_1)^2. \qquad (113) \end{aligned}$$

If we stop at order $\mathcal{O}(\eta^0)$

$$|< \bar{N}_R(t)|N_R(0)>|^2 = \frac{1}{2}(1-\cos\mu t)(2\alpha_1\beta_1)^2. \qquad (114)$$

For the $N_R - N_R$ transition

$$\begin{aligned} < N_R(t)|N_R(0)> &= \frac{1}{2}\left[(1+\frac{\eta}{4})^2 e^{im_1 t} + (1-\frac{\eta}{4})^2 e^{im_2 t}\right](\alpha_1^2+\beta_1^2), \qquad (115) \\ |< N_R(t)|N_R(0)>|^2 &= \frac{1}{2}(1+\cos\mu t)(\alpha_1^2+\beta_1^2)^2. \qquad (116) \end{aligned}$$

By normalizing one gets

$$\frac{(2\alpha_1\beta_1)}{\sqrt{(\alpha_1^2+\beta_1^2)^2+(2\alpha_1\beta_1)^2}} = \frac{1}{\sqrt{2}}, \quad (117)$$

$$\frac{(\alpha_1^2+\beta_1^2)}{\sqrt{(\alpha_1^2+\beta_1^2)^2+(2\alpha_1\beta_1)^2}} = \frac{1}{\sqrt{2}}. \quad (118)$$

So finally:

$$|<S(t)|N_R(0)>|^2 = |<\bar{N}_R(t)|N_R(0)>|^2 = \frac{1}{4}(1-\cos\mu t), \quad (119)$$

$$|<N_R(t)|N_R(0)>|^2 = |<\bar{S}(t)|N_R(0)>|^2 = \frac{1}{4}(1+\cos\mu t). \quad (120)$$

Note that we did not explicitly calculate $\bar{S}(t) - N_R$ transition, but with the instruments that we gave it is easy to verify the last equation. As already mentioned we are interested in neutrinos that decay too, so when we write the gauge states in terms of the mass eigenstates we should include the decay in the time evolution:

$$e^{-im_1 t} \to e^{-i(m_1 - i\frac{1}{2}\Gamma_1)t}, \quad (121)$$

$$e^{-im_2 t} \to e^{-i(m_2 - i\frac{1}{2}\Gamma_2)t}. \quad (122)$$

By assuming $\Gamma_1 = \Gamma_2 = \Gamma$ one finds

$$\int_0^\infty |<S(t)|N_R(0)>|^2 dt = \int_0^\infty |<\bar{N}_R(t)|N_R(0)>|^2 dt = \int_0^\infty \frac{1}{4} e^{-\Gamma t}(1-\cos\mu t)dt$$
$$= \frac{1}{4\Gamma}\frac{\mu^2}{\Gamma^2+\mu^2}, \quad (123)$$

$$\int_0^\infty |<N_R(t)|N_R(0)>|^2 dt = \int_0^\infty |<\bar{S}(t)|N_R(0)>|^2 dt = \int_0^\infty \frac{1}{4} e^{-\Gamma t}(1+\cos\mu t)dt$$
$$= \frac{1}{4\Gamma}\left(1+\frac{\Gamma^2}{\Gamma^2+\mu^2}\right) \quad (124)$$

and the sum of the four is $1/\Gamma$.

1.6 Neutrino-antineutrino oscillation in the Inverse See-Saw for three generations

We present the final results for three generations. The matrix V now reads

$$V = \begin{pmatrix} V_L & i\xi^\dagger & \xi^\dagger \\ 0 & -\frac{i}{\sqrt{2}}U_R^\star & \frac{1}{\sqrt{2}}U_R^\star \\ -V_R\xi V_L & \frac{i}{\sqrt{2}}V_R & \frac{1}{\sqrt{2}}V_R \end{pmatrix}$$

where, as in Chapter 3, U_R and V_R are the unitary matrices diagonalizing M_R, V_L is the unitary matrix that diagonalize m_ν. In this section we will use Latin letters for the mass states and Greek letters for the gauge states, so:

$$\begin{aligned} N_\alpha &= V_{i\alpha}N_i \\ \bar{N}_\beta &= V^\star_{j\beta}\bar{N}_j. \end{aligned} \tag{125}$$

So, we get for the gauge states N_R:

$$\begin{aligned} < N_{R\beta}(t)|N_{R\alpha}(0) > &= < N_j(t)|V^\star_{j\beta}V_{i\alpha}|N_i(0) > \\ < \bar{N}_{R\beta}(t)|N_{R\alpha}(0) > &= < \bar{N}_j(t)|V_{j\beta}V_{i\alpha}|N_i(0) > \end{aligned} \tag{126}$$

with $\alpha, \beta = 4, 5, 6$. By following the same procedure as in one generation case one gets:

$$\begin{aligned} \int_0^\infty | < N_R(t)|N_R(0) > |^2 dt &= \frac{1}{2}V^\star_{j\beta}V_{j\alpha}\left[\frac{1}{\Gamma_j} + \frac{1}{\Gamma_k} + \frac{4(\Gamma_j+\Gamma_k)}{4(\Delta m_{jk})^2 + (\Gamma_j+\Gamma_k)^2}\right]V^\star_{j\alpha}V_{j\beta} \\ \int_0^\infty | < \bar{N}_R(t)|N_R(0) > |^2 dt &= \frac{1}{2}V_{j\beta}V_{j\alpha}\left[\frac{1}{\Gamma_j} + \frac{1}{\Gamma_k} - \frac{4(\Gamma_j+\Gamma_k)}{4(\Delta m_{jk})^2 + (\Gamma_j+\Gamma_k)^2}\right]V^\star_{j\alpha}V^\star_{j\beta}, \end{aligned}$$

with $j = 4, 5, 6, k = j + 3$.

Acknowledgements

These years spent in Valencia have been years of personal and intellectual growth for me. I have known traditions and ways of living different from mine, festivals, songs and dances that represent the liveliness of this city. Despite initial concerns and homesickness, I would say that living in a foreign country is one of those things that everyone should try at least once. It is something that completes you and transforms you into a citizen of the world.
I want to acknowledge the financial support from the Santiago Grisolia scholarship granted from the Valencian Community.

This thesis is the result of all the work done during these years of PhD in Valencia and now I want to thank all people who supported me.
First of all, I want to thank my supervisor Martin Hirsch. He introduced me to the world of neutrino physics, he gave me the opportunity to learn new concepts of physics always proposing interesting and stimulating topics and it is thanks to him that the writing of this thesis has become possible. Thank you, not only for being a great scientist, not only for all the brilliant discussions, not just for all the tips and advice, but for the great person you are, for your empathy, your patience, for how you transmit your love for the science and your encouragement.
Next, my thanks go to José Valle, as well an exceptional physicist, an incredible leader of the group, always full of ideas to stimulate his students and postdocs. It was an honor and a pleasure to be part of the AHEP group. I also want to thank all the people who collaborated with me to carry out the works summarized in this thesis. The first thanks goes to Enrico Nardi, a great physicist and a special person. Without him I probably would not have undertaken this route in Valencia. Our meeting represents

the turning point of my academic life and I will always be grateful to him for being immediately interested in my studies, kind and supportive all the time. Second, I would like to thank my collaborator and friend Renato Fonseca. First of all for the computational code he wrote to fit solar data and Super-K atmospheric data. Speaking of his genius is superfluous, so I will limit myself to thank him for all the explanations given every time I asked a question and for all the scientific knowledge he gave me. Last but not least, I thank Juan Carlos for the precious advice, kind and helpful during his visits in Valencia.
I would like to thank all the ahepians encountered during these years that have made the working days more enjoyable: Mariam and Avelino for their support and their innumerable advice, Sergio for having always taken care of all the bureaucratic problems (not even his jokes will easily be forgotten), Carolina who is the first person I met in Valencia and welcomed me into her house, Marcela for her smiles and the shared wine glasses, Cesar and Rahul for their presence in moments of fragility, Alma, Lucho, Sofiane, David, Masud, Thomas, Christoph, Ricardo, Pablo, Stefano, Salva, Mario, Pedro.
Thanks all those with whom a great friendship was born: Nicolás, Félix, amigo Carlos, Roberto. Thank you for all the times we have sung Riccardo Cocciante songs, for all the times we dance Raffaella Carrá music, for all the beers drunk, the existential discourses, the tears that you patiently consoled and the laughter that you gave me.
Gracias a las "chicas del IFIC": Giulia, Rebecca, Valentina y Paulina. Por todos los momentos pasados, por compartir ansiedades y paranoias así como alegría y ligereza. Gracias a Adriana y Esther, aunque haya cambiado cuatro casas en Valencia, ¡en mi corazón sois mis únicas compañeras de piso! Nuestra vida diaria juntas fue maravillosa, realmente compartimos todo y nunca olvidaré cómo siempre nos hemos ayudado mutuamente. Gracias a Raffaele y MariaJosé por darme la bienvenida a su casa, por sus historias sobre el mundo, los fines de semana en Chelva, donde también he sido juez en una competencia de paella y gracias a Nabil por ser un ejemplo de fuerza y positividad.
Grazie ai miei amici di sempre, per il bene che ci vogliamo e per come siamo legati nonostante la distanza. E infine grazie ad Andrea, che capisce i miei sogni e li incoraggia e non mette freni alla mia libertá.

Bibliography

[1] A. B. McDonald, Rev. Mod. Phys. **88**, 030502 (2016).

[2] T. Kajita, Rev. Mod. Phys. **88**, 030501 (2016).

[3] R. N. Mohapatra and P. B. Pal, World Sci. Lect. Notes Phys. **41** (1991) 1.

[4] J. W. F. Valle and J. C. Romao, Wiley, 2015

[5] P. F. de Salas, D. V. Forero, C. A. Ternes, M. Tortola and J. W. F. Valle, arXiv:1708.01186 [hep-ph].

[6] S. Weinberg, Phys. Rev. Lett. **43**, 1566 (1979).

[7] A. Abada, C. Biggio, F. Bonnet, M. B. Gavela and T. Hambye, JHEP **0712** (2007) 061 doi:10.1088/1126-6708/2007/12/061 [arXiv:0707.4058 [hep-ph]].

[8] R. N. Mohapatra and J. W. F. Valle, Phys. Rev. **D 34** (1986) 1642.

[9] F. Bonnet, M. Hirsch, T. Ota, W. Winter, JHEP, **1207**, 153, 2012, arXiv:1204.5862[hep-ph]

[10] D. Aristizabal Sierra, A. Degee, L. Dorame and M. Hirsch, JHEP, **1503**, 040, 2015

[11] R. Cepedello, R. Fonseca and M. Hirsch, Systematic classification of three-loop realizations of the Weinberg operator, 2018

[12] F. Bonnet, D. Hernandez, T. Ota and W. Winter, JHEP, **0910**, 076, 2009

[13] R. Cepedello, M. Hirsch and J. C.Helo, JHEP, **07**, 079, 2017

[14] R. Cepedello, M. Hirsch and J. C. Helo, JHEP, **01**, 009, 2018, arXiv:1709.03397 [hep-ph]

[15] B. Kayser, eConf **C 040802** (2004) L004 [hep-ph/0506165].

[16] L. Wolfenstein, Phys. Rev. **D 17** (1978) 2369. doi:10.1103/PhysRevD.17.2369

[17] P. Minkowski, Phys.Lett. **B 67**, 421 (1977).

[18] T. Yanagida, Conf.Proc. **C 7902131**, 95 (1979).

[19] M. Gell-Mann, P. Ramond, and R. Slansky, Conf.Proc. C790927, 315 (1979), Supergravity, P. van Nieuwenhuizen and D.Z. Freedman (eds.), North Holland Publ. Co., 1979.

[20] R. N. Mohapatra and G. Senjanovic, Phys. Rev. Lett. **44**, 912 (1980).

[21] M. Magg and C. Wetterich, Phys.Lett. **B 94**, 61 (1980).

[22] J. Schechter and J. Valle, Phys. Rev. **D 22**, 2227 (1980).

[23] C. Wetterich, Nucl.Phys. **B 187**, 343 (1981).

[24] G. Lazarides, Q. Shafi, and C. Wetterich, Nucl.Phys. **B 181**, 287 (1981).

[25] R. N. Mohapatra and G. Senjanovic, Phys. Rev. **D 23**, 165 (1981).

[26] T. P. Cheng and L.-F. Li, Phys. Rev. **D 22**, 2860 (1980).

[27] R. Foot, H. Lew, X. He, and G. C. Joshi, Z.Phys. **C 44**, 441 (1989).

[28] S. Kanemura and K. Yagyu, Radiative corrections to electroweak parameters in the Y=1 Higgs triplet model and implication with the recent Higgs boson searches at the CERN LHC, (2012).

[29] F. F. Deppisch, L. Graf, S. Kulkarni, S. Patra, W. Rodejohann, N. Sahu and U. Sarkar, Phys. Rev. **D 93**, no. 1, 013011 (2016) doi:10.1103/PhysRevD.93.013011 [arXiv:1508.05940 [hep-ph]].

[30] G. Anamiati, M. Hirsch and E. Nardi, JHEP **1610** (2016) 010 doi:10.1007/JHEP10(2016)010 [arXiv:1607.05641 [hep-ph]].

[31] J. Casas and A. Ibarra, Nucl.Phys. **B 618**, 171 (2001), arXiv:hep-ph/0103065.

[32] I. Avignone, Frank T., S. R. Elliott, and J. Engel, Rev.Mod.Phys. **80**, 481 (2008), arXiv:0708.1033.

[33] F. F. Deppisch, M. Hirsch, and H. Päs, J.Phys. **G 39**, 124007 (2012), arXiv:1208.0727.

[34] W.-Y. Keung and G. Senjanovic, Phys.Rev.Lett. **50**, 1427 (1983).

[35] J. C. Pati and A. Salam, Phys.Rev. **D 10**, 275 (1974).

[36] R. Mohapatra and J. C. Pati, Phys.Rev. **D 11**, 2558 (1975).

[37] J. Helo, M. Hirsch, H. Päs, and S. Kovalenko, Phys.Rev. **D 88**, 073011 (2013), arXiv:1307.4849.

[38] M. Fukugita and T. Yanagida, Phys. Lett. **B 174**, 45 (1986).

[39] W. Buchmuller, P. Di Bari, and M. Plumacher, Annals Phys. **315**, 305 (2005), arXiv:hep-ph/0401240.

[40] S. Davidson, E. Nardi, and Y. Nir, Phys. Rept. **466**, 105 (2008), arXiv:0802.2962.

[41] C. S. Fong, E. Nardi, and A. Riotto, Adv. High Energy Phys. **2012**, 158303 (2012), arXiv:1301.3062.

[42] E. K. Akhmedov, M. Lindner, E. Schnapka, and J. W. F. Valle, Phys. Rev. **D 53**, 2752 (1996), arXiv:hep-ph/9509255.

[43] E. K. Akhmedov, M. Lindner, E. Schnapka, and J. W. F. Valle, Phys. Lett. **B 368**, 270 (1996), arXiv:hep-ph/9507275.

[44] S. Bray, J. S. Lee and A. Pilaftsis, Nucl. Phys. **B 786**, 95 (2007) [hep-ph/0702294 [HEP-PH]].

[45] J. Kersten and A. Y. Smirnov, Phys. Rev. **D 76**, 073005 (2007) [arXiv:0705.3221 [hep-ph]].

[46] ATLAS Collaboration, G. Aad *et al.*, Eur.Phys.J. **C 72**, 2056 (2012), arXiv:1203.5420.

[47] ATLAS, G. Aad *et al.*, JHEP **07**, 162 (2015), arXiv:1506.06020.

[48] CMS Collaboration, report CMS-PAS-EXO-12-017 (2012).

[49] CMS, V. Khachatryan *et al.*, Eur. Phys. J. **C 74**, 3149 (2014), arXiv:1407.3683.

[50] See articles referring to [49]: http://inspirehep.net/record/1306295/citations

[51] F. F. Deppisch, T. E. Gonzalo, S. Patra, N. Sahu and U. Sarkar, Phys. Rev. **D 90**, no. 5, 053014 (2014) doi:10.1103/PhysRevD.90.053014 [arXiv:1407.5384 [hep-ph]].

[52] M. Heikinheimo, M. Raidal and C. Spethmann, Eur. Phys. J. **C 74**, no. 10, 3107 (2014) doi:10.1140/epjc/s10052-014-3107-9 [arXiv:1407.6908 [hep-ph]].

[53] B. A. Dobrescu and Z. Liu, Phys. Rev. Lett. **115**, no. 21, 211802 (2015) doi:10.1103/PhysRevLett.115.211802 [arXiv:1506.06736 [hep-ph]].

[54] J. Brehmer, J. Hewett, J. Kopp, T. Rizzo and J. Tattersall, JHEP **1510**, 182 (2015) doi:10.1007/JHEP10(2015)182 [arXiv:1507.00013 [hep-ph]].

[55] K. Cheung, W. Y. Keung, P. Y. Tseng and T. C. Yuan, Phys. Lett. **B 751**, 188 (2015) doi:10.1016/j.physletb.2015.10.029 [arXiv:1506.06064 [hep-ph]].

[56] B. Allanach, S. Biswas, S. Mondal and M. Mitra, Phys. Rev. **D 91**, no. 1, 011702 (2015) doi:10.1103/PhysRevD.91.011702 [arXiv:1408.5439 [hep-ph]].

[57] CMS Collaboration [CMS Collaboration], CMS-PAS-EXO-17-011.

[58] P. S. Bhupal Dev and R. N. Mohapatra, Phys. Rev. Lett. **115**, 181803 (2015), arXiv:1508.02277.

[59] F. F. Deppisch, P. S. Bhupal Dev and A. Pilaftsis, New J. Phys. **17**, no. 7, 075019 (2015)

[60] A. Das, P. S. B. Dev and R. N. Mohapatra, Phys. Rev. **D 97** (2018) no.1, 015018 doi:10.1103/PhysRevD.97.015018 [arXiv:1709.06553 [hep-ph]].

[61] D. Forero, M. Tortola, and J. Valle, Phys.Rev. **D 90**, 093006 (2014), arXiv:1405.7540.

[62] C. Hati, S. Patra, P. Pritimita and U. Sarkar, Front. in Phys. **6** (2018) 19.

[63] Y. Nir, Conf. Proc. **C 9207131**, 81 (1992).

[64] G. Anamiati, R. M. Fonseca and M. Hirsch, Phys. Rev. **D 97** (2018) no.9, 095008 doi:10.1103/PhysRevD.97.095008 [arXiv:1710.06249 [hep-ph]].

[65] S. Abe et al. (KamLAND), Phys. Rev. Lett. **100** (2008) 221803, arXiv:0801.4589 [hep-ex].

[66] L. Wolfenstein, Nucl. Phys., **B 186** (1981) 147–152.

[67] J. W. F. Valle, Phys. Rev. **D 27** (1983) 1672–1674.

[68] S. T. Petcov, Phys. Lett. **110 B** (1982) 245–249.

[69] M. Doi et al., Prog. Theor. Phys. **70** (1983) 1331.

[70] G. Dutta and A. S. Joshipura, Phys. Rev. **D 51** (1995) 3838–3842, arXiv:hep-ph/9405291 [hep-ph].

[71] A. S. Joshipura and S. D. Rindani, Phys. Lett. **B494** (2000) 114–123, arXiv:hep-ph/0007334 [hep-ph].

[72] S. M. Bilenky and B. Pontecorvo, Sov. J. Nucl. Phys. **38** (1983) 248, [Yad. Fiz.38,415(1983)].

[73] S. M. Bilenky and S. T. Petcov, Rev. Mod. Phys. **59** (1987) 671, [Erratum: Rev. Mod. Phys.60,575(1988)].

[74] C. Giunti, C. W. Kim and U. W. Lee, Phys. Rev. **D 46** (1992) 3034–3039, arXiv:hep-ph/9205214 [hep-ph].

[75] Y. Nir, JHEP, **06** (2000) 039, arXiv:hep-ph/0002168 [hep-ph].

[76] P. H. Frampton, M. C. Oh and T. Yoshikawa, Phys. Rev. **D 65** (2002) 073014, arXiv:hep-ph/0110300 [hep-ph].

[77] X.-G. He, Eur. Phys. J. **C 34** (2004) 371–376, arXiv:hep-ph/0307172 [hep-ph].

[78] B. Brahmachari and S. Choubey, Phys. Lett. **B 531** (2002) 99–104, arXiv:hep-ph/0111133 [hep-ph].

[79] A. Zee, Phys. Lett. 95B, 461 (1980).

[80] A. Geiser, Phys. Lett., **B 444** (1999) 358, arXiv:hep-ph/9901433 [hep-ph].

[81] W. Krolikowski, Acta Phys. Polon. **B 31** (2000) 663–672, arXiv:hep-ph/9910308 [hep-ph].

[82] K. R. S. Balaji, A. Kalliomaki and J. Maalampi, Phys. Lett., **B 524** (2002) 153–160, arXiv:hep-ph/0110314 [hep-ph].

[83] E. Ma and P. Roy, Phys. Rev., **D 52** (1995) R4780–R4783, arXiv:hep-ph/9504342 [hep-ph].

[84] S. Goswami and A. S. Joshipura, Phys. Rev., **D 65** (2002) 073025, arXiv:hep-ph/0110272 [hep-ph].

[85] K. S. Babu and R. N. Mohapatra, Phys. Lett. **B 522** (2001) 287, arXiv:hep-ph/0110243 [hep-ph]

[86] A. de Gouvea, W.-C. Huang and J. Jenkins, Phys. Rev. **D 80** (2009) 073007, arXiv:0906.1611 [hep-ph].

[87] M. Cirelli, G. Marandella, A. Strumia and F. Vissani, Nucl. Phys. **B 708** (2005) 215–267, arXiv:hep-ph/0403158 [hep-ph].

[88] J. F. Beacom et al., Phys. Rev. Lett., **92** (2004) 011101, arXiv:hep-ph/0307151 [hep-ph].

[89] A. Esmaili, Phys. Rev., **D 81** (2010) 013006, arXiv:0909.5410 [hep-ph].

[90] A. Esmaili and Y. Farzan, JCAP, **1212** (2012) 014, arXiv:1208.6012 [hep-ph].

[91] A. S. Joshipura, S. Mohanty and S. Pakvasa, Phys. Rev. **D 89** (2014) 3 033003, arXiv:1307.5712 [hep-ph].

[92] M. Kobayashi and C. S. Lim, Phys. Rev. **D 64** (2001) 013003, arXiv:hep-ph/0012266 [hep-ph].

[93] Y. H. Ahn, S. K. Kang and C. S. Kim, JHEP, **10** (2016) 092, arXiv:1602.05276 [hep-ph].

[94] G. J. Stephenson, Jr., J. T. Goldman, B. H. J. McKellar and M. Garbutt, Int. J. Mod. Phys. **A 20** (2005) 6373–6390, arXiv:hep-ph/0404015 [hep-ph].

[95] K. L. McDonald and B. H. J. McKellar, Int. J. Mod. Phys. **A 22** (2007) 2211–2222, arXiv:hep-ph/0401073 [hep-ph].

[96] D. Chang and O. C. W. Kong, Phys. Lett., **B 477**, (2000) 416–423, arXiv:hep-ph/9912268 [hep-ph].

[97] V. Berezinsky, M. Narayan and F. Vissani, Nucl. Phys., **B 658**, (2003) 254–280, arXiv:hep-ph/0210204 [hep-ph].

[98] L. A. Sanchez, W. A. Ponce and R. Martinez, Phys. Rev., **D 64**, (2001) 075013, arXiv:hep-ph/0103244 [hep-ph].

[99] R. M. Fonseca and M. Hirsch, Phys. Rev., **D 94**, (2016) 11 115003, arXiv:1607.06328 [hep-ph].

[100] S. Abel, A. Dedes and K. Tamvakis, Phys. Rev., **D 71**, (2005) 033003, arXiv:hep-ph/0402287 [hep-ph].

[101] Q. R. Ahmad et al. (SNO), Phys. Rev. Lett., **89**, (2002) 011301, arXiv:nucl-ex/0204008 [nucl-ex].

[102] K. Abe et al. (Super-Kamiokande), Phys. Rev., **D 91** (2015) 052019, arXiv:1410.2008 [hep-ex].

[103] N. Agafonova et al. (OPERA), JHEP, **06**, (2015) 069, arXiv:1503.01876 [hep-ex].

[104] P. Adamson et al. (MINOS, Daya Bay), Phys. Rev. Lett. **117** (2016) 15 151801, arXiv:1607.01177 [hep-ex].

[105] M. G. Aartsen et al. (IceCube), Phys. Rev., **D 95**, (2017) 11 112002, arXiv:1702.05160 [hep-ex].

[106] P. Adamson et al. (NOvA), (2017), arXiv:1706.04592 [hep-ex].

[107] K. N. Abazajian et al., arXiv:1204.5379 [hep-ph].

[108] S. Gariazzo et al., J. Phys. **G 43**, (2016) 033001, arXiv:1507.08204 [hep-ph].

[109] F. James, Hackensack, USA: World Scientific (2006) 345 p

[110] K. Abe et al. (Super-Kamiokande), Phys. Rev. **D 94**, (2016), 5 052010, arXiv:1606.07538 [hep-ex].

[111] G. Bellini et al. (BOREXINO), Nature, **512**, (2014), 7515 383–386.

[112] G. Bellini et al., Phys. Rev. Lett., **107**, (2011), 141302, arXiv:1104.1816 [hep-ex].

[113] T. Kajita, Ann. Rev. Nucl. Part. Sci., **64**, (2014), 343–362.

[114] P. Adamson et al. (MINOS), Phys. Rev. Lett. **110**, (2013), 25 251801, arXiv:1304.6335 [hep-ex].

[115] K. Abe et al. (T2K), Phys. Rev. **D 91**, (2015), 7 072010, arXiv:1502.01550 [hep-ex].

[116] F. P. An et al. (Daya Bay), Phys. Rev. **D 95**, (2017) 7 072006, arXiv:1610.04802 [hep-ex].

[117] The KamLAND Collaboration, Phys. Rev. **D 88** (2013) no.3,0333001, arXiv: 1303.4667

[118] U. S. KamLand Collaboration, Proposal for US Participation in KamLAND, March, 1999

[119] B.T. Cleveland et al., Ap. J. 496, 505 (1998); K. Lande and P. Wildenhain, Nucl. Phys. **B 118** (Proc. Suppl.), 49 (2003); R. Davis, Nobel Prize Lecture (2002).

[120] F. Kaether et al., Phys. Lett. **B 685**, 47 (2010); W. Hampel et. al. (GALLEX Collaboration), Phys. Lett. **B 447**, 127 (1999); J.N. Abdurashitov et al. (SAGE collaboration), Phys. Rev. **C 80**, 015807 (2009).

[121] K.S. Hirata et al. (KamiokaNDE Collaboration), Phys. Rev. Lett. **63**, 16 (1989); Y. Fukuda et al. (SuperKamiokande Collaboration), Phys. Rev. Lett. **81**, 1562 (1998); J.P. Cravens et al. (SuperKamiokaNDE Collaboration), Phys. Rev. **D 78**, 032002 (2008).

[122] Q.R. Ahmad et al. (SNO Collaboration), Phys. Rev. Lett. **87**, 071301 (2001); B. Aharmim et al. (SNO Collaboration), Phys. Rev. **C 75**, 045502 (2007); B. Aharmim et al. (SNO Collaboration), Phys. Rev. **C 81**, 055504 (2010).

[123] J.N. Bahcall, A. Serenelli, and S. Basu, Ap. J. Suppl. **165**, 400 (2006).

[124] J. Hosaka et al., Phys. Rev. **D 73**, 112001 (2006).

[125] K. Anderson *et al.*, FERMILAB-DESIGN-1998-01.

[126] D. G. Michael *et al.* [MINOS Collaboration], Phys. Rev. Lett. **97** (2006) 191801

[127] T2K Collaboration, (2003), letter of Intent: Neutrino Oscillation Experiment at JHF.

[128] K. Abe et al. (T2K Collaboration), Nucl. Instrum. Meth. **A 659**, 106 (2011).

[129] K. Abe et al. (T2K Collaboration), Phys. Rev. Lett. **107**, 041801 (2011).

[130] K. Abe et al. (T2K Collaboration), Phys. Rev. **D 85**, 031103 (2012).

[131] Y. Fukuda et al., Nucl. Instrum. Meth. **A 501** (2003).

[132] D. Beavis, A. Carroll, I. Chiang, et al., Physics Design Report, BNL 52459 (1995).

[133] The T2K Collaboration, Phys. Rev. **D 87**, 012001 (2013), arXiv: 1211.0469.

[134] F. An et al. (JUNO), J. Phys., **G 43**, 3 030401, (2016).

[135] Y. F. Li, J. Cao, Y. Wang and L. Zhan, Phys. Rev. **D 88** (2013) 013008, arXiv:1303.6733 [hep-ex].

[136] F. Suekane, for the KamLAND collaboration, Progress in Particle and Nuclear Physics, **57** (2006), 106-126

[137] Liang Zhan, Yifang Wang, Jun Cao, Liangjian Wen , Phys. Rev. **D 78:111103**, 2008, arXiv: 0807.3203

[138] G. Anamiati, Oscar Castillo-Felisola, Renato M. Fonseca, J. C. Helo, M. Hirsch, in phase of publication, arxiv: 1806.07264

[139] P. Minkowski, Phys. Lett. B, **67**, 421, 1977

[140] T. Yanagida, Conf. Proc., **C 7902131**, 95, 1979

[141] M. Gell-Mann, P. Ramond, R. Slansky, Conf. Proc., **C 790927**, 315, 1979

[142] R.N. Mohapatra, G. Senjanovic, Phys. Rev. Lett. **44**, 912, 1980

[143] M. Magg, C. Wetterich, Phys. Lett., **B 94**, 61, 1980

[144] C. Wetterich, Nucl. Phys., **B 187**, 343, 1981

[145] G. Lazarides, Q. Shafi, C. Wetterich, Nucl. Phys., **B 181**, 287, 1981

[146] Cheng and Li, Phys. Rev., **D 22**, 2860, 1980

[147] R. Foot, H. Lew, X. He, G. C. Joshi, Z. Phys., **C 44**, 441, 1989

[148] C. Patrignani et al., Collaboration Particle Data Group, Chin. Phys., **C 40**, 100001, 2016

[149] Y. Cai, J. Herrero-García, M. A.Schmidt, A. Vicente and R. R. Volkas, Front. in Phys. **5**, 63, 2017

[150] A. Zee, Phys. Lett., **B 93**, 389, 1980

[151] A. Zee, Nucl. Phys., **B 264**, 99, 1986

[152] K. S.Babu, Phys. Lett., **B 203**, 132, 1988

[153] L. M.Krauss, S. Nasri and M. Trodden, Phys. Rev., **D 67**, 085002, 2003

[154] M. Gustafsson, J. M. No and M. A.Rivera, Phys. Rev. Lett. **110**, 211802, 2013, Erratum: Phys. Rev. Lett. 112, no. 25, 259902, 2014

[155] K. S.Babu, S. Nandi and Z. Tavartkiladze, Phys. Rev., **D 80**, 071702, 2009

[156] I. Picek and B. Radovcic, Phys. Lett., **B 687**, 338, 2010, arXiv:0911.1374 [hep-ph]

[157] K. Kumericki, I. Picek and B. Radovcic, Phys. Rev. **D 86**, 013006, 2012, arXiv:1204.6599 [hep-ph]

[158] Y. Liao, JHEP, **06**, 098, 2011, arXiv:1011.3633 [hep-ph]

[159] K. L.McDonald, JHEP, **07**, 020, 2013, arXiv:1303.4573

[160] K. L.McDonald, JHEP, **11**, 131, 2013, arXiv:1310.0609 [hep-ph]

[161] T. Nomura, H. Okada, Phys. Rev., **D 96**, 095017, 2017), arXiv:1708.03204 [hep-ph]

[162] T. Nomura, H. Okada, Phys. Rev., **D 94**, 055012, 2016, arXiv:1605.02601 [hep-ph]

[163] E. Ma, Phys. Rev. Lett. **81**, 1171, 1998, arXiv:hep-ph/9805219 [hep-ph]

[164] E. Ma, Phys. Rev., **D 73**, 077301, 2006, arXiv:hep-ph/0601225 [hep-ph]

[165] Y. Liao, Phys. Lett., **B 694**, 346, 2011, arXiv:1009.1692 [hep-ph]

[166] ATLAS-CONF-2017-053, 2017

[167] R. C.Read, K. L.McAvaney, 77–89, 1981

[168] K. Grotz and H.V. Klapdor, *The weak Interaction in Nuclear Particle and Astrophysics*, 0th Edition, CRC Press, 1990.